

On the Morphology and Interfaces of Nanostructured Hematite Photoanodes for Solar-Driven Water Splitting

THÈSE N° 5180 (2011)

PRÉSENTÉE LE 14 OCTOBRE 2011

À LA FACULTÉ SCIENCES DE BASE

LABORATOIRE DE PHOTONIQUE ET INTERFACES

PROGRAMME DOCTORAL EN CHIMIE ET GÉNIE CHIMIQUE

ÉCOLE POLYTECHNIQUE FÉDÉRALE DE LAUSANNE

POUR L'OBTENTION DU GRADE DE DOCTEUR ÈS SCIENCES

PAR

Florian LE FORMAL

acceptée sur proposition du jury:

Prof. J.-E. Moser, président du jury

Prof. M. Grätzel, directeur de thèse

 Prof. X. Hu, rapporteur

 Prof. L. Peter, rapporteur

 Prof. P. Schmuki, rapporteur



ÉCOLE POLYTECHNIQUE
FÉDÉRALE DE LAUSANNE

Suisse

2011

“We are like tenant farmers chopping down the fence around our house for fuel when we should be using Natures inexhaustible sources of energy — sun, wind and tide. ... I'd put my money on the sun and solar energy. What a source of power! I hope we don't have to wait until oil and coal run out before we tackle that.”

Thomas Alva Edison, in conversation with Henry Ford. 1931

ABSTRACT

A sustainable route to store the energy provided by the Sun, is to directly convert sunlight into molecular hydrogen using a semiconductor performing water photolysis. Hematite ($\alpha\text{-Fe}_2\text{O}_3$) is promising for this application due to its ample abundance, chemical stability and significant light absorption (with a band gap of 2.0 – 2.2 eV). Despite these advantageous properties, several drawbacks restrain the utilization of iron oxide for photoelectrochemical water splitting. The first limitation, namely the conduction band edge lower than the water reduction potential, can be straightforwardly overcome by adding a second solar system in tandem, which can absorb a complementary part of the solar spectrum and bring the electron at an energetic level higher than the hydrogen evolution potential.

The second drawback arises from the disaccord between the short charge carrier diffusion length and the large light penetration depth. It is therefore necessary to control the hematite morphology on a length scale similar to the hole transport length. To further enhance the photoelectrochemical performance, a new concept for water splitting is introduced in this thesis. The host-guest approach consists in decoupling the different tasks of the photoanode (on one side light harvesting and water oxidation center, on the other side electron conduction to the substrate) by depositing a thin layer of hematite onto a mesoporous host (WO_3 in this study). This concept has been demonstrated to increase the photocurrent by *ca.* 20% due to enhanced quantum efficiencies at long wavelengths. This demonstration has been nonetheless limited by the iron oxide thin films overall efficiency.

Thin films photoactivity is then investigated by two means: first by controlling their nucleation on a modified substrate and secondly by incorporating plasmonic nanoparticles aimed to localize absorption in the thin film. The formation of a SiO_x buffer layer on the substrate prior to deposition of hematite by $\text{Fe}(\text{acac})_3$ spray is shown to modify the film formation mode and its physical properties. These films exhibit photoactivity from an optical thickness of 12.5 nm (as compared to 25 nm without underlayer). The study of hematite photoanodes with gold nanoparticles, embedded or deposited on its surface, establish that charge transfer from metal nanoparticles is occurring only at overlapping wavelengths between the plasmonic resonance and the semiconductor absorption. Nevertheless, photoelectrochemical performances are reduced because of high recombination rate at the metal/semiconductor interface.

Finally the third limitation, *i.e.* the large overpotential required to observe the onset of water splitting photocurrent, is tackled in the last part. The onset potential of photocurrent is decreased by a very thin coating of Al_2O_3 (0.1 – 2 nm), deposited by ALD, on the nanostructured photoanode. The subsequent application of the Co^{2+} catalyst further reduces the overpotential and results in a record photocurrent at 0.9 V_{RHE} of over 0.4 mA cm^{-2} . This investigation clearly distinguishes two causes for this energy loss: surface traps and slow oxidation kinetics. The charge accumulation and the Fermi level pinning, observed at low bias potential and assigned to these surface states were further rationalized in an investigation on photocurrent and photovoltage transients.

Keywords:

Photoelectrochemistry, Water Splitting, Hydrogen Production, Oxygen Evolution, Metal-Oxide Semiconductors, Hematite, Iron Oxide, Nanostructures, Surface.

RESUME

Une méthode durable pour stocker l'énergie solaire, est de convertir directement les radiations solaires en molécules d'hydrogène, en utilisant un semi-conducteur pour effectuer la photolyse de l'eau. L'hématite ($\alpha\text{-Fe}_2\text{O}_3$) est un matériau prometteur pour cette application en raison de son abondance, de sa stabilité chimique et de sa capacité à absorber une partie importante de la lumière (avec une bande interdite de 2,0 – 2,2 eV). Malgré ces propriétés avantageuses, il existe des limites intrinsèques à l'utilisation de l'oxyde de fer pour le craquage photoélectrochimique de l'eau. La première contrainte, à savoir la position de la bande de conduction inférieure au potentiel de réduction de l'eau, peut être directement surmontée par l'ajout en série d'un seconde cellule solaire, en tandem, qui absorbera une partie complémentaire du spectre solaire et amènera les électrons à un niveau énergétique plus élevé que le potentiel de dégagement d'hydrogène.

Le second obstacle provient du désaccord entre la courte longueur de diffusion des porteurs de charge et la longue profondeur de pénétration de la lumière. Il est donc nécessaire de contrôler la morphologie des électrodes en hématite sur une échelle de taille similaire à la longueur de transport du trou. Pour améliorer les performances photoélectrochimiques, un nouveau concept pour le craquage de l'eau est introduit dans cette thèse. L'approche hôte-invité consiste à découpler les différentes fonctions de la photoanode (d'un côté l'absorption de la lumière et l'oxydation de l'eau, de l'autre la conduction des électrons jusqu'au substrat) en déposant une fine couche d'hématite sur un hôte mésoporeux (WO_3 dans cette étude). Ce concept a démontré une augmentation du photocourant de 20%, ce qui est expliqué par une meilleure conversion des longueurs d'onde élevées ($> 500 \text{ nm}$). Cependant l'efficacité de ce concept a été limitée par le faible rendement quantique des films minces d'oxyde de fer.

La photoactivité des films minces est ensuite étudiée selon deux axes: d'abord en contrôlant leur nucléation sur un substrat modifié, puis, en incorporant des nanoparticules plasmoniques dans le but de localiser l'absorption dans le film mince. La formation d'une sous-couche SiO_x sur le substrat avant le dépôt d'hématite par pyrolyse de spray à partir de $\text{Fe}(\text{acac})_3$, modifie le mode de nucléation du film ainsi que ses propriétés physiques. Ces films présentent de la photoactivité à partir d'une épaisseur optique de 12,5 nm (contre 25 nm sans sous-couche). L'étude des photoanodes d'hématite comprenant des nanoparticules d'or, dans le volume ou déposées en surface, établit que le transfert de charge à partir de nanoparticules métalliques se produit seulement à des longueurs d'onde où la résonance plasmonique et l'absorption du semi-conducteur se chevauchent. Néanmoins, les performances pour le craquage de l'eau ont diminué dû à des taux de recombinaison élevés à l'interface métal / semi-conducteur.

La troisième contrainte, précisément la surtension importante nécessaire pour observer l'apparition du photocourant lié à la décomposition de l'eau, est abordée dans la dernière partie. Le potentiel d'apparition du photocourant est diminué par une très fine couche d' Al_2O_3 (0,1 – 2 nm), déposée par ALD, sur des photoanodes nanostructurées. L'application successive du catalyseur Co^{2+} permet de réduire davantage la surtension et aboutit à un photocourant record de $0,4 \text{ mA cm}^{-2}$ à $0,9 \text{ V}_{\text{RHE}}$. Cette étude permet de distinguer clairement deux causes pour cette perte d'énergie: la présence de pièges de surface et une cinétique d'oxydation lente. L'accumulation de charge et l'immobilisation du niveau de Fermi, observées à faible

polarisation et attribuées à ces états de surface, ont été rationalisées dans une étude des photocourants et phototension transitoires.

Mots Clés:

Photoelectrochimie, Craquage de l'eau, Production d'hydrogène, Photoanode, Semi-conducteurs Metallo-organique, Hématite, Oxyde de Fer, Nanostructures, Surface.

LIST OF ABBREVIATIONS AND SYMBOLS

α	Absorption coefficient
AC	Alternating current
ALD	Atomic layer deposition
APCVD	Atmospheric pressure CVD
C	Capacitance (in F)
CVD	Chemical vapor deposition
DSC	Dye-sensitized solar cell
e	Elementary charge ($= 1.602 \cdot 10^{-19}$ C)
E_C	Potential of the edge of the conduction band (in V)
E_F	Fermi level (in V)
E_g	Bandgap energy (in eV)
E_{Redox}	Redox potential or electrolyte energy mediator (in V)
E_V	Potential of the edge of the valence band (in V)
ΔJ_{max}	Maximum of the photocurrent transient (in mA cm $^{-2}$)
ΔJ_{ss}	Photocurrent transient amplitudes in NaOH, difference between steady state values (in mA cm $^{-2}$)
$\Delta J_{ss, H_2O_2}$	Photocurrent transient amplitudes in NaOH + H $_2$ O $_2$, difference between steady state values (in mA cm $^{-2}$)
$\Delta NIPCE$	Difference in normalized IPCE measurements
ΔV_{ss}	Photovoltage transient amplitudes in NaOH, difference between steady state values (in V)
$\Delta V_{ss, H_2O_2}$	Photovoltage transient amplitudes in NaOH + H $_2$ O $_2$, difference between steady state values (in V)
ϵ_0	Permittivity of free space ($= 8.85419 \cdot 10^{-12}$ F m $^{-1}$)
ϵ, ϵ_{sc}	Dielectric constant
EIS	Electrochemical impedance spectroscopy
FTO	Fluorine-doped tin oxide
IPCE	Incident photon to current conversion efficiency
J	Current density (in A cm $^{-2}$ or mA cm $^{-2}$)
k_B	Boltzmann constant ($= 1.380 \cdot 10^{-23}$ J K $^{-1}$)
L_D	Diffusion length (in nm)
$L_{D, eff.}$	Effective diffusion length (in nm)
λ	Wavelength (in nm)
MS	Mott–Schottky
N_d	Donor density
OER	Oxygen evolution reaction
PC	Photocatalytic
PEC	Photoelectrochemical
PV	Photovoltaic
R	Resistance (in Ω)
RC	Resistor-capacitor
RHE	Reversible hydrogen electrode
SCE	Saturated calomel electrode
SCLJ	Semiconductor/liquid junction
STH	Solar-to-hydrogen conversion efficiency
τ	Time constant (in s)
T	Temperature (in K or °C)

TEOS	Tetraethyl orthosilicate
V_b or $V_{Appl.}$	Applied bias potential (in V)
$V_{Eq.}$	Potential at equilibrium (in V)
V_{fb}	Flat-band potential (in V)
V_{RHE}	Volts vs. RHE
V_{SCE}	Volts vs. SCE
W_{SC}	Depletion layer width (in nm)

CONTENTS

Abstract.....	3
Résumé	5
List of abbreviations and symbols	7
Contents.....	9
CHAPTER 1. General Introduction.....	13
1.1. Motivation	13
1.1.1. The solar challenge	14
1.1.2. Hydrogen as an energy vector	15
1.1.3. Sustainable routes to hydrogen production	17
1.2. Semiconductor photoelectrochemistry	18
1.2.1. Water splitting reaction	18
1.2.2. The band model.....	20
1.2.3. Choice of semiconductor	24
1.3. Efficiency and characterizations	27
1.4. Objectives	28
1.5. References.....	29
CHAPTER 2. Solar Water Splitting Using Hematite Photoelectrodes	31
2.1. Introduction	32
2.2. Hematite as a promising material.....	35
2.2.1. Overview of properties.....	35
2.2.2. Early efforts with hematite for water splitting	40
2.3. Decreasing the overpotential with surface modification	43
2.4. Increasing photocurrent with morphology control.....	45
2.4.1. Porous thin films from solution-based colloidal methods.....	45
2.4.2. Fe ₂ O ₃ nanowire arrays	49
2.4.3. Electrochemical Fe ₂ O ₃ nanostructuring	51
2.4.4. Spray pyrolysis techniques.....	53
2.4.5. Atmospheric pressure chemical vapor deposition	54
2.4.6. Extremely thin absorber approach.....	57
2.4.7. Nanostructuring method comparison.....	58
2.5. Advanced understanding using electrochemical impedance spectroscopy (EIS).....	60
2.6. Summary and outlook.....	63
2.7. References.....	65
CHAPTER 3. The Host-Guest Approach (or Extremely Thin Absorber, ETA).....	73
3.1. Introduction	74
3.2. Experimental.....	75
3.2.1. Choice of the host material.....	75
3.2.2. WO ₃ film preparation	76
3.2.3. APCVD of silicon doped Fe ₂ O ₃	77
3.2.4. Photoelectrochemical and crystallographic characterisation	77

3.3. Results and discussion	78
3.3.1. Morphology and crystallography of the host –guest system.....	78
3.3.2. Photoelectrochemical enhancement	80
3.3.3. Benefits from the architecture.....	83
3.4. Conclusion	86
3.5. References.....	86
 CHAPTER 4. Control of Iron Oxide Thin Film Photoactivity	 89
4.1. Introduction	90
4.2. Experimental.....	91
4.2.1. Substrate preparation	91
4.2.2. Fe ₂ O ₃ thin film preparation	91
4.2.3. Photoelectrochemical characterization	92
4.2.4. Optical and spectroscopic measurement	92
4.3. Results and discussion	93
4.3.1. TEOS pretreatment characterization	94
4.3.2. Water photo-oxidation performance of ultra-thin hematite film	98
4.3.3. Film thickness and APCE	100
4.3.4. Morphology and film growth	102
4.3.5. Crystallinity and photocurrent transients	104
4.4. Conclusion	109
4.5. References.....	110
 CHAPTER 5. Effect of Plasmonic Nanoparticles on the Photoactivity of Hematite Photoanodes	 113
5.1. Introduction	114
5.2. Experimental.....	117
5.2.1. Gold nanoparticle preparation and deposition.....	117
5.2.2. Hematite ultra thin film deposition by spray pyrolysis.....	118
5.2.3. Hematite nanoplatelets deposition	119
5.2.4. Photoelectrochemical characterization.....	119
5.3. Results and discussion	120
5.3.1. Morphological and optical properties.....	120
5.3.2. Films photoactivity	123
5.3.3. Spectral response enhancement.....	125
5.3.4. Eliminating the possibility of an electronic effect	127
5.3.5. Evidence of the plasmonic effect.....	129
5.4. Conclusion	130
5.5. References.....	130
 CHAPTER 6. Passivating Surface States on Hematite Photoanodes with Alumina Overlays	 133
6.1. Introduction	134
6.2. Experimental.....	135
6.2.1. Hematite thin films by APCVD	135
6.2.2. Atomic layer deposition of overlays.....	136
6.2.3. Photoelectrochemical characterizations	136
6.2.4. Additional characterization	137

6.3. Results and discussion	137
6.3.1. Photoelectrochemical performances	137
6.3.2. Photocurrent transients	142
6.3.3. Eliminating the possibility of a catalytic effect.....	143
6.3.4. Other evidence of surface passivation	145
6.4. Conclusion	151
6.5. References.....	151
 CHAPTER 7. Photovoltage and Photocurrent Transients of Hematite	
Photoanodes.....	155
7.1. Introduction	156
7.2. Experimental.....	158
7.2.1. Hematite photoanode preparation	158
7.2.2. Photoelectrochemical characterization.....	158
7.3. Methodology	160
7.3.1. Photocurrent characterization.....	160
7.3.2. Photocurrent and photovoltage transients.....	163
7.3.3. Data treatments	166
7.4. Results and discussion	168
7.4.1. Photocurrent transient amplitudes	168
7.4.2. Charge accumulation.....	175
7.4.3. Photovoltage amplitudes	178
7.4.4. Time Constants	181
7.5. Conclusion	184
7.6. References.....	185
 CHAPTER 8. Final Conclusions and Outlook 189	
8.1. The Host-Guest Approach.....	190
8.2. Hematite extremely thin film photoactivity.....	190
8.3. Surface passivation and characterization	191
8.4. Outlook	192
8.5. References.....	193
 Appendix A. Supporting Information to Chapter 5 195	
Appendix B Supporting Information to Chapter 6 205	
Acknowledgements 209	
Curriculum vitae 211	

CHAPTER 1.

GENERAL INTRODUCTION

1.1. Motivation

Since the beginning of the industrial era, the energy required for economic development and growth has been supplied mainly by coal, oil and natural gases. These fossil energy sources possess a very high energy density and can be stored or transported easily. Nowadays the use of these resources faces major problems: first only a limited amount of these fuels is available, second they are responsible for anthropogenic ecological problems (greenhouse effect, acid rain and high ozone concentration in urban areas) and third they also cause geopolitical tensions linked to international conflicts.

Because of the rapid increase of the population growth as well as the increase in energy consumption per capita, the energy demand is also growing tremendously fast. Accordingly, the world primary energy consumption grew by 5.6% in 2010, which is the largest increase (in percentage terms) since 1973.¹ It is therefore extremely important to develop sustainable and renewable energy sources able to replace the principal energy source of today, the fossil fuels. The utilization of clean and widely available energy sources will not only supply the energy required for global economic growth but will also reduce the anthropogenic impact on the environment.

1.1.1. The solar challenge

The German Advisory Council on Global Change (WBGU) produced a report in 2003 aiming to comprehensively present the prime concerns surrounding today's energy systems to policy makers. This document also suggests the criteria that need to be met to turn energy systems towards sustainability and sets out a possible path for transforming the global energy system within the 21st century.²

The scenario for the global transformation of energy systems created in this report is built upon the stabilization of CO₂ concentration in the atmosphere (at a maximum of 450 ppm) and take into account high growth rates for both energy use (three-fold growth by 2050) and economic development (six-fold growth by 2050). This suggested route, shown on Figure 1.1, is in principle technologically and economically feasible. It is based on three pillars: declining use of fossil fuels, rising use of renewables and growing energy productivity. However, energy production from fossil fuels will remain a necessity over the next decades because of a lack of infrastructures and mature technologies for the economically competitive harvesting of renewable energy sources. The expert panel advocates that further development in infrastructure and technologies linked to energy productions from traditional fossil fuel can be converted to future conversions to renewable energy sources. They expect that from 2050, renewable energies will account for the greater proportion of energy production. In fact, they project that the proportion of energy produced from renewables will account for 50% of total production by 2050 and 90% by 2100. Within the different types of renewable sources, solar energy holds by far the largest potential capacity. Indeed, our planet receives about 174×10^3 TW of solar radiation, which in other terms means that the energy shining on Earth every 10 minutes is equivalent to the total yearly human consumption today (15 TW). Even if only a fraction of this energy could be harvested the solar energy source can provide enough energy to reach the goals set by the WGBU plan.

There are several different technologies able to convert the energy provided by the sun including photovoltaic cells, large-scale concentrating solar thermal power and personal or industrial solar water heaters. Photovoltaic cells convert sunlight directly into electricity and are predominantly made of semiconductors such as crystalline silicon or various thin-film materials. Photovoltaics can provide small amounts of power for mobile applications (e.g. watches) all the way up to megawatts for injection into the electric grid. Concentrating solar thermal power technologies use reflective materials to concentrate the sun's heat energy and ultimately drive a water

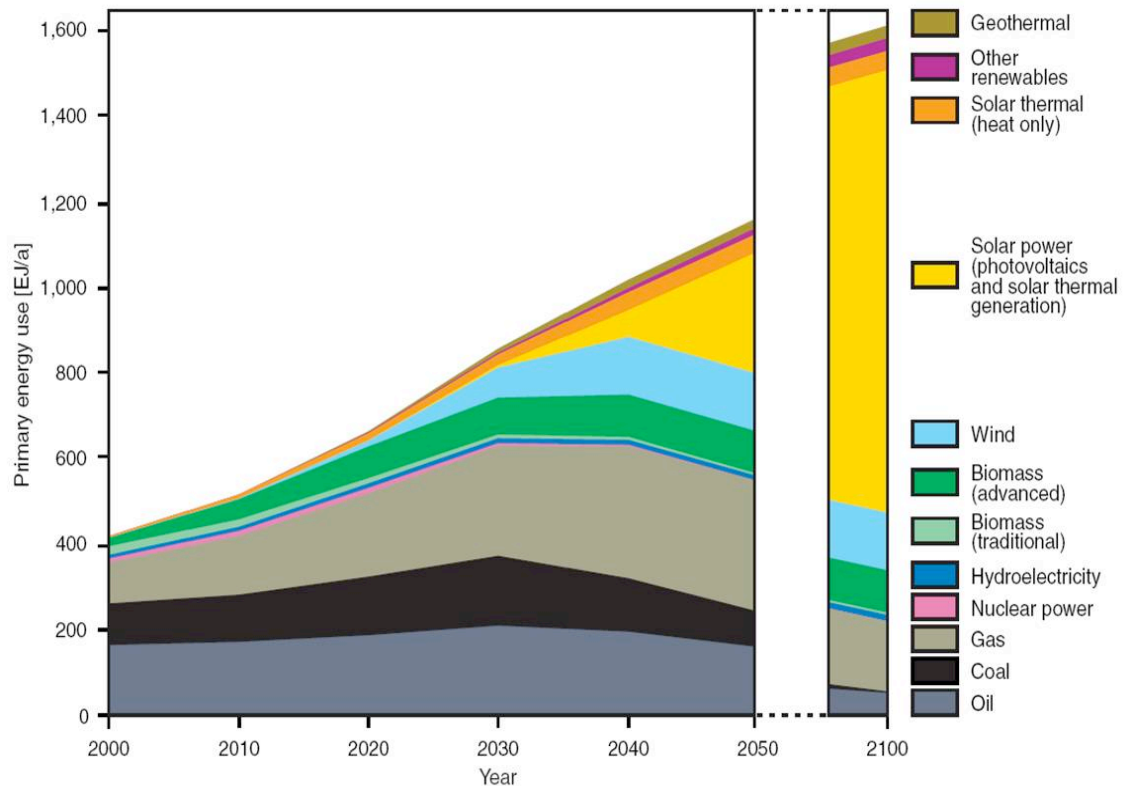


Figure 1.1: Forecasted global primary energy use in EJ/annum (500 EJ/annum corresponding to 15.85 TW) from 2000 to 2050 (extended to 2100) according to one feasible scenario (from [2]).

turbine to produce electricity. These technologies include dish/engine systems, parabolic troughs, and central power towers. Finally, low-temperature solar collectors also absorb the sun's heat energy, but the heat is used directly for hot water or space heating in residential, commercial, and industrial facilities.

These technologies have all in common to convert the sun energy into an energy vector, electricity or heat, which cannot be easily stored. As we will see in the next section, hydrogen can play this role. It is a promising energy carrier, which has a low impact on the environment, if we can produce it from solar energy.

1.1.2. Hydrogen as an energy vector

Hydrogen in its pure molecular form, H_2 , is a colorless, odorless, nontoxic gas. Hydrogen is the lightest gas and the most energy-dense fuel per mass. One pound of hydrogen holds 55 MJ, three times the energy of a pound of gasoline.³ Like oil and natural gas, hydrogen can be transported via pipeline or shipped in containers. When burned or used to power a fuel cell, hydrogen produces zero emissions besides water vapor. Because of these advantageous properties, hydrogen is widely seen as a future transport fuel in replacement of the fossil fuels. The idea of a society

based energetically on hydrogen, embraced in the concept of *hydrogen economy*, was initially raised at the time of the first oil crisis in 1970s. The term of *hydrogen economy* was first used by John Bockris during a talk he gave in 1970 at General Motors (GM) Technical Center,³ and this concept includes the development of systems for transport, storage, usage and production of hydrogen. These four components of the hydrogen economy have been discussed in detail in a book edited by D. Scholten.⁴

One of the main advantages of hydrogen is that it can benefit from the existing natural gas infrastructure for distribution. In fact, a natural gas company from the Netherlands has already demonstrated this concept by transporting a mixture of hydrogen and natural gas via the existing natural gas network in 2004 (see Alexis Duret thesis for more details).⁵ In its simplest form, hydrogen can be highly compressed and densified to be transported in containers.

The storage of hydrogen is nowadays limiting the development of a hydrogen-based society, especially for mobile applications that requires a great amount of energy in a small volume. Although hydrogen possesses the best energy density by weight due to its low molecular weight, it has very a low energy density by volume as a gas at ambient conditions (10 times less than oil for example). Three main technologies are used or in development for storage: physical storage, chemical storage and molecular adsorption. The physical storage technologies would simply compress pure hydrogen gas to high pressure (order of 50 – 100 MPa) or liquefy it (at 20 K under 0.1 MPa), in order to provide sufficient storage capacity. Increasing gas pressure improves the energy density by volume, making for smaller, but not lighter container tanks. Liquefied hydrogen requires double vessel tanks to allow thermal isolation. Even if the physical hydrogen storage technologies are the most established and most considered by industrials, these systems suffer from an expensive energy cost (to maintain high pressure and low temperature) and from hydrogen leakage, leading to the embrittlement or weakening of its container. Alternatively hydrogen can be stored as a chemical hydride or in some other hydrogen-rich compounds. Hydrogen gas is reacted with some other materials to produce the hydrogen storage material that can be transported relatively easily. At the point of use the hydrogen storage material can be made to decompose, yielding hydrogen gas. This method is highly promising but has been mainly limited up to now by the high pressure and temperature required for hydride formation and hydrogen release. A third approach is to absorb molecular hydrogen into a solid storage

material (without chemical reaction). Hydrogen densities similar to liquefied hydrogen can be achieved with appropriate materials. This last approach is still at an early stage of investigation and the main media studied are metal organic frameworks, carbon-based nanostructures (including nanotubes) and clathrate hydrate. A comprehensive and comparative study of the different storage possibilities can be found elsewhere.⁶

The fuel cell is one of several conversion technologies that can be fueled by hydrogen. Basically, hydrogen fuel cells operate via reversed electrolysis: hydrogen gas and oxygen from the air combine in a catalyzed electrochemical reaction to produce an electric current, heat and water. Aside from being pollution-free, fuel cells can achieve efficiencies that are two- to three-times greater than internal combustion engines. The scalability of fuel cells makes them ideal for a wide variety of applications – including laptops (50-100 Watts) and central power generation (1-200 MW). However, further development is necessary in order to increase durability and bring down cost so they can compete economically. Finally, one can also use hydrogen in internal combustion engines (ICEs) with slight modifications to the engine. Hydrogen burns much cleaner and more efficiently than gasoline, which makes hydrogen ICEs a realistic short-term transition technology. However, fuel cells, with higher efficiencies and zero emissions will likely be a more popular utilization technology in the longer term.

1.1.3. Sustainable routes to hydrogen production

Today, about 96% of hydrogen is made from fossil fuels: 48% from natural gas, 30% from liquid hydrocarbons and 18% from coal.⁷ According to the energy challenge discussed in the first section, a shift to production of hydrogen by clean and renewable energy sources should be completed to fit in the future energy economy. Figure 1.2 shows different paths for carbon-neutral hydrogen production. The energy sources derived from the solar energy (wind, hydroelectric, natural photosynthesis) or other sources (nuclear, geothermal, tidal) will not be discussed herein due to the lack of available resources and their non-universality. One way to utilize our most abundant and renewable source of energy with current technology is to first convert the solar energy, into grid electricity using conventional solar cells or solar thermal plants. Hydrogen can be subsequently produced from electricity through a water electrolyzer. This strategy has been employed in Iceland during the European project ECTOS.⁸ Within this program, three hydrogen-powered buses (fuel cells) have been carrying passengers on the streets of Reykjavik for more than two

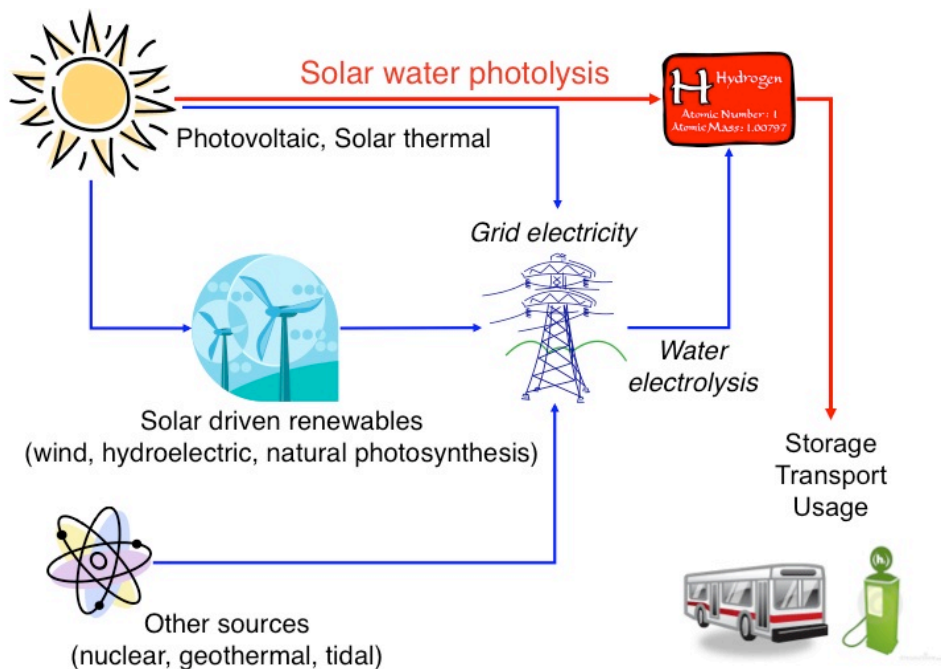


Figure 1.2: Scheme representing different paths for carbon-free hydrogen production.

years (2003 – 2005). Hydrogen was produced with an electrolyzer in one of the public petrol station from Iceland's electricity grid based on hydro and geothermal energy. It offered the first example of a zero-emission fuel economy.

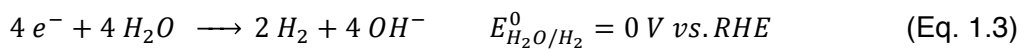
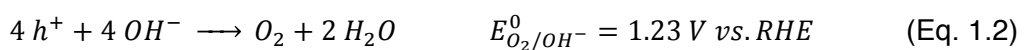
However, the production of intermediates, here electricity, causes invariably significant energy losses (more steps inducing more losses), which will consequently increase the overall cost of stored renewable energy. Bossel *et al.*⁹ calculated an energy loss of 75% that is associated with the (renewable) electricity-to-hydrogen-to-electricity conversion. To avoid this, a more elegant, practical and potentially more efficient route is to directly convert the solar energy into the hydrogen fuel. Among all possibilities, the use of a semiconductor is particularly attractive to perform direct solar water photolysis. The second part of the introduction will therefore discuss how to use a semiconductor to produce hydrogen.

1.2. Semiconductor photoelectrochemistry

1.2.1. Water splitting reaction

Other solar fuels such as methanol or acid formic are also candidates to be the energy vector of renewable sources. However, given the abundance of water on earth, the water photolysis reaction, is the most appealing pathway for artificial photosynthesis.

Separating water in molecular oxygen and hydrogen is an endoenergetic reaction with a standard Gibbs free energy of $\Delta_r G^\circ = 237.2 \text{ kJ}$, corresponding to an electrochemical potential of 1.23 V. In terms of heat, this reaction is endothermic with a standard dissociation enthalpy of $\Delta_r H^\circ = 280.1 \text{ kJ}$, corresponding to 1.45 V.¹⁰ Therefore, energy should be provided to a system containing water for it to evolve the desired gases. The Sun can supply this energy to a semiconductor by promoting an electron in the conduction band (excited state) and leaving a hole (a positive charge carrier) in the valence band through the absorption of photons (Eq. 1.1). Holes react at the semiconductor-electrolyte interface with hydroxyl ions from the solution to evolve oxygen (Eq. 1.2). In order to separate physically the water oxidation and reduction, the photogenerated electrons in the conduction band are transferred through an external circuit to a cathode (a metallic wire such as platinum *e.g.*). At the metal cathode, the electron reduces water to evolve hydrogen (Eq. 1.3). In basic media, it gives the following reactions:



The overall water photoelectrolysis reaction involves four photons that generate four electron – hole pairs for every two hydrogen molecules and one oxygen molecule produced (Eq. 1.4). Kinetically, the photolysis reaction is limited by the photo oxidation as this step involves a 4-electron reaction (Eq. 1.2).



For this reaction to take place, the energy level of the conduction band of the semiconductor needs to be positioned at a more negative potential than the reduction potential of water (Eq. 1.3) while the valence band needs to be more positive than the oxidation reaction. The assumption that reaction 1.2 and 1.3 are exclusively responsible for this external photocurrent allows its use as a measure for the hydrogen evolution rate.

The different steps of water photolysis with a n-type semiconductor are detailed on Figure 1.3. Step (1) corresponds to the absorption of a photon, generating an electron - hole pair in the material. Step (2) is the diffusion of holes towards the interface with electrolyte where water oxidation takes place (3). Step (4)

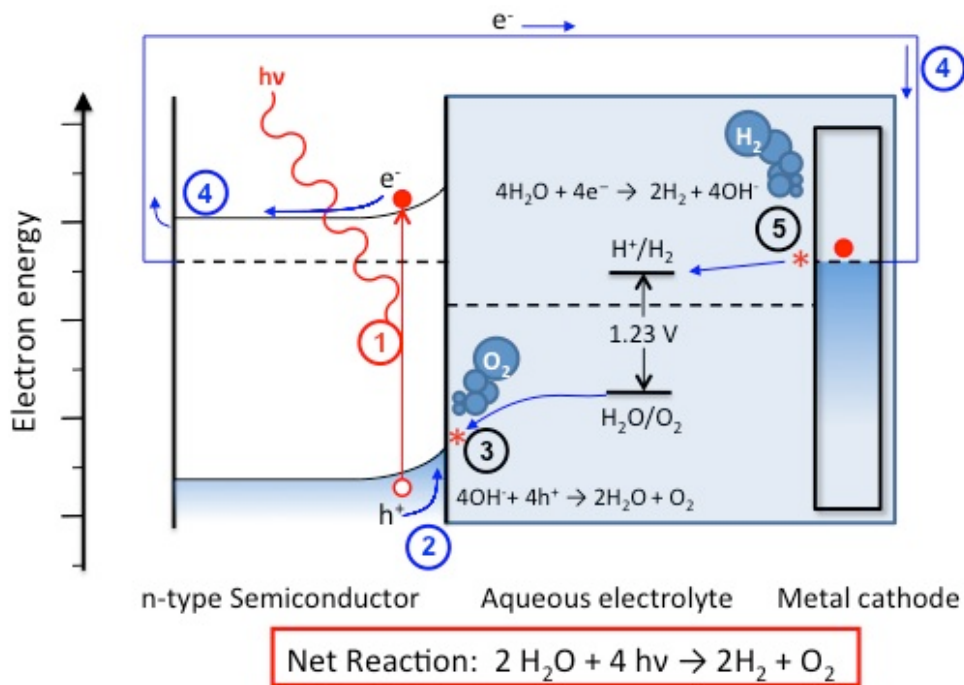


Figure 1.3: Schematic representation of the relevant processes involved in the photo-oxidation of water using a n-type semiconductor as a photo-anode. The different steps (1 to 5) are detailed in the text.

represents the transport of electrons through the semiconductor and the external circuit and step (5) is the water reduction that occurs at the metallic cathode surface.

As shown on Figure 1.3, the solar-to-hydrogen efficiency of a semiconductor in water will be influenced by the light absorption (1), the charge transport (2 and 4) and the reaction kinetics (3 and 5). The latter parameter can be modified by adding a catalyst on the surface and is therefore not critical for a semiconductor that is a bad catalyst for the oxygen evolution reaction (in case of a n-type semiconductor). The other parameters are intrinsic properties of the material. They will be discussed in the next section with the behavior of the semiconductor in contact with an electrolyte containing a redox couple.

1.2.2. The band model

Semiconductors are defined by the forbidden energy gap (band gap or E_g) separating the valence bands, which are located below this gap and filled with electrons (at 0K and standard conditions), and the conduction bands that correspond to the first excited levels above the gap (empty at 0K). The bottom of the conduction bands is labeled E_C , the top of the valence bands is called E_V and the difference between E_C and E_V defines the band gap (E_g). The band gap is typically in the range 1 to 4eV for semiconductors. It will determine the light absorption of the semiconductor as only electromagnetic waves with wavelengths lower than the band

gap (higher in energy, $\lambda = hc/E$) can be harvested by promoting an electron between two bands (in case of allowed transition).

The Fermi level and the Fermi distribution described the distribution of electrons and holes over all the available energy levels in a solid. The Fermi function ($f(E)$) corresponds to the average number of electron per energy level at the energy E and is given by:

$$f(E) = \frac{1}{1 + e^{\frac{E - E_F}{k_B T}}} \quad (\text{Eq. 1.5})$$

where E_F is the Fermi level that corresponds to the energy level where the probability of finding one electron per available state is equal to 0.5, k_B the Boltzmann constant and T the temperature in Kelvin. It should be mentioned here that the Fermi distribution is valid only at thermodynamic equilibrium. The Fermi level position also distinguishes the different class of materials, as E_F is located in the valence band for metals (that provides good electron conduction) and in the forbidden gap for semiconductors and insulators. The two latter types of materials are differentiated by the band gap energy ($E_g > 4$ eV for insulators).

The behavior of a semiconductor when immersed in electrolyte has been comprehensively discussed in a book edited by R. Memming.¹¹ The model presented by Gerischer is the most widely used to describe the phenomena occurring in the semiconductor and in the electrolyte when they are brought in contact.¹² A brief summary of this theory is developed in the following (see Reference 11 and 12 for more details).

The charge transfer between the semiconductor and the redox species is considered in terms of electronic energies in the solid and energy levels in solution. The electrochemical potentials of the different redox species in the electrolyte form the energy levels of the solution and an energy mediator can be calculated according to the ions concentrations, the interactions between them and their solvation energies. The electrolyte energy mediator (or redox energy, labeled E_{Redox}) is sometimes called the Fermi level of the electrolyte in analogy to energy levels in the semiconductor, even if these concepts are distinct.

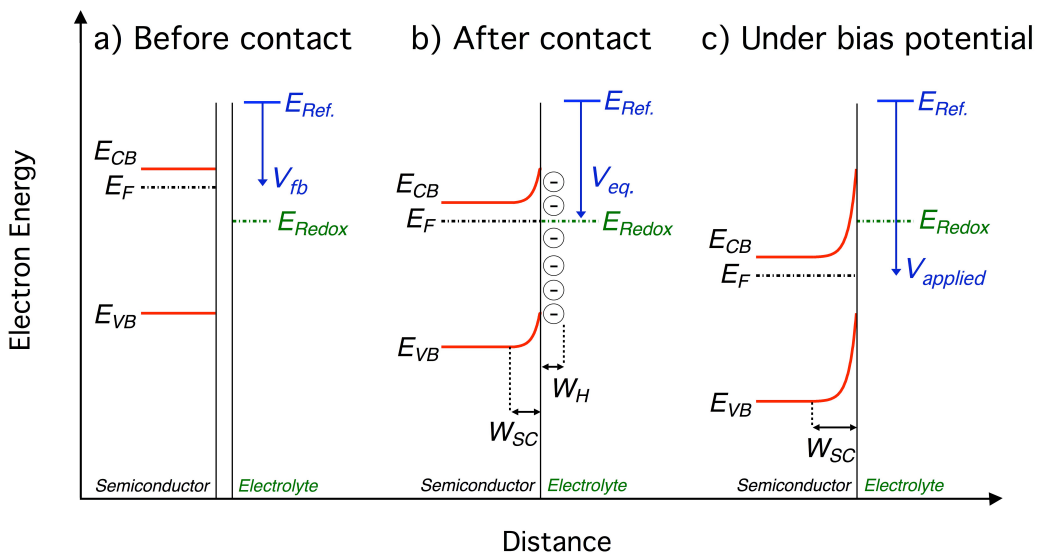


Figure 1.4: Schemes representing the band model of a semiconductor electrode in contact with an electrolyte containing a redox couple in three different configurations: a) before contact, b) after contact and c) under bias potential. W_H and W_{SC} correspond to the width of the Helmholtz layer and to the space charge layer respectively. Not to scale.

When the semiconductor is brought in contact with an electrolyte with E_{Redox} different of E_F , equilibrium of the electrochemical potential in the two components is achieved by electron exchange at the interface. On one side (a n-type semiconductor for example with a higher charge density than the electrolyte), the electrons are transferred to the electrolyte and are depleted in a certain thickness of the material (space charge layer). Thus Fermi levels are adjusted due to the formation of an electric double layer between the solid and the electrolyte (Schottky junction). This process is shown on Figure 1.4 (a and b). The depletion of electrons at the surface of the semiconductor will induce an electric field between the bulk of the semiconductor and its surface, corresponding to bending of the valence and conduction bands (these two bands being pinned at the surface due to interactions of the semiconductor surface with the electrolyte). The potential profile as a function of the distance from the surface ($x = 0$ at the surface and $x = \infty$ in the bulk) can be obtained in a n-type semiconductor with solving Poisson's equation and assuming $k_B T$ negligible compared to the potential drop in the depletion layer, a volumetric charge density equal to $e N_D$ (extrinsic n-type) and using the potential of the bulk as a reference ($V_{bulk} = 0$). This relation is shown in Eq. 1.6.

$$V(x) = -\frac{e N_D}{2 \epsilon \epsilon_0} (x - W_{SC})^2 \quad (\text{Eq. 1.6})$$

where ε is the relative dielectric constant, ε_0 the permittivity of vacuum, e the electronic charge, N_D the donor density, and W_{SC} is the space charge layer thickness. Under the depletion layer condition, it is possible using Eq. 1.6 to calculate the space charge layer thickness (W_{SC}). It corresponds to the distance between the surface and where the bands flatten.

$$W_{SC} = \left(\frac{2 \varepsilon \varepsilon_0}{e N_D} |V - V_{fb}| \right)^{1/2} \quad (\text{Eq. 1.7})$$

where V_{fb} is the flat band potential. It corresponds to the particular redox potential of the electrolyte or to the applied potential (vs. E_{Redox}), when there is no excess charge in the semiconductor and therefore no band bending. If we consider a certain redox couple, the flat band potential is the potential from which positive charges are attracted to the surface (negative charges depleted close to the surface) and cathodically negative charges are attracted to the surface (positive charges depleted close to the surface). V_{fb} is indicated in Figure 1.4a (before contact) for clarity but is only valid when the semiconductor has flat bands from bulk to surface and is in contact with the electrolyte. In our case, the depletion of charges in the space charge layer will repulse the electron from the surface and attract holes to it. Consequently a Helmholtz layer (W_H), which consists of a continuous layer of anions, is formed in the electrolyte to balance the positive surface of the semiconductor.

When a positive difference of potential is applied ($V_{applied}$) between the n-type semiconductor and a reference electrode (fixed to the electrolyte redox potential) the band bending of the semiconductor is modified (Fig. 1.4c). If the concentration of the majority charge carrier is not significant, the potential drop will occur mainly in the semiconductor. The Fermi level in the semiconductor is shifted by ($V_{applied} - V_{eq.}$) from its equilibrium position and increase the potential drop in the space charge, extending the space charge region in the semiconductor.

Illumination will also modify the band bending of a semiconductor in equilibrium with an electrolyte as the electron density and the hole density are increased due to light absorption. The electrons and the holes will be characterized therefore by different electrochemical potentials: the quasi Fermi level (QFL) of electrons and the quasi Fermi level of holes. These QFL depend on the quantity of free carriers before the illumination and on the extra concentration due to light absorption. In a n-type semiconductor, the total major carrier concentration does not vary significantly (especially if highly doped) upon illumination. On the contrary the concentration of holes (minority carriers in a n-type) is increased significantly and the

QFL of holes will increase strongly (decrease on a electron energy scale). The QFL of holes is important in a system where holes react at the surface (e.g. in a water splitting photoanode) as it corresponds roughly to the oxidizing power of holes.

This model does not explicitly consider bulk traps (defects in the crystal lattice for example) or surface states (due to dangling bonds or adsorbed species on the surface). The bulk traps act as recombination center between photogenerated charges and will consequently decrease the efficiency of charge separation. The surface states can act as donor or acceptor species and will influence the electrochemical and photoelectrochemical properties of a semiconductor (surface recombination). They are also thought to be responsible for Fermi level pinning.

Finally another model, distinct from Gerischer's theory, has been developed for semiconductors for which electron conduction is still occurring in the conduction band with involving multiple trapping in bulk states.^{13,14} In contrary to the classical theory, the valence band and the conduction band are flat, from the bulk to the interface with electrolyte, at all applied potentials, predominantly due to charge screening in the semiconductor by ions on the surface. This model has been applied especially to nanostructured electrodes with small feature size and low donor density (e.g. dye-sensitized solar cells, DSC).¹⁴ Recently, Pendlebury *et al.* used this model to explain their optical characterization of water splitting photoanodes.¹⁵ The application of these two models to water splitting model is further discussed in Chapter 7.

1.2.3. Choice of semiconductor

The semiconductors have to fulfilled several requirements to be considered for application in a water splitting device. These criteria include low cost, high chemical stability, good visible light absorption, conduction and valence band edges straddling the reduction and oxidation potentials of water and rapid interfacial charge transfer.

First of all, the material must be water stable. The stability (and photostability) of a material depends on the relative position of the band edges, the Fermi level of electrons (in dark) and the QFL of electrons and holes (under illumination) compared to the cathodic and anodic decomposition potentials.¹⁶ The inadequate positions of these bands lead some materials such as silicon, germanium or cadmium sulphide, to readily corrode in water. In addition the material should absorb a large portion of the solar spectrum. Hence the band gap should be as small as possible. However, the energy difference between the oxidizing hole and the reducing electron should be

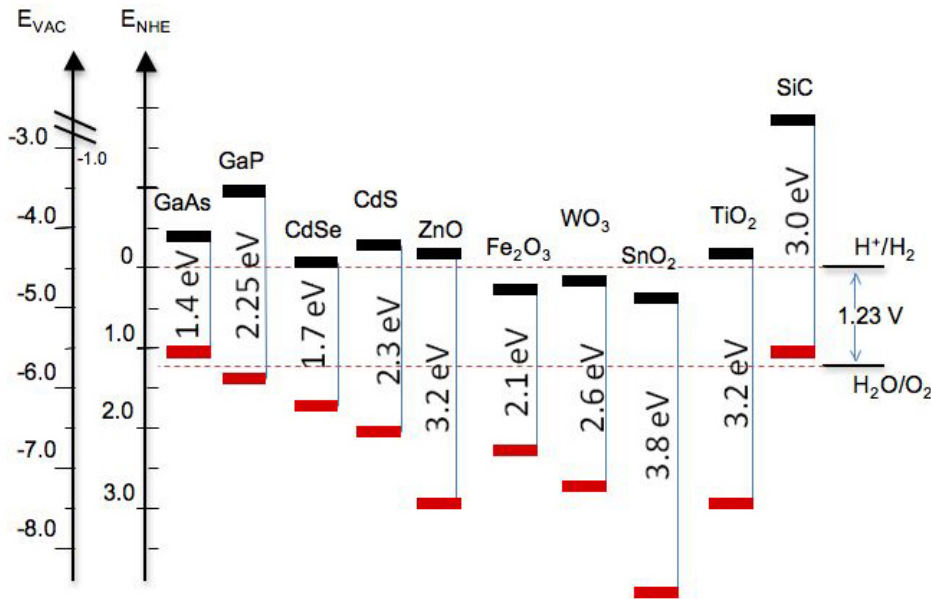


Figure 1.5: Band edges of selected semiconductors relative to the reversible oxidation and reduction potential of water (at pH = 0). The lower edge of the conduction band (black) and the upper edge of valence band in (red) are presented along with the band gap in electron volts. Adapted from [17].

higher than the water dissociation electrochemical potential (1.23 V). One should also take in account some overpotential for both water oxidation and reduction in order to overcome kinetic limitations. Consequently a band gap of 1.6 – 2.0 eV is considered to be the best compromise for the water splitting reaction. Another critical criterion is the position of the energetic bands, as the valence band shall be below the redox potential of O₂ formation and the conduction band shall be above the redox potential of H₂ formation. Figure 1.5 shows different semiconductor candidates for the water splitting along with their valence and conduction band edges.¹⁷

Despite the large amount of research effort since the pioneering work of J.P Boddy¹⁸ and A. Fujishima¹⁹ with TiO₂ in 1968 and 1972, respectively, these requirements have not yet been fulfilled by any candidate. III-V compounds are unstable under aqueous conditions, cadmium is highly toxic and transition metal oxides do not have suitable absorption or position of bands. Nevertheless, metal oxide semiconductors remain promising as water splitting electrode because they can be produced by low cost routes and are typically much more stable in aqueous environments than other semiconductors. In all case, the problem of material whose conduction band is lower than the energy level of water reduction can be overcome using a tandem system.

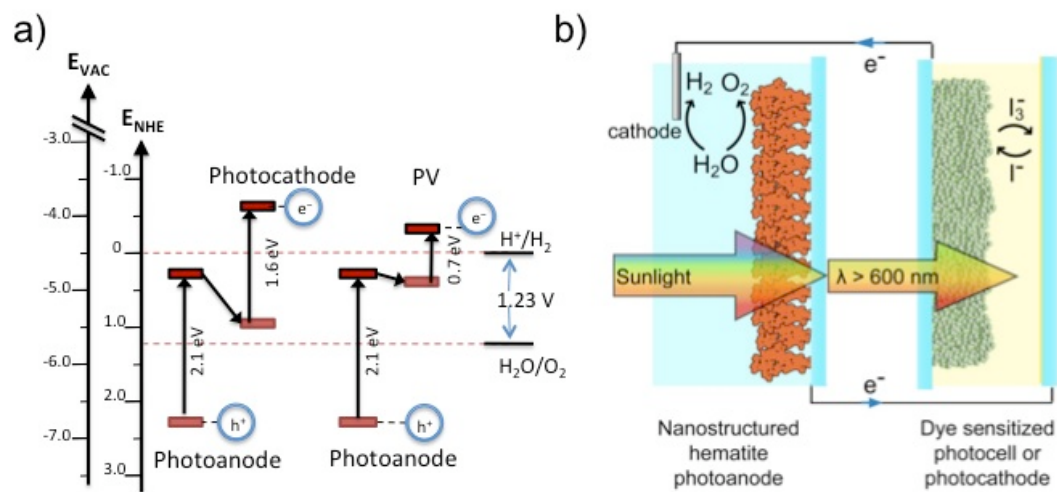


Figure 1.6: a) Principle of a tandem system for water splitting composed of a photoanode set in series with a photocathode or a photovoltaic cell. b) Scheme of a tandem cell (iron oxide photoanode / DSC) operation under white light illumination. The blue part of the solar spectrum generate electron-hole pairs in the hematite layer, the holes can oxidize water while the electrons are transmitted to the DSC where their energy are raised by the red part of the solar spectrum to make them suitable for water reduction, which happen at the cathode.

When the free electron generated by light absorption in the semiconductor is not energetically high enough to produce hydrogen at the cathode, it can gain the additional energy by the contribution of another energy source. The photoanode can be assembled in a tandem device where a photocathode or an inexpensive photovoltaic (PV) cell (e.g. DSC) is connected in series to apply extra bias for completing the water splitting reaction, as shown on Figure 1.6a. Moreover, as only a portion of the solar spectrum is absorbed by the photoanode, the second solar system solar cells convert the complementary light (longer wavelengths), enabling light harvesting from a broader part of the solar spectrum and hence a higher conversion efficiency than in a single junction cell (Figure 1.6b). Tandem cells work in close analogy to the “Z-scheme” that operates in natural photosynthesis and which requires 2 photons to oxidize water to oxygen while producing sugar (photosystems I and II).

Among all metal oxides, three materials have been identified as candidates and investigated: TiO_2 , WO_3 and Fe_2O_3 . As shown above, the inadequate position of the conduction band relative to the hydrogen evolution potential can be neglected; therefore one should compare their maximum efficiency in terms of light absorption. According to their different band gap, titanium oxide ($E_g = 3.0 \text{ eV}$), tungsten trioxide ($E_g = 2.6 \text{ eV}$) and iron oxide ($E_g = 2.1 \text{ eV}$) offer very different maximum solar-to-hydrogen efficiencies: 4%, 8% and 16% respectively. Due to this relative maximum

efficiency but also to its low cost and abundance, hematite is the most attractive metal oxide semiconductor for water splitting.

1.3. Efficiency and characterizations

The conversion efficiency of sunlight into stored energy (the solar fuel) is commonly named solar-to-hydrogen efficiency (STH) and can be expressed in terms of energy input and output. The energy input can be defined as the solar spectrum air mass 1.5 Global at 100 mW/cm² and any applied bias voltage (V). STH efficiency can be defined in two ways. The first one accounts for the chemical combustion of the fuel (if we use hydrogen in a heat engine) and therefore the energy stored is $\Delta_r H^\theta$ of the water dissociation (1.45 V, Eq. 1.8). The second accounts for the Gibbs energy stored in H₂ (if we use fuel cell to extract the energy) and the energy stored is $\Delta_r G^\theta$ for the water dissociation reaction (1.23 V, Eq. 1.9). As the flux of electrons measured under irradiance in the external circuit should only be due to the water splitting reaction, it is practical to express the conversion efficiency in terms of photocurrent density. The two equations describing the efficiencies are:

$$\eta_{STH,\Delta H} = \left[\frac{J_{ph} \times (1.45 - V_{bias})}{P_{illumination}} \right] \quad (\text{Eq. 1.8})$$

$$\eta_{STH,\Delta G} = \left[\frac{J_{ph} \times (1.23 - V_{bias})}{P_{illumination}} \right] \quad (\text{Eq. 1.9})$$

where J_{ph} is the photocurrent density (in mA cm⁻²) obtained under an applied potential V_{bias} (in V) and $P_{illumination}$ the solar power at AM 1.5 G (= 100 mW cm⁻²). As the required bias potential is supplied by the second solar system in a tandem cell, no additional bias voltage is required and V_{bias} is 0 for the determination of the tandem cell efficiency. It should also be mentioned that the STH in terms of Gibbs free energy has been chosen as the efficiency measurement in an recent review aiming to standardize semiconductor photoelectrochemistry characterization.²⁰

In order to characterize the photoactivity of the hematite photanodes, and the additional voltage that should be supplied, photocurrent densities were measured and compared to dark conditions while sweeping the applied potential. The measurement was performed in a three electrode configuration with 1 M NaOH (pH = 13.6)²¹ as electrolyte, Ag/AgCl/sat. KCl as reference and a platinum wire as counter electrode. In order to allow comparison with other conditions and materials, the applied potential was reported against the reversible hydrogen electrode (RHE) according to Eq. 1.10.

$$E_{RHE} = E_{AgCl} + 0.059 \text{ pH} + E_{AgCl}^0 \quad \text{with} \quad E_{AgCl}^0 = 0.1976 \text{ at } 25^\circ\text{C} \quad (\text{Eq. 1.10})$$

where E_{RHE} is the potential of the reference hydrogen electrode (RHE), E_{AgCl} the potential of the Ag/AgCl/sat. KCl reference electrode and E_{AgCl}^0 the standard potential of the Ag/AgCl/sat. KCl reference electrode. Sunlight is simulated with a 450 W xenon-lamp (Osram, ozone free) by cutting off the infrared (>720 nm) and short UV-light (<320 nm) with a KG3 filter (3 mm, Schott) while the light intensity is adjusted so that a Si-photodiode covered with another KG3 filter gives the same photocurrent as in global AM 1.5.²²

Another common characterization used in this thesis is the measurement of incident-photon-to-current efficiency (IPCE) that characterizes the photoactivity of the electrode at fixed applied potential (vs. RHE) for different incident light wavelengths. Photocurrent action spectra are obtained under light from a 300 W Xe-lamp with integrated parabolic reflector (Cermax PE 300 BUV) passing through a monochromator (Bausch & Lomb, bandwidth 10 nm FWHM). The wavelength is scanned at 2 nm/s. The monochromatic photocurrent of the Fe_2O_3 electrode is then compared with that of a UV enhanced Si-photodiode (Oriel 71883) of known IPCE spectrum to calculate the photoanode IPCE.

1.4. Objectives

Concepts and results presented in this thesis contribute to the optimization of hematite photoanodes for water splitting and further our understanding of semiconductor electrochemistry. Shortly before the beginning of this thesis, atmospheric pressure chemical vapor deposition of hematite (doped with silicon) had been developed by A. Kay and I. Cesar in our laboratory.²³ This technique produced thin films exhibiting solar-to-hydrogen efficiency of 3.3 %, which equaled the best performance obtained with a metal oxide electrode (tungsten trioxide). This result confirmed the great potential of $\alpha\text{-Fe}_2\text{O}_3$ but also showed that further investigations were required for this material to accomplish performance closer to its maximum STH efficiency of 16 %. Therefore, this work presents the results of new strategies to obtain high photoactivity and furthers our fundamental understanding of phenomena occurring in this material.

First, a review detailing the basic material properties, and comparing recent progress attained using different deposition methods is presented in Chapter 2. This section also highlights the attractive aspects and the challenges for the use of hematite in a water splitting device. A new method to overcome the first drawback,

namely the dilemma between the large absorption depth and the small charge carrier diffusion length is discussed in Chapter 3. There a new host-guest or ETA concept for water splitting that decouples the different tasks of the photoanode to achieve enhancement of the long wavelengths conversion is introduced. The poor efficiency of extremely thin film of hematite (<50 nm) is the main limitation for this concept and will be discussed in the following two chapters. Thin films efficiency is first improved with the intercalation of a buffer layer that modifies the film growth mode and properties (Chapter 4). Chapter 5 focuses on the influence of plasmonic gold nanoparticles on the thin film photactivity.

Another major drawback of hematite, *i.e.* the large overpotential observed for water splitting, is tackled in the last part of the thesis. The energy loss in terms of applied potential is reduced by the deposition of an alumina overlayer by atomic layer deposition. This study, detailed in Chapter 6, distinguishes the observed overpotential reduction from a catalytic effect and assigns it to passivation of surface states. This overpotential is also investigated in Chapter 7 with transient photocurrent and photovoltage dynamic measurements in the potential range from flat band potential to the onset of the dark current. Herein, material properties are quantified and discussed with different models. Finally, general conclusions and outlooks are given in Chapter 8.

1.5. References

- (1) BP Statistical Review of World Energy, **2011**,
<http://www.bp.com/statisticalreview>
- (2) World in Transition: Turning Energy Systems Towards Sustainability, German Advisory Council on Global Change (WBGU), **2003**, www.wbgu.de, (Summary:
http://www.wbgu.de/fileadmin/templates/dateien/veroeffentlichungen/hauptgutachten/jg2003/wbgu_jg2003_kurz_engl.pdf)
- (3) National Hydrogen Association; United States Department of Energy,
<http://www.fchea.org>
- (4) Scholten D., *Hydrogen and Fuel Cells*, **2010**, WILEY-CH, Weinheim
- (5) A. Duret, *Mesoscopic thin films of hematite as photoanode for water photoelectrolysis*, EPFL, Lausanne, **2005**.
- (6) Züttel, A.; Borgschulte, A.; Schlapbach, L., *Hydrogen as a future energy carrier*, **2008**, Wiley-VCH, Weinheim

Chapter 1

- (7) World Nuclear Association, data from June 2010, <http://www.world-nuclear.org/info/inf70.html>
- (8) http://ec.europa.eu/research/environment/newsanddoc/article_3894_en.htm
- (9) U. Bossel, *Proceedings of the Ieee* **2006**, *94* (10), 1826
- (10) Harrison, K. W.; Remick, R.; Martin, G. D.; Hoskin, A. Hydrogen Production: Fundamentals and Case Study Summaries. In *Hydrogen and Fuel Cells*; Stolten, D., Ed.; Wiley: Weinheim, **2010**.
- (11) Memming, R. *Semiconductor Electrochemistry*, **1998**, Wiley-VCH, Weinheim
- (12) Gerischer, H. *J Electroanal Chem* **1975**, *58*, 263.
- (13) Bisquert, J. *Phys. Chem. Chem. Phys.* **2008**; *10*, p 49.
- (14) Bisquert, J. *J Phys Chem C* **2007**, *111*, 17163.
- (15) Pendlebury, S. R.; Barroso, M.; Cowan, A. J.; Sivula, K.; Tang, J.; Graetzel, M.; Klug, D.; Durrant, J. R. *Chem Commun* **2011**, *47*, 716.
- (16) Gerischer, H. *J Electroanal Chem* **1977**, *82*, 133.
- (17) Grätzel, M. *Nature* **2001**, *414*, 338.
- (18) Boddy, P. *J Electrochem Soc* **1968**, *115*, 199.
- (19) Fujishima, A.; Honda, K. *Nature* **1972**, *238*, 37.
- (20) Chen, Z.; Jaramillo, T. F.; Deutsch, T. G.; Kleiman-Shwarsctein, A.; Forman, A. J.; Gaillard, N.; Garland, R.; Takanabe, K.; Heske, C.; Sunkara, M.; McFarland, E. W.; Domen, K.; Miller, E. L.; Turner, J. A.; Dinh, H. N. *J Mater Res* **2010**, *25*, 3.
- (21) Kennedy, J.; Frese, K. *J Electrochem Soc* **1978**, *125*, 723.
- (22) Seaman, C. *Sol Energy* **1982**, *29*, 291.
- (23) Kay, A.; Cesar, I.; Graetzel, M. *J Am Chem Soc* **2006**, *128*, 15714.

CHAPTER 2.

SOLAR WATER SPLITTING USING HEMATITE PHOTOELECTRODES

This chapter is based on the following review: Sivula, K.; Le Formal, F.; Grätzel, M. *Chem. Sus. Chem* **2011**, 4, 432.¹

Photoelectrochemical (PEC) cells offer the ability to convert electromagnetic energy from our largest renewable source, the Sun, to stored chemical energy through the splitting of water into molecular oxygen and hydrogen. Hematite ($\alpha\text{-Fe}_2\text{O}_3$) has emerged as a promising photo-electrode material due to its significant light absorption, chemical stability in aqueous environments, and ample abundance. However, its performance as a water-oxidizing photoanode has been crucially limited by poor optoelectronic properties that lead to both low light harvesting efficiencies and a large requisite overpotential for photoassisted water oxidation. Recently, the application of nanostructuring techniques and advanced interfacial engineering has afforded landmark improvements in the performance of hematite photoanodes. In this chapter, insights into the basic material properties, the attractive aspects, and the challenges in using hematite for photoelectrochemical (PEC) water splitting are first examined. Next, recent progress enhancing the photocurrent by precise morphology control and reducing the overpotential with surface treatments are detailed and compared. The latest efforts using advanced characterization techniques, particularly electrochemical impedance spectroscopy, are finally presented.

2.1. Introduction

Energy from the Sun can easily provide enough power for all of our energy needs if it can be efficiently harvested. While there already exist a number of devices that can capture and convert electromagnetic energy, the most common—a photovoltaic cell—produces electricity, which must be used immediately or stored in a secondary device like a battery or a flywheel. A more elegant, practical, and potentially more efficient route to storing Solar power is to convert the electromagnetic energy directly into chemical energy in the form of molecular bonds analogous to the photosynthesis process exploited by nature.² Plant photosynthesis effectively rearranges electrons in H₂O and CO₂ to store solar energy in the form of carbohydrates. However, the extremely low overall efficiency that natural photosynthesis exhibits implies the requirement of vast amounts land and farming resources to meet our energy demands.^{3,4} Because of this, artificial photosynthetic routes including photoelectrochemical (PEC) and photocatalytic (PC) solar energy conversion have been intensely investigated over the last four decades. Given the abundance of H₂O on the Earth, the water splitting reaction, H₂O → ½ O₂ + H₂ ($E^0 = 1.23$ V), is the most appealing pathway for artificial photosynthesis. Indeed solar water splitting would form the basis for a sustainable hydrogen-based energy economy.

A distinction can be made between the different approaches to artificial photosynthesis: Photocatalytic (PC) water splitting systems use a dispersed material in pure water and accordingly produce hydrogen and oxygen homogeneously throughout the solution. This approach is under examination with both inorganic colloid materials^{5,6} and molecular complexes.⁷ In contrast, photoelectrochemical (PEC) systems employ photoactive materials as electrodes. As in conventional water electrolysis, oxidation (O₂ evolution) occurs at the anode, reduction (H₂ evolution) occurs at the cathode, and an aqueous electrolyte completes the current loop between the electrodes and an external circuit. One or both of the electrodes can be a photoactive semiconductor, in which a space-charge (depletion) layer is formed at the semiconductor-liquid junction (SCLJ). Upon irradiation, photogenerated carriers are separated by the space-charge field and the minority carriers (holes for an n-type photoanode and electrons for a p-type photocathode) travel to the SCLJ to perform one half of the water splitting reaction. The schematic for an n-type photoanode is

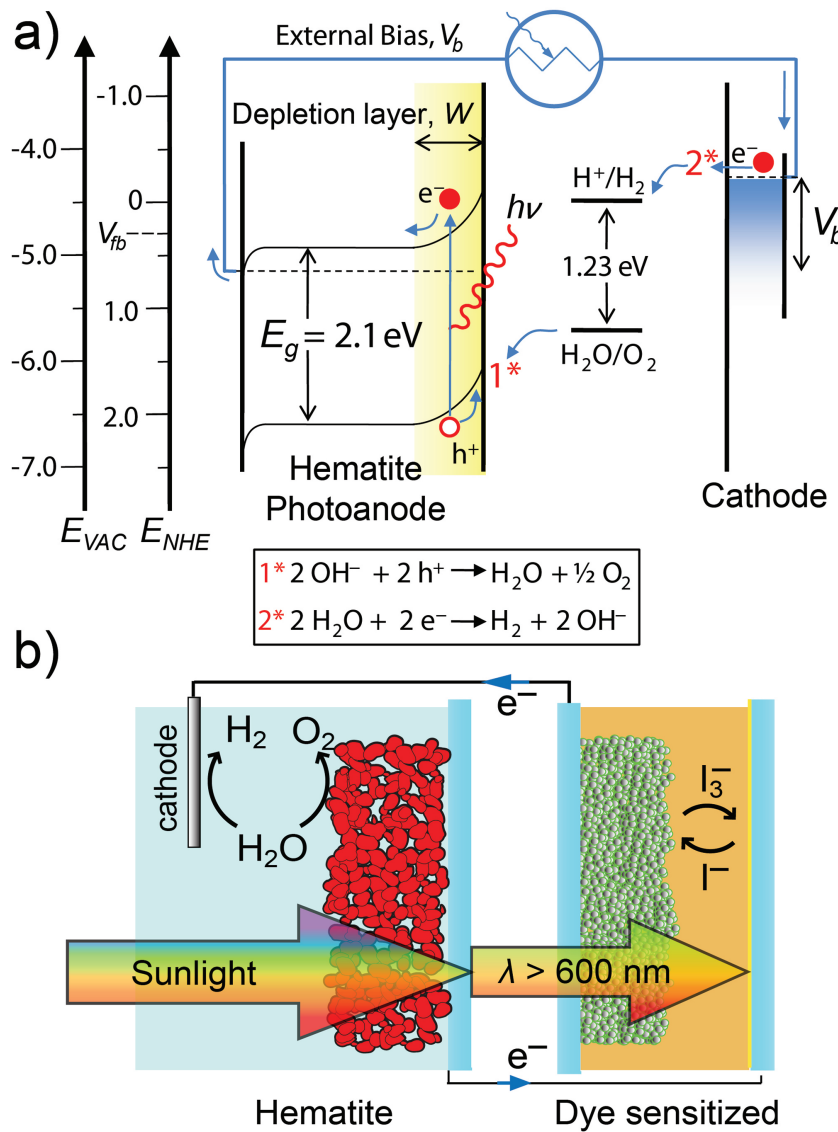


Figure 2.1: a) Energy diagram for photoelectrochemical water splitting with an n-type photoanode (hematite) performing the oxygen evolution (oxidation) reaction and a cathode performing the hydrogen evolution (reduction) reaction. The photoanode bandgap, E_g , flat band potential, V_{fb} , and the applied bias, V_b are indicated. b) Photoanode/Photovoltaic water splitting tandem cell concept is shown with a dye sensitized solar cell (DSC). Reprinted from [1].

shown in Figure 2.1a. The advantage of the PEC route is that it allows the spatially separate production, and therefore collection, of H_2 and O_2 .

Despite the difference between PC and PEC water splitting, the requirements of the materials employed are essentially the same, and ever since the seminal demonstration of PEC water splitting with TiO_2 ,^{8,9} scientists and engineers have sustained a vigorous search for a material combining the essential requirements: a small semiconductor bandgap for ample solar light absorption, conduction and valence band energies that straddle the water oxidization and reduction potentials,

high conversion efficiency of photogenerated carriers to the water splitting products, durability in aqueous environments, and low cost. However to date, no single semiconducting material has been found to meet all of these requirements.² Transition metal oxides like TiO₂ possess adequate stability but only absorb a small fraction of solar illumination due to their large band gap ($E_g = 3.2$ eV for anatase TiO₂). Many other semiconductors have smaller bandgaps and appropriate energy levels, such as InP ($E_g = 1.3$ eV), but they exhibit poor stability in aqueous environments.¹⁰ While much work continues to focus on identifying an ideal material using combinatorial¹¹ and ab initio (density-functional theory)^{12,13} approaches, an alternative approach borrows again from biologic photosynthesis, which uses two photosystems in tandem.

By relaxing the constraint that only one material (whose bandgap energy levels straddle the water redox potentials) can be used, combinations of complementary semiconductors can be employed.¹⁴ For example, a photoanode and a photocathode or a photoelectrode and a photovoltaic (PV) device can be used in tandem to afford overall solar water splitting with two or more photon absorption events. Systems delivering record solar-to-hydrogen (STH) efficiency over 12% have been demonstrated using III-V semiconductor materials with this approach, but their cost and stability remain major disadvantages.¹⁵ Alternatively, inexpensive and stable oxide photoanodes, such as WO₃ ($E_g = 2.6$ eV),^{16,17} with conduction band edges too-low in energy to reduce water, can receive an external bias from an economical PV device like a dye sensitized solar cell (DSC), which harvests solar photons not absorbed by the semi-transparent photoanode. This photoanode/DSC concept is shown in Figure 2.1b. Using a WO₃ photoanode it has demonstrated an overall water splitting efficiency of 4.5%.² Unfortunately due to its relatively large bandgap and expected kinetic losses, a maximum of only 8 % STH is possible with WO₃.¹⁸

Nevertheless, a tandem water splitting device holds great promise if a photoanode can be developed that combines sufficient light absorption, stability, and performance using raw materials of ample availability and low cost. Iron(III) oxide, Fe₂O₃, is a promising material in light of these requirements. With a potential to convert 16.8% of the sun's energy into hydrogen,¹⁸ it has been extensively examined for application to solar water splitting. In this chapter the advantageous properties of Fe₂O₃ as well as the challenges it presents to photoelectrochemical water splitting are presented. The most recent efforts at controlling water oxidation at the SCLJ,

improving photon harvesting by nanostructuring, and increasing the understanding of this promising material for solar energy conversion are critically examined.

2.2. Hematite as a promising material

Iron is the fourth most common element in the earth's crust (6.3 % by weight) and since iron is readily oxidized in air to the ferrous (+2) and ferric (+3) states, iron oxide is ubiquitous. For example, both the geological formations in the southwest United States and a rusty automobile fender take their distinctive red-brown color from the presence of iron oxides. These chromatic characteristics also exemplify iron oxide's ability to absorb solar irradiation. This coupled with its abundance and non-toxicity make iron oxide a particularly attractive material for use in solar energy conversion. Since the ferrous and ferric forms of iron are separated by a relatively small energy difference, many well-defined crystalline forms of iron oxide and oxyhydroxide exist in nature. The distinct properties of all of the iron oxides are comprehensively presented in a recent book by Cornell and Schwertmann.¹⁹ In this section, the important and unique properties of the most important iron oxide for solar energy conversion, $\alpha\text{-Fe}_2\text{O}_3$ (hematite), are presented and the seminal efforts to use this material in PEC water splitting are then detailed.

2.2.1. Overview of properties

Crystalline and magnetic structure

Hematite is the most thermodynamically stable form of iron oxide under ambient conditions and as such, it is also the most common form of crystalline iron oxide. The iron and oxygen atoms in hematite arrange in the corundum structure, which is trigonal-hexagonal scalenohedral (class $-3\ 2/m$) with space group R-3c, lattice parameters $a = 5.0356 \text{ \AA}$, $c = 13.7489 \text{ \AA}$, and six formula units per unit cell.¹⁹ It is easy to understand hematite's structure based on the packing of the anions, O^{2-} , which are arranged in a hexagonal closed-packed lattice along the [001] direction. The cations (Fe^{3+}) occupy the two-thirds of the octahedral interstices (regularly, with two filled followed by one vacant) in the (001) basal planes, and the tetrahedral sites remain unoccupied. The arrangement of cations can also be thought of producing pairs of FeO_6 octahedra that share edges with three neighboring octahedra in the same plane and one face with an octahedron in an adjacent plane in the [001] direction (Figure 2). The face sharing is responsible for a trigonal distortion of the octahedra as the proximal iron atoms are repelled to optimize the crystal's Madelung energy. Consequently, hematite exhibits a C_{3v} symmetry and there are two different

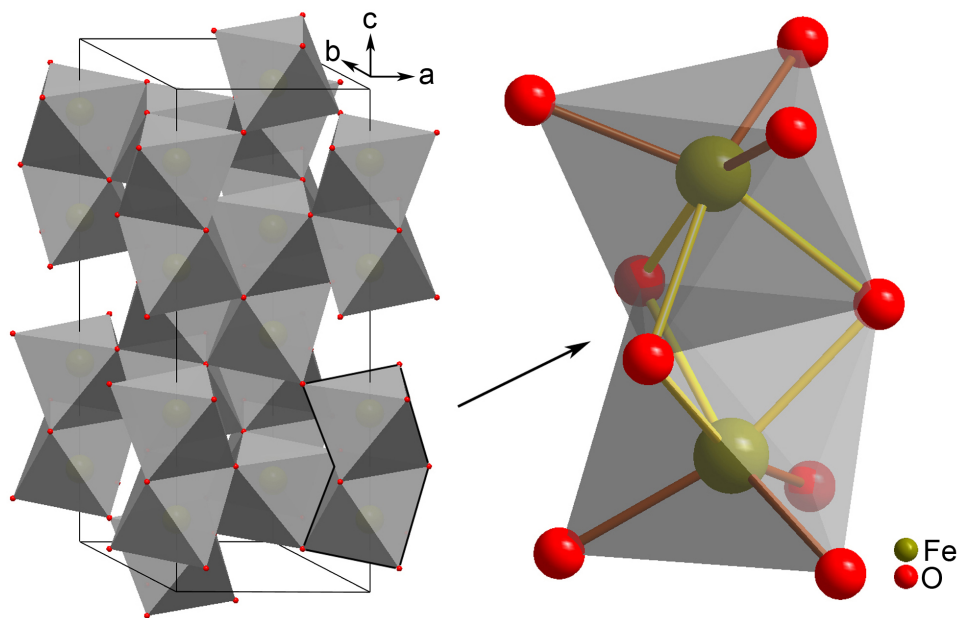


Figure 2.2: The unit cell (left) of hematite shows the octahedral face-sharing Fe_2O_9 dimers forming chains in the c direction. A detailed view (right) of one Fe_2O_9 dimer shows how the electrostatic repulsion of the Fe^{3+} cations produce long (yellow) and short (orange) $\text{Fe}-\text{O}$ bonds. Reprinted from [1].

$\text{Fe}-\text{O}$ bond lengths as illustrated in Figure 2.2. However, the electronic structures of the distorted FeO_6 octahedral are thought to be quite similar to undistorted clusters.¹⁹

The arrangement of the oxygen anions and the high-spin (d^5) cations naturally affect the orientation of the iron atoms' spin magnetic moment and thus the observed bulk magnetic properties. The diverse magnetic properties of all the iron(III) oxides have been recently reviewed.²⁰ In brief, hematite is antiferromagnetic at temperatures below 260 K and a weak (parasitic) ferromagnet at room temperature. The latter is due to the ferromagnetic coupling of the spins within the (001) basal planes and antiferromagnetic coupling between iron layers along the [001] direction.²¹ Here the trigonal distortion of the FeO_6 octahedra produces a slightly canted (about 5°) spin arrangement causing the destabilization of their perfectly antiparallel arrangement (parasitic ferromagnetism). While the magnetic properties of hematite are not particularly pertinent to its photoelectrochemical performance, the iron spin configuration does influence the optoelectronic and carrier transport properties of hematite. These attributes should be properly understood for its application as a semiconductor for solar water splitting. Decades of research have passed scrutinizing the mechanisms of charge transport and light absorption, and while hematite is still not completely understood, much progress has been made.

Optoelectronic characteristics

The absorption of photons by hematite begins in the near infra-red spectral region where weak absorption bands (with absorption coefficients, α , of the order 10^3 cm^{-1}) are due to $d-d$ transition states between electron energy levels of the Fe^{3+} ion, which are split by an intrinsic crystal field.²² While photoexcitation of hematite at these wavelengths has been shown in one case to increase its conductivity,²³ sustained photocurrent is not observed in a photoelectrochemical system upon irradiation below the band gap energy, E_g (which, depending on the method of preparation of hematite, is usually reported to be between 1.9 and 2.2 eV corresponding to $\lambda = 650$ to 560 nm).²⁴ The absorption coefficient of pure hematite increases abruptly at the bandgap energy and further up the electromagnetic spectrum α continues to increase with additional absorption features having been observed centered on 2.4, 3.2 and 5.8 eV (with α on the order of 10^5 cm^{-1}) in samples of polycrystalline hematite.²⁵ Hematite's strong absorption of yellow to ultraviolet photons in the visible region and transmission of orange to infrared photons gives it a characteristic red color. However, its fairly uniform reflectivity as a function of visible light wavelength gives specular hematite a metallic appearance.

Since the electronic nature of the bandgap in hematite is of great interest to understand its performance as a material for solar energy conversion, much work has focused on this aspect. The Tauc analysis of the bandgap absorption onset, which assumes that the energy bands are parabolic with respect to the crystal momentum, most frequently indicates an indirect (phonon-assisted) bandgap transition.²⁶ However, a few recent reports of a direct bandgap in hematite have been attributed to quantum size-effects.^{27,28} The initial orbital assignments of the bandgap suggested it was due to an indirect transition of $\text{Fe}^{3+} d-d$ origin,^{23,29} and that a stronger direct transition involving a charge transfer from an O $2p$ orbital to Fe $3d$ did not occur until 3.2 eV.²⁹ This led to a hypothesis that two different types of p-type charge carriers (holes) could be produced in hematite, depending on the excitation mechanism, and were responsible for the observed difference in photoelectrochemical (PEC) performance as a function of wavelength.^{30,31} However, the most recent ab initio calculations to determine the electronic structure of hematite by the Hartree-Fock approach³² and density functional theory with a local spin-density approximation and coulomb correlation^{33,34} both predict that the highest occupied energy states are primarily O- p in character and the lowest unoccupied states are from an empty Fe- d band. This conclusion is also supported by soft-x-ray

(O K-edge) absorption and emission spectroscopy, which, when compared to photoemission spectra from configuration-interaction FeO_6 cluster calculations, confirm that the valence band is at least strongly hybridized and indicates further that it is mostly of O 2p character.³⁵ These latest results not only suggest that pure stoichiometric hematite is a charge transfer insulator, and not a Mott-Hubbard type insulator—a detail that affects conduction models—but also contradicts the suggestion that two types of holes, originating from different transitions, could cause different PEC behavior.

Carrier transport

For use as a photoelectrode the efficient transport of majority charge carriers in hematite is essential. The earliest work by Morin on pure sintered polycrystalline samples describes very low electrical conductivities (ca. $10^{-14} \Omega^{-1} \text{ cm}^{-1}$),³⁶ conduction electron concentrations of 10^{18} cm^{-3} at 1000 K, and an activation-energy type electron mobility on the order of $10^{-2} \text{ cm}^2 \text{ V}^{-1} \text{ s}^{-1}$.³⁷ Studies on pure single-crystals showed conductivities below $10^{-6} \Omega^{-1} \text{ cm}^{-1}$ and were deemed unsuitable for further electronic characterization.³⁸ These unusually small values obliged electrical conduction to be explained by $\text{Fe}^{3+}/\text{Fe}^{2+}$ valence alternation on spatially localized 3d orbitals. Modeling studies have had success matching empirical data by describing the conduction mechanism with a small polaron model that includes the effect of the larger size of the Fe^{2+} ion and the associated lattice distortion (polaron).^{39,40} Conduction of electrons or holes are then best described by the hopping of polarons with an activation energy. This mechanism causes the mobility of carriers to increase with increased temperature, as transport phonon-assisted.⁴¹ The localized electron-small polaron model has been supported by further experimental results including pulse radiolysis⁴² and femtosecond laser spectroscopy on nanoparticles.⁴³

Further studies of hematite single crystals identified a highly anisotropic electron transport with conduction along the iron bilayer (001) basal plane up to four orders of magnitude greater than perpendicular directions (parallel to [001]).^{44,45} This discrepancy cannot be explained by the proximity of iron cations alone, as the shortest Fe–Fe distances are actually along the [001] direction.⁴⁶ However the anisotropic conductivity can be classically explained considering Hund's rule and the magnetic structure of hematite. The ferromagnetic coupling of the spins in the (001) basal planes and antiferromagnetic coupling along the [001] direction create an environment where electrons can move (n-type conductivity) within the iron bilayers (an environment of parallel spins) but are forbidden to hop across the oxygen planes

to an iron bilayer with the opposite spins. As such, conduction in the [001] direction could only involve the movement of holes in the form of $\text{Fe}^{3+} \rightarrow \text{Fe}^{4+}$ electron transfer. This process is significantly slower in hematite.⁴¹ While this classical explanation is generally accepted, recent ab initio electron structure calculations combined with electron transfer (Marcus) theory have correctly predicted the large transport anisotropy in hematite, but suggested it arises from the slowness of both hole and electron mobility across basal oxygen planes.²¹ This explanation does not consider electron transport to be forbidden in the [001] direction, but instead identifies the most important factor that influences the carrier mobility to be the electronic coupling—a quantity found to depend on both a superexchange interaction between the bridging oxygen atoms and the d-shell electron spin coupling.

While the specific details of the conduction mechanism and observed anisotropy are clearly important for orientating hematite crystals in a photoelectrode, its intrinsic conduction properties have been shown to be inadequate for PEC applications. Its conductive properties must be significantly enhanced by adding impurities to act as electronic dopants. Indeed, it is possible to increase conductivities and obtain both p-type or n-type $\alpha\text{-Fe}_2\text{O}_3$ by substitutional doping using atoms such as (non exhaustive list) Mg^{2+} , Cu^{2+} (p-type) or with Ti^{4+} , Sn^{4+} , Zr^{4+} , Nb^{5+} (n-type).⁴¹ By substituting at sufficient levels, high carrier conductivities can be attained. For example, Zr^{4+} was doped into single crystals to give donor densities on the order of 10^{19} cm^{-3} , conductivities around $0.1 \Omega^{-1} \text{ cm}^{-1}$, and increased electron mobility (perhaps due to a increase in dielectric constant) of $0.1 \text{ cm}^2 \text{ V}^{-1} \text{ s}^{-1}$.³⁸ A review by Shinar and Kennedy outlines the substitutional dopants used for n-type iron oxide and their affect on electronic and photoelectrochemical properties.⁴⁷ In general, optimum impurity concentrations are *ca.* 1 at% or less, and while substitutional transition metal impurities have been predicted to introduce inter-bandgap energy states³⁴, the same dopants have not been reported to significantly change E_g or a .^{38,48-50}

Photogenerated carrier lifetime

In addition to the conduction of majority charge carriers, a water splitting photoelectrode must efficiently transport photogenerated minority charges to the semiconductor-liquid junction to attain high conversion efficiency. For this, the lifetime of the photogenerated carriers is an important metric. Luminescence studies on nanoparticles show that the excitation of hematite with photons (3.2 eV) results in fluorescence quantum yields of order 10^{-5} .⁴³ This extremely low value of radiative

carrier recombination suggests that fast nonradiative processes such as carrier trapping and phonon coupling are limiting the excited state lifetime.⁵¹ Indeed, the ultra fast dynamics of excited states in hematite have been studied in colloidal nanoparticles, single crystals, and even nanostructured thin films using femtosecond laser spectroscopy.^{43,51,52} In nanoparticles it was found that the excited state decay profiles were independent of the pump power and the probe wavelength, and were not affected by lattice doping. However, the lifetime of the excited state was determined to be very short — 70% of the transient absorption had disappeared after just 8 picoseconds and could not be detected after 100 ps.⁴³ Studies on epitaxially-grown thin films (100 nm thick and made using an oxygen plasma assisted molecular beam) reduced the influence of bulk and surface defect states compared to the nanoparticle case, but found similar excited state dynamics, which were described by the following scenario: initially, hot electrons relax to the conduction band edge within 300 fs. Then their recombination with holes and trap states occurs within 3 ps. The resulting trap states can exist for hundreds of picoseconds before recombination to the ground state.⁵¹ The dominant carrier trapping mechanism was ascribed to mid-gap Fe³⁺ *d-d* states 0.5 – 0.7 eV below the conduction band edge giving them an optical transition of about 1.5 eV.^{53,54} These are likely the same spin-forbidden transitions intrinsic to hematite which were discussed above. In contrast to the short lifetime observed in hematite at neutral conditions, when a large anodic bias was applied to deplete electrons from an undoped hematite electrode, photogenerated holes were found to have a remarkably long lifetime of 3 ± 1 s.⁵² Further investigation of the lifetime in doped films under polarization would thus be an interesting next step.

The overall consequences of the observed trapping states, low carrier mobility, short photogenerated lifetime will next be discussed in the context of hematite as a photoelectrode for water splitting.

2.2.2. Early efforts with hematite for water splitting

Hardee and Bard⁵⁵ first turned to Fe₂O₃ as a material for water photolysis in 1976 seeking a photoanode material that was both stable under anodic polarization and capable of absorbing light with wavelengths longer than 400 nm. They prepared thin films of Fe₂O₃ on Ti and Pt substrates by chemical vapor deposition (CVD) of Fe(AcAc)₃ and observed photocurrent from their electrodes under illumination of 500 nm light at a potential of +0.8 V *vs.* the saturated calomel electrode (V_{SCE}) in 0.5 M KCl as electrolyte. Soon after Quinn *et al.*⁵⁶ showed that the (012) face of flux grown single crystals had collection efficiencies of around 20% at +0.5 V_{SCE} in 2 M NaOH

(+1.57 V vs. the reversible hydrogen electrode, V_{RHE}) with 475 nm light. Further work by Kennedy et al. showed that (Pb^{2+} and Ca^{2+} doped) p-type doping produced electrodes with high resistivity, but Si^{4+} , Sn^{4+} , and Ge^{4+} doped n-type hematite performed better than Ti^{4+} doped hematite.⁴⁸ Over the next decade numerous reports were published describing continuing studies with pure and doped Fe_2O_3 made by various routes. Notable extensive photoelectrochemical studies were performed on Ti doped polycrystalline sintered hematite pellets,^{26,31} and Nb doped single crystals⁵⁷ — the latter reporting champion performance with an incident photon conversion efficiency (IPCE) of about 37 % at 370 nm and +1.23 V_{RHE} in 1 M NaOH (27% at +1.06 V_{RHE}).

A good review of these seminal studies on hematite has been given by Lindgren et al.²⁴ and in summary, as an n-type photoanode, hematite was found to have excellent stability and a faradaic efficiency towards water oxidation of unity. However the first decade of work identified many challenges of employing this material for photoelectrochemical water splitting: i) a flat band potential, V_{fb} , too low in energy for water reduction (see Figure 1a),^{31,56} ii) a large requisite overpotential for water oxidation,³¹ iii) a relatively low absorption coefficient, requiring 400–500 nm thick films for complete light absorption,^{58,59} iv) poor majority carrier conductivity,^{54,57} and v) a short diffusion length ($L_D = 2\text{--}4 \text{ nm}$) of minority carriers.²⁶ Limitation (i) can nominally be overcome with the external bias provided by a PV or a photocathode in tandem. However, the large overpotential required (limitation ii) requires the use of 2 PVs to provide adequate bias.⁶⁰ This drawback and the remaining limitations deterred much further interest in hematite, as it appeared that highly efficient conversion of solar energy was not possible.

Specifically, drawback (iv) requires high doping levels to increase the ionized donor concentration and thus the conductivity. This in turn reduces the width of the space-charge layer.⁶¹ For example, donor dopant concentrations in the champion Nb doped single crystals were found to be $5 \times 10^{19} \text{ cm}^{-3}$ by Mott-Schottky analysis.⁵⁷ Assuming classical depletion layer theory,⁶¹ this would result in a depletion layer width, W , of 7 nm at a band bending of 0.25 V (i.e. $V_b = V_{fb} + 0.25 \text{ V}$) and a dielectric constant, ϵ_r , of 100. The low absorption coefficient in hematite (challenge iii) then implies that most of the incident photons will not be absorbed in the space-charge region if the geometry of the photoanode is planar because the absorption depth (defined according to the Beer-Lambert law as $a^{-1} = \text{depth at which } 63 \% \text{ of the photons are absorbed}$) for hematite ranges from 120 nm to 46 nm for photon

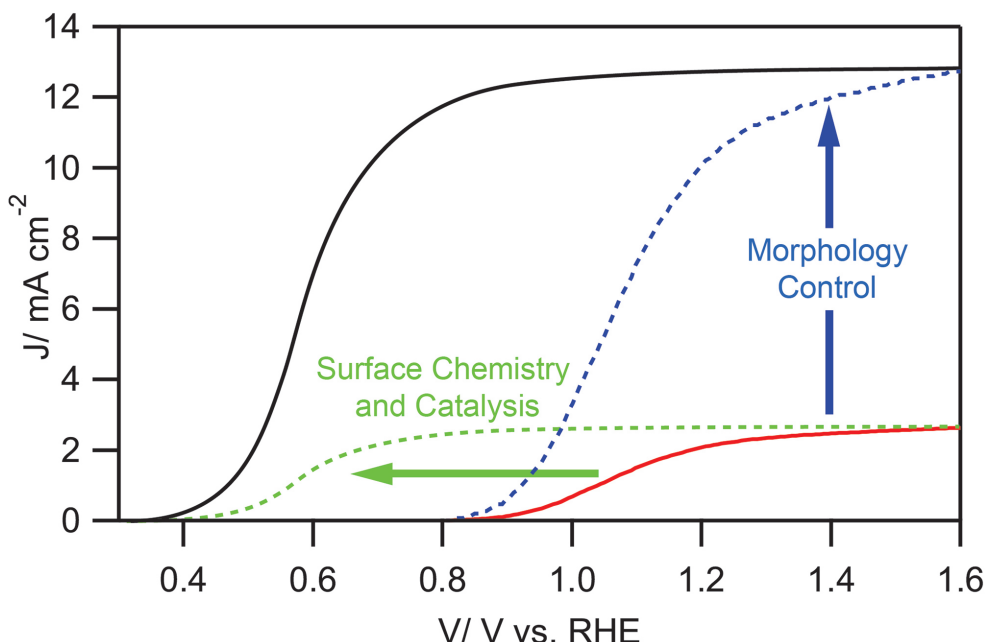


Figure 2.3: The two-part strategy for improving hematite performance is shown with respect to the photocurrent density, J , vs. voltage behavior for an idealized hematite photoanode (solid black trace) compared to the typical performance (solid red trace) under AM 1.5 G (100 mW cm^{-2}) simulated sunlight, and the expected effects of improving the surface chemistry and the morphology. Reprinted from [1].

wavelengths from 550 to 450 nm.²⁵ This would not be problematic if L_D was large compared to the absorption depth, but, due to the ultra-fast recombination of photogenerated holes, L_D is only 2–4 nm.²⁶ It is important to note that this value is significantly smaller compared to other oxides used for PEC water splitting. For example, values of L_D up to 104 nm and 150 nm have been reported for TiO_2 ⁶² and WO_3 ,⁶³ respectively.

The effect of limitations (iii)–(v) emerges as low quantum efficiencies especially for the longer wavelengths, even when the electrode is placed under large anodic bias. For example, with the highly-efficient Nb doped single crystal electrodes, the peak quantum efficiency was close to 30 % at $\lambda = 370 \text{ nm}$, but dropped to below 5 % at 450 nm, and even though all of the incident irradiation was absorbed at 550 nm in the 0.1 mm thick films used, the quantum efficiency at that wavelength was less than 1%.⁵⁷ A maximum photocurrent density of 12.6 mA cm^{-2} is possible with hematite based on its absorption and the AM 1.5 G solar spectrum (100 mW cm^{-2}), but the photocurrent delivered by this Nb doped photoanode would be only *ca.* 0.5 mA cm^{-2} based on the quantum efficiency reported. This is because the distribution of photons in the solar spectrum puts half of hematite's maximum possible solar photocurrent density in the wavelength range of 500 – 600 nm. Indeed, the mismatch

between the absorption depth of photons with energy close to E_g (*ca.* 100 nm) and the carrier harvesting width ($W + L_D = 10$ nm) suggests that the standard planar single crystal or sintered disk electrode geometries are not suitable for hematite. However, recent efforts with hematite have shown that optimizing the electrode morphology can significantly increase the water splitting photocurrent density. These recent and exciting advances in hematite structuring are described in detail in the section 2.4. The renewed efforts have also instigated further research into reducing the overpotential required by employing various surface treatments, which are examined in the next section. By combining these two strategies it is possible to approach the performance of an ideal hematite photoanode (Figure 2.3).

2.3. Decreasing the overpotential with surface modification

Based on the V_{fb} usually reported for hematite, an external bias of only 0.3 – 0.4 V_{RHE} should be necessary to initiate the water splitting reaction.[24] Once the applied bias is greater than V_{fb} , the band bending drives photogenerated holes to the SCLJ. However, the onset of water oxidation photocurrent is usually not observed until 0.8 – 1.0 V_{RHE} even at a high pH of 13.6 (1 M NaOH) and for single crystal electrodes. The remaining overpotential of *ca.* 0.5 – 0.6 V is a major drawback for the implementation of hematite-based tandem cells⁶⁰ and has been attributed to two distinct surface properties. Firstly there is evidence that mid-bandgap energy states resulting from both oxygen vacancies^{25,31,64} and crystalline disorder⁶⁵ can trap holes at the surface. This can even result in Fermi level pining in some electrodes.⁶⁶ Secondly, the oxygen evolution reaction (OER) kinetics are sluggish, not just due to the complicated four-electron mechanism that must occur, but also compared to other oxides semiconductors.⁶⁷ This may be due to the increased Fe³⁺ character of the valence band compared to other oxides.³¹

To overcome the limitation of poor OER kinetics, various catalysts have been attached to the surface of hematite photoanodes. For example, water oxidation at cobalt has been extensively studied and is known to be particularly rapid.⁶⁸ The treatment of Fe₂O₃ photoanodes (prepared by a CVD method) with a monolayer of Co²⁺ resulted in a *ca.* 0.1 V reduction of the photocurrent onset potential.⁶⁹ Since this treatment also increased the plateau photocurrent it was good evidence that the reaction rate was increased, and the Co²⁺ did not just fill surface traps. The application of a recently-reported amorphous cobalt-phosphate (Co-Pi) based water oxidation catalyst⁷⁰ on Fe₂O₃ gave a composite photoanode with a similar

photocurrent onset potential to that of the Co^{2+} treatment.⁷¹ However, the increased efficacy of the Co-Pi catalyst at more neutral pH afforded a noticeable enhancement of the overpotential reduction at pH 8.⁷² A drawback of this approach is the unproductive light absorption by the Co-Pi catalyst, which allows only a thin layer to be deposited.

The material often reported as the most effective catalyst for the OER is IrO_2 .^{73,74} For example, nanoparticles (~ 2 nm diameter) deposited onto a glassy carbon electrode achieve quantitative faradaic efficiency of water oxidation and an unequalled current density of 0.5 mA cm^{-2} at an overpotential of 0.25 V .^{75,76} The application of these nanoparticles to the surface of hematite by electrophoretic deposition resulted in an impressive shift of the photocurrent onset by about 200 mV giving $J = 0.3 \text{ mA cm}^{-2}$ at 0.9 V and 1.16 mA cm^{-2} at $1.0 \text{ V}_{\text{RHE}}$.⁷⁷ This specific result is detailed further in the following section, but the fact that even the best OER catalyst leaves a significant overpotential remaining (0.3–0.4 V) suggests that the other surface limitation—*i.e.* surface trapping states—still plays an important role for hematite photoanodes.

The presence of trapping states on the surface has been verified by using sacrificial electron donors in the electrolyte,⁵³ and been shown to be controllable by altering the oxidizing environment of the hematite preparation conditions.⁶⁴ However, since this is not always possible when using a preparation method designed for nanostructuring, a method to address surface trapping states on already-prepared hematite is necessary. It has also been evidenced that surface trapping states can be passivated with extremely thin Al_2O_3 overlayers made by atomic layer deposition (ALD).⁷⁸ This study, presented in Chapter 6, shows that even just one ALD cycle of Al_2O_3 on a Fe_2O_3 photoanode shifted the photocurrent onset potential by about 100 mV. The subsequent application the Co^{2+} catalyst further reduced the overpotential and resulted in a record photocurrent at $0.9 \text{ V}_{\text{RHE}}$ of over 0.4 mA cm^{-2} . This result shows that separately addressing both of the surface limitations can afford a significant reduction of the overpotential, however, to enable the realistic use of tandem water splitting device with a hematite photoanode, a further reduction of the overpotential is required. Essentially, the maximum (plateau) photocurrent density (up to 12.6 mA cm^{-2}) must be obtained at only *ca.* $0.6 \text{ V}_{\text{RHE}}$. With typical onset behavior, this implies an overpotential of only 0.1–0.2 V.

A different approach, recently reported by Hu *et al.* holds promise to reach the high photocurrents at $0.6 \text{ V}_{\text{RHE}}$. Here the authors observed a shift of V_{fb} in the

cathodic direction by 150 mV (as measured by the Mott-Schottky technique) using a surface modification with fluoride.⁷⁹ Attaining unassisted water splitting with hematite could even be possible with this technique if V_{fb} could be moved cathodic of 0 V_{RHE}. In a practical device a combination of all three surface treatment strategies would be employed to afford the highest photocurrent density at the lowest applied potential.

Overall surface treatments have shown great promise in reducing the applied potential necessary to onset photocurrent with hematite photoanodes. However, increasing the solar photocurrent from the *ca.* 0.5 mA cm⁻² in the single crystal case towards the maximum possible 12.6 mA cm⁻² is more critical for establishing the viability of hematite as a material for solar energy conversion. Methods to address this challenge are discussed in the next section.

2.4. Increasing photocurrent with morphology control

The small carrier harvesting depth ($W + L_D$) discussed in section 2.2.2 suggests that the ideal morphology of a hematite photoanode would be one where all of the material is within 10 – 20 nm of the SCLJ. Of course, one could simply deposit a 10 nm layer of hematite on a transparent substrate using a traditional deposition method. The relatively poor absorptivity of such a film could then be overcome by stacking multiple layers in tandem, assuming the substrate used was a transparent conductor like fluorine doped tin oxide (FTO). This approach was suggested by Itoh and Bockris in 1984.⁵⁹ While this could fundamentally resolve the issue, it is cumbersome and expensive to implement, and in practice the thin iron oxide films were found to exhibit poor performance due to the increased recombination of the photogenerated holes.⁵⁸ Fortunately the recent development of tools to control the dimensions and morphology of materials at the nanometer length scale has offered more practical solutions for hematite. The application of nanostructuring techniques to PEC solar hydrogen production has indeed led to advances with many materials. A general overview of this topic is presented by recent review articles.^{80,81} This section will analyze how different deposition techniques have allowed the morphology control of hematite and affected its performance as a photoanode.

2.4.1. Porous thin films from solution-based colloidal methods

A straightforward way to create nanostructured photoelectrodes is to coat a dispersion of nanoparticles and a porogen onto a conductive substrate. Drying and then heating these films in air burns away the porogen and sinters the remaining oxide leaving a porous structure of interconnected particles. This concept has been

employed effectively with TiO_2 for the DSC, and was first attempted with hematite in 1994.⁸² In this seminal work, Fe_2O_3 sols created by the hydrolysis of FeCl_3 were combined with Triton-X100 before they were doctor-bladed onto FTO and sintered at 560 °C. Micron-thick, porous films of necked hematite were observed to have good adhesion to the substrate and a primary particle size in the 25–75 nm range. However the incident photon-to-current efficiency (IPCE) of these photoanodes towards water splitting was quite low—on the order of 1 % at 0.4 V_{SCE} in 0.1 M NaOH (1.4 V_{RHE}) with 400 nm incident irradiation. The IPCE was 100 times lower when the anode was illuminated from the hematite/electrolyte interface as compared to the substrate/hematite interface and the quantum efficiency did not improve when LiI was added as a hole scavenger. This led the authors to conclude that charge carrier recombination was the critical factor controlling the photocurrent. The higher quantum efficiency of similar particles when dispersed in electrolyte⁸³ pointed to grain boundaries in the porous films to be the cause of the excessive recombination and poor performance. This limitation was later addressed by altering the film thickness to optimize the light absorption/carrier transport issue.⁸⁴ However no significant improvement was obtained.

Recently the hypothesis that the limitation of these porous films was the transport and collection of majority carriers was confirmed, and relatively high water splitting photocurrents were obtained after successfully incorporating dopants at sufficient concentration.⁸⁵ In this work hematite nanoparticles 5 – 10 nm in diameter, which had been prepared by thermal decomposition of $\text{Fe}(\text{CO})_5$ in the gas phase, were dispersed in 2-propanol with acetylacetone and hydroxypropyl cellulose and coated on FTO or Pt substrates. While no water splitting photocurrent was observed with these electrodes upon sintering at 400 or 700 °C, 20 min at 800 °C was sufficient to diffuse and activate dopants (Sn^{4+} or Pt^{4+} from the substrate) and afford relatively high photocurrents. Under standard illumination conditions (AM 1.5G 100 mW cm⁻²) 0.56 mA cm⁻² at 1.23 V_{RHE} and over 1.0 mA cm⁻² before the onset of dark current (1.55 VRHE) were obtained.⁸⁶ The same high sintering temperature of 800 °C was found to be necessary to afford photoactivity even when (Ti^{4+}) dopant atoms were included in the colloidal dispersion.⁸⁵ This observation suggests a minimum activation energy is required to overcome a barrier for the diffusion and activation of doping cation impurities in the hematite lattice, and is supported by the report of a drastic change in the diffusion coefficient of $^{55}\text{Fe}^{+3}$ isotopes in hematite⁸⁷ and the further increase in the C_{3v} crystal distortion (see section 2.2.1),⁸⁸ both of which have

been reported to occur at approximately the same temperature. The latter of these effects was shown to be directly correlated to an increased absorption coefficient in films sintered at these high temperatures suggesting that this lattice relaxation is an important aspect influencing the optoelectronic properties of hematite.⁸⁶

Another effect of the high temperature treatment is the increase of the feature size from the original 5 – 10 nm to more than 50 nm via sintering (see Figure 2.4c). This large particle size prevents the photocurrent densities from surpassing the single crystal or sintered disk approaches. To overcome this limitation a method to independently control the feature size and functionality with nanostructured oxide electrodes using an encapsulation approach was recently developed.⁸⁹ First, the as-deposited films were subjected to a “morphological” annealing to remove the porogen, give good inter-particle connections, and set the feature size. Next the films were encapsulated with mesoporous SiO_2 using a solution-based precipitation approach. The SiO_2 acted as a confinement scaffold during the high temperature, “functional” annealing (800 °C) which followed to diffuse and activate the dopant (Ti^{4+} included in the deposition solution). The subsequent removal of the SiO_2 by dissolution revealed the functional electrode with a feature size controlled by the first annealing step. The outcome of applying this approach is shown in Figure 2.4.

The effect the encapsulation technique had on the nanostructure was immediately evident by eye when comparing the resulting electrode to a control heated to 800 °C without a confinement scaffold. The larger feature size in the control electrode resulting from sintering without the SiO_2 scatters visible light and the electrode appears translucent with a high opacity. In stark contrast, feature sizes in the confined electrode (500 °C morphological annealing) remain too-small to scatter ambient light and the electrode remains transparent (Figure 2.4a). Scanning electron micrographs clearly show the difference of the final feature size, which remains at *ca.* 25 nm with the encapsulation approach and grows to 100 – 200 nm in the control case (Figure 2.4 b and c). As the encapsulated electrode’s smaller feature size allows the photogeneration of holes closer to the SCLJ, a marked increase in the water oxidizing photocurrent was also observed. The photocurrent of the encapsulated electrode reached 1.86 mA cm^{-2} at $1.43 \text{ V}_{\text{RHE}}$ with a maximum photocurrent of 2.34 mA cm^{-2} before the onset of the dark current while the control electrode gave only a maximum of 1.5 mA cm^{-2} (Figure 2.4d). This remarkable increase of photocurrent was shown to be due an increase of the photon conversion efficiency (IPCE) especially in the longer wavelength range.

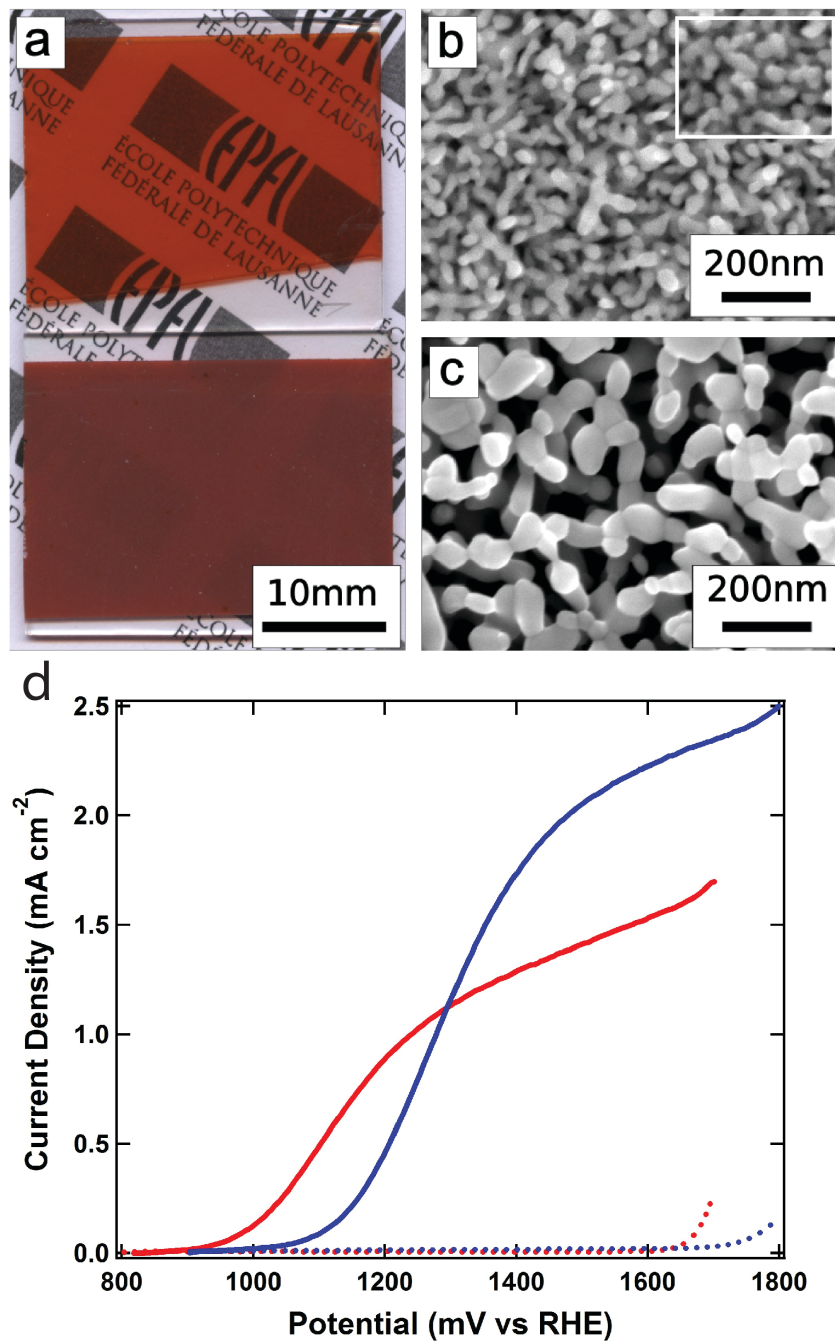


Figure 2.4: Electrodes prepared using a solution-based colloidal approach with an encapsulation technique to control the morphology. The visual appearance (a, top corresponds to the encapsulated sample, bottom corresponds to control sample) and scanning electron micrographs of encapsulated (b) and control (c) porous hematite electrodes are shown. The inset in (b) shows the morphology before encapsulation. (d) Electrochemical water oxidation photocurrent (solid lines) and dark current (dotted lines) vs. applied voltage curves of control (red) and encapsulated (blue) photoanodes under simulated solar light (AM 1.5G 100 mW cm^{-2} , spectrally corrected) in 1 M NaOH electrolyte. Reprinted with permission from [89].

Despite the demonstrated efficacy of the encapsulation technique certain drawbacks prevent it from reaching further improvement of the photocurrent. First, a

considerable anodic shift of the photocurrent onset potential was observed (Figure 2.4d). This might result from the diffusion a large concentration of Si from the confinement scaffold into the surface of hematite creating defect states, and could potentially be addressed with a subsequent etching step. Second, the conditions found to give a the maximum photocurrent were with a 500 °C morphological annealing giving a feature size of *ca.* 25 nm, however attempts to use a lower morphological annealing temperature resulted in films with less photocurrent despite a smaller feature size (which should allow more photogenerated holes to reach the SCLJ). Altering the film thickness suggested that a tortuous path for electron conduction with many grain boundaries limited electron transport in films prepared with a morphological annealing temperature less than 500 °C. Ultimately, while the solution-based nature of this approach generates much interest in this technique higher photocurrents would be possible if the electron transport limitation could be avoided.

2.4.2. Fe₂O₃ nanowire arrays

An obvious solution to the problem of majority carrier transport in hematite films created from the colloidal approach is to use nano-sized rod or wire arrays. An array of single-crystal nanorods with diameters in the 10 nm range, attached and oriented orthogonally to a conducting substrate would eliminate grain boundaries, and provide a direct path for electron collection while still allowing photogenerated holes to efficiently reach the SCLJ. A simple method to create hematite arrays on a variety of substrates from the controlled precipitation of Fe³⁺ in aqueous solution was first reported by Hagfeldt and coworkers,⁹⁰ and investigated for water photoelectrolysis soon after.⁶⁷ Bunches of individual 5 nm nanorods with an average diameter of 50 nm and a length of 0.1 to 1.5 μm (see Figure 2.5, right) were investigated in perpendicular and parallel orientations to the substrate. While the authors were able to show a small improvement when controlling the orientation (5 % IPCE at 360 nm for the perpendicular nanorods *vs.* 3% for the parallel) the overall photocurrents remained low under white light illumination, even with the hole-scavenging iodide present. The large difference between the electrode performance when illuminating from different sides of the semitransparent photoanode observed in this work,⁶⁷ and a recent report⁹¹ examining the surface photovoltage on electrodes prepared in the same way, suggests that bulk or surface defects are the major factors limiting the performance hematite prepared by this route. Indeed, aqueous methods of preparing hematite typically pass through a phase containing iron

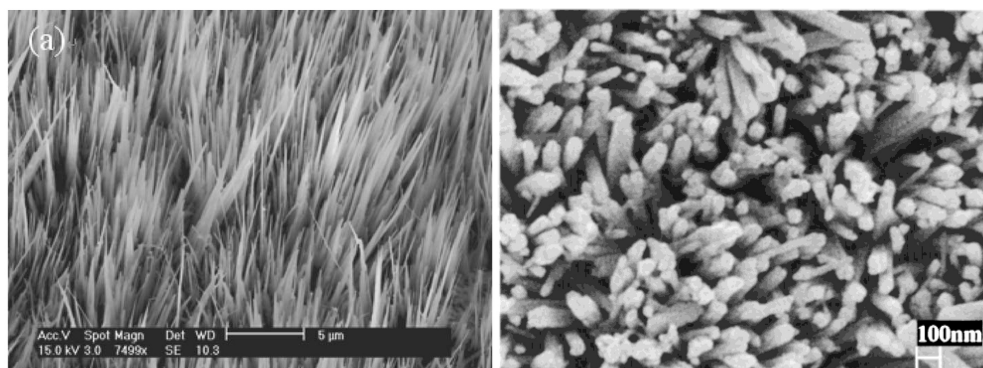


Figure 2.5: Examples of hematite nanowire morphologies: SEM images of hematite prepared by the thermal oxidation method (left image, reprinted with permission from [93], copyright 2005 American Institute of Physics) and aqueous method (right image, reprinted with permission from [90], copyright 2001 American Chemical Society).

hydroxide (*e.g.* akaganeite, lepidocrocite or goethite) and despite the fact that primarily hematite is detected after annealing at 500 °C, it has been shown that at temperatures up to 800 °C, a nonstoichiometric composition remains in hematite prepared by aqueous methods.⁹² As such, residual hydroxyl groups or vacancies are likely to blame.

Another facile method to produce hematite nanowires is by the simple thermal oxidation of iron foils and has been reported by many groups.⁹³⁻⁹⁷ Due to the increased volume of the oxide over the metal, when foils of iron are thermally oxidized under the right conditions, arrays of Fe₂O₃ nanowires spontaneously grow from the surface of the foil. With diameters of 20 – 40 nm and lengths of up to 5 μm (see Figure 5, left) these nanowire arrays would have large surface area, sufficient light absorption and a direct path for the conduction of electrons to the substrate (since basal planes are oriented perpendicular to the substrate⁹⁶), making them a very attractive morphology for hematite. This simple thermal oxidation method has been demonstrated on multiple (even transparent) substrates,⁹⁷ and methods for doping the wires have been employed.⁹³ However, no convincing reports of activity towards water oxidation have appeared. This may be due to the defects present in nanowires prepared this way or the presence of suboxides near the interface of the substrate which greatly enhance recombination.⁹⁸

Recently, a method to prepare hematite nanorod arrays using an anodic aluminum oxide (AAO) template was reported.⁹⁹ Gold was sputtered onto one side of a 60 μm thick AAO membrane with 200 nm diameter pores. Electrodeposition of iron oxide from aqueous solution, annealing at 500 °C, and the subsequent removal of the AAO by dissolution gave the final structure. The length of the rods could be varied by

changing the deposition duration. Despite the absence of any intentional doping, a 10 μm thick rod array showed water oxidation photocurrent densities of about 1 mA cm^{-2} at a potential of 1.5 V_{RHE} under AM 1.5 illumination. However, no defined photocurrent plateau was observed, suggesting a majority carrier transport limitation in spite of the nanostructure. The incorporation of dopants and annealing at 800 °C may afford higher photocurrents with this approach. However, based on the known minority carrier transport properties of hematite the pore size should also be reduced to less than 25 nm to afford a significant increase in photocurrent.

2.4.3. Electrochemical Fe_2O_3 nanostructuring

The recent development of nanostructuring techniques using potentiostatic anodization has provided another possible route to create structured hematite photoelectrodes. Prakasam *et al.* first showed that iron foils could be nanostructured using anodization in a glycerol-based electrolyte containing 1 % NH_4F + 1 % HF + 0.2 % HNO_3 .¹⁰⁰ Ordered nanopores were observed with pore size ranging from 20 to 250 nm and depths up to 600 nm depending on the anodization voltage and time. Under simulated solar illumination these photoanodes produced a photocurrent of 0.05 mA cm^{-2} at 0.4 V_{SCE} in 1 M NaOH (1.45 V_{RHE}). Work by the same group on anodized Ti-Fe-O electrodes is notable here due to the high photocurrent densities reported (1.1 mA cm^{-2} at 1.4 V_{RHE} in 1 M NaOH) despite the presence of both hematite and rutile in photoanode prepared at the optimized conditions.¹⁰¹ In contrast, very well defined nanotube arrays of pure iron oxide created from iron foils have been subsequently reported by a different research group.¹⁰² In this work, a single anodization step with 0.1 M NH_4F + 3 vol% water in ethylene glycol created nanotubes with walls less than 50 nm and lengths of about 1.5 μm . After an optimized annealing treatment these electrodes were found to be a mixture of both hematite and maghemite by XRD and had only small photocurrents ($160 \mu\text{A cm}^{-2}$, 1.23 V_{RHE} under AM 1.5 illumination compared to $120 \mu\text{A cm}^{-2}$ dark current). However, a double step anodization procedure with the addition of sodium tripolyphosphate in the electrolyte, and the subsequent annealing created a dendrite-like morphology situated over the tube array. Electrodes prepared this way exhibited a photocurrent of about 1 mA cm^{-2} under AM 1.5 illumination and at 1.23 V_{RHE} . A large carrier concentration (10^{21} cm^{-3}) was found via Mott-Schottky indicating a large amount of dopant or impurity present. The authors attribute the high photocurrent to the double layered structure which includes both a large surface area for water oxidation and a vertically orientated nanotube array for electron transport.

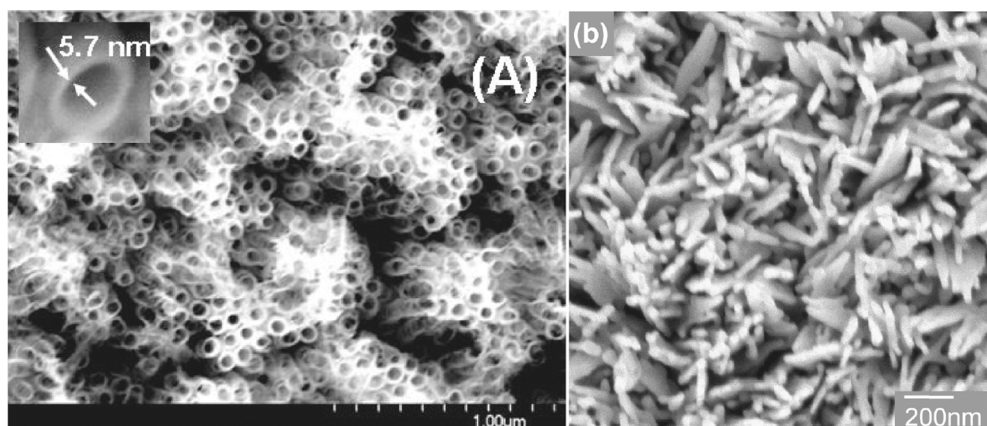


Figure 2.6: Hematite morphologies accessible by electrochemical techniques: The left SEM image is from a sono-electrochemical anodization (Reprinted with permission from [103], Copyright 2009 American Chemical Society). The right SEM image is from a controlled anodic electrodeposition (Reprinted with permission from [106], Copyright 2009 American Chemical Society).

In subsequent work by the same group, a sono-electrochemical anodization method was employed to obtain either nanoporous or nanotubular Fe_2O_3 depending on the anodization conditions.¹⁰³ The optimization of conditions gave nanotubes with walls an impressive 5 – 6 nm thick and microns in length (see Figure 2.6, left). Annealing these films resulted in pure hematite, which gave similar photocurrents (*ca.* 1 mA cm⁻² at AM 1.5 and 1.23 V_{RHE}) and similar carrier densities to the previous work. While the initial tube size presented in this work is remarkable and an important step for obtaining hematite with the ideal morphology, the tubes were initially amorphous Fe_2O_3 . The annealing step necessary for crystallinity and photoactivity almost certainly demolishes the meticulous nanostructuring through the sintering of the material.

Nanostructured hematite photoanodes also have been prepared by the electrodeposition of precursors from solution. Recently McFarland and coworkers reported a method to deposit of iron hydroxides from FeCl_3 solutions under cathodic polarization. The subsequent annealing at high temperature (700 °C) then resulted in porous hematite films.^{28,104} This method readily allows for the incorporation of dopants which were found to have an effect on the morphology of the sintered electrodes. Feature sizes down to 40 nm were observed and an IPCE of 8 % with 400 nm illumination at 1.2 V_{RHE} in 1 M NaOH with 15 % Mo doping were reported. In a subsequent report, an isovalent substitutional dopant Al^{3+} was added to the hematite to modulate the lattice strain — a factor predicted to benefit polaron migration and offer a novel way to increase conductivity.¹⁰⁵ However, the generally-

observed large particle size obtained with this technique remains a limitation to higher photocurrent densities.

Another example of electrodeposition has been recently reported by Spray and Choi¹⁰⁶ using an anodic electrodeposition. They were able to demonstrate impressive morphology control ranging from wires arrays (see Figure 2.6, right) to porous films by varying the solution pH. The films were photoactive in an electrolyte containing iodide, but water oxidation photocurrents were not reported suggesting surface recombination issues. In general, while impressive morphologies can be obtained with electrochemical deposition techniques, water splitting photocurrents have been limited by the quality of the material produced.

2.4.4. Spray pyrolysis techniques

Despite the deliberate attempts to nanostructure hematite using the methods described above, a simple spray pyrolysis technique consistently produces electrodes with superior performance. First reported in 1984,¹⁰⁷ an aqueous or ethanolic solution of Fe^{3+} is simply sprayed onto a hot ($400 - 500 \text{ }^\circ\text{C}$) substrate in air and photocurrent densities in the $0.5 - 1.0 \text{ mA cm}^{-2}$ range are typically obtained under simulated solar illumination ($1 \text{ M NaOH}, 1.6 \text{ V}_{\text{RHE}}$)^{66,108-110} with the exception of one report¹¹¹ of high photocurrent attributable to excess UV in the light source.¹¹² Surprisingly, reasonable photoactivity can be obtained with this method even without intentionally adding dopants to increase the conductivity of the Fe_2O_3 . Commonly used precursors like FeCl_3 or $\text{Fe}(\text{AcAc})_3$ likely leave chlorine or carbon residues behind that act as electric dopants. Films produced are generally compact (not porous) and the surface area limits the photocurrent produced under standard illumination conditions. However, the ease and reproducibility of this technique has led to valuable fundamental studies on dopants^{108,113} and substrate effects.¹⁰⁹ Rigorous optimization has also produced films with a very high quantum efficiency (IPCE = 25% at 400 nm and $1.42 \text{ V}_{\text{RHE}}$).¹¹³ In a recent report from Duret and Grätzel, the spray pyrolysis technique was modified to create nanostructured films by using an ultrasonic spray nozzle to produce very fine droplets of the precursor solution which were entrained in a rapid flow of air and transported horizontally over a heated substrate.⁶⁶ Under optimized conditions, a slow growth rate (ca. 100 nm h^{-1}) produced hematite with a leaflet type structure consisting of 100 nm-sized platelets of $5 - 10 \text{ nm}$ thickness bundled into 50 nm sheets oriented perpendicular to the FTO support. These ultrasonic spray pyrolysis (USP) films performed remarkably as water splitting photoanodes, producing 1.3 mA cm^{-2} under AM 1.5G (100 mW cm^{-2})

simulated solar irradiation in 1 M NaOH at 1.23 V_{RHE}. The IPCE was found to be 16 % with 375 nm illumination at the same applied potential, and over 30 % at 1.6 V_{RHE}. Subsequent work on these films revealed the importance of Si doping, which was found to be leaching from the silicon tubing used in the previous work.^{114,115} In addition, the platelets were found to be preferentially orientated with the (001) basal planes normal to the substrate and the flat surface of the platelets presenting the basal plane. While this morphology should facilitate electron transport to the FTO substrate it also requires the holes to be conducted across oxygen layers. Both this detail and the poor kinetics of water oxidation were thought to be restricting the photocurrent produced.

2.4.5. Atmospheric pressure chemical vapor deposition

Continuing efforts to improve the performance beyond the USP films led to the development of a simple, yet effective process to make nanostructured films of hematite from the thermal decomposition and oxidation of iron pentacarbonyl in an atmospheric pressure chemical vapor deposition (APCVD) reactor.¹¹⁵ Briefly, Fe(CO)₅ vapors were transported, along with tetraethyl orthosilicate (TEOS) as a source of silicon dopant, by an carrier gas (dry air), and directed vertically onto a heated substrate. The poor thermal stability of the Fe(CO)₅ (the half life for decomposition at 300 °C is 5.3 ms¹¹⁶) caused the homogenous nucleation of nanoparticles in the gas phase.¹¹⁷ These particles were then subjected to a thermophoretic force which limited their approach to the hot substrate and resulted in fractal-like cauliflower structures characteristic of a diffusion-limited aggregation mechanism (in contrast to surface reaction limited).⁶⁵ In 2006 Kay et al. reported APCVD films optimized with a substrate temperature of 420 °C and using a carrier gas flow rate of 2 L min⁻¹. Cauliflower-type structures with a minimum feature size of 5–10 nm grew on FTO substrates at rate of about 100 nm min⁻¹. The best film produced a photocurrent density of 1.8 mA cm⁻² at 1.23 V_{RHE} under standard illumination in 1 M NaOH and was further increased to 2.2 mA cm⁻² by treating the surface with Co²⁺ ions. Similar to the films prepared by the USP method, the silicon dopant was found to affect the nanostructure, producing a smaller feature size in both cases and an alignment of the basal crystal plane normal to the substrate.^{69,115}

In continuing work with this deposition technique ferrocene and tetramethyl orthosilicate (TMOS) were found to be viable sources of iron and silicon, respectively.^{118,119} The use of ferrocene is notable for replacing the toxic iron pentacarbonyl, however the photocurrent density obtained remained less than 1 mA

cm^{-2} . With the standard $\text{Fe}(\text{CO})_5$ / TEOS system Cesar et al. showed a large temperature effect on the nanostructure which corresponded to the performance of the electrodes.⁶⁵ Higher temperatures were found to decrease the deposition rate, lead to a larger particle size, and reduced the photocurrent density. A Mott-Schottky analysis gave the calculated donor density, N_d , of the Si doped Fe_2O_3 films as $1.7 \times 10^{20} \text{ cm}^{-3}$ —close to the predicted $6 \times 10^{20} \text{ cm}^{-3}$ if the known incorporation of silicon (1.6 at% Si)⁶⁹ was substitutionally incorporated into the lattice as Si^{4+} . Based on classic depletion layer theory,⁶¹ this led the authors to suggested that a space-charge layer of *ca.* 5 nm could still be present and aiding hole transport the SCLJ even in the small features on the top of the APCVD film. In addition, changing the deposition time defined an optimum thickness (500 nm) for photocurrent production from front side illumination (*i.e.* upon the hematite/electrolyte interface). A slow decrease in photocurrent was observed for thicker films resulting in less than 1 mA cm^{-2} for $1 \mu\text{m}$ thick films. This implied an electron transport limitation, which was subsequently addressed by tuning the particle to precursor ratio.

An important parameter governing the structure and quality of nanostructured prepared by particle-assisted CVD systems, like the APCVD of $\text{Fe}(\text{CO})_5$, is the particle to precursor ratio.¹²⁰ By changing the carrier gas flow rate, keeping the same concentration of iron precursor, and re-optimizing the other experimental parameters, the amount of time the precursors resided in the critical region of particle nucleation and growth above the deposition substrate was effectively tuned. It was found that using a carrier gas flow rate three times higher than the previous result (6 L min^{-1}) enhanced the preferential orientation of the basal planes normal to the substrate (enhancing majority carrier transport), but did not change the primary particle size.¹²¹ This resulted in an optimized thickness of 800 nm, and photocurrents above 3 mA cm^{-2} (see Figure 2.7). To improve upon the overpotential reduction found with the Co^{2+} treatment, the IrO_2 nanoparticle OER catalyst was then deposited onto the Fe_2O_3 cauliflower by an electrophoretic process. This produced a 200 mV shift in the photocurrent onset potential and photocurrent of 3.3 mA cm^{-2} at $1.23 \text{ V}_{\text{RHE}}$ under standard testing conditions.⁷⁷

The photocurrent produced was further verified by measuring the photoanode IPCE at $1.23 \text{ V}_{\text{RHE}}$. Over 50 % of the photons with $\lambda = 300 \text{ nm}$, 39 % at 400 nm, and a remarkable 20% at 500 nm were effectively harvested using this nanostructure. Moreover, the integration of the product of the IPCE and the standard AM 1.5G solar photon flux over the entire wavelength range gave a photocurrent of 3.01 mA cm^{-2} ,

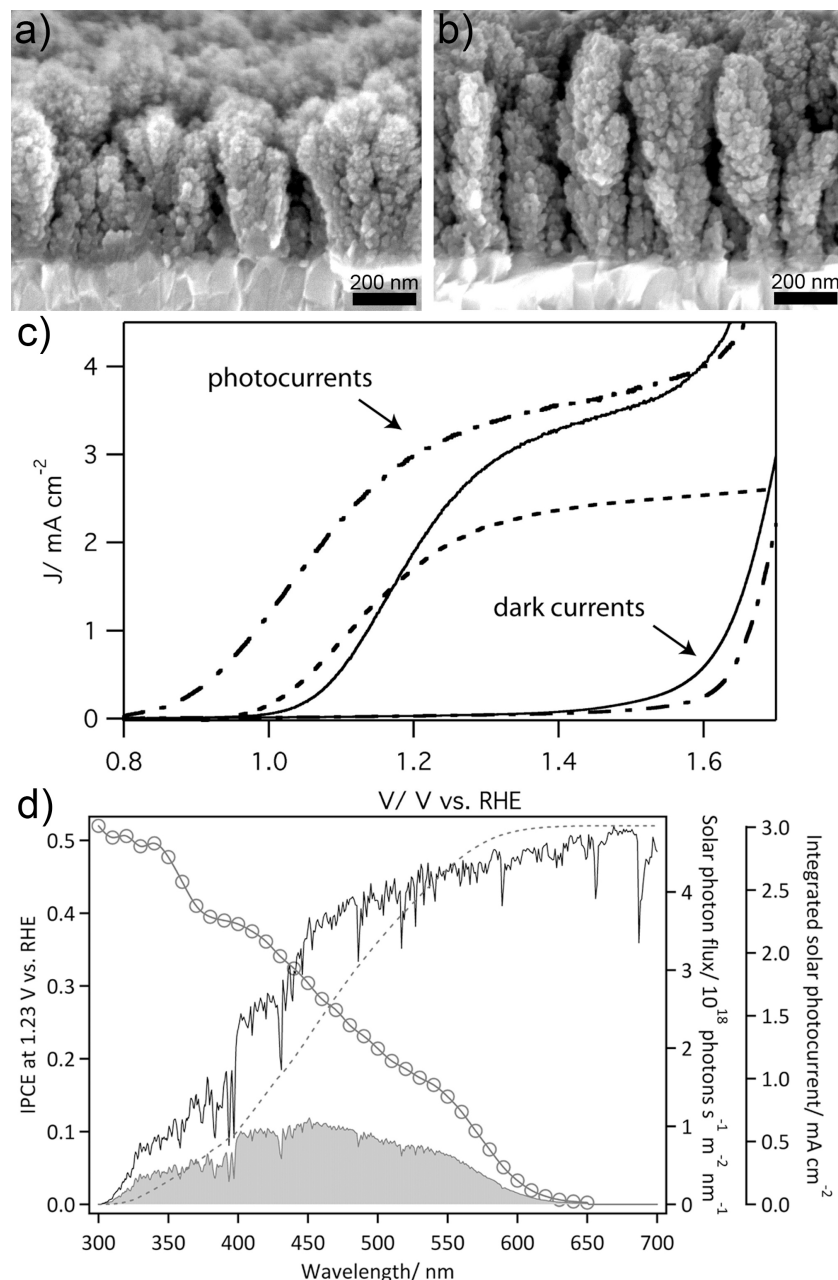


Figure 2.7: Characterization of Si-doped Fe_2O_3 electrodes prepared by the APCVD technique. (a) and (b) show the cross-sectional morphologies of optimized electrodes prepared with carrier gas flow rates of 2 and 6 L min^{-1} , respectively. (c) J - V curves of an unmodified hematite photoanode prepared at 6 L min^{-1} (solid trace) and the same anode after functionalization with IrO_2 nanoparticles (— — trace) in 1 M NaOH solution (pH 13.6). The dashed trace is the photocurrent for an electrode prepared at 2 L min^{-1} . Photocurrents correspond to AM 1.5 G 100 mW cm^{-2} simulated sunlight. (d) The incident photon conversion efficiency (IPCE) at an applied potential of $+1.23 \text{ V}_{\text{RHE}}$ (circles) and the AM 1.5 G 100 mW cm^{-2} solar spectrum (black trace) are multiplied together to give the number of photons stored in the form of hydrogen (shaded area). The dashed trace is the integrated photocurrent and reaches 3.01 mA cm^{-2} . Reprinted from [77]. Copyright 2010 John Wiley and Sons.

verifying the light source used for the J - V measurements. The photocurrent was found to be stable for many scans, however under extended measurement the IrO_2

nanoparticles detached from the surface and the photocurrent onset potential shifted back to the original value. Despite this limitation, which could possibly overcome using an appropriate linking strategy, this result clearly demonstrated that water oxidizing photocurrents over 3 mA cm^{-2} at relatively low bias potentials are possible with hematite using the combined strategy of morphology control and surface modification. This demonstration also thrusts the performance of hematite past the other oxides studied for PEC water oxidation to be the most efficient at converting solar light into energy stored in a tandem cell. If the bias required was applied by two PV cells in tandem each delivering 0.6 V and 6.6 mA cm^{-2} , a total solar to hydrogen efficiency of 4.8 % would be obtained.

While this is a considerable step towards high performance hematite, the photocurrent density remains far from the 12.6 mA cm^{-2} possible. This is because, despite absorbing almost all of the light (with $h\nu > E_g$) the quantum conversion efficiencies are still relatively low for wavelengths near the band edge ($500 < \lambda < 600$) where, half of hematite's possible solar photocurrent is available. This can be primarily attributed to the cauliflower-type morphology, which has an appropriate feature size of 10 nm at the SCLJ, but the individual cauliflower structures consist of thick stems which increase the number of photons absorbed far from the SCLJ.

2.4.6. Extremely thin absorber approach

The techniques discussed until now attempt to increase the photocurrent by nanostructuring the hematite itself. However, another strategy that can place all of the hematite in proximity to the SCLJ and include sufficient material for light absorption is to coat an extremely thin layer on a high-surface area, nanostructured scaffold in analogy to the DSC¹²² and extremely thin absorber (ETA) PVs.¹²³

This concept, described in Chapter 3, was recently demonstrated using a nanostructured WO_3 as the host scaffold.¹²⁴ In this work the scaffold was coated with a thin layer (*ca.* 60 nm) of Fe_2O_3 by the APCVD method and a 20 % increase in the photocurrent was observed over control samples prepared on flat FTO substrates. This enhancement was attributed to an increase in the absorbed photon to current efficiency (APCE), especially in the wavelength range from 500 to 600 nm. However, the thickness-optimized 60 nm layer of hematite was too thick based on the known hole transport limitations. Attempts to use thinner films of iron oxide resulted in poor performance, similar to other reports of thin films Fe_2O_3 ,⁵⁸ and pointed to a high recombination of photogenerated holes at the hematite/scaffold interface.

This limitation has recently been addressed by including a SnO_2^{109} or a SiO_x^{125} buffer layer between the substrate and the hematite film. For the latter report, presented in Chapter 4, a simple spray deposition was used to make highly uniform compact films of Fe_2O_3 on FTO substrates to first examine the effect of the thickness on the interfacial recombination. A minimum thickness of 22 nm was required to observe appreciable photoanode behavior. However when a SiO_x buffer layer was deposited on the FTO, reasonable photocurrents were obtained with only a 12.5 nm thick layer of Fe_2O_3 . In addition, comparing films of similar thickness with and without the buffer layer showed less recombination upon examining photocurrent transient behavior. Moreover, it was found that the buffer layer significantly altered the film nucleation and growth characteristics, and consequently the crystallinity. Unfortunately, the best ultra-thin hematite films with employed buffer layer showed slightly lower values for the APCE compared to the state-of-the-art APCVD films. This is possibly due to the high reflectivity of the compact and flat films. In general, the ETA/buffer layer/scaffold approach provides a clear path to overcoming all of hematite's limitations by decoupling the light absorption and the charge transport. Research using hematite with this approach is relatively new and further investigations into buffer layers and appropriately structured scaffolds should ultimately produce photocurrents higher than Fe_2O_3 prepared by the APCVD technique.

2.4.7. Nanostructuring method comparison

Several different approaches have been taken to nanostructure Fe_2O_3 for use in photoelectrochemical water splitting, and at least as many methods of characterizing the electrodes have also appeared. As such it can be difficult to compare the results in the literature, especially when variations in light sources give large overestimations of photocurrents due to superfluous UV light. A recent review addresses these issues and outlines standardized techniques for assessing photoelectrodes.¹²⁶ While not all of the reports discussed in this section have followed these suggestions it can still be helpful to compare the major accomplishments from the different structuring techniques and the resulting performance. This is done in Table 2.1.

Overall it is clear there is a strong dependence of the performance of synthetic hematite on the deposition technique. Interestingly, while methods like spray pyrolysis and CVD consistently produce electrodes photoactive for water oxidation at low temperatures (400 – 500 °C), solution-based methods like the

colloidal and electrodeposition approaches require much higher temperatures (700 – 800 °C) to produce photoactive hematite. This is certainly related to the quality of the prepared material in terms of crystallinity, impurity concentrations, and dopant incorporation, and a further understanding of this aspect is important to pursue.

Technique	Feature size	Dopant	Performance
Single crystal ⁵⁷	micron	Nb	IPCE 37% at 370 nm and 1.23 V _{RHE}
Sintered polycrystalline disk ⁴⁷	micron	Si	IPCE 34% at 400 nm and 1.23 V _{RHE}
Colloidal deposition of porous films ⁸⁹	25 nm	Ti	2.34 mA cm ⁻² at 1.63 V _{RHE} and AM 1.5 (100 mW cm ⁻²) and IPCE 40% at 400 nm and 1.6 V _{RHE}
Solution-based nanowires ²⁷	50 nm × 500 nm	none	IPCE 7% at 400nm and 0.9 V _{RHE} (in KI)
Potentiostatic anodization (nanotubes) ¹⁰³	6 nm × 1 μm	none	Before annealing: None reported After annealing: 1.0 mA cm ⁻² at 1.23 V _{RHE} and AM 1.5 (87 mW cm ⁻²)
Electro-deposition ²⁸	20–50 nm	Mo	IPCE 8% at 400 nm and 1.2 V _{RHE}
Ultrasonic spray pyrolysis ^{66,114}	10 nm × 300 nm	Si	1.5 mA cm ⁻² at 1.23 V _{RHE} and AM 1.5 (100 mW cm ⁻²) and IPCE 14% at 400 nm and 1.23 V _{RHE}
Atmospheric pressure CVD ⁷⁷	5 nm × 800 nm	Si	3.3 mA cm ⁻² at 1.23 V _{RHE} and AM 1.5 (100 mW cm ⁻²) and IPCE 39% at 400 nm (50% at 325 nm and 16% at 550 nm) and 1.23 V _{RHE}
Extremely thin absorber ¹²⁴	50 nm film	Si	1.3 mA cm ⁻² at 1.23 V _{RHE} and AM 1.5 (100 mW cm ⁻²) and IPCE 26% at 400 nm and 1.43 V _{RHE}

Table 2.1: Comparison of hematite photoanode structuring methods.

Also worth noting is that the IPCE values at *ca.* 400 nm rarely exceed that of the single crystal or sintered polycrystalline electrodes prepared during the first decade of work. The champion electrodes made by APCVD show only a modest increase in the conversion efficiency with 400 nm photons. The explanation for the significant increase in photocurrent observed with the APCVD and the colloidal solution-deposited electrodes has, of course, been the nanostructuring, that has allowed increases conversion of the longer wavelengths of light. Further work on the

nanostructuring will, no doubt, see solar photocurrents rise, but the increase in IPCE beyond 40 % at 400 nm and 1.23 V_{RHE} will require further research directed at increasing the understanding of hematite photoanodes.

2.5. Advanced understanding using electrochemical impedance spectroscopy (EIS)

Many electrochemical techniques have been used to characterize hematite photoanodes with the goal of understanding its performance and limitations. The most often employed— electrochemical impedance spectroscopy (EIS) — has proven to be valuable for ideal systems like single crystals. However, the many different preparation techniques and the advent of nanostructured electrodes have complicated efforts to understand and compare results obtained from EIS. Fortunately, recent efforts have provided significant advances in applying this classic technique to increase the understanding of hematite photoelectrodes. In this section the latest developments characterizing hematite photoanodes with EIS are discussed.

As a modulation technique, EIS consists of applying a time-dependant signal to the electrode, usually a sinusoidal perturbation of bias potential, and measuring the complex response of the electrode. By varying the excitation frequency, processes with different time constants can be resolved. The further analysis of the frequency-dependant response using an electronic model can separate the different aspects of charge transport, charge trapping, and charge transfer at the interface with electrolyte. During an EIS experiment the electrode dark- or photo- current density is typically recorded while applying a modulated voltage signal with frequency, f ($0.1 \text{ Hz} < f < 10^6 \text{ Hz}$), superimposed on the bias potential. A major advantage of EIS over other spectroscopic techniques is that it allows sample characterization under working conditions (in electrolyte under bias potential). The application of the well-known Mott-Schottky (MS) relation allows the extraction of V_{fb} and N_d by plotting the inverse square of the capacitance versus the applied bias. Typically, the capacitance is determined by fitting the frequency responses with a simple resistor–capacitor (RC) circuit model (see Figure 2.8a). A single frequency,^{30,50,56} multiple frequencies,¹⁰⁵ extrapolating to an infinite frequency,^{54,57,127} or an entire range of high frequencies^{65,128,129} have been used to fit the circuit model. Consistent values of V_{fb} from 0.4 – 0.6 V_{RHE} and N_d on the order of 10^{17} cm^{-3} (for undoped) to 10^{21} cm^{-3} (for heavily doped samples) have been reported for both planar and structured electrodes.^{24,128,129}

However since the classic MS relation relies on a simple parallel-plate capacitor model the application of EIS data from real systems has often been problematic. For example, frequency dispersion in MS plots is often observed at low frequencies. This has been attributed to non-idealities such as roughness of the samples, relaxation of the dielectric constant in the space charge region, and surface trapping states,¹³⁰ and explains the preferential use of high frequency to determine the sample capacitance. In addition, MS plots of hematite photoanodes have exhibited large deviations from linearity when $V_b \gg V_{fb}$. This phenomenon has been attributed to deep energetic levels partially ionized in the space charge region (Goodman model).¹³¹ To account for this, the observed EIS response was fitted with a more sophisticated circuit model taking in to account these intra-bandgap states (Figure 2.8b). Using this model, these states were found to lie 0.5 – 0.6 eV below the conduction band^{30,54,132} and associated with a trapping time constant about 0.4 ms. Some studies also established the presence of shallow donors, or trap states located at 0.1 – 0.2 eV under the conduction band using this model at low bias potential. Nevertheless McAlpine and Fredlein¹³³ observed severe limitations to this model and more recent studies using nanostructured hematite have not reported similar behavior, possibly due to small features exhibiting low bulk-to-surface ratio. For nanostructures, a superlinear trend of the MS plot has also been observed. This has recently been explained in terms of decrease in the surface area contributing to the capacitance.⁶⁵ As the hematite photoanode is biased in the anodic direction, the large overpotential causes the full depletion of the smallest surface features or curvature of the nanostructured surface resulting in a decrease of the effective electrode area and thus a decrease in capacitance.

An additional issue using EIS with nanostructures is illustrated in Figure 2.8d. Here a typical impedance response of a nanostructured hematite photoanode (prepared by APCVD) is shown in a Nyquist plot (real vs. imaginary impedance) at several bias potentials. The classically-used high frequency response can be observed at low impedance (close to the origin of the plot), and is characterized by a semicircle easily-fit by the simple R-(RC) circuit as shown in Figure 2.8a. At low frequency signals (large impedance, far from the origin), a second semicircle appears, and at certain potentials (e.g. 0.8 V_{RHE} in Figure 2.8d) this second feature is not easily distinguishable from the high frequency response. Gomes and VanMaekelbergh¹³⁰ interpreted the two semicircles in the Nyquist plot in terms of a two-step electron or charge transfer process mediated via surface states or reaction

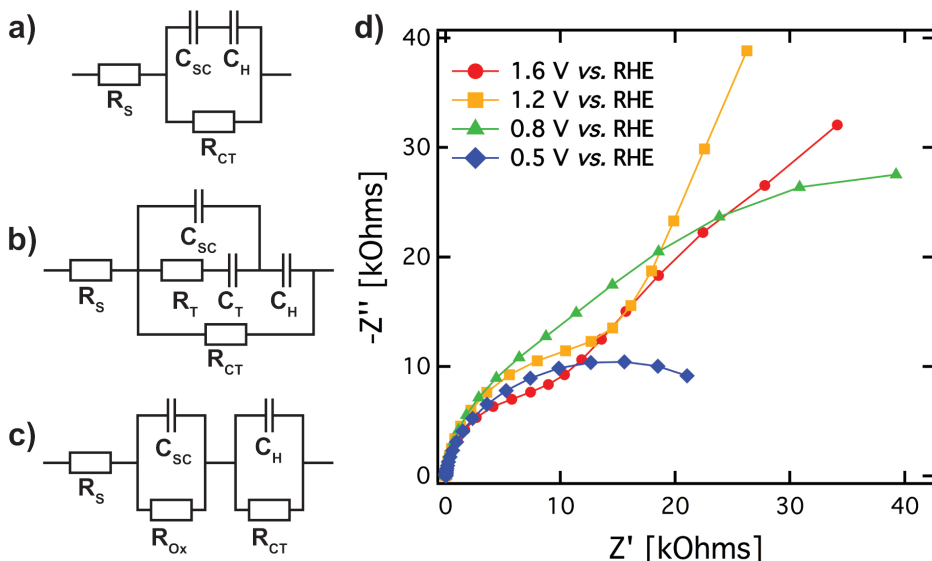


Figure 2.8: a, b and c) Common electronic models describing iron oxide behavior in EIS spectroscopy: model (a) represents a simple RC circuit (Helmholtz capacitance, C_H , constant) used to calculate the flat band potential and the donor density from Mott-Schottky equation, applicable at high frequency. Model (b) represents the electronic circuit that takes in account trap states (*i.e.* surface states at low bias potential, bulk states far from the flat band). Model (c) accounts for a non-negligible Helmholtz capacitance due to the presence of a high surface area (nanostructure) or surface states. d) Typical response of a hematite electrode (prepared by APCVD to electrochemical impedance spectroscopy (presented by a Nyquist plot) scanning the frequency from 1 MHz to 0.05 Hz at different applied bias potentials. At high frequency (small impedance), only one semicircle is distinguishable whereas at low frequency (large impedance) a second semicircle appears. Often the two are difficult to distinguish (*e.g.* at 0.8 V_{RHE}). Reprinted from [1].

intermediates. This hypothesis in combination with the recent development of high surface area nanostructures has led some authors to believe that the Helmholtz layer capacitance could vary significantly over the applied potential during EIS. Indeed recently, a varying Helmholtz layer capacitance has been taken in account with a model comprising a resistance in series with two RC elements. One element represents the space charge region and the other corresponds to charge transfer and Helmholtz layer (see Figure 2.8c).¹³⁴⁻¹³⁶ Surface states are not specifically addressed with this model but are assumed to be closely coupled with the measured Helmholtz layer. Aroutounian *et al.*¹³⁶ introduced a more complex system including the double RC model and a Warburg element characterizing a diffusion-limited process (in the space charge or in the Helmholtz layer). While this model fit well to their observations with Fe₂O₃ sintered pellets doped with 1% Ti, it has yet to be verified by application to another system.

In general, EIS has been shown to be useful to assert the limitations of hematite in a PEC system, especially through the determination of the flat band

potential and consequently the overpotential required for water splitting. The deeper understanding of the complex impedance spectra obtained by EIS leads to detailed characterization of electronic features, such as intra-bandgap states or surface states that presumably cause the two major drawbacks of hematite for water splitting. Nevertheless, the impedance response—especially at low frequencies—of hematite is complex and not yet fully understood. Further work will eventually lead to increase the knowledge on the electronic behavior of iron oxide.

2.6. Summary and outlook

Decades of research examining the properties of hematite have identified specific limitations which prevent high solar light harvesting efficiencies. However hematite's positive characteristics (i.e. bandgap of 2.0 eV, exceptional stability, and abundance) make it a unique and obvious choice for solar energy storage via photoelectrochemical water splitting. The optoelectronic properties create a conundrum that can be addressed by precisely controlling substitutional doping and the morphology. In combination with specific techniques to address electrochemical losses at the surface, these nanostructuring approaches have shown a remarkably rapid increase in the photocurrent produced by hematite at standard conditions. An overview of the progress in recent years is shown graphically in Figure 2.9.

From 2000 – 2005 the spray pyrolysis and ultrasonic spray pyrolysis methods produced higher photocurrents than the single crystal and polycrystalline sintered disks studied in the first decades of work with hematite photoanodes. In the past 5 years cauliflower-type films prepared by a particle-assisted APCVD method have produced record water splitting photocurrents. After coating these films with a layer of IrO_2 nanoparticles to reduce the overpotential for water oxidation, photocurrent densities over 3 mA cm^{-2} at $1.23 \text{ V}_{\text{RHE}}$ and standard illumination conditions have been demonstrated. These sudden advances suggest that a photocurrent density approaching the maximum possible 12.6 mA cm^{-2} can be produced with hematite using the appropriate morphology and surface treatments. Indeed, many recent reports have demonstrated rational nanostructuring techniques that offer a clear path to further increasing the photocurrent. Noteworthy advancements in solar photocurrents using solution-based colloidal methods, and electrodeposition techniques indicate that many routes to highly photoactive hematite exist. Based on the progress and limitations of all of the different approaches to morphology control, the nanowire array and the ETA approaches offer the greatest possibility for

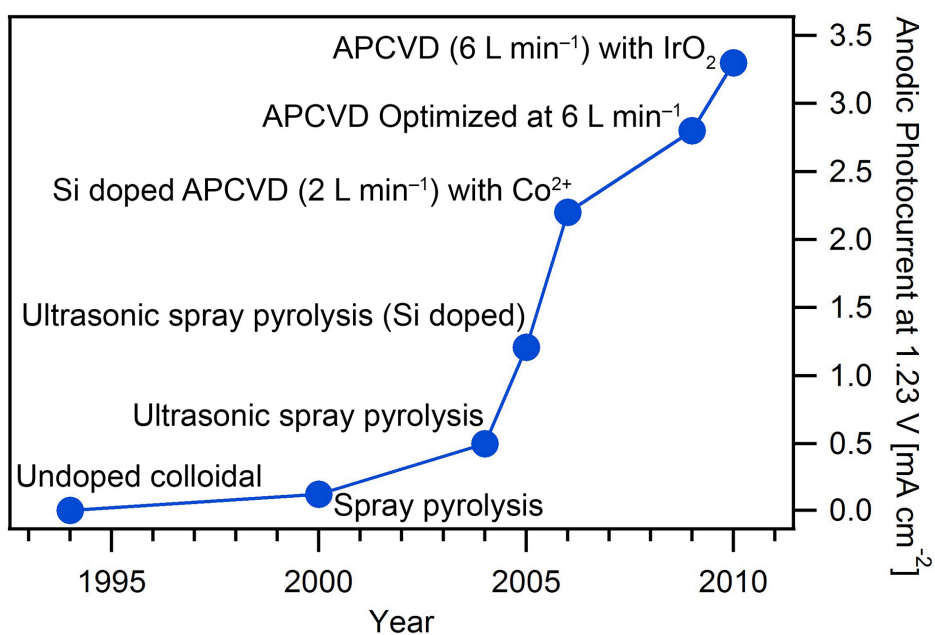


Figure 2. 9: Overall progress of recent efforts to nanostructure hematite and decrease overpotential with surface treatments shown by the water oxidation photocurrent as a function of the water oxidation photocurrent at 1.23 V_{RHE} and standard illumination conditions as a function of the year. The nanostructuring method used is indicated next to each point.
Reprinted from [1].

improvement. For the former approach, attaining single-crystalline nanowires of the appropriate diameter (10 – 20 nm), the proper orientation, and doping will realize high photocurrents. A templating technique⁹⁹ will likely be successful in this regard. On the other hand, the ETA (extremely thin absorber) approach has an attractive advantage as doping, and crystal orientation may not be necessary, but the suitable scaffold and buffer layer must be developed to eliminate interfacial recombination. Parallel with developing these approaches to morphology control, more work needs to be done to further understand hematite's intrinsic limitations. For example, the sub-50 % quantum efficiencies (even at short wavelengths in optimized single crystal photoanodes), the ultrafast carrier recombination, and the interband-gap states found in hematite suggest photocurrents approaching 12.6 mA cm⁻² will be difficult, if not impossible, to achieve given our lack of understanding. However, recent combinatorial efforts to optimize both the alloy composition^{11,137} and doping in hematite¹³⁸ may indicate new avenues for investigation. In addition, a significant reduction of the overpotential for water oxidation is urgently required. In comparison to the extensive work done on TiO₂,¹³⁹ relatively little is known about the surface chemistry of hematite. Only recently have some important and interesting reactivity

differences on hematite surfaces have been observed,^{140,141} and further work on this topic is necessary.

In many ways the development of Fe_2O_3 reported here can be considered analogous to the development of silicon photovoltaics. At the beginning of the terrestrial photovoltaic industry in the 1970s, the conventional wisdom was that crystalline silicon solar cells were hopelessly expensive and too inefficient to be a viable energy source.¹⁴² However the fact that silicon possessed ideal properties for a photovoltaic device could not be ignored, and today silicon solar cells are the dominate form of photovoltaic energy conversion thanks to the extensive technological effort put into its development. Hematite similarly possesses many ideal characteristics for solar water splitting. The recent developments presented here give strong prospect that continued efforts will bring photoanodes with performances sufficient for commercial application.

2.7. References

- (1) Sivula, K.; Le Formal, F.; Grätzel, M. *Chemsuschem* **2011**, 4, 432.
- (2) Gratzel, M. *Nature* **2001**, 414, 338.
- (3) Pimentel, D.; Marklein, A.; Toth, M. A.; Karpoff, M.; Paul, G. S.; McCormack, R.; Kyriazis, J.; Krueger, T. *Energies* **2008**, 1, 41.
- (4) Turner, J.; Sverdrup, G.; Mann, M. K.; Maness, P. C.; Kroposki, B.; Ghirardi, M.; Evans, R. J.; Blake, D. *Int. J. Energy Res.* **2008**, 32, 379.
- (5) Hernandez-Alonso, M. D.; Fresno, F.; Suarez, S.; Coronado, J. M. *Energy & Environmental Science* **2009**, 2, 1231.
- (6) Maeda, K.; Domen, K. *J. Phys. Chem. Lett.* **2010**, 1, 2655.
- (7) Esswein, A. J.; Nocera, D. G. *Chemical Reviews (Washington, DC, United States)* **2007**, 107, 4022.
- (8) Boddy, P. *J Electrochem Soc* **1968**, 115, 199.
- (9) Fujishima, A.; Honda, K. *Nature* **1972**, 238, 37.
- (10) Szkłarczyk, M.; Bockris, J. O. *Journal of Physical Chemistry* **1984**, 88, 5241.
- (11) Woodhouse, M.; Parkinson, B. A. *Chem. Soc. Rev.* **2009**, 38, 197.
- (12) Walsh, A.; Wei, S. H.; Yan, Y.; Al-Jassim, M. M.; Turner, J. A. *Physical Review B* **2007**, 76.
- (13) Greeley, J.; Jaramillo, T. F.; Bonde, J.; Chorkendorff, I. B.; Norskov, J. K. *Nature Materials* **2006**, 5, 909.

- (14) Minggu, L. J.; Daud, W. R. W.; Kassim, M. B. *International Journal of Hydrogen Energy* **2010**, *35*, 5233.
- (15) Khaselev, O.; Turner, J. *Science* **1998**, *280*, 425.
- (16) Ni, M.; Leung, M. K. H.; Leung, D. Y. C.; Sumathy, K. *Renew Sust Energ Rev* **2007**, *11*, 401.
- (17) Santato, C.; Ullmann, M.; Augustynski, J. *J Phys Chem B* **2001**, *105*, 936.
- (18) Murphy, A. B.; Barnes, P. R. F.; Randeniya, L. K.; Plumb, I. C.; Grey, I. E.; Horne, M. D.; Glasscock, J. A. *Int J Hydrogen Energ* **2006**, *31*, 1999.
- (19) Cornell, R. M.; Schwertmann, U. *The iron oxides : structure, properties, reactions, occurrences, and uses*; 2nd, completely rev. and extended ed.; Wiley-VCH: Weinheim, 2003.
- (20) Zboril, R.; Mashlan, M.; Petridis, D. *Chemistry of Materials* **2002**, *14*, 969.
- (21) Iordanova, N.; Dupuis, M.; Rosso, K. M. *J. Chem. Phys.* **2005**, *122*.
- (22) Galuza, A. I.; Beznosov, A. B.; Eremenko, V. V. *Low Temp. Phys.* **1998**, *24*, 726.
- (23) Marusak, L.; Messier, R.; White, W. *J Phys Chem Solids* **1980**, *41*, 981.
- (24) Lindgren, T.; Vayssieres, L.; Wang, H.; Lindquist, S. E. *Chemical Physics of Nanostructured Semiconductors* **2003**, *83*.
- (25) Gardner, R. F. G.; Tanner, D. W.; Sweet, F. *Journal of Physics and Chemistry of Solids* **1963**, *24*, 1183.
- (26) Kennedy, J. H.; Frese, K. W. *Journal of the Electrochemical Society* **1978**, *125*, 709.
- (27) Beermann, N.; Vayssieres, L.; Lindquist, S. E.; Hagfeldt, A. *Journal of the Electrochemical Society* **2000**, *147*, 2456.
- (28) Kleiman-Shwarsctein, A.; Hu, Y. S.; Forman, A. J.; Stucky, G. D.; McFarland, E. W. *Journal of Physical Chemistry C* **2008**, *112*, 15900.
- (29) Debnath, N. C.; Anderson, A. B. *Journal of the Electrochemical Society* **1982**, *129*, 2169.
- (30) Kennedy, J. H.; Frese, K. W. *Journal of the Electrochemical Society* **1978**, *125*, 723.
- (31) Dareedwards, M. P.; Goodenough, J. B.; Hamnett, A.; Trevellick, P. R. *Journal of the Chemical Society-Faraday Transactions I* **1983**, *79*, 2027.
- (32) Catti, M.; Valerio, G.; Dovesi, R. *Physical Review B* **1995**, *51*, 7441.
- (33) Butler, W. H.; Bandyopadhyay, A.; Srinivasan, R. *Journal of Applied Physics* **2003**, *93*, 7882.

- (34) Velev, J.; Bandyopadhyay, A.; Butler, W. H.; Sarker, S. *Physical Review B* **2005**, *71*.
- (35) Ma, Y.; Johnson, P. D.; Wassdahl, N.; Guo, J.; Skytt, P.; Nordgren, J.; Kevan, S. D.; Rubensson, J. E.; Böske, T.; Eberhardt, W. *Physical Review B* **1993**, *48*, 2109.
- (36) Morin, F. J. *Physical Review* **1951**, *83*, 1005.
- (37) Morin, F. J. *Physical Review* **1954**, *93*, 1195.
- (38) Launay, J. C.; Horowitz, G. *Journal of Crystal Growth* **1982**, *57*, 118.
- (39) Bosman, A. J.; Vandaal, H. J. *Adv. Phys.* **1970**, *19*, 1.
- (40) Chang, R. H.; Wagner, J. B. *Journal of the American Ceramic Society* **1972**, *55*, 211.
- (41) Goodenough, J. B. *Progress in Solid State Chemistry* **1971**, *5*, 145.
- (42) Dimitrijevic, N. M.; Savic, D.; Micic, O. I.; Nozik, A. J. *Journal of Physical Chemistry* **1984**, *88*, 4278.
- (43) Cherepy, N. J.; Liston, D. B.; Lovejoy, J. A.; Deng, H. M.; Zhang, J. Z. *Journal of Physical Chemistry B* **1998**, *102*, 770.
- (44) Nakau, T. *Journal of the Physical Society of Japan* **1960**, *15*, 727.
- (45) Benjelloun, D.; Bonnet, J. P.; Doumerc, J. P.; Launay, J. C.; Onillon, M.; Hagenmuller, P. *Materials Chemistry and Physics* **1984**, *10*, 503.
- (46) Rosso, K. M.; Smith, D. M. A.; Dupuis, M. J. *Chem. Phys.* **2003**, *118*, 6455.
- (47) Shinar, R.; Kennedy, J. H. *Solar Energy Materials* **1982**, *6*, 323.
- (48) Kennedy, J. H.; Anderman, M.; Shinar, R. *Journal of the Electrochemical Society* **1981**, *128*, 2371.
- (49) McGregor, K. G.; Calvin, M.; Otvos, J. W. *Journal of Applied Physics* **1979**, *50*, 369.
- (50) Turner, J. E.; Hendewerk, M.; Parmeter, J.; Neiman, D.; Somorjai, G. A. *Journal of the Electrochemical Society* **1984**, *131*, 1777.
- (51) Joly, A. G.; Williams, J. R.; Chambers, S. A.; Xiong, G.; Hess, W. P.; Laman, D. M. *Journal of Applied Physics* **2006**, *99*.
- (52) Pendlebury, S. R.; Barroso, M.; Cowan, A. J.; Sivula, K.; Tang, J.; Gratzel, M.; Klug, D.; Durrant, J. R. *Chemical Communications (Cambridge, United Kingdom)* **2011**, *47*, 716.
- (53) Ahmed, S. M.; Leduc, J.; Haller, S. F. *Journal of Physical Chemistry* **1988**, *92*, 6655.
- (54) Horowitz, G. *Journal of Electroanalytical Chemistry* **1983**, *159*, 421.

- (55) Hardee, K. L.; Bard, A. J. *Journal of the Electrochemical Society* **1976**, *123*, 1024.
- (56) Quinn, R. K.; Nasby, R. D.; Baughman, R. J. *Materials Research Bulletin* **1976**, *11*, 1011.
- (57) Sanchez, C.; Sieber, K. D.; Somorjai, G. A. *Journal of Electroanalytical Chemistry* **1988**, *252*, 269.
- (58) Itoh, K.; Bockris, J. O. *Journal of Applied Physics* **1984**, *56*, 874.
- (59) Itoh, K.; Bockris, J. O. *Journal of the Electrochemical Society* **1984**, *131*, 1266.
- (60) Brillet, J.; Cornuz, M.; Le Formal, F.; Yum, J. H.; Graetzel, M.; Sivula, K. *Journal of Materials Research* **2010**, *25*, 17.
- (61) Gartner, W. W. *Physical Review* **1959**, *116*, 84.
- (62) Maruska, H. P.; Ghosh, A. K. *Solar Energy Materials* **1979**, *1*, 237.
- (63) Butler, M. A. *Journal of Applied Physics* **1977**, *48*, 1914.
- (64) Leygraf, C.; Hendewerk, M.; Somorjai, G. *Journal of Solid State Chemistry* **1983**, *48*, 357.
- (65) Cesar, I.; Sivula, K.; Kay, A.; Zboril, R.; Graetzel, M. *Journal of Physical Chemistry C* **2009**, *113*, 772.
- (66) Duret, A.; Gratzel, M. *Journal of Physical Chemistry B* **2005**, *109*, 17184.
- (67) Lindgren, T.; Wang, H. L.; Beermann, N.; Vayssieres, L.; Hagfeldt, A.; Lindquist, S. E. *Solar Energy Materials and Solar Cells* **2002**, *71*, 231.
- (68) Brunschwig, B. S.; Chou, M. H.; Creutz, C.; Ghosh, P.; Sutin, N. *Journal of the American Chemical Society* **1983**, *105*, 4832.
- (69) Kay, A.; Cesar, I.; Gratzel, M. *Journal of the American Chemical Society* **2006**, *128*, 15714.
- (70) Kanan, M. W.; Nocera, D. G. *Science* **2008**, *321*, 1072.
- (71) Zhong, D. K.; Sun, J. W.; Inumaru, H.; Gamelin, D. R. *Journal of the American Chemical Society* **2009**, *131*, 6086.
- (72) Zhong, D. K.; Gamelin, D. R. *Journal of the American Chemical Society* **2010**, *132*, 4202.
- (73) Kiwi, J.; Gratzel, M. *Angewandte Chemie-International Edition in English* **1978**, *17*, 860.
- (74) Kiwi, J.; Gratzel, M. *Angewandte Chemie-International Edition in English* **1979**, *18*, 624.

- (75) Nakagawa, T.; Beasley, C. A.; Murray, R. W. *Journal of Physical Chemistry C* **2009**, *113*, 12958.
- (76) Nakagawa, T.; Bjorge, N. S.; Murray, R. W. *Journal of the American Chemical Society* **2009**, *131*, 15578.
- (77) Tilley, S.; Cornuz, M.; Sivula, K.; Grätzel, M. *Angewandte Chemie, International Edition in English* **2010**, *49*, 6405.
- (78) Le Formal, F.; Tetreault, N.; Cornuz, M.; Moehl, T.; Gratzel, M.; Sivula, K. *Chemical Science* **2011**, *2*, 737.
- (79) Hu, Y. S.; Kleiman-Shwarsctein, A.; Stucky, G. D.; McFarland, E. W. *Chemical Communications (Cambridge, United Kingdom)* **2009**, 2652.
- (80) Alexander, B. D.; Kulesza, P. J.; Rutkowska, L.; Solarzka, R.; Augustynski, J. *Journal of Materials Chemistry* **2008**, *18*, 2298.
- (81) Van de Krol, R.; Liang, Y. Q.; Schoonman, J. *Journal of Materials Chemistry* **2008**, *18*, 2311.
- (82) Bjorksten, U.; Moser, J.; Gratzel, M. *Chemistry of Materials* **1994**, *6*, 858.
- (83) Moser, J.; Gratzel, M. *Helvetica Chimica Acta* **1982**, *65*, 1436.
- (84) Qian, X.; Zhang, X.; Bai, Y.; Li, T.; Tang, X.; Wang, E.; Dong, S. *J. Nanopart. Res.* **2000**, *2*, 191.
- (85) Sivula, K.; Brillet, J.; Gratzel, M.; 1 ed.; Idriss, H., Wang, H., Eds.; SPIE: San Diego, California, USA, 2010; Vol. 7770, p 77700G.
- (86) Sivula, K.; Zboril, R.; Le Formal, F.; Robert, R.; Weidenkaff, A.; Tucek, J.; Frydrych, J.; Grätzel, M. *Journal of the American Chemical Society* **2010**, *132*, 7436.
- (87) Atkinson, A.; Taylor, R. I. *Journal of Physics and Chemistry of Solids* **1985**, *46*, 469.
- (88) Pailhe, N.; Wattiaux, A.; Gaudon, M.; Demourgues, A. *Journal of Solid State Chemistry* **2008**, *181*, 2697.
- (89) Brillet, J.; Grätzel, M.; Sivula, K.. *Nano Letters* **2010**, *10*, 4155.
- (90) Vayssières, L.; Beermann, N.; Lindquist, S. E.; Hagfeldt, A. *Chemistry of Materials* **2001**, *13*, 233.
- (91) Peng, L. L.; Xie, T. F.; Fan, Z. Y.; Zhao, Q. D.; Wang, D. J.; Zheng, D. *Chemical Physics Letters* **2008**, *459*, 159.
- (92) Gualtieri, A. F.; Venturelli, P. *American Mineralogist* **1999**, *84*, 895.
- (93) Fan, Z. Y.; Wen, X. G.; Yang, S. H.; Lu, J. G. *Applied Physics Letters* **2005**, *87*.

- (94) Fu, Y. Y.; Chen, J.; Zhang, H. *Chemical Physics Letters* **2001**, *350*, 491.
- (95) Wang, R. M.; Chen, Y. F.; Fu, Y. Y.; Zhang, H.; Kisielowski, C. *Journal of Physical Chemistry B* **2005**, *109*, 12245.
- (96) Wen, X. G.; Wang, S. H.; Ding, Y.; Wang, Z. L.; Yang, S. H. *Journal of Physical Chemistry B* **2005**, *109*, 215.
- (97) Yu, T.; Zhu, Y. W.; Xu, X. J.; Yeong, K. S.; Shen, Z. X.; Chen, P.; Lim, C. T.; Thong, J. T. L.; Sow, C. H. *Small* **2006**, *2*, 80.
- (98) Han, Q.; Xu, Y. Y.; Fu, Y. Y.; Zhang, H.; Wang, R. M.; Wang, T. M.; Chen, Z. Y. *Chemical Physics Letters* **2006**, *431*, 100.
- (99) Mao, A.; Han, G. Y.; Park, J. H. *Journal of Materials Chemistry* **2010**, *20*, 2247.
- (100) Prakasam, H. E.; Varghese, O. K.; Paulose, M.; Mor, G. K.; Grimes, C. A. *Nanotechnology* **2006**, *17*, 4285.
- (101) Mor, G. K.; Prakasam, H. E.; Varghese, O. K.; Shankar, K.; Grimes, C. A. *Nano Letters* **2007**, *7*, 2356.
- (102) Rangaraju, R. R.; Panday, A.; Raja, K. S.; Misra, M. *Journal of Physics D-Applied Physics* **2009**, *42*.
- (103) Mohapatra, S. K.; John, S. E.; Banerjee, S.; Misra, M. *Chemistry of Materials* **2009**, *21*, 3048.
- (104) Hu, Y. S.; Kleiman-Shwarsctein, A.; Forman, A. J.; Hazen, D.; Park, J. N.; McFarland, E. W. *Chemistry of Materials* **2008**, *20*, 3803.
- (105) Kleiman-Shwarsctein, A.; Huda, M. N.; Walsh, A.; Yan, Y. F.; Stucky, G. D.; Hu, Y. S.; Al-Jassim, M. M.; McFarland, E. W. *Chemistry of Materials* **2010**, *22*, 510.
- (106) Spray, R. L.; Choi, K.-S. *Chemistry of Materials* **2009**, *21*, 3701.
- (107) Murthy, A. S. N.; Reddy, K. S. *Materials Research Bulletin* **1984**, *19*, 241.
- (108) Kumari, S.; Tripathi, C.; Singh, A. P.; Chauhan, D.; Shrivastav, R.; Dass, S.; Satsangi, V. R. *Current Science* **2006**, *91*, 1062.
- (109) Liang, Y. Q.; Enache, C. S.; van de Krol, R. *International Journal of Photoenergy* **2008**, 739864.
- (110) Kumari, S.; Singh, A. P.; Tripathi, C.; Chauhan, D.; Dass, S.; Shrivastav, R.; Gupta, V.; Sreenivas, K.; Satsangi, V. R. *International Journal of Photoenergy* **2007**.
- (111) Khan, S. U. M.; Akikusa, J. *Journal of Physical Chemistry B* **1999**, *103*, 7184.
- (112) Hagglund, C.; Gratzel, M.; Kasemo, B. *Science* **2003**, *301*, 1673B.

- (113) Sartoretti, C. J.; Alexander, B. D.; Solarska, R.; Rutkowska, W. A.; Augustynski, J.; Cerny, R. *Journal of Physical Chemistry B* **2005**, *109*, 13685.
- (114) Cesar, I., Ecole Polytechnique Fédérale de Lausanne, 2007.
- (115) Cesar, I.; Kay, A.; Martinez, J. A. G.; Gratzel, M. *Journal of the American Chemical Society* **2006**, *128*, 4582.
- (116) Orthner, H. R.; Roth, P. *Materials Chemistry and Physics* **2002**, *78*, 453.
- (117) Wen, J. Z.; Goldsmith, C. F.; Ashcraft, R. W.; Green, W. H. *Journal of Physical Chemistry C* **2007**, *111*, 5677.
- (118) Saremi-Yarahmadi, S.; Tahir, A. A.; Vaidhyanathan, B.; Wijayantha, K. G. U. *Materials Letters* **2009**, *63*, 523.
- (119) Saremi-Yarahmadi, S.; Wijayantha, K. G. U.; Tahir, A. A.; Vaidhyanathan, B. *Journal of Physical Chemistry C* **2009**, *113*, 4768.
- (120) An, W.-J.; Thimsen, E.; Biswas, P. *The Journal of Physical Chemistry Letters* **2009**, *1*, 249.
- (121) Cornuz, M.; Grätzel, M.; Sivula, K. *Chemical Vapor Deposition* **2010**, *16*, 291.
- (122) Grätzel, M. *Chemistry Letters* **2005**, *34*, 8.
- (123) Ernst, K.; Belaïdi, A.; Konenkamp, R. *Semicond. Sci. Technol.* **2003**, *18*, 475.
- (124) Sivula, K.; Le Formal, F.; Grätzel, M. *Chemistry of Materials* **2009**, *21*, 2862.
- (125) Le Formal, F.; Grätzel, M.; Sivula, K. *Advanced Functional Materials* **2010**, *20*, 1099.
- (126) Chen, Z. B.; Jaramillo, T. F.; Deutsch, T. G.; Kleiman-Shwarsctein, A.; Forman, A. J.; Gaillard, N.; Garland, R.; Takanabe, K.; Heske, C.; Sunkara, M.; McFarland, E. W.; Domen, K.; Miller, E. L.; Turner, J. A.; Dinh, H. N. *Journal of Materials Research* **2010**, *25*, 3.
- (127) McCann, J.; Badwal, S. *Journal of the Electrochemical Society* **1982**, *129*, 551.
- (128) Tahir, A. A.; Wijayantha, K. G. U.; Saremi-Yarahmadi, S.; Mazhar, M.; McKee, V. *Chemistry of Materials* **2009**, *21*, 3763.
- (129) Glasscock, J. A.; Barnes, P. R. F.; Plumb, I. C.; Savvides, N. *Journal of Physical Chemistry C* **2007**, *111*, 16477.
- (130) Gomes, W.; Vanmaekelbergh, D. *Electrochimica Acta* **1996**, *41*, 967.
- (131) Goodman, A. *Journal of Applied Physics* **1963**, *34*, 329.
- (132) Leduc, J.; Ahmed, S. M. *Journal of Physical Chemistry* **1988**, *92*, 6661.

- (133) McAlpine, N.; Fredlein, R. *Journal of Electroanalytical Chemistry* **1988**, *252*, 61.
- (134) Wielant, J.; Goossens, V.; Hausbrand, R.; Terryn, H. *Electrochimica Acta* **2007**, *52*, 7617.
- (135) Aroutiounian, V.; Arakelyan, V.; Shahnazaryan, G.; Stepanyan, G.; Khachaturyan, E.; Turner, J. *Cr Chim* **2006**, *9*, 325.
- (136) Aroutiounian, V.; Arakelyan, V.; Shahnazaryan, G.; Stepanyan, G.; Turner, J.; Kocha, S. *Electrochimica Acta* **2000**, *45*, 1999.
- (137) Woodhouse, M.; Parkinson, B. A. *Chemistry of Materials* **2008**, *20*, 2495.
- (138) Jang, J. S.; Lee, J.; Ye, H.; Fan, F. R. F.; Bard, A. J. *Journal of Physical Chemistry C* **2009**, *113*, 6719.
- (139) Fujishima, A.; Zhang, X. T.; Tryk, D. A. *Surf. Sci. Rep.* **2008**, *63*, 515.
- (140) Yanina, S. V.; Rosso, K. M. *Science* **2008**, *320*, 218.
- (141) Eggleston, C. M.; Shankle, A. J. A.; Moyer, A. J.; Cesar, I.; Gratzel, M. *Aquatic Sciences* **2009**, *71*, 151.
- (142) Swanson, R. M. *Progress in Photovoltaics: Research and Applications* **2006**, *14*, 443.

CHAPTER 3.

THE HOST-GUEST APPROACH (OR EXTREMELY THIN ABSORBER, ETA)

This chapter has been published as K. Sivula, F. Le Formal, M. Grätzel, *Chem. Mater.* **2009**, *21*, 2862.¹

In this chapter we introduce a new concept for water splitting which addresses one of the challenges discussed in the previous chapter, namely the mismatch between the short hole diffusion length and the large light absorption depth. It consists of decoupling the light absorption and the water oxidation roles from the electron transport, depositing a thin layer of hematite onto a mesoporous conductive semiconductor. The effectiveness of this new morphology has been demonstrated using a nanostructured host scaffold (WO_3) prepared by atmospheric pressure chemical vapor deposition to support a thin layer of Fe_2O_3 nanoparticles deposited by a similar method. A 20% increase in the photocurrent was observed in host-guest electrodes as compared to control films with the same amount of hematite (equivalent to a 60 nm film) deposited without the host scaffold. The improvement is attributed to an increase in the absorbed photon conversion efficiency (APCE), especially for longer wavelengths where the photon penetration depth is large in hematite. For light with a wavelength of 565 nm, the APCE improves to 8.0%, as compared to 5.7% with the control films because of the host/guest architecture.

3.1. Introduction

Hematite ($\alpha\text{-Fe}_2\text{O}_3$) has been considered to be a promising material for direct solar-to-hydrogen production (see Chapter 1). With a favorable band gap of 2.0 – 2.2 eV, chemical stability in aqueous environments, and matchless abundance, its use as a photocatalyst to produce dihydrogen at a scale corresponding to the world energy demand is realistic. In Chapter 2, we have examined in detail this material as an oxygen-evolving photoanode for water splitting in the past, and pointed out its limitations. One major drawback of hematite arises from its very small hole diffusion length (2 – 4 nm)² as compared to the light penetration depth ($\alpha^{-1} = 118$ nm at $\lambda = 550$ nm).³ This causes most photons to be absorbed in the bulk far from the SCLJ, creating photogenerated holes with low probability of participating in water oxidation. In the recent past, nanostructuring techniques have proven useful in increasing the performance of hematite for water-splitting,⁴ and several groups have reported various approaches.⁵⁻⁷ Kay *et al.* has reported benchmark performance with nanostructured and silicon doped hematite thin films prepared by atmospheric pressure chemical vapor deposition (APCVD, see experimental section).⁸ However, the efficiency of such hematite films remains low compared to the theoretical value of 16.8% predicted for a material with this bandgap.⁹ Even in this nanostructured system the quantum conversion efficiencies are relatively low and are especially poor (< 20%) in the region where hematite has an indirect band-gap transition ($\lambda = 610$ – 450 nm). Importantly, there is over 10 mA cm⁻² of solar photocurrent available in this wavelength range. The poor performance here is largely due to the cauliflower-type morphology consisting of thick stems which increase the number of photons absorbed far from the SCLJ. The work presented in this chapter aims to further develop this promising iron oxide system by overcoming this limitation.

An answer to the persisting problem of small hole diffusion length and large photon penetration depth proposed by Itoh and Bockris is to use ultra-thin films in a stacked formation to increase the proximity of the photogenerated holes to the SCLJ.¹⁰ While this solution could fundamentally resolve the issue, it is cumbersome and expensive to implement, and in practice the thin iron oxide films were found to have poor performance due to the increased recombination of the photogenerated holes.¹¹ An increased photoresponse should also be obtainable by coating these thin films conformally on a suitable nanostructured collector with a large specific surface area, in analogy to the DSSC.¹² In the case of the DSSC, the photoanode is constructed from a light absorbing dye molecule anchored to a high surface area

mesoporous TiO₂ scaffold, which transports and collects the photo-excited electrons. The DSSC's host-scaffold/guest-absorber approach effectively decouples light harvesting and charge transport while maximizing the incident photon-to-current efficiency (IPCE) by means of the thin (mono) layer of absorber on the high surface area, transparent collector. Given the success of this concept for photovoltaic energy conversion as well as the light absorbing and carrier transport limitations of α-Fe₂O₃, we sought to apply this powerful design to hematite photoanodes for PEC water splitting to improve on the silicon-doped photoanodes developed in our lab. While reports of hematite-sensitized large-band-gap oxides as photocatalysts have appeared,¹³ no confirmation of the effectiveness of the host/guest concept for improving the quantum efficiency of hematite films for water-splitting has yet been demonstrated. Here we present affirmation that this approach can increase the photocurrent and absorbed photon conversion efficiency for thin-film hematite photoanodes using a nanostructured scaffold made from WO₃.

3.2. Experimental

3.2.1. Choice of the host material

To implement a host/guest architecture with hematite as the guest absorber, a scaffold host material must be chosen to fulfill a few essential requirements. First, the conduction band of the scaffold material must lie lower in energy than the conduction band of hematite to allow efficient electron transport across the host/guest interface and second, the scaffold material should have a larger band gap than hematite so as to not compete with the light absorption. Few oxide semiconductors meet both of these requirements. Both ZnO and SnO₂ have sufficiently large band-gaps (3.4 and 3.6 eV, respectively) and conduction bands close to that of hematite, but their investigations in composite architectures with hematite has not been effective, as the conduction band is too negative¹⁴ for ZnO and recombination is increased in some cases at the SnO₂/hematite interface.^{11,15,16} The other materials tested as underlayers, related to their performance, are listed in Table 3.1.

Investigations of TiO₂, niobium doped TiO₂ and MoO₃ as scaffolds resulted in no photocurrent whereas hematite photoanodes using Nb₂O₅ and WO₃ as host have shown an improvement in terms of performance. Further study of the photoanode architecture were performed with tungsten trioxide, due to the higher surface area obtained with APCVD as compared to the spray pyrolysis technique used for niobium oxide deposition. As previously mentioned, tungsten trioxide has been extensively

investigated as a photoanode material. While the experimental value of the conduction band of WO_3 varies slightly, it has been reported to be positioned 0.1 – 0.4 eV below that of hematite.^{4,14} In addition, with a band gap of 2.7 eV, it satisfies the second criterion for a host material for $\lambda > 460 \text{ nm}$. With this compliance, and the good electron conductivity shown by high photocurrents for WO_3 ,¹⁷ this material was investigated as a host scaffold.

Underlayer Material	Deposition Method	Results
TiO_2	Spray pyrolysis of TiCl_4	No photocurrent
MoO_3	APCVD of $\text{Mo}(\text{CO})_6$	No photocurrent
Nb:TiO_2	Spray pyrolysis of $\text{TiCl}_4 + \text{NbCl}_5$	Minimal photocurrent
Nb_2O_5	Spray pyrolysis of NbCl_5	Higher onset & plateau
WO_3	APCVD of $\text{W}(\text{CO})_6$	Higher onset & plateau

Table 3.1 : List of materials tested as underlayers for host / guest architecture photoanode based on hematite. The deposition method for the underlayer as well as the photoelectrochemical results of a photoanode consisting of the underlayer covered with 1min APCVD of $\text{Fe}(\text{CO})_5$ are also mentionned.

3.2.2. WO_3 film preparation

Given our experience with the APCVD of Fe_2O_3 from iron pentacarbonyl,⁸ we chose a similar method to deposit thin films of WO_3 with high roughness to serve as the scaffold.¹⁸ Thin films of WO_3 with high roughness were prepared on transparent conductive substrates (F:SnO_2 , TEC15, $15 \Omega \square^{-1}$, Hartford Glass Co., $60 \text{ mm} \times 60 \text{ mm} \times 2.3 \text{ mm}$) by the atmospheric pressure chemical vapor deposition of tungsten hexacarbonyl (99%, Acros) using the following procedure. The substrate was placed on a 3 mm thick slab of ceramic glass covering the surface of a PID-controlled high temperature hot plate (Harry Gestigkeit GMBH). The hot plate was heated to 400°C , and a center strip of the conducting glass substrate ($60 \text{ mm} \times 12 \text{ mm}$) was masked with an additional piece of glass for later electrical contact. The solid tungsten hexacarbonyl (500 mg) was spread evenly on a standard glass frit (40 mm diameter) of a vacuum filtration funnel assembly (70 mm funnel diameter). The inverted vacuum filtration funnel assembly with the $\text{W}(\text{CO})_6$ was placed over the substrate so the top of the funnel was 50 mm from the substrate. A 7.1 L min^{-1} flow of dry air

which had been heated to 120 °C by PID-controlled thermal resistant heaters was directed into the stem of the funnel assembly, over the W(CO)₆ through the glass frit and onto the hot substrate where the pyrolytic decomposition of the tungsten hexacarbonyl vapor occurred. The entire amount of W(CO)₆ was allowed to sublime (about 15 min) and the substrate was subsequently annealed for 45 min more at the same temperature and flow of heated air. The substrate was cooled and diced into 30 mm × 12 mm pieces for the iron oxide deposition. The films were uniform, slightly yellow with increased haze as compared to the TEC15 substrate.

3.2.3. APCVD of silicon doped Fe₂O₃

These films were then subjected to the APCVD of silicon doped Fe₂O₃ from iron pentacarbonyl and tetraethyl orthosilicate (TEOS) in a cold wall APCVD chamber. For this work we constructed a new deposition system, based on our previous work,⁸ which offered increased parameter control plus improved stability and reproducibility over the former system. The new APCVD set up has been detailed elsewhere.¹⁹ The deposition of α-Fe₂O₃ at approximately 100 nm min⁻¹ (after a latency time)¹⁶ at a substrate temperature of 420 °C resulted in a red-orange spot approximately 1 cm in diameter on the substrate. Depositions were performed for 1 min or 4 min on both the WO₃ films and, as a control, on the bare F:SnO₂ substrates without any surface treatment.

3.2.4. Photoelectrochemical and crystallographic characterisation

Photocurrent measurements were performed to determine the solar to hydrogen energy conversion efficiency in a three electrode configuration with 1 M NaOH (pH 13.6)² as electrolyte using Ag/AgCl in saturated KCl as a reference electrode. The hematite electrode was scanned at 50 mV sec⁻¹ between -300 to 800 mV vs. Ag/AgCl. The potential is reported relative to the reversible hydrogen electrode potential (RHE).⁸ The samples were illuminated with simulated sunlight from a 450 W Xenon lamp (Osram, ozone free) using a KG3 filter (3 mm, Schott). Spectral mismatch factors to estimate the difference of the electrode photoresponse obtained from simulated sun light and real sun light at AM 1.5 G were calculated according to the method described by Seaman *et al.*²⁰ Photocurrent action spectra and the UV-Vis transmittance were measured to determine the absorbed photon to current conversion efficiency (APCE). Photocurrent action spectra were obtained under light from a 300 W Xe-lamp with integrated parabolic reflector (Cermax PE 300 BUV) passing through a monochromator (Bausch & Lomb, bandwidth 10 nm FWHM).

The photoanode transmittance was measured on a Hewlett-Packard 8452A diode array spectrophotometer. All samples were measured by illuminating the photoanode from the hematite/electrolyte interface.

The WO_3 scaffold on the F: SnO_2 -coated glass was also analyzed by X-ray diffraction on a PANalytical X'Pert PRO diffractometer before and after the deposition of the Fe_2O_3 using $\text{Cu K}\alpha 1$ radiation (0.1540 nm) at a small incident angle to maximize signal intensity.

3.3. Results and discussion

3.3.1. Morphology and crystallography of the host –guest system

Scanning electron micrographs (Figure 3.1) of the WO_3 and the $\text{WO}_3/\text{Fe}_2\text{O}_3$ films give insight to the nanostructured morphology obtained by the used deposition techniques. Figure 3.1a shows the surface morphology of the WO_3 film before the iron oxide deposition. The film consisted of faceted grains of WO_3 in the size range of 20 – 200 nm grown from the surface F:SnO_2 substrate creating a porous structure with increased roughness over the underlying substrate (Figure 3.1e).

Upon the deposition of the iron oxide for one minute, the WO_3 scaffold was completely covered with *ca.* 10 nm particles of silicon doped iron oxide (Figure 3.1c); however some of the original porosity can be distinguished, suggesting the iron oxide deposits conformally on the WO_3 . This is remarkable given the homogeneous-nucleation-and-attachment growth mechanism supposed for this deposition,¹⁶ and is further indicated by observing a position on the film near the edge of the iron oxide deposition spot (Figure 3.1b). Here we note the rounded iron oxide nanoparticles beginning to attach to all sides of the WO_3 surface, and can subsequently suggest that surface nucleation may be critical to the nanostructure obtained from the APCVD of Fe_2O_3 from carbonyl. Finally, a cross-sectional micrograph (Figure 3.1d) reveals the rounded iron oxide nanoparticles covering the faceted WO_3 nearly down to the F:SnO_2 substrate. The observed film thickness of *ca.* 300 nm is consistent with a 200 nm WO_3 film accounting for the additional height of the Fe_2O_3 (approximately 60 – 100 nm).

The WO_3 scaffold on the F: SnO_2 -coated glass was secondly analyzed by x-ray diffraction before and after the deposition of the Fe_2O_3 at a small incident angle to maximize signal intensity. The diffractograms are presented in Figure 3.2.

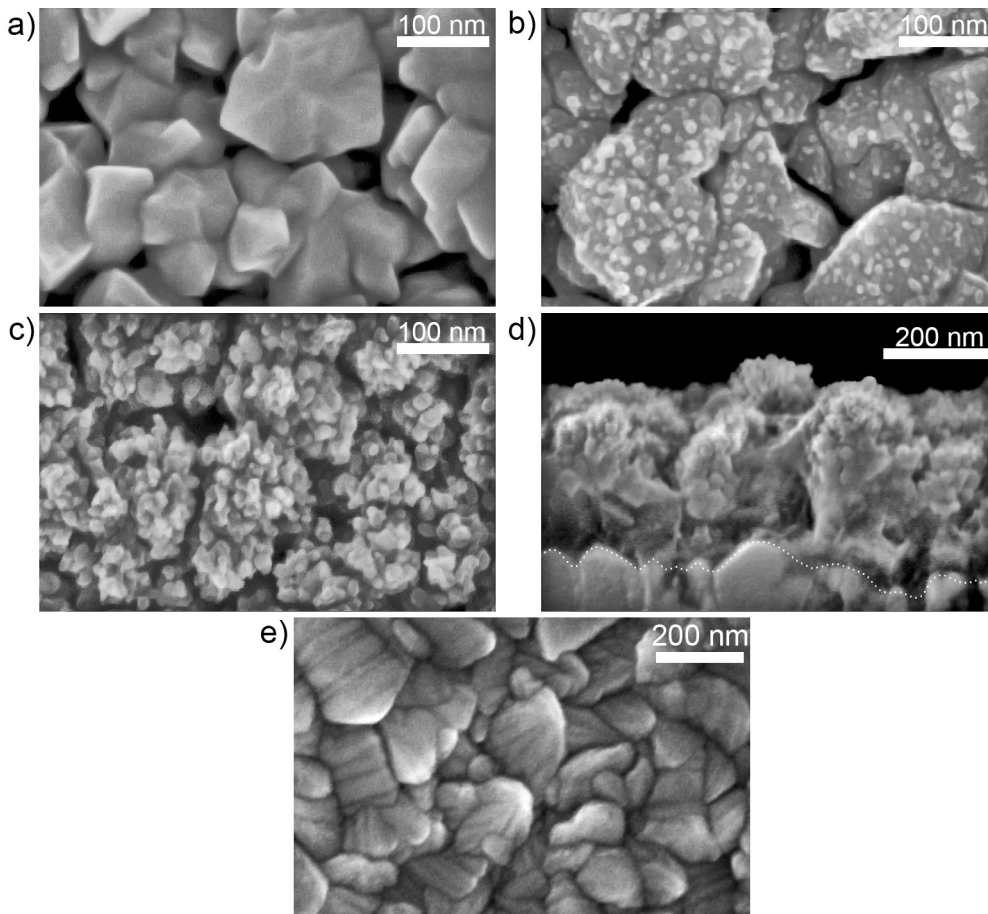


Figure 3.1: Scanning electron micrographs of the WO₃/Fe₂O₃ host/guest system in a top-down (a-c) and cross-sectional (d) perspective. Image (a) shows the morphology of the WO₃ host scaffold before iron oxide deposition. After one minute of Fe₂O₃ deposition at the standard deposition rate ($\sim 100 \text{ nm min}^{-1}$) the WO₃ film is covered in iron oxide nanoparticles (c) while at a lower deposition rate ($\sim 10 \text{ nm min}^{-1}$, edge of growth spot) the iron oxide nanoparticles are seen just starting to cover the WO₃ scaffold (b). The cross-section of the WO₃/Fe₂O₃ film, corresponding to (c), is shown in (d). The dotted white line indicates the F:SnO₂/WO₃ interface. For comparison with image (a), a top-down view of the F:SnO₂ substrate is shown in (e). Adapted from [1]

Both XRD characterizations of the WO₃ scaffold and of the scaffold covered with hematite (1 minute deposition) show features related to the SnO₂ substrate (green full circles). Before deposition of the guest, the acquired diffraction pattern indicates the presence of monoclinic WO₃ (black filled squares).¹⁷ After the deposition of the iron oxide the expected peaks of hematite (red open circles) are observed in addition to the WO₃ scaffold features.

These studies confirm we obtained the desired architecture, with rounded iron oxide nanoparticles covering totally the WO₃ mesoporous host layer. From the electronic microscopy images, the contact between the two layers seems good and both materials are crystalline according to their respective X-ray diffraction patterns.

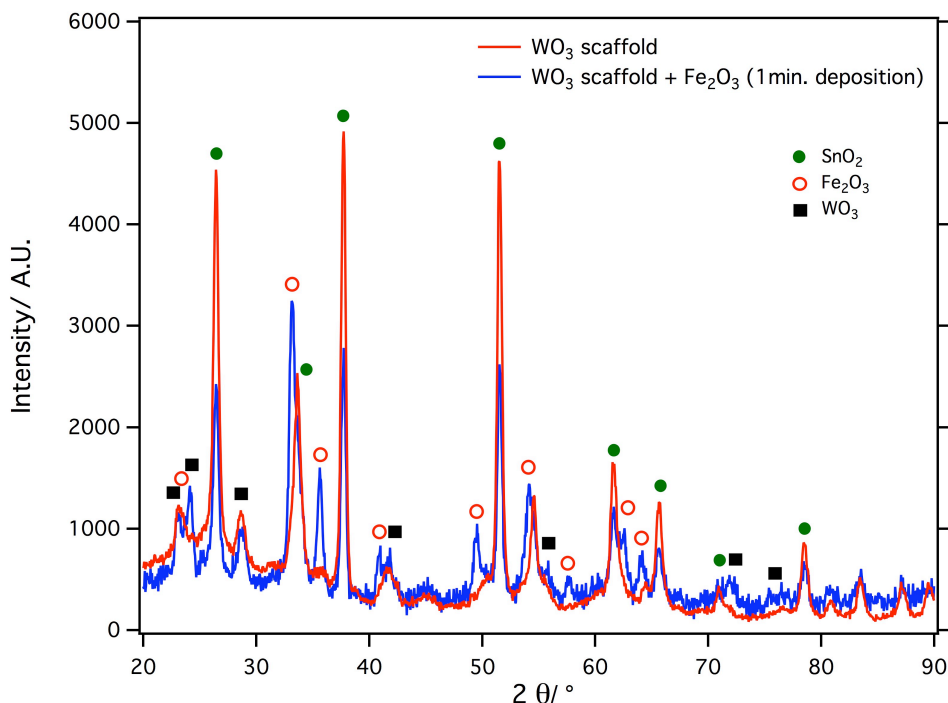


Figure 3.2: Thin film X-ray diffractograms of the WO₃ scaffold before and after the deposition of iron oxide. Peaks corresponding to SnO₂, WO₃, and Fe₂O₃ are indicated by green full circles, red open circles, and black filled squares, respectively

3.3.2. Photoelectrochemical enhancement

To quantify the effectiveness of the WO₃/Fe₂O₃ host/guest approach for water splitting, the photoanodes were analyzed independently from a tandem system as the working electrode in a potentiostatic cell with 1 M NaOH (pH 13.6)²¹ as the electrolyte, a Pt counter electrode, and an Ag/AgCl reference electrode. The current density, corresponding to oxygen evolution at the photoanode SCLJ, as a function of potential with respect to RHE of the 1 min and 4 min iron oxide depositions are shown in Figure 3.3 in the dark and in simulated sunlight (AM 1.5G, 100 mW cm⁻²).

In general, when scanned in the anodic direction, the electrode's dark current remains small until the onset of water electrolysis around 1.6 V_{RHE}. Under illumination the photocurrent increases sharply around 1.0 V_{RHE} and reaches a plateau before the onset of the dark current. For electrodes prepared with a 1 min iron oxide deposition (Figure 3.3a) we see a significant increase in the photocurrent plateau in the WO₃/Fe₂O₃ photoanode over the control electrode prepared without the WO₃ scaffold (1.71 and 1.41 mA cm⁻², respectively at 1.43 V_{RHE} corresponding to a 21% increase). This effect is reduced upon longer deposition times (4 min, Figure 3.3b) due to the increased thickness of the iron oxide guest layer. However, increased photocurrent was still observed after this longer deposition time at voltages approaching the dark

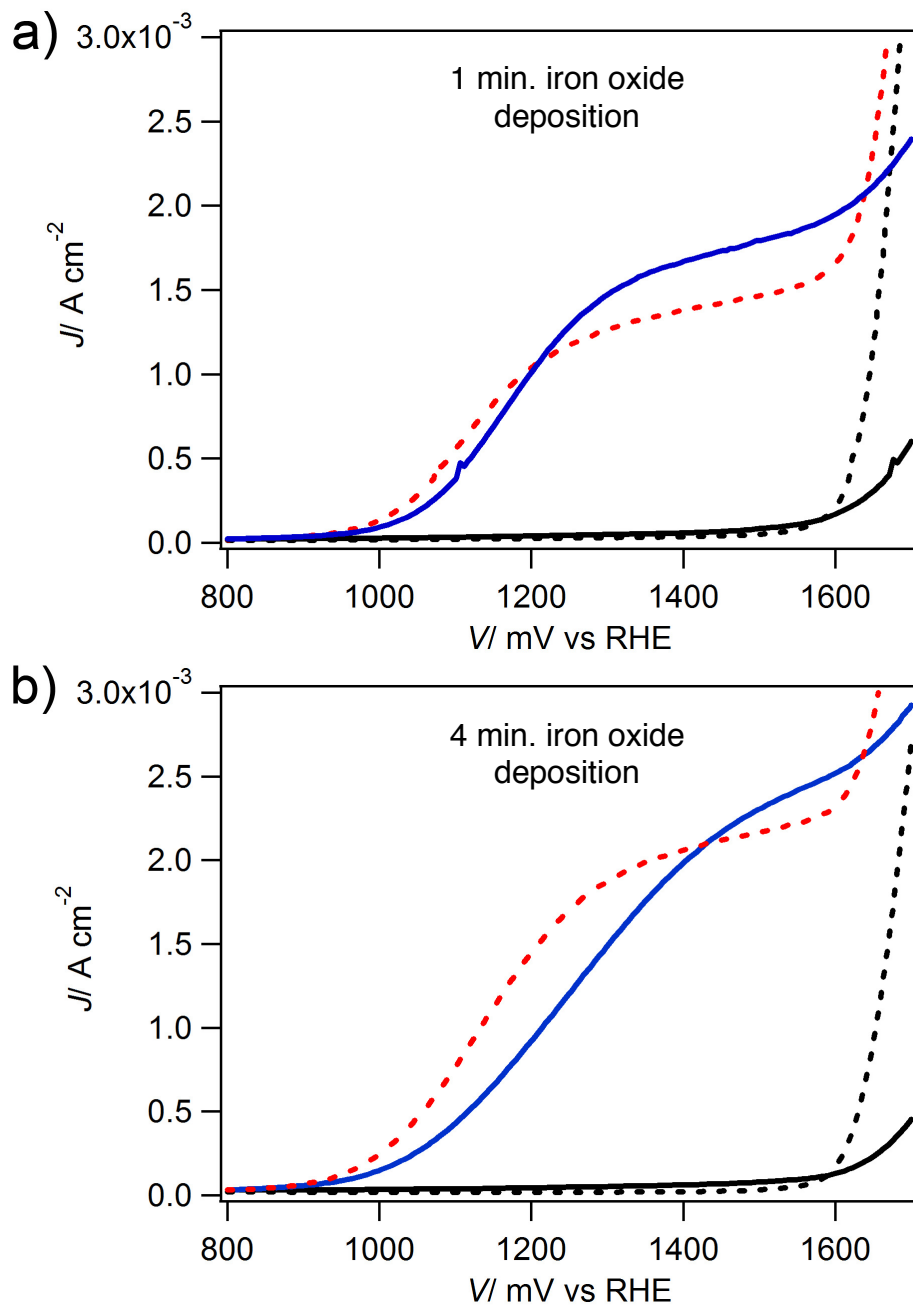


Figure 3.3: Current densities, J , of the prepared photoanodes in the dark (black curves) and under simulated solar illumination (colored curves) are shown as a function of the applied potential, V , with respect to the reversible hydrogen electrode (RHE). The top panel (a) shows the electrode performance with a Fe_2O_3 deposition time of 1 min while the bottom (b) corresponds to a deposition time of 4 min. The host/guest ($\text{F:SnO}_2/\text{WO}_3/\text{Fe}_2\text{O}_3$) and the control ($\text{F:SnO}_2/\text{Fe}_2\text{O}_3$) electrode current densities are indicated by solid (blue) and broken (red) lines, respectively. Reprinted from [1].

current onset. The observed photocurrent increase using the host/guest electrodes in Figure 3.3 was reproducible on several repeat samples and was stable for multiple scans of each photoanode despite tungsten trioxide's solubility in aggressively basic solutions. While extensive stability testing was not performed, this result suggests the iron oxide could effectively protect the WO_3 from contact with the electrolyte.

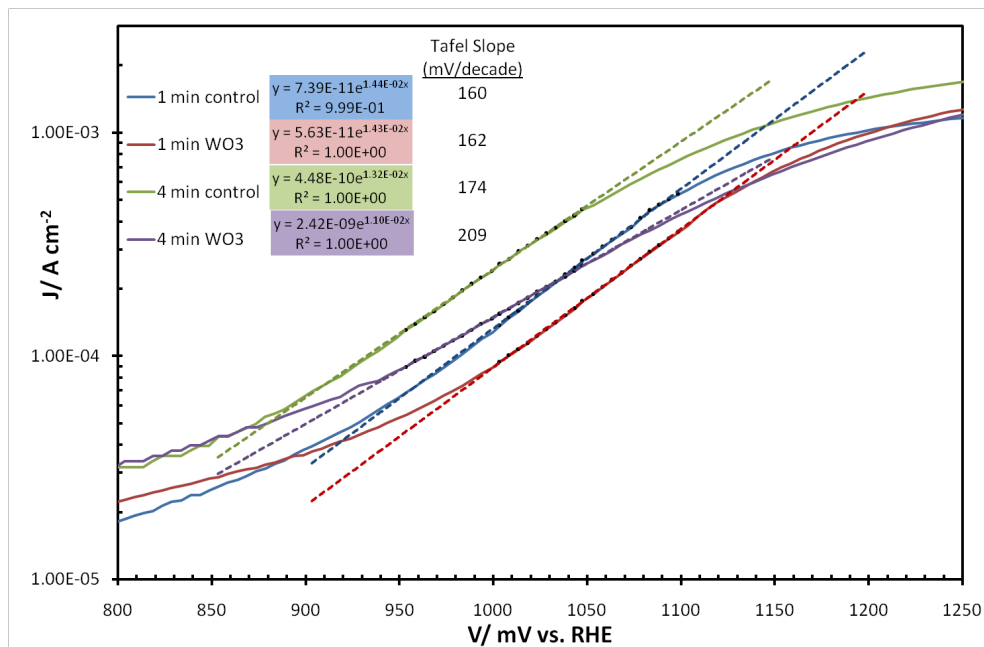


Figure 3.4 : Log-lin plot of the photocurrents presented in Figure 3.3. The back circles on each curve indicate the fitting range used for the curves (1000 – 1100 and 950 – 1050 mV for the 1 min and 4 min cases, respectively). The fitted trend lines are overlaid as broken lines, and the fitted equations along with the calculated Tafel slope are included in the legend.

In addition to quantifying the performance with the photocurrent plateau value, the photocurrent onset behavior can give indication of the differences in photoanode operation. In both the 1 min and 4 min iron oxide depositions, we observe a minimal shift in the photocurrent onset potentials ($1.00 \text{ V}_{\text{RHE}}$ for the control vs. $1.03 \text{ V}_{\text{RHE}}$ for the host/guest for both deposition times); a slight change that may be due to small barrier for electron transport over the $\text{Fe}_2\text{O}_3/\text{WO}_3$ interface. Moreover, the difference between the rise of the measured photocurrents, characterized by Tafel slopes, exhibit the different behavior of the $\text{WO}_3/\text{Fe}_2\text{O}_3$ photoanode as compared to the Fe_2O_3 reference sample. The Tafel plot is a representation of the current-voltage relation between the potentials where occur the onset and the saturation of the photocurrent (for a photoelectrode) in a log-lin scale. The slope of the observed line is then related to the ability of an electrode to perform an electrochemical reaction. As shown in Figure 3.4, the Tafel slope coefficient is indistinguishable for both electrodes after 1 min of iron oxide deposition indicating matching water oxidation kinetics. However the Tafel slope increases dramatically from 174 (control) to 209 mV decade^{-1} for the host/guest electrode after 4 min of deposition which indicates increased non-ideality in the photocurrent onset, according to the development made by Wang *et al.* for WO_3 photoanodes.²²

This result could be due to the rough scaffold's influence on fully developing the cauliflower-type morphology and the previously-observed crystalline alignment⁸ associated with these iron oxide films after 4 min of deposition, and is consistent with our observations depositing on F:SnO₂ with increasing roughness. Finally, we note the change in the dark current onset, which in the control case occurs at 1.6 V_{RHE} as previously reported. With the host/guest photoanodes the dark current becomes significant at the same potential, but has more gradual onset due to the WO₃ scaffold, demonstrating a strong effect of the scaffold on the dark current.

3.3.3. Benefits from the architecture

An increased photocurrent is expected using the host/guest approach for hematite over our previous cauliflower-type nanostructure because more of the iron oxide is closer to the hematite/electrolyte interface allowing a greater fraction of the photo-produced holes to transfer to the SCLJ and participate in water oxidation. The beneficial effects of the host/guest morphology should be diminished if the thickness of the guest layer far exceeds the photoexcited carrier transport length. Our observed photocurrent results with 1 min and 4 min iron oxide depositions are consistent with this hypothesis. However, it is possible that the increase in photocurrent for the 1 min deposition is wholly a result of the presence of more iron oxide due to the greater surface area of the scaffold material. In addition, since the goal of the host/guest approach is to increase the internal quantum efficiency of the guest material, especially in the wavelength region near the absorption band edge, proper confirmation of the effectiveness of the WO₃/Fe₂O₃ host guest approach should come from examining the quantum efficiency of these electrodes. To this end, we acquired photoaction and UV-Vis transmittance spectra of the host/guest and control electrodes from the 1 min iron oxide deposition. The internal quantum efficiency of the electrodes was then estimated by calculating the absorbed photon to current efficiency (APCE) as previously described.¹⁶ The results for the electrode transmittance and APCE acquired at a potential on the photocurrent plateau (1.43 V_{RHE}) as a function of the illumination wavelength for the 1 min films are shown in Figure 3.5.

The transmission spectra of the host/guest and control electrodes show a practically identical light absorption by the two films in the region where only iron oxide is absorbing (500 – 600 nm). This indicates that there is the same amount of iron oxide in both of the 1 min films, and interestingly, suggests that the deposition rate of iron oxide does not depend on the roughness of the substrate during the first

minute. In the wavelength band from 350 to 500 nm the transmittance of the host/guest electrode is found to decrease more compared to the control electrode due to the increased absorbance of the WO_3 scaffold. Since the penetration depth of photons in iron oxide increases beyond 100 nm near the band edge, these photons are generally absorbed deep within the iron oxide film, but due to the host/guest architecture, more of the iron oxide should be closer to the SCLJ and the quantum efficiency of the longer wavelengths should be increased over that of a cauliflower-type structure.

Indeed, comparing the APCE of the host/guest electrode to the control confirms this and the effectiveness of the host/guest approach. An increased APCE is observed over all photon energies, which could be explained by better electron transport through the host/guest architecture. However, near the band edge from 2.1 to 2.5 eV (600 – 500 nm) the improvement of the APCE increases significantly more, reaching a maximum of 40 % (8.0 and 5.7 % respectively for the host/guest and control, respectively) at 565 nm. Since this extra improvement is observed only for wavelengths near the band edge we can presume it is due to the facilitation of photogenerated holes to the SCLJ. In addition, there is no disproportionate increase in the APCE of the host/guest photoanode around 460 nm (2.7 eV) eliminating the possibility that the increased photocurrent observed is due to light absorption by WO_3 followed by hole transfer to the Fe_2O_3 . Another possible explanation for the increased performance of the iron oxide, is the incorporation of some of the tungsten from the scaffold. It is true that hematite photoanodes are very sensitive to small levels of impurities. However, it is unlikely in this case relatively low synthesis temperatures and the preferential increase of the quantum efficiency at the longer wavelengths. We would expect an equal increase of the performance for all wavelengths if a tungsten dopant was playing an important role. Still, an interesting feature of the APCE trace is observed in this and previous work as an abrupt change in slope at 500 nm (2.5 eV) for both cases. In our improved host/guest electrode the APCE enhancement seems to be greatest for photon energies lower than this value. Hematite is reported to have direct electronic transition at $\lambda < 400\text{nm}$ ($\text{O}^{2-} 2\text{p}^6 \rightarrow \text{Fe}^{3+} 3\text{d}$) and an indirect transition between 400 and 620 nm ($\text{Fe}^{3+} 3\text{d} \rightarrow 3\text{d}$).²³ However, we are not able to explain this transition at 500 nm, but as it is clearly an important feature of APCE results for the host/guest approach.

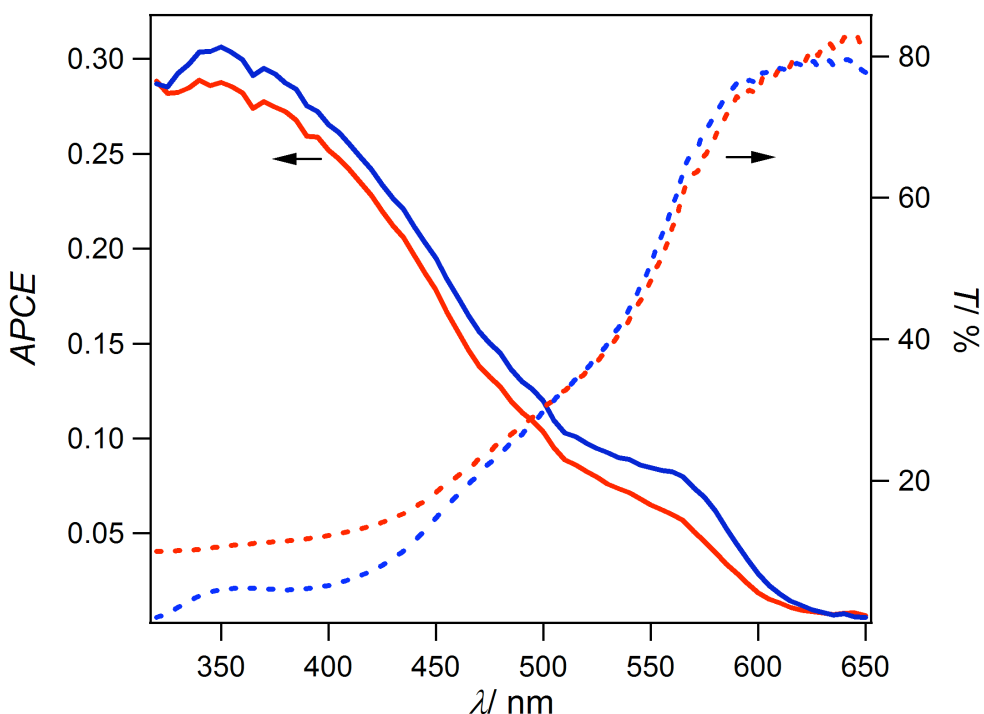


Figure 3.5 : The absorbed photon to current efficiency, APCE, (solid lines) at 1.43 V_{RHE} and the percent transmittance, T, (broken lines) of photoanodes prepared with a 1 min Fe₂O₃ deposition time plotted against the incident light wavelength, λ . The host/guest (F:SnO₂/WO₃/Fe₂O₃) and the control (F:SnO₂/Fe₂O₃) electrode responses are indicated by blue and red lines, respectively. Reprinted from [1].

The increased photocurrent and APCE data represent the initial demonstration of the host/guest approach to enhance photon harvesting in hematite for photoelectrochemical water splitting. While the improvement observed is modest it represents an important first step in the complex nanostructuring that will be necessary to fully realize the potential of hematite. Further improving the quantum efficiency of hematite using the host/guest approach will be accomplished by using an even thinner layer of iron oxide. This, coupled with an increased roughness and porosity of the scaffold layer, should allow the increase of the photocurrent above the state-of-the-art reported for hematite. However, the depositions methods which have been shown to be most effective for this material exhibit a photo-inactive “dead” layer near the interface with the substrate.¹⁶ This manifests as a negligible photocurrent for the thinnest films. While our results for the 1 min films suggest some improvement of this dead layer, our efforts to deposit even thinner layers of hematite on the WO₃ scaffold with the APCVD method gave results consistent with interfacial limitations; this issue is addressed in the two next chapters.

3.4. Conclusion

We have shown that host/guest approach, already successfully employed for other electrochemical systems like the DSSC, can be applied to hematite for photoelectrochemical water splitting. A *ca.* 20 % increase in photocurrent was observed when using $\text{WO}_3/\text{Fe}_2\text{O}_3$ host/guest photoanodes as compared to control devices. Accordingly, increased quantum efficiency, especially from wavelengths near the hematite absorption edge where photons have long penetration depths, was also observed, as a greater fraction of photons could be absorbed closer the hematite/electrolyte interface. Continued perfection of the nanostructure while also addressing the limiting interfacial issues will no doubt allow the host/guest approach to reveal the full potential of hematite for solar hydrogen production in a tandem cell system.

3.5. References

- (1) Sivula, K.; Le Formal, F.; Graetzel, M. *Chem Mater* **2009**, *21*, 2862.
- (2) Kennedy, J.; Frese, K. *J Electrochem Soc* **1978**, *125*, 709.
- (3) Balberg, I.; Pinch, H. *J Magn Magn Mater* **1978**, *7*, 12.
- (4) Van De Krol, R.; Liang, Y.; Schoonman, J. *J. Mater. Chem.* **2008**; *18*, 2311.
- (5) Glasscock, J. A.; Barnes, P. R. F.; Plumb, I. C.; Savvides, N. *J Phys Chem C* **2007**, *111*, 16477.
- (6) Hu, Y.-S.; Kleiman-Shwarsctein, A.; Forman, A. J.; Hazen, D.; Park, J.-N.; McFarland, E. W. *Chem Mater* **2008**, *20*, 3803.
- (7) Liang, Y.; Enache, C. S.; Van De Krol, R. *Int J Photoenergy* **2008**, 739864.
- (8) Kay, A.; Cesar, I.; Graetzel, M. *J Am Chem Soc* **2006**, *128*, 15714.
- (9) Murphy, A. B.; Barnes, P. R. F.; Randeniya, L. K.; Plumb, I. C.; Grey, I. E.; Horne, M. D.; Glasscock, J. A. *Int J Hydrogen Energ* **2006**, *31*, 1999.
- (10) Itoh, K.; Bockris, J. *J Electrochem Soc* **1984**, *131*, 1266.
- (11) Itoh, K.; Bockris, J. *J Appl Phys* **1984**, *56*, 874.
- (12) Gratzel, M. *Chem Lett* **2005**, *34*, 8.
- (13) Liu, H.; Gao, L. *J Am Ceram Soc* **2006**, *89*, 370.
- (14) Xu, Y.; Schoonen, M. *Am Mineral* **2000**, *85*, 543.
- (15) Cesar, I. *EPFL Thesis 2007, Lausanne, Switzerland*.
- (16) Cesar, I.; Sivula, K.; Kay, A.; Zboril, R.; Grätzel, M. *J. Phys. Chem. C* **2009**, *113*, 772.
- (17) Santato, C.; Ulmann, M.; Augustynski, J. *J Phys Chem B* **2001**, *105*, 936.

- (18) Tanner, R.; Szekeres, A.; Gogova, D.; Gesheva, K. *Appl Surf Sci* **2003**, *218*, 162.
- (19) Cornuz, M.; Grätzel, M.; Sivula, K. *Chem. Vap. Deposition* **2010**, *16*, 291.
- (20) Seaman, C. *Sol Energy* **1982**, *29*, 291.
- (21) Kennedy, J.; Frese, K. *J Electrochem Soc* **1978**, *125*, 723.
- (22) Wang, H.; Lindgren, T.; He, J.; Hagfeldt, A.; Lindquist, S. *J Phys Chem B* **2000**, *104*, 5686.
- (23) Dare-Edwards, M.; Goodenough, J.; Hamnett, A.; Trevellick, P. *J Chem Soc Farad T 1* **1983**, *79*, 2027.

CHAPTER 4.

CONTROL OF IRON OXIDE THIN FILM PHOTOACTIVITY

This chapter is based on the following publication, F. Le Formal, M. Grätzel, K. Sivula, *Adv. Funct. Mater.* **2010**, *20*, 1099.¹

The preceding chapter presented a promising route to increase the performance of hematite ($\alpha\text{-Fe}_2\text{O}_3$) photoelectrodes for solar hydrogen production through water splitting with using an extremely thin layer of this visible light absorber on a nano-structured scaffold. However, the typically poor performance of ultra-thin (*ca.* 20 nm) films of hematite has been the limiting factor to implement this approach. The surprising effect of a substrate pretreatment using tetraethoxy silicate (TEOS), before deposition of iron oxide by spray pyrolysis, is reported in this chapter. The substrate treatment drastically improves the photo-performance of 12.5 nm thick films of hematite, which exhibit a water oxidation photo-current onset potential at 1.1 V *vs.* the reversible hydrogen electrode (RHE) and a plateau current of 0.63 mA cm^{-2} at 1.5 V *vs.* RHE under standard illumination conditions, representing the highest reported performance for ultra-thin hematite films. In contrast, almost no photoactivity was observed for the photoanode with the same amount of hematite on an untreated substrate. A detailed study of the effects of the TEOS treatment shows that a monolayer of SiO_x is formed which acts to change the hematite nucleation and

growth mechanism, increases its crystallinity and reduces the concentration of carrier trapping states of the ultra-thin films.

4.1. Introduction

In the search for a semiconductor that can facilitate the efficient storage of solar energy in the form of hydrogen via water splitting, hematite ($\alpha\text{-Fe}_2\text{O}_3$) is considered as promising material. The seminal efforts to study hematite as an oxygen-evolving photoanode for water decomposition, expressing its promising aspects and limitations, are detailed in Chapter 2 and in other relevant publications.³⁻⁹ One major restriction of hematite for water splitting arises from the contradiction between its electronic and optical properties. To summarize, hematite has a very short excited state lifetime (on the order of 10 picoseconds)^{10,11} and poor minority charge carrier mobility ($0.2 \text{ cm}^2 \text{ V}^{-1} \text{ s}^{-1}$)¹² which result in a small hole diffusion length ($2 - 4 \text{ nm}$)⁶ as compared to the light penetration depth ($a^{-1} = 118 \text{ nm}$ at $\lambda = 550 \text{ nm}$).² The large concentration of donor dopant atoms required to afford suitable majority carrier conductivity in hematite causes a further dilemma for the transport of holes to the semiconductor liquid junction (SCLJ) by also causing the space-charge layer to be extremely thin (*ca.* 10 nm).^{2,9,13}

These limitations suggest that the control of hematite morphology on a length scale similar to the hole transport length is needed, and indeed, recent nanostructuring techniques such as electrodeposition,¹⁴ anodic nanotube arrays,¹⁵ and ultrasonic spray pyrolysis¹⁶ have proven useful in increasing the performance of hematite for water-splitting.¹⁷ The state-of-the-art hematite photoanodes produced by atmospheric pressure chemical vapor deposition (APCVD)¹⁸ possess a cauliflower-type morphology with feature sizes down to 5 nm and exhibit an overall solar-to-hydrogen conversion efficiency of 3.3 % when used in a tandem configuration. However, this efficiency remains low compared to the theoretical value of 16.8 % predicted for a material with this band-gap.¹⁹ This gap between measured and theoretical efficiency is due to the relatively low external quantum efficiencies (< 20%) at long wavelengths ($\lambda = 610 - 450 \text{ nm}$) — a region where over 10 mA cm^{-2} of solar photocurrent is available. It suggests that, even in this nanostructure, the longer wavelengths are absorbed in the thick stems of the cauliflower, far from the SCLJ.

The promising nanostructuring approach, presented in Chapter 3, implies the light absorption, even of the longer wavelength, to occur closer to the SCLJ. This concept consists of using an extremely thin film of hematite coated on a high surface

area host scaffold and has been demonstrated to increase the conversion efficiency of hematite near the band edge absorption by positioning a greater portion of the hematite in high proximity to the SCLJ.²⁰ However, like others who have investigated ultra-thin films of hematite,²¹ the performance has been limited by recombination for films below *ca.* 50 nm. In order for this host-scaffold/guest-extremely-thin-absorber approach to be useful for hematite, a film thickness of *ca.* 10 nm must achieve an absorbed-photon-to-current efficiency (APCE) superior to the state-of-the-art films. As such, the goal of this work has been to understand and control the photoactivity of ultra-thin films of hematite. In this chapter, a surprising effect of a substrate (F:SnO₂, FTO) pretreatment with tetraethoxy silicate (TEOS) on the photoactivity of ultra-thin hematite films prepared by spray pyrolysis is reported, and linked this effect with the observed properties of the thin film.

4.2. Experimental

4.2.1. Substrate preparation

The electrodes were prepared using the following procedure. Substrates of fluorine-doped tin oxide (FTO) glass 30×12 mm² (TEC 15, Hartford Glass Co. 15 Ω □⁻¹) were cleaned by sonication in a pure acetone bath (15 min), sonication in a 3 % soap in deionized water solution (15 min), rinsed 10 times with deionized water, and finally sonication in 2-propanol (15 min). Control samples were also cleaned in this way before Fe₂O₃ deposition.

Substrates were then pretreated with TEOS by first heating to *ca.* 400 °C on a hot plate in air, and then approximately 3 mL per cleaned substrate of a diluted TEOS solution (10% vol. in ethanol) was hand-sprayed with a glass atomizer onto the hot substrates. These samples were cooled before heating again to deposit the Fe₂O₃.

4.2.2. Fe₂O₃ thin film preparation

Two columns of 5 substrates (10 in total adjacent to one another and alternating between pretreated and control samples) were then subjected to iron (III) acetylacetone spray. The spray setup consisted of an ultrasonic spray head (Lechler company, US1 30°) set 30 cm over the substrates, which were placed on a hot plate heated at 550 °C (corresponding to a measured substrate surface temperature of 400 °C). An automatic syringe pump was used to deliver 1mL of a solution containing 10mM of Fe(acac)₃ (99.9+%, Aldrich) in EtOH (\geq 99.8% Fluka) to the spray head, every 30 seconds at a speed of 12 mL min⁻¹ (spray length of 5 seconds). The carrier gas (compressed air) flow, directing the spray to the substrates

was set to 15 L min^{-1} . Three different amounts of liquid sprayed were tested: 10 mL, 20 mL and 30 mL. After the spray the samples were annealed for 5 min at ca. 450°C before cooling to room temperature.

4.2.3. Photoelectrochemical characterization

Photocurrent measurements were performed to estimate the solar photocurrent of the photoanodes in a three-electrode configuration with 1 M NaOH (pH 13.6)⁶ as electrolyte using Ag/AgCl in saturated KCl as a reference electrode. The hematite electrode was scanned at 50 mV s^{-1} between -300 and 800 mV vs. Ag/AgCl. The potential is reported relative to the reversible hydrogen electrode potential (RHE)¹⁸. The samples were illuminated with simulated sunlight from a 450 W xenon lamp (Osram, ozone free) using a KG3 filter (3 mm, Schott) with a measured intensity of 1 sun (100 mW cm^{-2}) at the sample face. Spectral mismatch factors to estimate the difference of the electrode photoresponse obtained from simulated sun light and real sun light at AM 1.5 G were calculated according to the method described by Seaman *et al.*²². Photocurrent action spectra and the UV-vis transmittance were measured to determine the absorbed photon to current conversion efficiency (APCE). Photocurrent action spectra were obtained under light from a 300 W Xe-lamp integrated parabolic reflector (Cermax PE 300 BUV) passing through a monochromator (Bausch & Lomb, bandwidth 10 nm fwhm). The transient photocurrent response was obtained by chopping the incident light with an externally controlled shutter at a rate of about 0.5 s^{-1} and scanning the potential at a reduced rate of 10 mV s^{-1} .

4.2.4. Optical and spectroscopic measurement

The UV-vis absorbance spectra were taken with a Varian Cary 5 spectrophotometer fitted with an 11 cm diameter integrating sphere coated with polytetrafluoroethylene (PTFE) according to the method developed by Rothenberger *et al.*²³ This setup allowed measuring the total transmittance and the total reflectance of samples of interest. The absorption was calculated from these measurements with the formula $A = 1 - T - R$ with A the absorptance, T the total transmittance and R the total reflectance.

The attenuated total reflection – Fourier transform Infrared spectra (ATR-FTIR) were measured for all the samples using a Digilab FTS 7000 FTIR spectrometer fitted with a DTGS detector. All the data reported here were taken with

the “Golden Gate” 45° diamond anvil ATR accessory. Spectra were derived from 64 scans at a resolution of 2 cm⁻¹.

X-ray photoelectron spectroscopy (XPS) data were collected by Axis Ultra (Kratos analytical, Manchester, UK) under ultra-high vacuum condition (<10⁻⁸ Torr), using a monochromatic Al K_α X-ray source (1486.6 eV), in the Surface Analysis Laboratory of CIME at EPFL. The source power was maintained at 150 W (10 mA, 15kV). The emitted photoelectrons were sampled from a square area of 350 mm². Gold (Au 4f_{7/2}) and copper (Cu 2p_{3/2}) lines at 84.0 and 932.6 eV, respectively, were used for calibration, and the adventitious carbon 1s peak at 285 eV as an internal standard to compensate for any charging effects.

X-ray diffraction (XRD) patterns of Fe₂O₃ films with and without the TEOS treatment on SnO₂ glass substrate were measured between 2θ = 32° and 2θ = 37° using a Bruker D8 Advance XRD instrument with Cu K_α 1 radiation (0.1540 nm) locked coupled mode, source slit width 2 mm, step size 0.001°, 1150 s per step. The spectra were normalized to the SnO₂ (101) peak.

The morphology of the sprayed hematite thin films were also characterized using a high-resolution scanning electron microscope (SEM, FIB NVision 40 from the company Zeiss). The acceleration voltage was 1 keV while an in-lens detector was employed with a working distance of 1.5 mm in order to have response from atoms close to surface. The samples were investigated after the photoelectrochemical measurements and sample positions coincided with the illuminated area.

4.3. Results and discussion

In order to understand the performance of hematite thin films we have investigated many different thin film underlayers and substrates with the goal of eliminating the so-called “dead-layer”—the poorly performing first *ca.* 50 nm of hematite.² Our initial investigations showed that films thinner than 50 nm showed poor photoactivity on many different substrates (Au, Pt, F:SnO₂, WO₃), and for different deposition methods (ultrasonic spray pyrolysis, conventional spray pyrolysis, APCVD, and atomic layer deposition). The inactivity of ultra-thin films of hematite has been suggested to be due to the electron cloud of the fluorine-doped SnO₂ extending into the Fe₂O₃ film and thus enhancing recombination.²¹ Indeed, if the enhanced recombination rate at the SnO₂/Fe₂O₃ interface is an intrinsic property of this system, there would be far-reaching consequences for the prospects of using hematite efficiently in a host-scaffold/guest-absorber approach. However, since a previous

work with the APCVD deposition of Fe_2O_3 had suggested a TEOS pretreatment could have a beneficial effect on 300 nm films of Si doped Fe_2O_3 ,¹⁸ we chose to study the effect of the TEOS pretreatment in detail on ultra-thin films. Conducting glass substrates (FTO) pretreated with TEOS were studied first with FTIR and XPS to determine the surface modification engendered by the pretreatment—more precisely the deposition product of the TEOS spray.

4.3.1. TEOS pretreatment characterization

FTIR spectra of the pretreated substrate and a control substrate heated to the same temperature without treatment are shown in Figure 4.1. The broken line represents the spectrum of liquid TEOS, directly scanned on the ATR crystal. It exhibits sharp peaks at $\nu = 2974$, 2926 and 2890 cm^{-1} characteristic of the (C–H) bond stretching,²⁴ as well as several distinct features at frequencies between 1450 and 750 cm^{-1} corresponding to the numerous vibrational modes of molecular TEOS already assigned in a few publications.²⁴⁻²⁶ The spectra representing the pretreated and control FTO substrates, before iron oxide deposition, both exhibit a very broad absorbance peak in the IR wavelengths due to the plasma resonance frequency of FTO.²⁷ Nevertheless, a clear feature can be observed on the TEOS treated substrate at 1234 cm^{-1} with a shoulder around 1176 cm^{-1} more plainly visible on the subtracted (TEOS treated – control FTO) spectrum. Another feature peaking at 2322 and 2355 cm^{-1} , observable on both pretreated and non-pretreated substrate, was due to CO_2 and should be neglected. The feature appearing around 1200 cm^{-1} is not correlated to any peaks on the liquid TEOS spectrum, nor is it observed on the control sample spectrum, indicating the presence of a new species due to the reaction occurring between TEOS and the substrate surface heated to 550°C during the pretreatment spray. To eliminate the possibility that this new species could arise from the decomposition of the ethanol (used as a solvent for the TEOS) alone, an additional control was performed heating the sample to 550°C and spraying only ethanol. The resulting FTIR spectrum was identical to the control sample which was only heated in air, establishing that the newly formed species is a direct result of the decomposition of the TEOS.

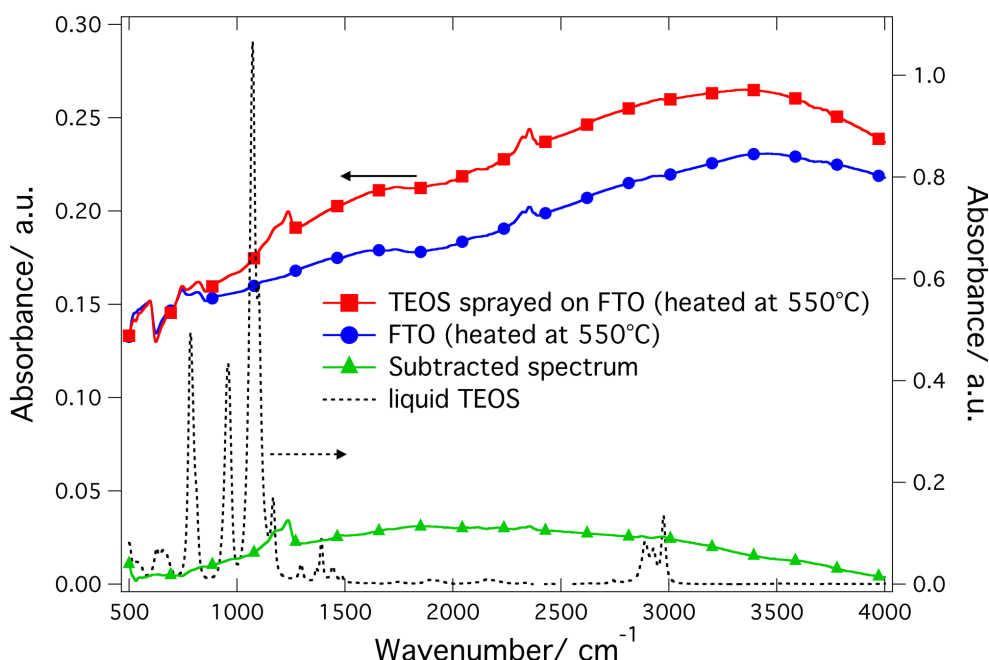


Figure 4.1: ATR-FTIR spectra for a FTO substrate heated at 550°C and subjected to the TEOS spray pretreatment (red/squares), a control sample of FTO heated at 550°C without TEOS spray (blue/circles), and liquid TEOS (dotted line). An identical control spectrum was obtained with the substrate heated to 550 °C and treated with only ethanol. The subtracted spectrum (green/triangles) representing the subtraction of the pretreated FTO spectrum by the non pretreated FTO spectrum is also shown to emphasize the observed change. Reprinted from [1].

The thermal decomposition of alkoxy silanes such as TEOS has been extensively studied in the past.^{24-26,28-32} These reactions can result in the production of SiO₂ at high temperature or lower weight ethoxysilyl intermediates with temperatures lower than ca. 475 – 525 °C depending on the reaction conditions.^{25,28} SiO₂ deposition from TEOS was found to be a self-limiting reaction in the absence of water or basic atmosphere.^{25,33} Indeed, we also observed that the effect of the pretreatment did not vary with the amount of TEOS sprayed, even if large amounts of the TEOS-ethanol mixture were used. This implies a film of SiO₂ is not grown under our conditions, but rather just a modification of the surface occurs. In FTIR studies of thin silicon dioxide films, vibrational mode fingerprints appeared mainly in the 400 – 1200 cm⁻¹ region^{24,25,32} whereas (Si-OH)²⁶ and (Si-C)³⁴ bonds showed an excitation at 3700 cm⁻¹ and around 1100 cm⁻¹, respectively. None of these peaks are present on the pretreated substrate spectrum in Figure 4.1. The peaks found in our study at 1234 and 1174 cm⁻¹ are similar in frequency to features that appear in infrared studies of thin SiO₂ films. These investigations observed a transverse-optical (TO) and a longitudinal optical (LO) vibrational phonon mode of the (Si-O-Si) bridge at 1075 and 1250 cm⁻¹ respectively.^{25,31,35,36} Moreover these two modes are known to

split into in-phase (AS_1) and out-of-phase (AS_2) motion of oxygen atoms. The latter mode is normally infrared inactive in bulk, but can be observed in very thin films at oblique incidence.^{35,36} These four peaks have been assigned by Kirk³⁶ as $\text{LO}(\text{AS}_1)$ at 1256 cm^{-1} , $\text{LO}(\text{AS}_2)$ at 1160 cm^{-1} , $\text{TO}(\text{AS}_1)$ at 1076 cm^{-1} and $\text{TO}(\text{AS}_2)$ at 1200 cm^{-1} . Thus, we attribute the feature observed between 1234 and 1150 cm^{-1} to the asymmetric vibration of ($\text{Si}-\text{O}-\text{Si}$) bridges, suggesting the formation of an ultra-thin film of SiO_2 atop our substrate surface. The presence of only two features and the slight difference in the peak positions from the literature could be explained by the crystal lattice mismatch between SnO_2 and SiO_2 , leading to stress in the bond angles of ($\text{Si}-\text{O}-\text{Si}$) bridges,³⁰ which are known to be slightly different between bulk, surface, and ultra-thin films depending on the thickness.^{31,37}

Other evidence of the modification of the substrate surface by a deposition of a very thin layer of SiO_2 was obtained with an XPS study of the TEOS pretreated and non-pretreated FTO substrates. The presence of five atoms (F, O, Sn, C, Si) was studied by quantifying their respective characteristic binding energy maximum peaks. Table 4.1 represents the results of this study.

Surprisingly, no fluorine atoms have been found on the surface of either substrate. This is probably due to the low sensibility of fluorine atoms; fluorine has been shown to be only detectable by XPS for high concentration of F in FTO deposited by CVD or DC reactive sputtering.³⁸ The amount of Si on the surface of the untreated substrate is very small and could be considered as extrinsic surface impurities or a small amount present in the FTO. A larger amount of silicon, eight times more, was detected on the TEOS treated substrate confirming the deposition of silicon-based compound on the surface. In contrast to the previous report¹⁸ only a slight attenuation of the Sn response was observed suggested the pretreatment layer is thinner than the 1 nm formerly assumed.

Carbon content should also give information about the nature of the deposition product from the TEOS spray. Less carbon was found on the pretreated surface than on the untreated one (2.35 vs. 3.21 at %) but both values are still in the same small order of magnitude, suggesting it is adventitious. Therefore, presence of ethoxy groups from the TEOS still bonded to the silicon atoms seems unlikely. Oxygen on surfaces also increased with the TEOS treatment. If we compare the ratio of oxygen atoms per metal atoms (Sn and Si), the difference is 0.35 to 0.26 in favor of TEOS treated FTO surface. Since these ratios are both lower than the expected stoichiometric ratio, we must conclude that the Si exists as a SiO_x layer and not

formally SiO_2 . In addition, since the amount of oxygen increased after the TEOS treatment, it could suggest that the untreated FTO is oxygen deficient and the TEOS treatment acts to fill oxygen vacancies on the surface. This would have important effects on the electronic nature of the interface with Fe_2O_3 , which will be discussed later.

Atoms	Peak of interest (related binding energy)	TEOS pretreated	Untreated
		FTO surface [at.%]	FTO surface [at.%]
F	1s (689 eV)	0	0
O	1s (531 eV)	25.2	19.8
Sn	3d (487 eV)	67.1	76.2
C	1s (285 eV)	2.35	3.21
Si	2p (102 eV)	5.35	0.82

Table 4.1: Relative amount of fluorine (F), oxygen (O), tin (Sn), carbon (C) and silicon (Si), found on the surface by XPS of TEOS sprayed FTO substrate and untreated FTO substrate, by XPS. The binding energy peak used to quantify the amount of each atom in this study is described on the second row of the table.

In summary, the FTIR data, the relatively small amount of Si detected by the XPS experiment, and the observed self-limiting nature of the reaction indicates that only a monolayer, or perhaps even a sub monolayer of SiO_x is deposited during the TEOS treatment. This self-limiting character reasonably can be explained by the presence of basic Sn–OH sites on FTO which could catalyze the decomposition of TEOS.³⁹ Once all of the surface sites had reacted, the deposition of the SiO_x would cease. In further support of our conclusion about the nature of the surface modification, no change in the appearance of the FTO surface was noticeable under high resolution scanning electronic microscopy. Nevertheless, this SiO_x layer induced significant differences in the photo-activity of ultra-thin iron oxide films prepared by spray pyrolysis.

4.3.2. Water photo-oxidation performance of ultra-thin hematite film

The spray pyrolysis deposition of Fe_2O_3 from a solution of iron (III) acetylacetone was chosen as a model system for our thin-film studies because of its ability to give uniform thin films over large areas with good performance.^{40,41} Figure 4.2 shows the water oxidation photocurrent density as a function of applied voltage of the ultra-thin-film hematite photoanodes prepared with different thicknesses (by spraying different amounts of precursor solution) on SiO_x treated and control (non-pretreated) substrates. Here we see the thinnest hematite electrode prepared on the control substrate (Sample F) showed no photoactivity, i.e. the dark current (broken line) and photocurrent (solid line) are the same. However, the electrode prepared at the same time using a SiO_x /FTO substrate (Sample E) showed an increased current density under illumination. In order to have a consistent comparison between samples and to quantify the behavior of the hematite photoelectrodes we chose to define the water oxidation current onset potential as the potential where the slope, dJ/dV , attained a value of $0.20 \times 10^{-3} \text{ mA cm}^{-2} \text{ mV}^{-1}$. This value is four times greater than the highest observed dJ/dV for the background current density (exchange current at potentials cathodic of water oxidation). Using this formalism, the water oxidation photocurrent onset for Sample E was at a potential of 1.32 V vs. the reversible hydrogen electrode (RHE) compared to the dark current onset at 1.56 V. Accordingly, the photocurrent density in Sample E rose to 0.20 mA cm^{-2} before the onset of the dark current. This represents a particularly surprising photoactivity, considering the low absorbance of these thin films over the entire wavelength spectrum.

Samples prepared by spraying 20 mL of $\text{Fe}(\text{acac})_3$ precursor solution (C and D) exhibited a more drastic effect of the substrate treatment. Sample D (prepared on a control FTO substrate) had a small but detectable photocurrent which onset at 1.38 V vs. RHE compared to a dark current onset at 1.47 V. In contrast, the performance of Sample C was significantly improved. Here the photocurrent was observed to rise at a voltage of 1.07 V and flatten out to a value of 0.63 mA cm^{-2} at 1.53 V before the dark current rose at 1.56 V. For the largest hematite thickness tested (Samples A and B prepared with 30 mL of precursor sprayed) the difference was less drastic. Sample B (control substrate, 30 mL precursor solution) showed a similar photoactivity to Sample C (SiO_x substrate, 20 mL precursor solution), and Sample A (SiO_x substrate, 30 mL precursor solution) exhibited the best overall performance with a

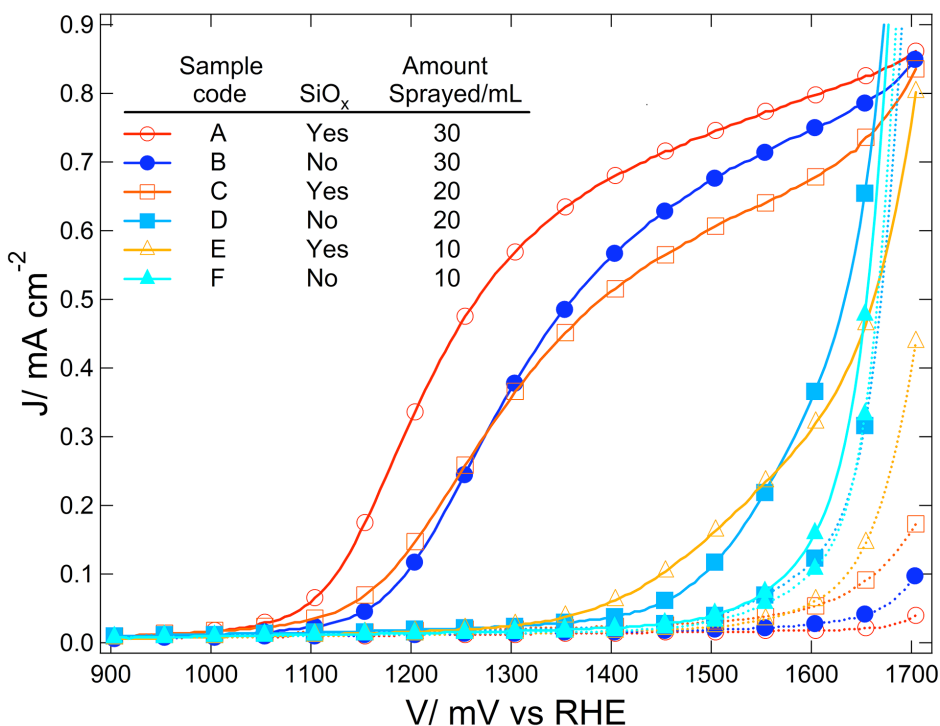


Figure 4.2: Current densities, J , in mA cm^{-2} of the prepared photoanodes in the dark (broken lines) and under simulated solar illumination (AM 1.5G 100 mW cm^{-2} , solid curves) are shown as a function of the applied potential, V , with respect to the reversible hydrogen electrode (RHE). Hematite electrodes prepared on SiO_x /FTO substrates (red/orange, empty markers) are compared to control electrodes prepared on untreated FTO substrates (blue, full markers). The amount of precursor sprayed for each sample condition is given in the figure legend. Reprinted from [1].

smaller photocurrent onset potential (1.03 V), and a higher plateau current of 0.762 mA cm^{-2} at 1.53 V. In addition, Sample A had the largest dark current onset potential at 1.65 V.

The water oxidation performance and the sample preparation conditions are summarized in Table 4.2. In general, the main differences between the photoresponses of electrodes prepared on SiO_x treated substrates and the control samples with the same amount of precursor solution used are: (i) a cathodically shifted photocurrent onset, (ii) a higher photocurrent density plateau, and (iii) a more positive potential to observe the onset of the water oxidation dark current. These differences are alike for all three amounts of precursor used. Moreover, the photoelectrochemical behavior of our samples was found to be highly reproducible when repeated at similar conditions, and even for samples prepared at different conditions (temperature, carrier gas flow rate, etc.) the effect of the SiO_x underlayer was apparent. However out of the conditions tested, the conditions reported gave the highest photoactivity at the lowest thickness and the widest-range response of electrode performance with respect to both the TEOS treatment and the thickness of

the film — an important distribution for the subsequent identification of the important factors which control the photoactivity. In addition, the fact that Sample B exhibits a photocurrent similar to Sample C eliminates the possibility that the Si is a requirement for photoactivity (*e.g.* by mechanism of the Si atoms diffusing from the SiO_x and doping the ultra-thin hematite layers), as there is no Si present in the control case.

Sample code	SiO_x layer	Amount		Water oxidation			
		Fe(acac) ₃ solution sprayed [mL]	Fe_2O_3 thickness [nm] ^[a]	onset potential [mV vs. RHE] ^[b]	(Dark) (Photo) ^[c]	Water oxidation photocurrent density [mA cm^{-2}]	@ 1230 mV @ 1530 mV
A	Yes	30	23.3	1647	1026	0.424	0.762
B	No	30	21.9	1601	1093	0.191	0.700
C	Yes	20	12.5	1557	1067	0.213	0.629
D	No	20	12.5	1473	1384	0.020	0.173
E	Yes	10	5.25	1562	1315	0.018	0.203
F	No	10	7.25	1477	1470	0.016	0.058

[a] as calculated from optical absorption. [b] defined as potential when $dJ/dV = 0.20 \times 10^{-3} \text{ mA cm}^{-2} \text{ mV}^{-1}$ (see text). [c] at AM 1.5G (100 mW cm^{-2}) and in 1 M NaOH, mV vs. RHE.

Table 4.2: Summary of the fabrication conditions and the current-voltage behavior of the different ultra-thin-film hematite electrodes.

4.3.3. Film thickness and APCE

An obvious explanation for the drastic difference in the photoactivity would be simply a variation in the hematite thickness. To estimate the thickness of the hematite deposited on the pretreated and control substrates UV-vis absorption data was used (see Figure 4.3a). The spectra for all six conditions tested exhibited similar shapes with an absorbance maximum around 400 nm and a slow decrease in absorbance until 600 nm (corresponding to 2.06 eV and consistent with the band gap of iron oxide of 2.0 – 2.2 eV commonly reported). Given the similarity between the spectra, the thicknesses could be estimated assuming a Lambertian absorption with an absorption coefficient, α , according to:

$$-\ln(1 - A) = \alpha \cdot l \quad (1)$$

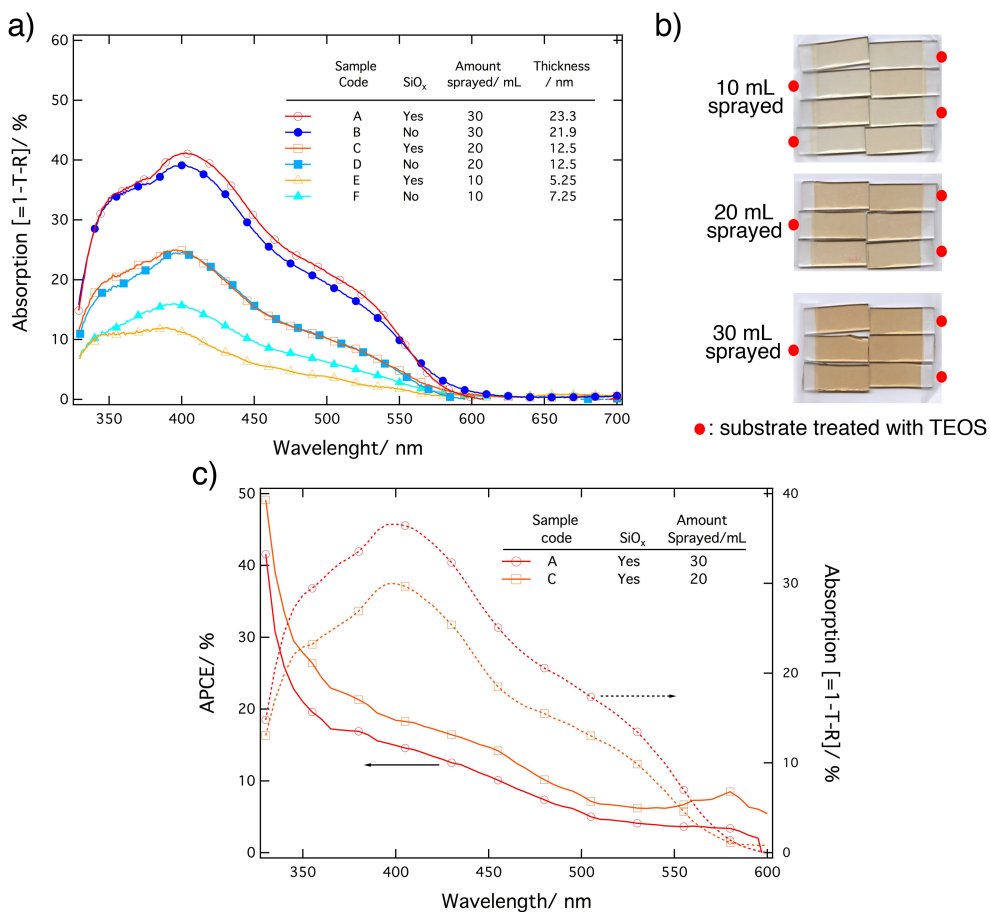


Figure 4.3: Percent absorbance, A, of photoanodes prepared with: 10 mL (triangles), 20 mL (squares) and 30 mL(circles) Fe(acac)₃ solution sprayed, plotted against the incident light wavelength, λ (nm). The absorbance A was calculated from transmittance, T, and reflectance, R, measurements with the formula: $A = 1 - T - R$. The substrates onto which the iron compound was sprayed, i.e. the bare FTO and the TEOS pretreated FTO are indicated by blue colors (with full markers) and red/orange colors (with empty markers), respectively. The absorbance of FTO (essentially for $\lambda < 400\text{nm}$) was subtracted from all spectra. b) Photographs of the as prepared Fe₂O₃ samples on FTO glass. Each individual substrate is 12 mm x 30 mm in dimension. The samples prepared on TEOS treated substrates are indicated with a red dot. c) Absorbed photon to current efficiency as a function of incident light wavelength for Samples A and C obtained at 1.43 V vs RHE. The APCE was calculated as previously described.² The absorption curves for these two samples are also shown as broken lines. The slight rise of the APCE for the 20 mL sprayed sample between 550 and 600 nm is due to the very small absorption of the sample which results in error in the calculation of the APCE, Reprinted from [1].

Where A is the absorptance, l is the path length (the hematite thickness in nm), and a an absorption coefficient taken as $(44 \text{ nm})^{-1}$ for a wavelength of 400 nm.⁴² This calculation gave the thicknesses, reported in Table 4.2, which increased linearly and ranged from ca. 6 nm for 10 mL sprayed to 22 nm for 30 mL sprayed.

The water oxidation photocurrent delivered by Sample C is quite remarkable given the thickness (12.5 nm) and absorption (only 25% of the incident radiation at its absorption maximum, $\lambda_{\max} = 400 \text{ nm}$) of the hematite present. Despite the small

amount of hematite present, the photocurrent is greater than other reports of thick films of hematite prepared by a comparable spray pyrolysis method without the addition of dopants.^{16,40,43} Moreover, contrary to a thickness explanation of the photocurrent enhancement, the hematite films prepared on TEOS treated substrates had approximately the same amount of hematite as the control films. In fact, for the thinnest films (E and F) slightly less hematite was deposited when the SiO_x underlayer was used. This was also clearly evident by visual inspection of these films (see Figure 4.3b). These observations suggest that the modification of the substrate radically changes the film formation resulting in this drastic effect on the photoelectrochemical performance.

The absorbance data also allows us to estimate how these ultra-thin films would perform if integrated into a host-scaffold/guest-absorber approach. The maximum photocurrent delivered by host-scaffold/guest-absorber electrode is related to the absorbed-photon-to-current efficiency (APCE, determined as a function of incident radiation wavelength) integrated over the solar spectrum.²⁰ The highest APCE was reached with Sample C: 30 % for $\lambda = 350$ nm and 20 % at 400 nm at 1.43 V vs. RHE. Sample A showed a lower APCE of about 20 % for $\lambda = 350$ nm and 17 % at 400 nm. The APCE for these two electrodes as a function of irradiation wavelength and their corresponding absorption curves are presented in Figure 4.3c. These values represent an unprecedented photo-activity of ultra-thin hematite films, but are still slightly less than the APCE of the state-of-the-art Fe₂O₃ films (38 % at 350 nm and 32 % at 400 nm).² However, the thickness was not rigorously optimized, and since it is clear that the performance is quite sensitive to the film thickness, a film of ca. 8 – 10 nm could perhaps have a higher APCE. Nevertheless, the current goal is to understand the nature of the drastic change affected by the TEOS treatment to enable the future integration of ultra-thin Fe₂O₃ films to the host-scaffold/guest-absorber approach. Thus, to understand and characterize the influence of the substrate treatment on the film formation and properties, and to gain insight into what the requirements are for a thin film of iron oxide to operate as a water oxidation photocatalyst, the iron oxide films were subsequently subjected to further electrochemical, morphological, and crystallographic characterization.

4.3.4. Morphology and film growth

Figure 4.4b and 4.4c show the top-down SEM images of Samples C and D, while Figure 4.4a shows the surface of FTO before the iron oxide deposition (no difference was observed between the TEOS and untreated substrate in this case).

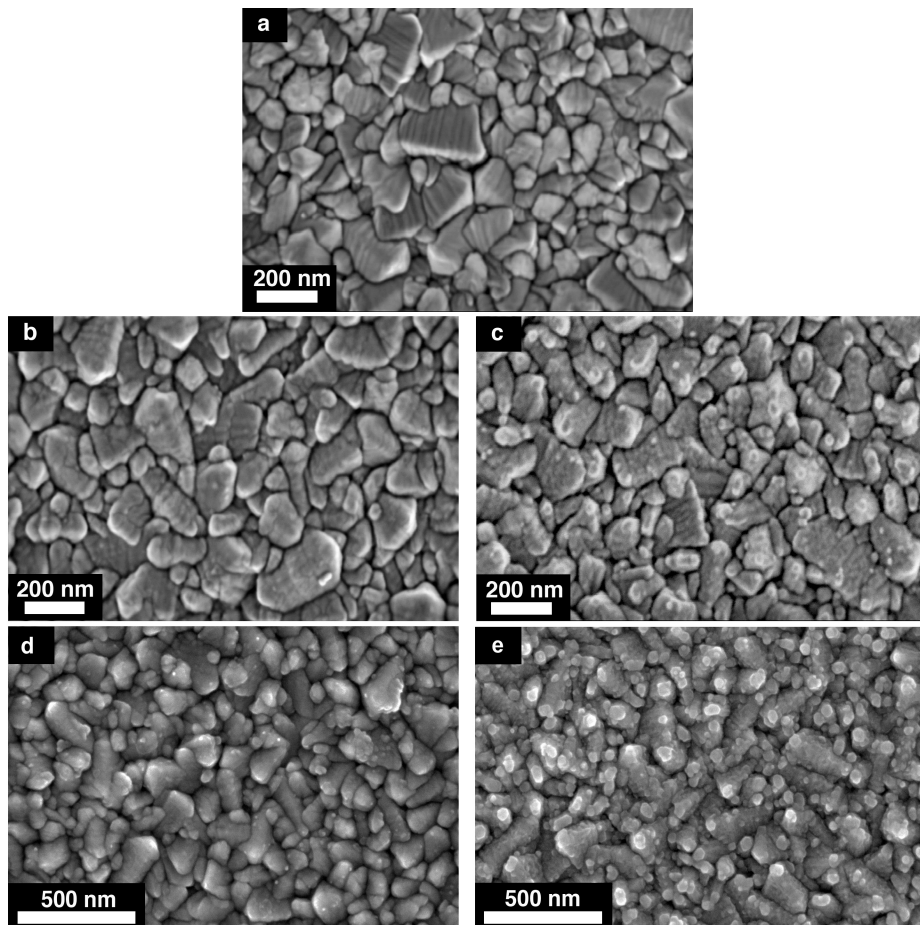


Figure 4.4: Top-down scanning electron micrographs of (a) the untreated FTO substrate before hematite deposition, (b) Sample C (c) Sample D, (d) Sample A and (e) Sample B. The beginning of island formation (Stranski-Krastanov) can be seen in (c) and (d).

The latter exhibits sharp, well-defined blocky crystal grains of SnO_2 30 – 300 nm in size and characterized by stripes clearly visible on the casserite crystal faces. These characteristic stripes have been observed by other groups and are perhaps due to crystal stacking faults.^{44,45} After the deposition of Fe_2O_3 on the control substrate, the roughness of the surface appears to increase dramatically with ca. 5 – 20 nm islands of iron oxide, which nucleate on both faces and edges of the FTO. The iron oxide can be clearly distinguished by the observed surface charging which appears as small white areas (spheres or dots on surfaces, and lines on edges) atop the SnO_2 crystallites. In sharp contrast, in the Fe_2O_3 film deposited on the SiO_x underlayer (Figure 4.4b), no clear iron oxide domains can be observed. The SnO_2 crystallites with their characteristic stripes are still visible, but the crystal edges appear softer—without the same sharpness seen in Figure 4a. This suggests a conformal coating of the Fe_2O_3 .

The considerable difference in the thin film morphology, induced by the SiO_x underlayer, can be explained by different nucleation and growth processes.⁴⁶ In the case of the control Sample D, the observed morphology is consistent with a Volmer-Weber (VW) type film growth. This growth type results in the formation of three-dimensional hematite clusters, or islands, due to the stronger interaction between adsorbed species (ad-species) compared with the interaction between an ad-species and the substrate. In the case of sample C, the uniform deposition is consistent with Franck-van der Merwe (FM) growth, *i.e.* ad-species attach preferentially to surface sites resulting in smooth, fully formed layers. However, upon the continued deposition of iron oxide (Sample A) we did observe clusters formation (See Figure 4.4d) suggesting that after a critical Fe_2O_3 film thickness, island formation commences (Stranski-Krastanov growth). The difference in ad-species interactions and film growth type is commonly explained by a difference in interfacial strain due to crystal lattice mismatch.⁴⁶

The voltages at which the water oxidation dark currents onset, $V_{\text{on,dark}}$, as observed in the current-voltage characterization (Figure 4.2 and Table 4.2), also agree with our suggested film formation modes. The onset of the dark current appears at lower potentials for the electrodes prepared on control substrates, especially for the thinner films (samples D and F) where 1.47 V was required to start water oxidation in the dark. The FTO substrate itself, with or without the SiO_x underlayer, shows an onset of the dark current at a similar potential of about 1.5 V vs. RHE with faster water oxidation kinetics (higher Tafel slope, not shown) than any of the iron oxide electrodes. In contrast, the dark current of the electrodes prepared on the SiO_x underlayer exhibit much higher onset potential with $V_{\text{on,dark}} = 1.56$ V vs. RHE for both Samples C and E. This suggests that the FTO is not fully covered in the case of Samples D and F while the FTO is completely covered with Fe_2O_3 in Samples C and E, as the lower conductivity of the Fe_2O_3 would delay the onset of the dark current only if no FTO was exposed to the electrolyte. According to the film growth hypothesis, as the film thickness of Fe_2O_3 increases, we would eventually expect (even in island growth mode) total coverage of the FTO and higher dark current onset potentials. Indeed, for samples A and B, $V_{\text{on,dark}} = 1.65$ and 1.60 V vs. RHE, respectively.

4.3.5. Crystallinity and photocurrent transients

The initial report, mentioning the effect of the TEOS treatment on 300 nm Fe_2O_3 films prepared by APCVD,¹⁸ suggested the effect was electronic in nature (the

SiO_x forming a metal-insulator-semiconductor junction), however the above results strongly point to another explanation. Based our proposed film growth differences, supported by both the SEM analysis and the dark current onset potentials, the SiO_x layer is reasonably acting as an amorphous buffer that reduces the interfacial strain between the SnO_2 and the Fe_2O_3 . The reduced interfacial strain would directly lead to better Fe_2O_3 film organization at an atomic level, and be observable by a difference in crystallinity. While the X-ray diffraction signal intensity is difficult to observe with the small amounts of material present on our ultra-thin films of Fe_2O_3 , Figure 4.5 shows a difference in crystallinity in samples C and D. Here the XRD spectra, acquired with an extremely slow scan rate to allow for sufficient detector response, are shown between $2\theta = 32^\circ$ and $2\theta = 37^\circ$. A main peak is observed centered on $2\theta = 33.8^\circ$ for both spectra. This peak corresponds to the (101) plane of the dense tin oxide conductive layer ($0.4 \mu\text{m}$, cassiterite) according to the standard SnO_2 XRD pattern (JCPDS No. 77-0452). The interesting feature appears at $2\theta = 35.8^\circ$ as a hump observable for the iron oxide deposited on the SiO_x underlayer substrate and not in the control case. This peak has been assigned to the (110) reflection (in hexagonal coordinates) of $\alpha\text{-Fe}_2\text{O}_3$ (hematite).¹⁸ Here, it appears very broad due to the large X-ray source aperture used to maximize detector response, but it nevertheless confirms the better organization and crystallinity of the iron oxide layer when deposited on TEOS treated FTO substrate.

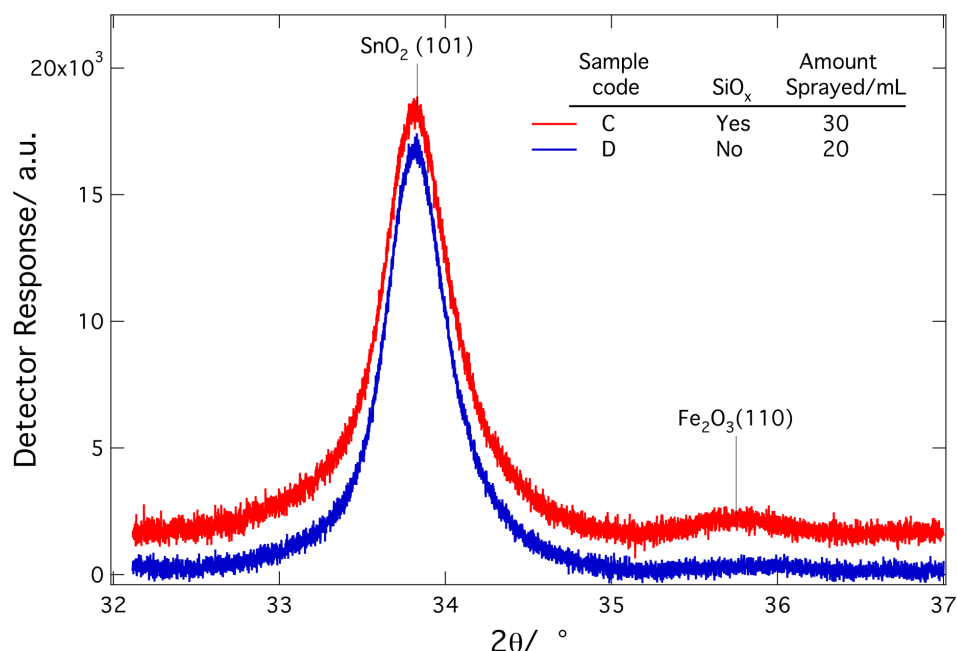


Figure 4.5 : X-ray diffraction pattern of Sample C (12.5 nm Fe_2O_3 on SiO_x/FTO , red line) and Sample D (12.5 nm Fe_2O_3 on bare FTO, blue line) between $2\theta = 32^\circ$ and 37° . The peak at $2\theta = 33.8^\circ$, associated with the (101) plane of SnO_2 has been used to normalized the two spectra. Reprinted from [1].

Further insight on the structure of the films can be gained from transient photocurrents generated by light chopping. The studies of iron oxide transient behavior already published have explained that light causes accumulation of charges at interfaces, especially holes at the semiconductor-liquid-junction (SCLJ) due to the slow reaction kinetics of the oxygen evolution reaction (OER).^{7,8,13} During the accumulation process, an anodic current spike is measured which decreases rapidly as the accumulated holes perturb the charge distribution in the space-charge layer. Eventually, a steady state between water oxidation and carrier recombination is attained which depends on the light intensity and the applied potential.¹³ When the light is turned off, the hole current stops and electrons flow to recombine with the accumulated holes; a cathodic transient spike is then observed. Figure 4.6 shows the results from light chopping experiment. The current densities, obtained while the voltage was swept from 0.6 to 1.8 V vs. RHE and light being chopped at regular intervals with a motor, showed transient behavior just after light was incident on the electrode (anodic transient) or blocked (cathodic transient). Due to the lack of perfect synchronization between the light chopping (performed with an externally controlled shutter) and the data acquisition, the precise time delay between the illumination switching and the following data point capture could not be controlled. This caused the observed transient amplitudes to erroneously appear to vary sinusoidally with

time. Nevertheless, a qualitative comparison of the transients provides interesting information. Samples C and D exhibit both cathodic and anodic transient behavior up to 1.4 V for C and 1.6 V for D (Figure 4.6a). We observe the same phenomenon with the thicker Samples A and B (Figure 4.6b). Here the sample A showed transient behavior until 1.35 V whereas sample B showed transients until 1.55 V bias.

In addition to accumulating at the SCLJ due to slow water oxidation kinetics, photo-generated holes can oxidize trap states in the bulk⁹ and on the surface⁸ to result in similar transient current spikes. It has been suggested that the transient behavior depends strongly on the density and energy of these trapping states which are a result of reduced crystalline quality of the surface,^{7,8} and the presence of other iron oxide phases (e.g. Fe₃O₄ or γ-Fe₂O₃).⁷ Therefore, the lower potential disappearance of the transients in Sample C implies that surface recombination decrease at lower potential as compared to the control case, possibly due to a smaller density of trapping states on the surface. In light of the XRD results, this reasonably comes from increased crystalline order. This trend is also observable for the thicker films but the transient disappearance potential is shifted cathodically in the control case (Sample B) probably due to the fact that a thicker layer implies increased crystallinity in films exhibiting VW-type film growth as more of the iron oxide is sufficiently distanced from the strain and disorder inducing substrate/film interface.

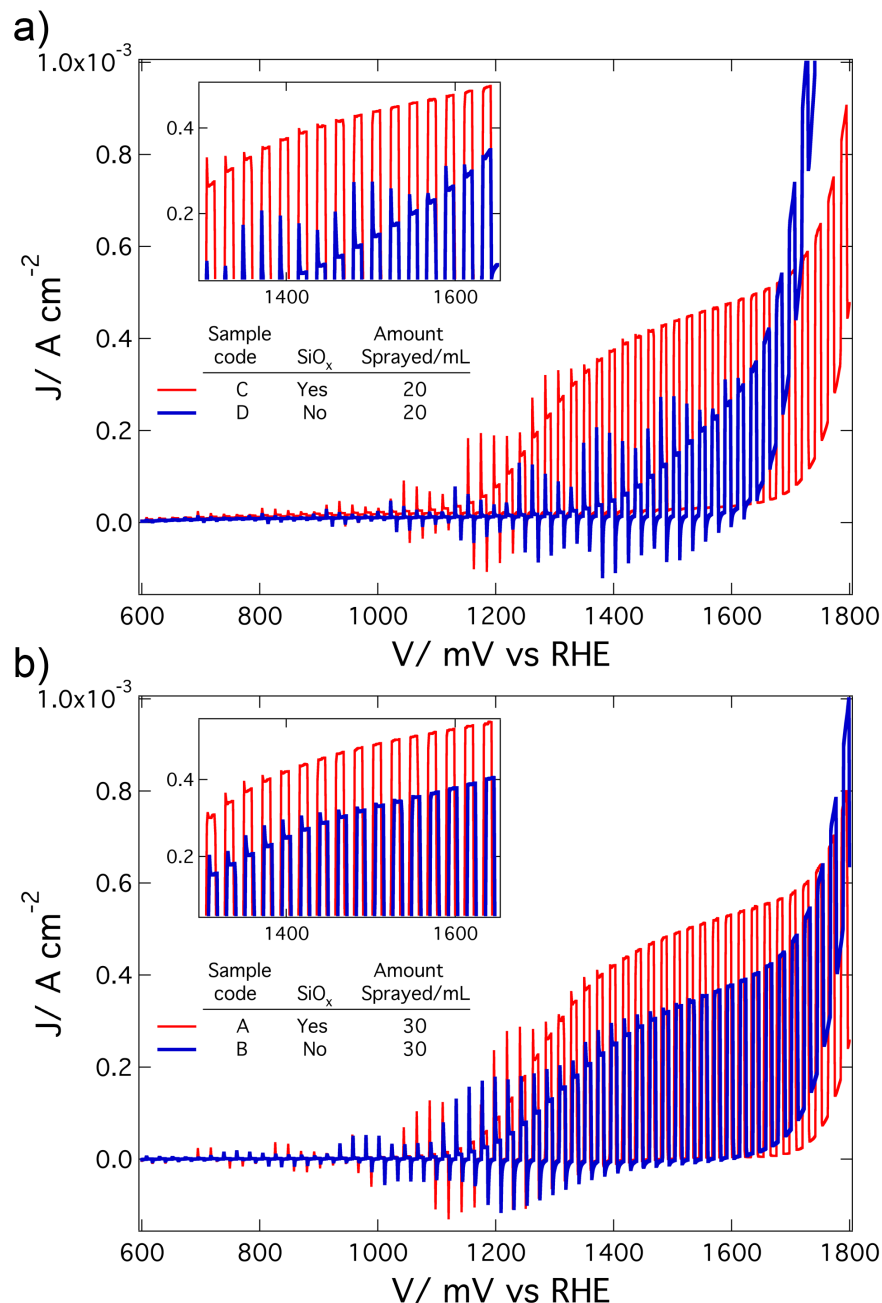


Figure 4.6: Transient photo-response shown by light chopping current densities J (light on/light off) as a function of the applied potential V , with respect to the reversible hydrogen electrode (RHE). Comparison of the transient behavior of iron oxide photoanodes using a SiO_x/FTO substrate (red, thin line) and a control FTO substrate (blue, thick line) for the (a) 12.5 nm (C and D) and the (b) 22 nm Fe_2O_3 films (A and B). Inset graphs show magnified views of the 1300–1650 mV region for both spectra. Reprinted from [1].

While the initial report of the inactivity of ultra-thin films of hematite suggested an electron cloud of the fluorine-doped SnO_2 extended into the Fe_2O_3 film and increased recombination,²¹ and a supposed effect of the TEOS treatment was electronic in nature (the SiO_x forming a metal-insulator-semiconductor junction),¹⁸ the results presented here strongly suggest the effect is rather due to the impact of the

surface treatment on the growth mode and crystallography of the iron oxide films. However, this change also affects the electronic interface between hematite and the FTO substrate: increased crystallinity of the iron oxide at the interface would lead to less recombination there. This explanation would account for the difference the TEOS treatment affects even on thick films of hematite.⁴⁷ However, we are unable to completely rule out any electronic effects arising from electronic issues not related to crystallinity. For example, The TEOS treatment could reduce the concentration of recombination-inducing oxygen vacancies at the interface, or the SiO_x layer could still be acting as electronically insulating layer resulting in an effect on the depletion layer formed at the interface between iron oxide and FTO. While our results point to only a monolayer of SiO_x , making the latter explanation unlikely, it could be tested by modifying the depletion layer through the addition of extra electronic charges carriers into hematite by doping with Si, Nb or Ti for example.

4.4. Conclusion

In this study, a clear improvement of photoactivity in ultra-thin hematite films for solar water-splitting has been demonstrated using a pretreatment of the FTO/glass substrate. A hematite electrode prepared by the spray pyrolysis of $\text{Fe}(\text{acac})_3$ on a pretreated substrate, with an amount of Fe_2O_3 equivalent to a 12.5 nm conformal layer (and absorbing only 25% of the incident light at its absorbance maximum, $\lambda_{max} = 400$ nm) exhibited a photo-current onset potential at 1.07 V vs. RHE and a plateau current of 0.55 mA cm^{-2} at 1.43 V vs. RHE, with 30% APCE at 350 nm at 1.43 V. In contrast, almost no photo-activity was observed for the photoanode with the same amount of hematite on an untreated FTO substrate. This pretreatment, consisting of spraying TEOS at high temperature on the substrate surface, was shown to result in the formation of approximately a monolayer of SiO_x on the FTO. The iron oxide thin films, analyzed by XRD and transient photocurrents, showed a better crystallinity and less trapping states when sprayed onto a TEOS pretreated substrate. The morphological analysis of these thin films suggests that the difference is due to separate film formation processes: a Franck-van der Merwe growth (full layer covering the substrate) on SiO_x modified substrate against a Volmer-Weber growth mode (island formation) on bare FTO substrate. This difference reasonably results from a difference in surface energy, perhaps due to the amorphous SiO_x layer acting as a lattice strain buffer.

With these results we can conclude that the crystalline organization as affected by the film nucleation and growth, is a critical parameter for the photo-activity of ultra-thin hematite films. This study has significantly contributed to a better understanding of the role of iron oxide crystallinity and hematite surface quality on the photo-activity of this promising material for solar energy conversion and storage as hydrogen. Importantly, we can further conclude that it is unlikely an intrinsic limitation exists with hematite ultra-thin films, as previously suggested.²¹ As such, the further study of very thin film electrodes of hematite including doping and other under-layers would be interesting in order to successfully realize this material in a host-scaffold/guest-absorber approach. Finally, the TEOS treatment will also find further application in similarly-prepared interfaces like those used for quantum-dot,⁴⁸ solid-state bulk heterojunction,⁴⁹ and ETA-type⁵⁰ solar energy conversion devices.

4.5. References

- (1) Le Formal, F.; Graetzel, M.; Sivula, K. *Adv Funct Mater* **2010**, *20*, 1099.
- (2) Cesar, I.; Sivula, K.; Kay, A.; Zboril, R.; Grätzel, M. *J. Phys. Chem. C* **2009**, *113*, 772.
- (3) Hardee, K.; Bard, A. *J Electrochem Soc* **1976**, *123*, 1024.
- (4) Kennedy, J.; Frese, K. *J Electrochem Soc* **1978**, *125*, 723.
- (5) Shinar, R.; Kennedy, J. *J Electrochem Soc* **1983**, *130*, 392.
- (6) Kennedy, J.; Frese, K. *J Electrochem Soc* **1978**, *125*, 709.
- (7) Iwanski, P.; Curran, J.; Gissler, W.; Memming, R. *J Electrochem Soc* **1981**, *128*, 2128.
- (8) Dare-Edwards, M.; Goodenough, J.; Hamnett, A.; Trevellick, P. *J Chem Soc Farad T 1* **1983**, *79*, 2027.
- (9) Horowitz, G. In *J Electroanal Chem* 1983; Vol. 159, p 421.
- (10) Joly, A.; Williams, J.; Chambers, S.; Xiong, G.; Hess, W.; Laman, D. *J Appl Phys* **2006**, *99*, 053521.
- (11) Cherepy, N.; Liston, D.; Lovejoy, J.; Deng, H.; Zhang, J. *J Phys Chem B* **1998**, *102*, 770.
- (12) Bosman, A.; Vandaal, H. *Adv Phys* **1970**, *19*, 1.
- (13) Sanchez, C.; Sieber, K.; Somorjai, G. *J Electroanal Chem* **1988**, *252*, 269.
- (14) Hu, Y.-S.; Kleiman-Shwarsctein, A.; Forman, A. J.; Hazen, D.; Park, J.-N.; McFarland, E. W. *Chem Mater* **2008**, *20*, 3803.

- (15) Mohapatra, S. K.; John, S. E.; Banerjee, S.; Misra, M. *Chem Mater* **2009**, *21*, 3048.
- (16) Duret, A.; Gratzel, M. *J Phys Chem B* **2005**, *109*, 17184.
- (17) Van De Krol, R.; Liang, Y.; Schoonman, J. *J. Mater. Chem.* **2008**, *18*, 2311.
- (18) Kay, A.; Cesar, I.; Graetzel, M. *J Am Chem Soc* **2006**, *128*, 15714.
- (19) Murphy, A. B.; Barnes, P. R. F.; Randeniya, L. K.; Plumb, I. C.; Grey, I. E.; Horne, M. D.; Glasscock, J. A. *Int J Hydrogen Energ* **2006**, *31*, 1999.
- (20) Sivula, K.; Le Formal, F.; Graetzel, M. *Chem Mater* **2009**, *21*, 2862.
- (21) Itoh, K.; Bockris, J. *J Appl Phys* **1984**, *56*, 874.
- (22) Seaman, C. *Sol Energy* **1982**, *29*, 291.
- (23) Rothenberger, G.; Comte, P.; Gratzel, M. *Sol Energ Mat Sol C* **1999**, *58*, 321.
- (24) Tejedor-Tejedor, M.; Paredes, L.; Anderson, M. *Chem Mater* **1998**, *10*, 3410.
- (25) Jurgens-Kowal, T.; Rogers, J. *J Phys Chem B* **1998**, *102*, 2193.
- (26) Ferguson, J.; Smith, E.; Weimer, A.; George, S. *J Electrochem Soc* **2004**, *151*, G528.
- (27) Shanthi, S.; Subramanian, C.; Ramasamy, P. *Cryst Res Technol* **1999**, *34*, 1037.
- (28) Kim, E.; Gill, W. *J Electrochem Soc* **1995**, *142*, 676.
- (29) Ivanov, M.; Kupryashkina, T.; Kompaniets, V.; Kopteva, M.; Konoplev, A. *J Appl Chem-Ussr+* **1985**, *58*, 1691.
- (30) Vamvakas, V.; Davazoglou, D. *J Electrochem Soc* **2004**, *151*, F93.
- (31) Bjorkman, C.; Yamazaki, T.; Miyazaki, S.; Hirose, M. *J Appl Phys* **1995**, *77*, 313.
- (32) Mondragon, M.; Castano, V.; Garcia, J.; Tellez, C. *Vib Spectrosc* **1995**, *9*, 293.
- (33) Crowell, J.; Tedder, L.; Cho, H.; Cascarano, F.; Logan, M. *J Vac Sci Technol A* **1990**, *8*, 1864.
- (34) Stefanescu, M.; Stoia, M.; Stefanescu, O.; Popa, A.; Simon, M.; Ionescu, C. *J Therm Anal Calorim* **2007**, *88*, 19.
- (35) Berreman, D. *Phys Rev* **1963**, *130*, 2193.
- (36) Kirk, C. *Phys Rev B* **1988**, *38*, 1255.
- (37) Olsen, J.; Shimura, F. *Appl. Phys. Lett.* **1988**, *53*, 1934.
- (38) Martinez, A. I.; Huerta, L.; de Leon, J. M. O.-R.; Acosta, D.; Malik, O.; Aguilar, M. *J Phys D Appl Phys* **2006**, *39*, 5091.
- (39) Lavallee, J. *Catal Today* **1996**, *27*, 377.
- (40) Sartoretti, C.; Alexander, B.; Solaraska, R.; Rutkowska, W.; Augustynski, J.; Cerny, R. *J Phys Chem B* **2005**, *109*, 13685.

Chapter 4

- (41) Liang, Y.; Enache, C. S.; Van De Krol, R. *Int J Photoenergy* **2008**, 739864.
- (42) Marusak, L.; Messier, R.; White, W. *J Phys Chem Solids* **1980**, *41*, 981.
- (43) Kumari, S.; Singh, A. P.; Tripathi, C.; Chauhan, D.; Dass, S.; Shrivastav, R.; Gupta, V.; Sreenivas, K.; Satsangi, V. R. *Int J Photoenergy* **2007**, *2007*, 1.
- (44) Paraguay-Delgado, F.; Miki-Yoshida, M.; Antunez, W.; Gonzalez-Hernandez, J.; Vorobiev, Y. V.; Prokhorov, E. *Thin Solid Films* **2008**, *516*, 1104.
- (45) Lee, S.; Park, B. *Thin Solid Films* **2006**, *510*, 154.
- (46) Venables, J.; Spiller, G.; Hanbucken, M. *Rep Prog Phys* **1984**, *47*, 399.
- (47) Cesar, I.; Kay, A.; Martinez, J.; Gratzel, M. *J Am Chem Soc* **2006**, *128*, 4582.
- (48) Feng, J.; Han, J.; Zhao, X. *Prog Org Coat* **2009**, *64*, 268.
- (49) Nanu, M.; Schoonman, J.; Goossens, A. *Nano Lett.* **2005**, *5*, 1716.
- (50) Levy-Clement, C.; Tena-Zaera, R.; Ryan, M.; Katty, A.; Hodes, G. *Adv. Mater.* **2005**, *17*, 1512.

CHAPTER 5.

EFFECT OF PLASMONIC NANOPARTICLES ON THE PHOTOACTIVITY OF HEMATITE PHOTOANODES

This chapter has been published as E. Thimsen, F. Le Formal, M. Grätzel, S.C. Warren, *Nano Lett.* **2011**, *11*, 35.¹

In this chapter, another strategy to enhance the photoactivity of iron oxide thin films has been pursued. It consists of increasing the absorption of the light in proximity to the semiconductor-liquid junction, using plasmonic nanoparticles. In the following, an experimental study of the influence of gold nanoparticles on $\alpha\text{-Fe}_2\text{O}_3$ photoanodes for photoelectrochemical water splitting is described. Two different configurations were tested: in the first one the metal particles were embedded in a hematite thin film and for the second they were deposited on the surface of a nanostructured photoanode. A relative enhancement in the water splitting efficiency at photon frequencies corresponding to the plasmon resonance in gold was observed. This relative enhancement was observed only for electrode geometries with metal particles that were localized at the electrode surface, consistent with the observation that minority carrier transport to the electrolyte is the most significant impediment to achieving high efficiencies in this system. The embedded configuration did not show any photoelectrochemical improvement due to the poor overlap between the hematite absorption and the plasmonic resonance caused by the red-shift of the gold nanoparticle response when embedded in hematite.

5.1. Introduction

As shown in the second chapter, a significant limitation in $\alpha\text{-Fe}_2\text{O}_3$ photoanode is the short diffusion length of holes. Moreover, as a consequence of the heavy doping required for electron conduction, the space charge layer near the electrolyte interface is very short, approximately 5 – 10 nm.² Consequently, it is desirable to absorb all of the incoming photons within the space charge layer of the semiconductor, as holes photogenerated in this region are primarily responsible for the water oxidation reaction, or photocurrent.³

This is a challenge because the absorption depth of near-band-gap photons in hematite is large (over 100 nm), much larger than the diffusion distance.⁴ Chapter 4 showed that control and enhancement of the hematite thin films was achievable with using a buffer layer at the semiconductor / substrate interface. In this chapter an alternative strategy is presented. This new approach consists in modifying the material to localize photon absorption at the semiconductor surface, and therefore in the space charge layer, through the use of the localized surface plasmon-induced near-field enhancement.⁵⁻⁷ Surface-localized photon absorption can be accomplished through incorporation of plasmonic metal nanoparticles into the semiconductor electrode.

There are four design considerations that must be addressed when selecting a target system that exploits localized surface plasmon effects for enhanced photoelectrochemical performance. The first is evaluation of the semiconductor (i.e. $\alpha\text{-Fe}_2\text{O}_3$) to determine whether it has inadequate light absorption and can therefore benefit from plasmon enhancement. Second, resonant coupling between the plasmonic metal nanoparticles and semiconductor must be considered, to ensure that energy transfer between the metal and semiconductor is an efficient process. The third consideration is difficult to know *a priori*, but contact between the metal and semiconductor can result in the formation of trap states at the interface, which promote recombination and Fermi level pinning. The fourth consideration is the work function of the metal and the corresponding Schottky barrier formed by the semiconductor-metal nanoparticle interface, which determines the maximum photovoltage achievable.⁸

Semiconductors with inadequate light absorption are good candidates for plasmon enhancement. Inadequate light absorption in this context has two meanings. It can mean that the overall light absorption is low, which for example would be the case for a film with a thickness less than the absorption depth. It can also mean that

photons are not absorbed in the desired location (*e.g.* being absorbed primarily in the bulk instead of in the space charge layer at the semiconductor/electrolyte interface). In the case of low overall light absorption, plasmonic metal nanoparticles can be used to capture the light that would simply pass through the thin film if the particles were not there. In the case where the photons are not absorbed in the desired location, the metal nanoparticles can be used to absorb photons and then transfer the energy to an adjacent semiconductor. In both cases, it is critical that the metal nanoparticle be energetically coupled to the semiconductor, in order to transfer its excitation energy and produce an electron-hole pair in the semiconductor instead of allowing the localized surface plasmon to decay to phonons.

In general, it is known that surface plasmons can excite semiconductors, and semiconductors can excite surface plasmons.⁹ To move forward with design and synthesis, a working hypothesis was developed, that resonant energy transfer occurs when the oscillator frequencies of a localized surface plasmon and semiconductor overlap. A localized surface plasmon is a collective oscillation of free electrons, typically in a metal, which for particles much smaller than the photon wavelength can be modeled as a dipole oscillator.^{10,11} The localized surface plasmon resonance frequency is a function of the size-dependent dielectric function,¹² inter-particle spacing,¹³ particle shape¹⁴ and dielectric medium in which it is embedded.¹² Au is an attractive metal that has a localized surface plasmon resonance in the visible portion of the electromagnetic spectrum.¹¹ Upon absorption of a photon at the plasmon resonance frequency, coherent oscillations in the free electrons are induced, and therefore a large alternating electric field near the metal nanoparticle is established. For semiconductors, the classical model of photon absorption is also an oscillator.¹⁵ For the oscillator in the metal (localized surface plasmon) to couple with the oscillator in the semiconductor to generate an electron-hole pair, the resonant frequencies must be the same. Within this framework, it is instructive to think about the metal nanoparticle as an antenna that absorbs the light, and the semiconductor as a reaction center that promotes the photochemistry (*i.e.* water oxidation). Thus, to determine if energetic coupling can be expected, the plasmon resonance as measured in the photon absorption spectrum of the metal nanoparticle (*i.e.* Au) can be compared to the measured photon absorption spectrum of the semiconductor (*i.e.* $\alpha\text{-Fe}_2\text{O}_3$) to assess the spectral overlap of the two oscillator frequencies.

It should be noted that the measured photon absorption spectrum of metal nanoparticles contains components from excitation of surface plasmons and

interband transitions. For Au, interband transitions partially overlap with the plasmon resonance¹⁶ at wavelengths less than 600 nm,¹⁷ and dominate for wavelengths less than 400 nm, while the local surface plasmon absorbance dominates for wavelengths longer than 520 nm. The absorbance in the wavelength range from 400 nm to 600 nm contains contributions from both interband transitions and surface plasmon excitation (see Appendix A).

The degree to which energetic coupling between the metal and semiconductor occurs is also a function of distance. The electric field near the metal nanoparticle can be strongly enhanced, but it decays rapidly with increasing distance from the metal surface.^{5,6} For Ag metal nanoparticles coated with TiO₂ and Ru-based N3 dye molecules, it was observed that when the photoactive dye molecules were separated from the metal nanoparticle by 2.0 to 4.8 nm of TiO₂, the short-circuit photocurrent enhancement decreased from 6 to 1, indicating no effect when the photoactive dye was separated from the metal by more than 5 nm of TiO₂.⁶ While the distance dependence is likely material dependent, the enhanced near-field in the semiconductor is only expected over a relatively short distance away from the metal.

The third design consideration is the formation of surface states at the metal/semiconductor interface that can create new pathways for recombination, therefore lowering overall performance.¹⁸ These defect states are strongly dependent on the interface and difficult to predict, but one must be aware of their effect to interpret results.

The fourth design criterion relates to the Schottky barrier formed between the semiconductor and metal nanoparticles.⁸ When in contact with a semiconductor, metal nanoparticles larger than 10 nm develop a Schottky barrier that is identical to a macroscopic metal-semiconductor contact. The height of the Schottky barrier determines the majority carrier current that flows from the semiconductor conduction band into the metal and, subsequently, the electrolyte.¹⁹ It is often observed in semiconductor-metal-electrolyte systems that the Schottky barrier at the metal-semiconductor interface is lower than that at the electrolyte-semiconductor interface; this is often caused by a high concentration of surface states at the metal-semiconductor interface that results in Fermi level pinning.²⁰ Because the basis of the photovoltaic effect at semiconductor junctions is the separation of electrons from holes, the greatly increased majority carrier dark current decreases the open-circuit photovoltage. Therefore, an important design criterion for such systems is to develop an electrode architecture that maximizes the metal-semiconductor barrier height.

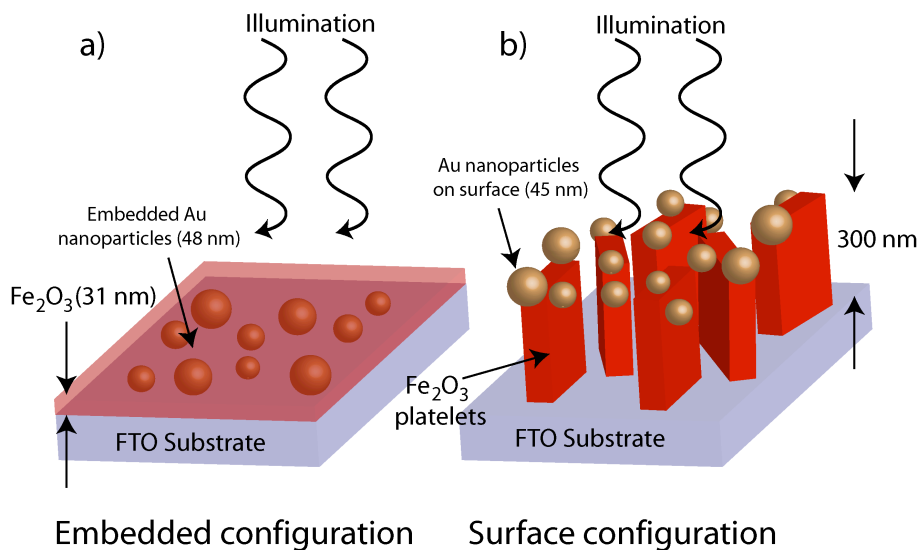


Figure 5.1: Different electrode configurations. (a) Embedded and (b) surface. The electrolyte, counter electrode and reference electrode are omitted for clarity. Reprinted from [1].

This may be achieved, for example, by using small (< 10 nm) nanoparticles, which have a higher Schottky barrier than larger particles,⁸ or by electronically isolating the metal with a thin insulating shell.

For this study, hematite α -Fe₂O₃ photoanodes incorporating Au nanoparticles with two different configurations were synthesized on F:SnO₂ FTO substrates and tested for photoelectrochemical water splitting performance. The two different configurations are illustrated in Figure 5.1, denoted "embedded" and "surface". For the embedded configuration, Au nanoparticles were first deposited by a flame aerosol reactor onto FTO,²¹ followed by a deposition of an ultra-thin compact α -Fe₂O₃ film by spray pyrolysis.²² For the surface configuration, a silicon-doped nanoplatelet α -Fe₂O₃ film was first deposited by ultrasonic spray pyrolysis,²³ followed by Au nanoparticle deposition by a flame aerosol reactor or by electrophoretic deposition of citrate-stabilized 15-nm nanoparticles (see Appendix A). Samples with Au nanoparticles were compared to Fe₂O₃-only samples as controls.

5.2. Experimental

5.2.1. Gold nanoparticle preparation and deposition

Au nanoparticles were synthesized and deposited in a single step using a premixed flame aerosol reactor (FLAR), adapted from a system described in detail elsewhere.^{21,24} The flame was generated by combustion of methane and oxygen. The combustion gas flow rates were 0.63 liters per minute (lpm) and 1.5 lpm for methane and oxygen respectively. The Au nanoparticles were generated via thermal

decomposition of gold chloride (HAuCl_4). A commercial Collison modified 1-jet modified MRE type nebulizer (BGI Instruments) was used to feed the HAuCl_4 into the flame as an aerosol. The spray solution was 13×10^{-3} M HAuCl_4 in ethanol ($\geq 99.8\%$ Fluka), and the carrier gas was argon that was supplied to the nebulizer at a pressure of 3 bar. The burner was a single stainless steel nozzle with an outlet area of approximately 0.08 cm^2 . The deposition substrate, either FTO (TEC 15, Pilkington Glass) for the embedded configuration, or nanoplatelet silicon-doped $\alpha\text{-Fe}_2\text{O}_3$ on FTO for the surface configuration, was placed onto a stainless steel, water-cooled substrate holder using a small amount of thermal paste (Arctic Silver 5, Arctic Silver Inc), and then suspended in the flame perpendicular to the flow direction at a controlled distance. The substrate was maintained at a lower temperature than the hot aerosol stream passing over it, and due to the thermal gradient between the hot gas and cold substrate, the Au nanoparticles were deposited by thermophoresis. The deposition time and burner-substrate distance for the embedded configuration was 4 min and 14 cm, while for the surface configuration it was 15 min and 16 cm. After deposition, the Au nanoparticles were imaged by scanning electron microscopy in an FEI XLF30 field-emitting scanning electron microscope (SEM) operating at an accelerating voltage of 15 kV. The particle size distribution was determined by first measuring the projected area of the particles using the Image J software package, then calculating the circle-equivalent diameter of each size bin, and finally fitting a log-normal curve to determine the distribution parameters.

Au nanoparticles were also prepared by citrate reduction of HAuCl_4 and electrophoretically deposited onto silicon doped Fe_2O_3 platelet electrodes. The procedure and results are in Appendix A. Unless otherwise stated, the main text contains results for flame-synthesized Au nanoparticles.

5.2.2. Hematite ultra thin film deposition by spray pyrolysis

For the embedded configuration, ultra-thin, compact pristine Fe_2O_3 films were synthesized by spray pyrolysis using iron (III) acetylacetone as the iron precursor. The spray setup, described in detail in Chapter 4,²² consisted of an ultrasonic spray head (Lechler company, US1 30°) set 30 cm over the substrates, which were placed on a hot plate heated to 550 °C (corresponding to a measured substrate surface temperature of 400 °C). An automatic syringe pump was used to deliver 1mL of a solution containing 10mM of $\text{Fe}(\text{acac})_3$ (99.9+%, Aldrich) in ethanol to the spray head every 30 seconds at a liquid feed rate of 12 mL min^{-1} (spray pulse duration of 5 seconds). The total volume of solution sprayed was 30 ml. Compressed air was used

as the carrier gas and the flow was set to 15 L min⁻¹. After spraying, the samples were annealed in-situ for 5 min at *ca.* 450°C before cooling to room temperature. The resulting Fe₂O₃ film was 31 nm in optical thickness as measured by ultraviolet-visible (UV-visible) absorption spectroscopy, assuming an absorption coefficient of 0.0135 nm⁻¹ at a photon wavelength of 500 nm.²

5.2.3. Hematite nanoplatelets deposition

For the surface configuration, silicon-doped α-Fe₂O₃ nanoplatelet films were synthesized by ultra-sonic spray pyrolysis (USP), which is described in detail in an earlier report from Duret *et al.*²³ The USP samples were prepared by the following procedure: the FTO substrates (3 cm x 9 cm) were sonicated in deionized water for several hours to clean the glass. The substrate was dried under a stream of compressed air and placed on a 3 cm x 9 cm heater. The substrate and heater were inserted into a glass tube (diameter = 5 cm). The glass tube was thermally insulated and open at both ends. A 20 mM Fe(acac)₃ (99.9%, Sigma Aldrich) solution in methanol was prepared; 0.15 mM tetramethylorthosilicate (TMOS) was added as a source of silicon dopant. The substrates were heated to 540 °C and allowed to equilibrate for 1 hour prior to deposition. The Fe(acac)₃ solution was fed into an ultrasonic sprayer at a rate of 0.23 g/min. Air was fed into the sprayer at a flow rate of 20 L/min. Droplets were sprayed vertically downwards into a 250 ml jar and a small proportion was collected at a right angle through a 1 cm circular opening in the side, with the remainder of the droplets impacting on the bottom of the jar. The droplets were then carried though the tube, over the FTO substrates. The deposition time was 8 hours, resulting in a 300 nm film with a silicon content of 3% as determined by SEM and X-ray energy dispersion spectroscopy (X-EDS). The resulting films were translucent red in appearance.

5.2.4. Photoelectrochemical characterization

Photocurrent measurements were performed to estimate the solar photocurrent of the photoanodes in a three-electrode configuration with 1 M NaOH (pH 13.6) as electrolyte and an Ag/AgCl reference electrode. The hematite electrode was scanned at 50 mV sec⁻¹ between 300 and 800 mV vs. Ag/AgCl. The measured electrode potential referenced to Ag/AgCl was converted to be referenced to the reversible hydrogen electrode (RHE) at pH 13.6 using the Nernst equation, shown in Chapter 1. The samples were illuminated with simulated sunlight from a 450 W xenon lamp (Osram, ozone free) using a KG3 filter (3 mm, Schott). Spectral

mismatch factors to estimate the difference of the electrode photoresponse obtained from simulated sun light and real sun light at AM 1.5 G were calculated according to the method described by Seaman et al.²⁵ Photocurrent action spectra were obtained by illuminating the sample under light from a 300 W xenon lamp integrated parabolic reflector (Cermax PE 300 BUV) passing through a monochromator (Bausch & Lomb, bandwidth 10 nm FWHM). The incident photon-to-current conversion efficiency (IPCE) was obtained by dividing the measured current at each wavelength by the photon flux, which was determined using a calibrated silicon photodiode. IPCE experiments were performed in triplicate on similar samples to ensure reproducibility. The UV-Visible absorbance spectra were measured by transmission measurements in a diode array spectrometer (8452A, Hewlett Packard) using a clean FTO substrate as the blank.

Open circuit photovoltage measurements were performed using the unfiltered output of the 450 W xenon lamp with an above-band gap photon flux ($\lambda < 600$ nm) that was 2.5 times higher than AM 1.5 with a significantly greater proportion of the photons in the UV than the AM 1.5 spectrum. The electrolyte was 1 M NaOH. A three-electrode setup as described above was used. The working electrode was exposed to the electrolyte through a small window such that the entire area of the sample exposed to the electrolyte was also irradiated by the xenon lamp. The change in the hematite working electrode potential was monitored during low-frequency light chopping (< 0.001 Hz) while maintaining open circuit conditions.

5.3. Results and discussion

5.3.1. Morphological and optical properties

The SEM images and resulting size distributions for the Au nanoparticles in the embedded and surface configurations are presented in Figure 5.2. For the embedded configuration, the geometric mean was 48 nm and the geometric standard deviation was 1.28. For the surface configuration, the geometric mean was 45 nm and the geometric standard deviation was 1.59.

In both the embedded and surface configurations, the Au nanoparticles exhibited plasmonic behavior and increased the UV-visible light absorbance of the electrodes. The UV-visible absorbance spectra for the different configurations is presented in Figure 5.3. The spectra of the pristine Au nanoparticles on FTO and the Fe₂O₃-only are included as controls. When deposited on the FTO substrate with no Fe₂O₃, the Au nanoparticles exhibited a prominent peak in the absorbance spectrum

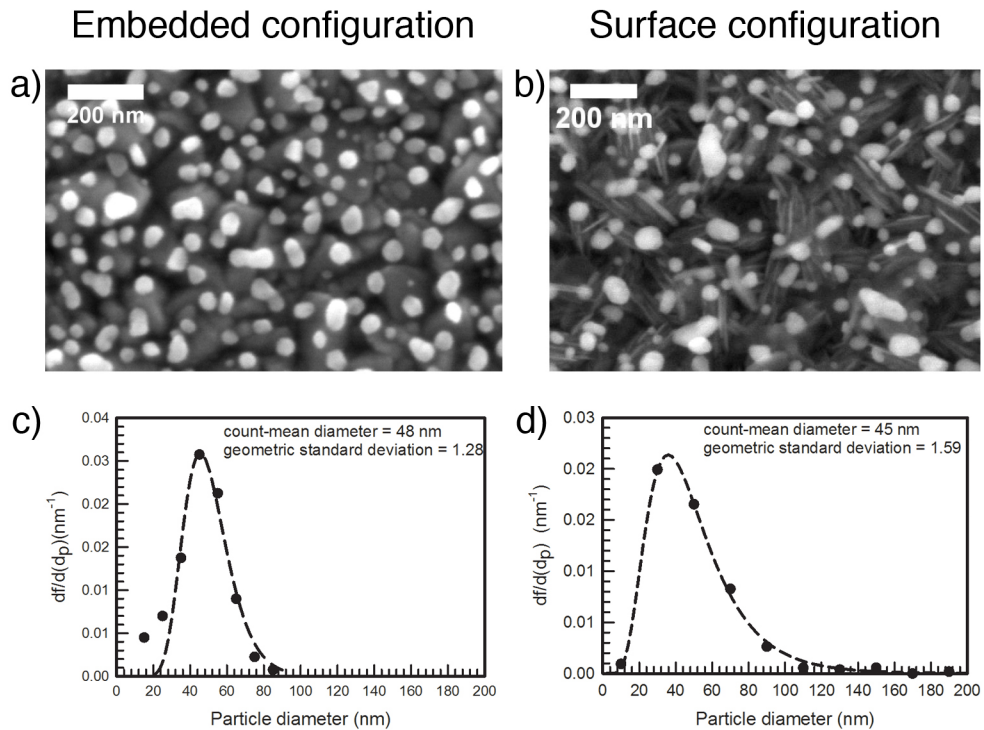


Figure 5.2: Top view SEM images of the Au particles used for the embedded configuration before Fe_2O_3 deposition (a) and on the Fe_2O_3 platelets used for the surface configuration (b). Size distribution of the particles used for the embedded configuration (c) and the surface configuration (d) Reprinted from [1].

at 560 nm, which corresponds to surface plasmon resonance. For Au nanoparticles, it is known that the frequency of interband transitions overlaps with the plasmon resonance.¹⁶ The contribution of interband excitations was calculated by estimating the contribution to the absorbance of the interband component of the dielectric function, as described in the Appendix A. The localized surface plasmon resonance dominated the absorbance at wavelengths greater than 465 nm, with a tail extending to 400 nm; while the interband transition component was larger for wavelengths less than 465 nm (Figure A1). After Fe_2O_3 deposition, in the embedded configuration, the plasmon absorbance red-shifted to approximately 670 nm, which is the expected absorbance maximum for Au particles of 48 nm embedded in Fe_2O_3 assuming dipole oscillator behavior, considering that the dielectric function of $\alpha\text{-Fe}_2\text{O}_3$ at 700 nm is 7.2,²⁶ and the size dependent dielectric function of 48 nm Au nanoparticles reaches -14.4 at 670 nm.^{12,27} When the Au nanoparticles were deposited on the surface of the silicon-doped $\alpha\text{-Fe}_2\text{O}_3$ platelets, no significant red-shift in the plasmon resonance was observed.

There are two consequences of the spectral behavior. First, the large red-shift and increase in absorbance for the plasmon resonance in the embedded

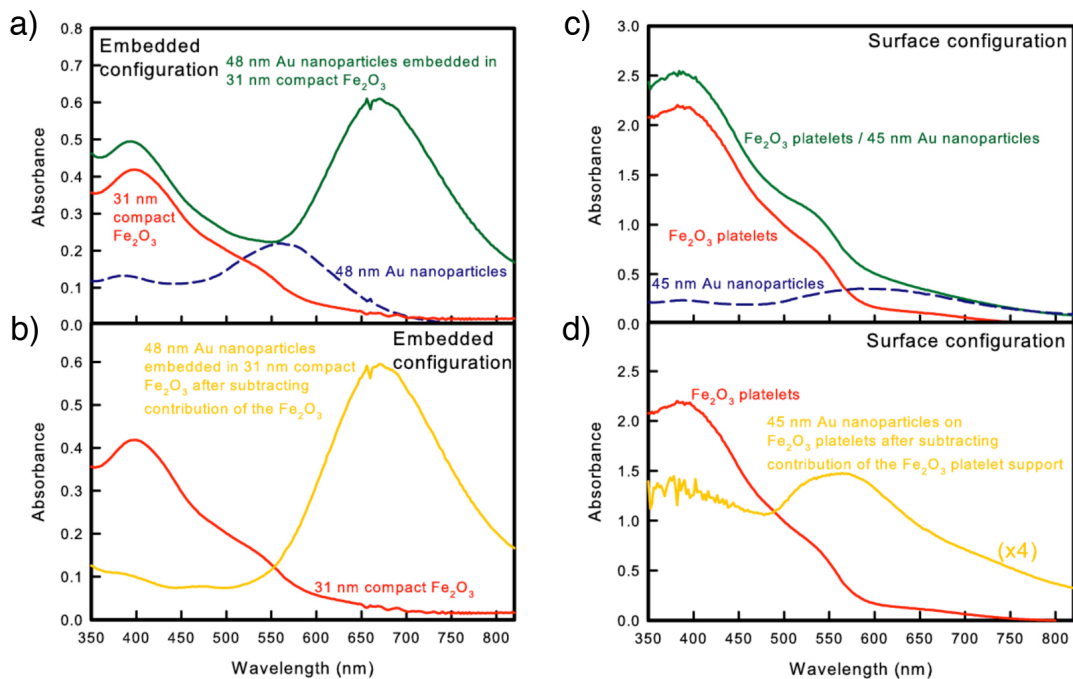


Figure 5.3: Absorbance spectra for the different electrodes: a) as-measured absorbance data for the embedded configuration; b) comparison of the spectral overlap between Au nanoparticle plasmon resonance and compact Fe₂O₃ absorbance for the embedded configuration; c) as-measured absorbance data for the surface configuration; d) comparison of the spectral overlap between the Au nanoparticle plasmon resonance and Fe₂O₃ platelet absorbance. Reprinted from [1].

configuration suggests a greater interaction than in the surface configuration, which is reasonable considering the larger interfacial area between the semiconductor and metal. The second consequence is the spectral overlap. It can be seen from Figure 5.3 that in the embedded configuration, the peak plasmon resonance was at a longer wavelength compared to the absorption of the semiconductor, indicating that coupling between the oscillator in the metal nanoparticle and the oscillator in the semiconductor was low due to mismatch of the frequencies. In the surface configuration, the plasmon resonance frequency remained constant because of the relatively small interfacial area between the metal and semiconductor. As a consequence, the plasmon resonance had a peak wavelength of approximately 560 nm, which was in the spectral region near the band gap of α-Fe₂O₃. Thus, in the surface configuration, the plasmon absorbance and semiconductor absorbance were matched and coupling could occur between the oscillator in the metal and the oscillator in the semiconductor.

In the embedded configuration, the overall light absorption of the compact ultra-thin α-Fe₂O₃ film would normally have been too low to efficiently absorb all of the incoming photons. The inclusion of the Au nanoparticles in the embedded

configuration served to increase the overall light absorption of the electrode. In the surface configuration, the overall light absorption of the $\alpha\text{-Fe}_2\text{O}_3$ platelets was sufficient to absorb the incoming photons, but the nanostructure was such that photons with energies near the band gap energy (2.5 eV to 2.1 eV) were predominantly absorbed in the bulk of the semiconductor, where they generated holes that could not be transported to the surface to react before they recombined. Thus, for photon energies near the band gap, the Au nanoparticles in the surface configuration served to localize light absorption at the surface of the platelets so that the produced holes could be collected efficiently at the surface.

5.3.2. Films photoactivity

The electrodes were photoactive and split water upon illumination by simulated sunlight with an applied potential. The measured current density as a function of potential in 1 M NaOH (pH 13.6) in the dark and under simulated AM1.5 illumination are presented in Figure 5.4.

For the embedded configuration, the photocurrent of the electrode containing the Au nanoparticles had approximately the same current-potential ($J-V$) characteristic as the $\alpha\text{-Fe}_2\text{O}_3$ control. The one notable difference was a lower onset potential for water oxidation in the dark for the embedded electrode containing Au nanoparticles, suggesting that not all of the Au nanoparticles were completely covered and that the Au catalyzes the water oxidation reaction. For the surface configuration, the electrode containing the Au nanoparticles produced less photocurrent than the $\alpha\text{-Fe}_2\text{O}_3$ -only electrode. Also, the onset potential of photocurrent was lower for $\alpha\text{-Fe}_2\text{O}_3$ platelets with Au, again suggesting that these Au nanoparticles catalyzed the water oxidation reaction.

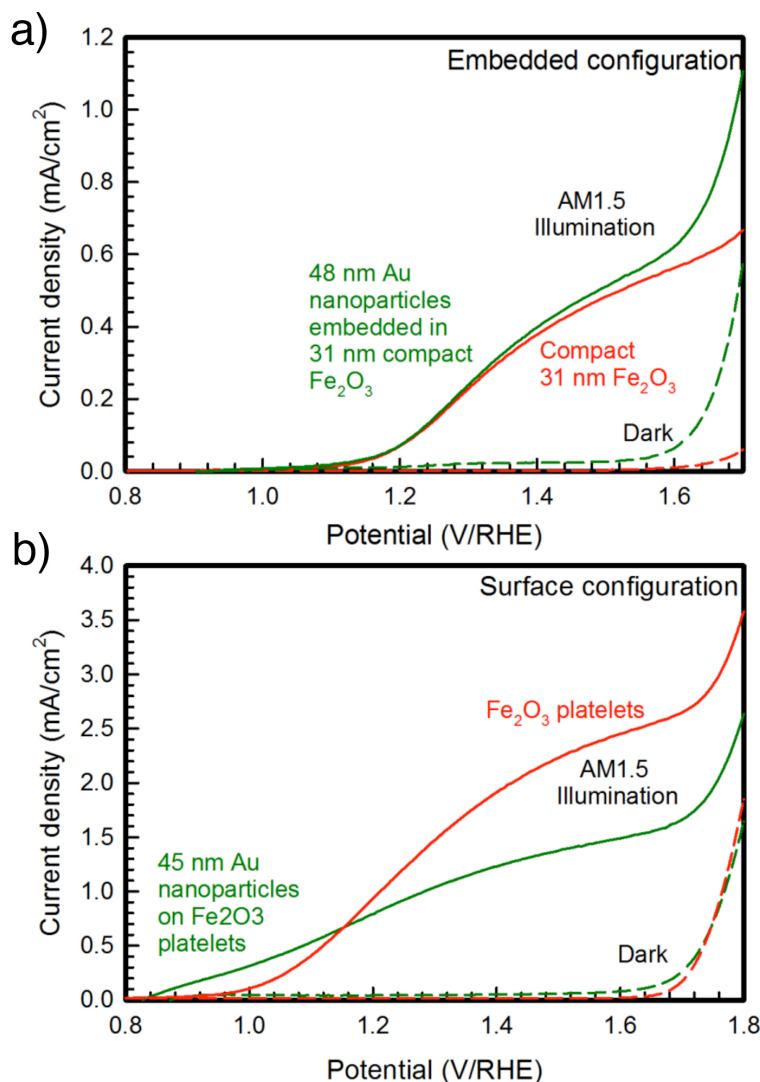


Figure 5.4: Current density, in mA cm^{-2} , as a function of electrode applied potential with respect to the RHE (a) for the embedded configuration; and (b) for the surface configuration. The solid lines were measured under simulated AM 1.5 illumination (100 mW cm^{-2}) and the dashed lines were measured in the dark. Reprinted from [1].

The observed trends in the J - V characteristics can be explained in terms of spectral overlap between the semiconductor absorbance and the plasmon resonance. In the embedded configuration, despite the increase in overall photon absorption, no enhancement was expected because of the poor spectral overlap between the plasmon resonance and the semiconductor absorbance spectrum. In the surface configuration, there was spectral overlap between the oscillator frequency of the plasmon and the oscillator frequencies of the semiconductor, and thus an enhancement in photocurrent was expected over the $\alpha\text{-Fe}_2\text{O}_3$ control due to surface-localized light absorption at photon energies near the band gap energy. In fact, an overall decrease was observed. This decrease can be understood by considering the

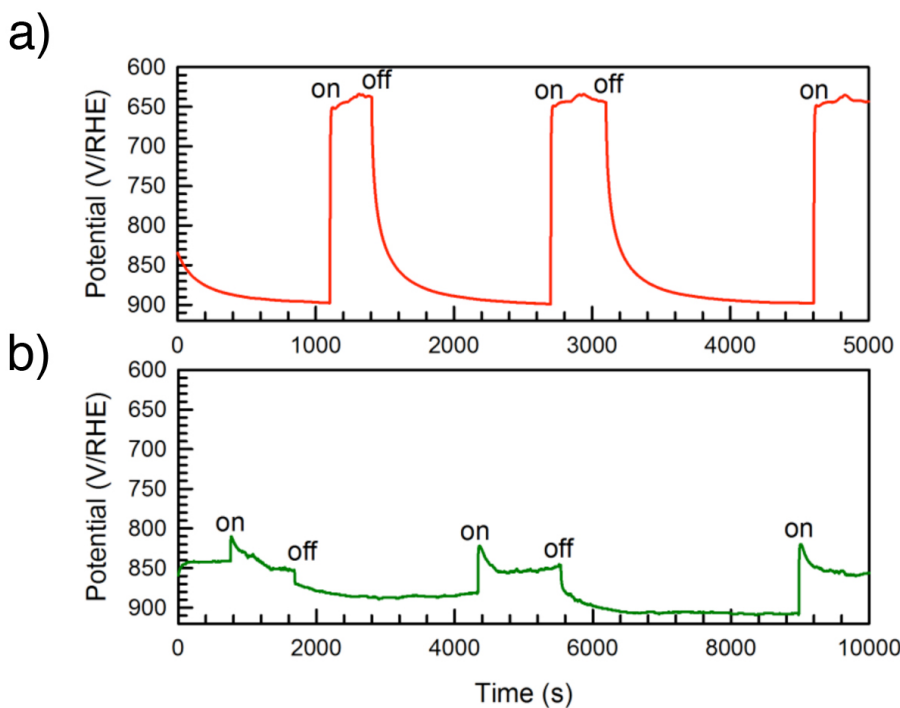


Figure 5.5: Photovoltage measurements, with respect to the RHE, of the (a) unmodified Fe_2O_3 platelets and (b) surface configuration under chopped illumination. Reprinted from [1].

third and fourth design criteria. Because the metal nanoparticles are larger than 10 nm and not electronically isolated from the semiconductor, the Schottky junction at the metal-semiconductor interface limits the open-circuit photovoltage.⁷ In addition, the possible creation of surface states at this interface may limit the open-circuit photovoltage and promote surface recombination. To examine these possibilities, the open-circuit photovoltage of a pristine hematite platelet electrode and a gold-modified platelet electrode (Figure 5.2b) were measured (Figure 5.5). It is apparent from these measurements that the open-circuit photovoltage decreased from 250 mV without gold to less than 100 mV with gold.

This finding is consistent with the lower photocurrent (Figure 4b). However, this does not rule out the possibility of a positive contribution from the coupling between the localized surface plasmon and the semiconductor, which would be observable in the spectral response of the photocurrent, or IPCE spectra.

5.3.3. Spectral response enhancement

The IPCE spectrum of each electrode was measured in 1 M NaOH under monochromatic illumination as a function of incident photon wavelength. Since the embedded configuration had a higher onset potential, the IPCE was measured at 1.5 V vs. RHE. The IPCE for the surface configuration was measured at 1.4 V vs. RHE.

By performing these experiments at relatively positive potentials, the catalytic effects of the metal are eliminated. Experiments on platelet-type samples reveal that catalysts reduce the onset potential but do not increase the photocurrent at high potentials (above 1.3 V vs. RHE).²⁸ Consequently, the role of the metal nanoparticles as catalysts can be ignored in the IPCE spectra, which are plotted in Figure 5.6. For the embedded configuration, the overall IPCE of the electrode containing Au was slightly lower than the α -Fe₂O₃ only case, suggesting that the interface between the Au and Fe₂O₃ introduces traps, which were partially empty at the lower light intensities used for the IPCE measurement, but were filled and had less of an impact at the higher light intensities used for the J-V measurement.

To examine the relative impact of the localized surface plasmon on the spectral response of the electrode, the IPCE spectra were normalized by the value at 350 nm, which was the maximum for all the electrodes used in this study and was the wavelength at which interband absorption processes dominated the spectra (Appendix A) and therefore no contribution from the localized surface plasmon resonance was expected. When the IPCE was normalized to the value at 350 nm, the embedded configuration revealed no difference between the electrode with Au nanoparticles and the Fe₂O₃-only control.

The IPCE for the surface configuration revealed a larger difference between the electrode with Au nanoparticles and the control than was observed in the J-V measurements, again suggesting partially empty traps at low light intensities. However, the normalized IPCE for the surface configuration revealed a higher response in the region of spectral overlap with the plasmon resonance, suggesting an enhancement due to coupling between the localized surface plasmon and semiconductor. It is unlikely that the observed change in the spectral behavior in the surface configuration is a result of light scattering, for several reasons. First, the absorption cross section for 48 nm Au nanoparticles is more than a factor of 10 larger than the scattering cross section in the wavelength range from 400 to 600 nm (see Appendix A). Thus the probability of scattering over absorption by the Au nanoparticles is very low. Second, the hematite electrodes are optically thick prior to the addition of gold nanoparticles and therefore scattering is not expected to significantly increase the proportion of light that is absorbed by the semiconductor. Furthermore, the corrugated nanostructure of the as-made hematite limits reflection losses by providing a gradual change in the refractive index. This minimizes the plasmon's role in decreasing reflection losses.²⁹ Third, a comparison of the extinction

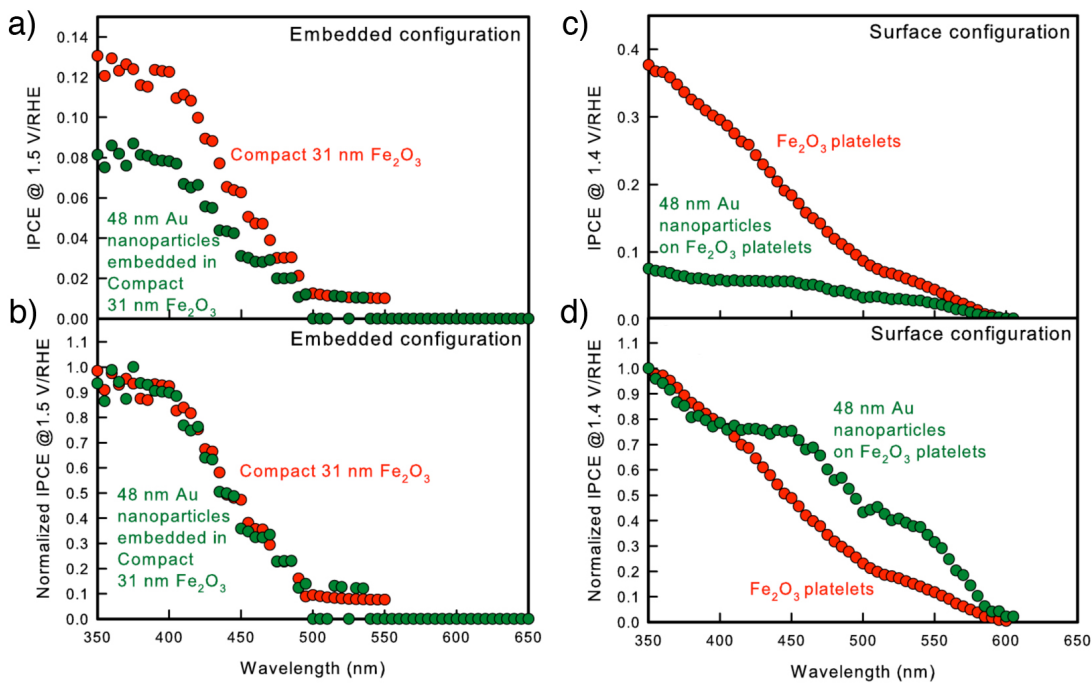


Figure 5.6: IPCE and normalized IPCE of the different electrodes. a) embedded configuration IPCE at an applied potential of 1.5 V vs. RHE; b) embedded configuration normalized spectral response at 1.5 V vs. RHE; c) surface configuration IPCE at 1.4 V vs. RHE; d) surface configuration normalized spectral response at 1.4 V vs. RHE. The normalized IPCE were normalized with respect to the IPCE maximum at 350 nm. Reprinted from [1].

spectrum of 50-nm gold nanoparticles in solution with the same nanoparticles adsorbed onto a platelet-type Fe₂O₃ electrode in the surface configuration revealed few differences (see Figure A3 in Appendix A). Because a large change in dielectric constant does not occur when adsorbing gold nanoparticles onto Fe₂O₃, the absence of changes in the extinction spectrum of the gold nanoparticles upon adsorption implies that no changes in the scattering characteristics have occurred. For these two reasons, the effect that is responsible for the enhanced IPCE between 400 and 600 nm cannot be assigned to scattering.

5.3.4. Eliminating the possibility of an electronic effect

To decouple the spectral enhancement from the electronic effects, such as a higher concentration of surface states at the metal/semiconductor interface and a lower photovoltage, 15 nm Au nanoparticles were deposited on the surface of the Fe₂O₃ platelets by electrophoretic deposition (Figure A4, Appendix A). It was expected that the smaller particle diameter and the lower areal surface coverage would make the optical characteristics of the Au-Fe₂O₃ composite electrodes nearly identical to the unmodified electrode because the plasmonic response of the metal

scales with volume. This allows the electronic effects of the metal nanoparticles on the semiconductor to be examined without significantly changing the optical characteristics of the electrodes. A decrease in the photocurrent under AM1.5 illumination was observed due to increased recombination, as expected (Figure A5). The coverage of 15 nm nanoparticles was such that they did not significantly affect the UV-visible absorbance of the electrode (Figure A6). A decrease in the IPCE was also observed, again because of increased recombination (Figure A6). However, the normalized IPCE spectra revealed very little difference between the as-made Fe_2O_3 platelets and those modified with 15 nm Au nanoparticles. As described previously, the metal nanoparticles induce several electronic and electrochemical effects on the electrode. These include the formation of surface states and a different band structure in the proximity of the metal nanoparticles. A lower barrier height at the metal-semiconductor interface facilitates the flow of electrons from the semiconductor into the metal, which lowers the magnitude of the photovoltage that the semiconductor junction is able to produce. Therefore, it is significant that despite these electronic effects the normalized IPCEs of the Fe_2O_3 and Fe_2O_3 -Au electrodes are nearly identical. This suggests that the various electronic effects do not depend strongly on the wavelength of the incident light. This is consistent with our expectations for the following reasons. First, the rate of charge carrier recombination via surface states is independent of the wavelength of light that created those carriers, as long as they have thermalized; thermalized carriers are expected in Fe_2O_3 because charge transport is via small polarons.^{28,30} Second, the lower photovoltage in the composite electrodes results from the increased reductive dark current that flows across the semiconductor-metal junction; because this is a dark current it is necessarily independent of photon wavelength. Third, the altered band structure in the vicinity of the metal particles will modify carrier transport within the semiconductor, particularly for holes that are photogenerated close to the metal. Because the location in which a carrier is absorbed depends strongly on wavelength, the altered band bending can induce a spectral dependence on the yield of photogenerated carriers that are transported to the semiconductor-electrolyte or semiconductor-metal interface. Apparently this is a relatively small effect, because the normalized IPCEs of the Fe_2O_3 and Fe_2O_3 -Au (15 nm particles) are nearly identical. Consequently, we conclude on the basis of theory and experiment that the electronic effects of the Au nanoparticles on the water splitting efficiency do not have a strong dependence on the wavelength of incident light. This supports the

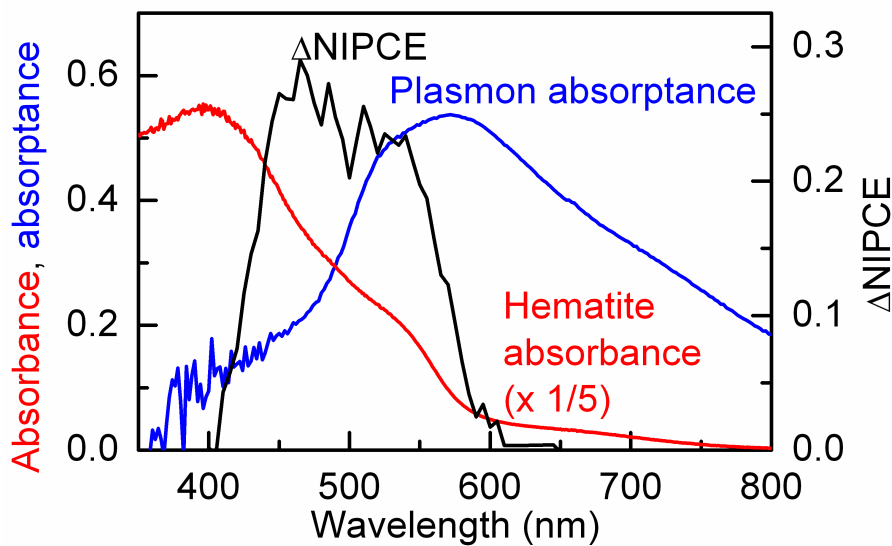


Figure 5.7: Difference between the normalized IPCE of the surface configuration and the as-made hematite platelets (black, right vertical axis), unmodified hematite absorbance (red, left vertical axis) and plasmon absorptance from the data in the supporting information (blue, left vertical axis). Reprinted from [1]

conclusion that the enhanced spectral response to water splitting for the 48-nm Au nanoparticles in the surface configuration originates from the region of overlapping oscillator frequencies of the localized surface plasmon and the semiconductor.

5.3.5. Evidence of the plasmonic effect

The difference in the normalized IPCE spectra (ΔNIPCE) between the as-produced Fe_2O_3 platelet electrode and one modified with 48 nm Au nanoparticles in the surface configuration is compared to the localized surface plasmon absorptance and hematite absorbance spectra. The hypothesis is that energy transfer from the surface plasmon to the semiconductor creates additional minority charge carriers, which results in a greater rate of water oxidation; this enhanced response should be apparent in the ΔNIPCE spectra.

The ΔNIPCE spectra should reflect the excitation spectra of the semiconductor and the plasmon, which can be approximated using the frequency response of the semiconductor and the plasmon absorptance assuming that all energy absorbed by the plasmon is transferred to the semiconductor, that is, a 100% branching ratio. The frequency response of hematite to the localized surface plasmon is difficult to determine without detailed computation modeling, which would have to take into account the localized electric field enhancement arising from the plasmon evanescent wave, semiconductor absorption coefficient, plasmon lifetime and the

time-scale associated with the excitation of an electron-hole pair. However, the absorbance spectrum of the Fe_2O_3 provides a qualitative first approximation of the frequency response of the semiconductor and can capture the general trend. The ΔNIPCE spectra, plasmon absorptance (determined using the data in Figure A1), and unmodified hematite absorbance are plotted in Figure 7. The plasmon absorbance sets the lower boundary at 400 nm; the hematite band gap sets the upper boundary at 600 nm. As predicted, an enhanced response in the ΔNIPCE is seen between 400 and 600 nm.

5.4. Conclusion

Au nanoparticles approximately 50 nm in diameter were incorporated into Fe_2O_3 electrodes with two configurations, one in which they were embedded in a compact 31 nm Fe_2O_3 ultra-thin film and another where the particles were deposited on the surface of Fe_2O_3 nanoplatelets. No enhancement was observed for the embedded configuration, possibly due to poor spectral overlap between the plasmonic metal nanoparticle and semiconductor. An enhancement in the spectral response of the electrode with the surface configuration was observed, which could not be explained by catalytic or electronic effects of the metal particles. The effect is assigned to the plasmonic absorption and subsequent energy transfer to the semiconductor. It was also observed that the metal nanoparticles decreased the photovoltage and resulted in a lower rate of hydrogen production. It will be necessary to raise the height of the Schottky barrier to maintain a large photovoltage.

One could also explore Ag nanoparticles as an alternative plasmonic material. Ag is less expensive than Au and the plasmon frequency can be shifted into the wavelength range of interest (500 nm to 600 nm) by embedding the particles in the α - Fe_2O_3 matrix.¹² In this configuration, care must be taken to stabilize the Ag, on one side to prevent recombination and on the other side to prevent corrosion when exposed to the electrolyte.

5.5. References

- (1) Thimsen, E.; Le Formal F.; Grätzel, M.; Warren S. C. *Nano Lett.* **2011**, *11*, 35.
- (2) Cesar, I.; Sivula, K.; Kay, A.; Zboril, R.; Grätzel, M. *J. Phys. Chem. C* **2009**, *113*, 772.
- (3) Warren, S. In *Photoelectrochemical Hydrogen production*; Krol, R.v.d., Grätzel, M., Eds; in press.
- (4) Kennedy, J.; Frese, K. *J Electrochem Soc* **1977**, *124*, C130.

- (5) Pala, R. A.; White, J.; Barnard, E.; Liu, J.; Brongersma, M. L. *Adv Mater* **2009**, *21*, 3504.
- (6) Standridge, S. D.; Schatz, G. C.; Hupp, J. T. *J Am Chem Soc* **2009**, *131*, 8407.
- (7) Atwater, H. A.; Polman, A. *Nat Mater* **2010**, *9*, 205.
- (8) Tsubomura, H.; Nakato, Y. *New J Chem* **1987**, *11*, 167.
- (9) Wei, H.; Ratchford, D.; Li, X. E.; Xu, H.; Shih, C.-K. *Nano Lett.* **2009**, *9*, 4168.
- (10) Bohren, C. F.; Huffman, D. R. *Absorption and scattering of light by small particles*; Wiley: New York, 2004.
- (11) Link, S.; El-Sayed, M. *J Phys Chem B* **1999**, *103*, 4212.
- (12) Rand, B. P.; Peumans, P.; Forrest, S. R. In *J. Appl. Phys.* 2004; Vol. 96, p 7519.
- (13) Jain, P. K.; Huang, W.; El-Sayed, M. A. *Nano Lett.* **2007**, *7*, 2080.
- (14) Tabor, C.; Murali, R.; Mahmoud, M.; El-Sayed, M. A. *J Phys Chem A* **2009**, *113*, 1946.
- (15) Haug, H.; Koch, S. W. *Quantum theory of the optical and electronic properties of semiconductors*, 4th ed.; World scientific: River Edge, NJ, 2004.
- (16) Kreibig, U.; Vollmer, M. *Optical properties of metal clusters*; Springer: Berlin, 1995.
- (17) Christensen, N.; Seraphin, B. *Phys Rev B-Solid St* **1971**, *4*, 3321.
- (18) Nakato, Y.; Ohnishi, T.; Tsubomura, H. *Chem Lett* **1975**, 883.
- (19) Memming, R. *Semiconductor Electrochemistry*; Wiley VCH: Weinheim, 2001.
- (20) Nakato, Y.; Tsubomura, H. *J Photochem* **1985**, *29*, 257.
- (21) Thimsen, E.; Biswas, P. *Aiche J* **2007**, *53*, 1727.
- (22) Le Formal, F.; Graetzel, M.; Sivula, K. *Adv Funct Mater* **2010**, *20*, 1099.
- (23) Duret, A.; Gratzel, M. *J Phys Chem B* **2005**, *109*, 17184.
- (24) Thimsen, E.; Rastgar, N.; Biswas, P. *J Phys Chem C* **2008**, *112*, 4134.
- (25) Seaman, C. *Sol Energy* **1982**, *29*, 291.
- (26) Tanaka, T. *Jpn J Appl Phys* **1979**, *18*, 1043.
- (27) Cooper, B.; Ehrenreich H., ; Philipp, H. *Phys Rev* **1965**, *138*, A494.
- (28) Dotan, H.; Sivula, K.; Graetzel, M.; Rothschild, A.; Warren, S. C. *Energy Environ. Sci.* **2011**, *4*, 958.
- (29) Spinelli, P.; Hebbink, M.; van Lare, C.; Verschuuren, M.; de Waele, R.; Polman, A. Plasmonic Anti-reflection Coating for Thin Film Solar Cells In *Optical Nanostructures for Photovoltaics*, OSA Technical Digest (CD) (Optical Society of America, **2010**)
- (30) Rosso, K.; Dupuis, M. *J Chem Phys* **2004**, *120*, 7050.

CHAPTER 6.

PASSIVATING SURFACE STATES ON HEMATITE PHOTOANODES WITH ALUMINA OVERLAYERS

This chapter is published as Le Formal, F.; Tétreault, N.; Cornuz, M.; Moehl, T.; Grätzel, M.; Sivula, K. *Chem. Sci.* **2011**, 2, 737.¹

Hematite is a promising material for inexpensive solar energy conversion via water splitting but new strategies to overcome specific challenges associated with this material are necessary for further improvement. Chapters 3, 4 and 5 presented work related to a new nanostructuring approach to overcome the mismatch between the light absorption depth and the poor electronic properties. Another limitation for the use of hematite in a water splitting device is the large overpotential (0.5 – 0.6 V) that must be applied to afford high water oxidation photocurrent. This has conventionally been addressed by coating it with a catalyst to increase the kinetics of the oxygen evolution reaction. However, surface recombination at trapping states is also thought to be an important factor for the overpotential, and herein a strategy to passivate trapping states using conformal overlayers applied by atomic layer deposition is investigated. While TiO_2 overlayers show no beneficial effect, an ultra-thin coating of Al_2O_3 is found to reduce the overpotential required with state-of-the-art nanostructured photo-anodes by as much as 100 mV and increases the photocurrent by a factor of 3.5 (from 0.24 mA cm^{-2} to 0.85 mA cm^{-2}) at +1.0 V vs. the reversible hydrogen electrode (RHE) under standard illumination conditions. The subsequent

addition of Co^{2+} ions as a catalyst further decreases the overpotential and leads to a record photocurrent density at 0.9 V vs. RHE (0.42 mA cm^{-2}). A detailed investigation into the effect of the Al_2O_3 overlayer by electrochemical impedance and photoluminescence spectroscopy reveals a significant change in the surface capacitance and radiative recombination, respectively, which distinguishes the observed overpotential reduction from a catalytic effect and confirms the passivation of surface states. Importantly, this work clearly demonstrates that two distinct loss phenomena affect charge recombination on the surface of high-performance hematite. These phenomena, namely the slow oxygen evolution kinetics and the charge trapping on the surface, are evidenced to cause the large overpotential observed. In addition, this work suggests a viable route to individually address them.

6.1. Introduction

Several major drawbacks should be overcome to allow the use of hematite in an efficient water splitting device, as summarized in Chapter 2. The first drawback, namely the contradiction between the short diffusion length of holes as compared to the long light penetration depth, can be surmounted by nanostructuring photoanodes. Chapters 3 to 5 address this issue with introducing a new concept for water splitting using extremely hematite thin films as well as presenting a comprehensive and explorative work on enhancing the solar-to-hydrogen efficiency of iron oxide thin films.

However, the second crucial drawback of hematite remains: a bias of over 1 V vs. the reversible hydrogen electrode (RHE) must be applied to afford significant water splitting photocurrent density. The bias is partly attributed to the position of the conduction band energy in hematite, which is 0.4 – 0.5 eV too positive to allow water reduction into hydrogen. While this can nominally be overcome using a tandem cell approach,² the additional high overpotential (0.5 – 0.6 V) required to initiate water oxidation represents a significant energy loss. Thus the second clear challenge is to reduce the overpotential and afford the highest water splitting photocurrent density at the lowest possible applied potential. Typically, the overpotential is attributed to poor oxygen evolution reaction (OER) kinetics and has been addressed by attaching various catalyst materials.³⁻⁵ Yet even when using IrO_2 — the most effective water oxidation catalyst — only 0.2 V of the overpotential was eliminated.³ Consequently, while a photocurrent density of over 3.0 mA cm^{-2} was observed at +1.23 V vs. RHE in these electrodes, only 10% of that (0.31 mA cm^{-2}) was available at 0.9 V.

The inability of a high-performance catalyst to completely eliminate the overpotential suggests that factors other than slow OER kinetics play an important role. Indeed, several groups have suggested surface traps as an additional loss mechanism in hematite photoelectrodes prepared using various methods.⁶⁻¹¹ Further investigation of these surface states using sacrificial electron donors in the electrolyte, such as pyrogallol,¹⁰ have suggested that hole traps at the surface can be eliminated. However, a feasible method to passivate surface states on hematite without sacrificial agents has not been put in evidence. In addition, the relative roles of both possible loss mechanisms — poor OER kinetics and surface traps — at the surface of nanostructured water splitting hematite photoanodes are not clear. In this chapter, the presence of surface trapping states is investigated on hematite prepared by APCVD and a method to passivate surface states without using sacrificial components is reported. To accomplish this, atomic layer deposition (ALD) was used to coat the hematite with thin oxide overlayers. Recently ALD has been gaining interest as a powerful research tool for creating highly conformal layers on nanostructured electrodes¹² and has even been used for surface state passivation of TiO₂ in dye sensitized solar cells.¹³ This chapter shows that an ultra-thin layer of Al₂O₃ deposited by ALD can decrease the overpotential for water photo-oxidation with nanostructured hematite. This observation and the supporting experiments confirm that there are two distinct loss processes at the surface of state-of-the-art hematite photoanodes.

6.2. Experimental

6.2.1. Hematite thin films by APCVD

The photoanodes were prepared according to the method developed by Kay *et al.* in 2006⁴ which was recently optimized by Cornuz *et al.*¹⁴ To summarize, this method consists of bringing the precursors—iron pentacarbonyl (Fe(CO)₅, Acros, 99.5%) and tetraethoxysilane (TEOS, Aldrich 99.9999%)—to the gas phase by bubbling argon in the liquids put in different vials at different flow rates. The flow rates were adjusted to optimize doping of the photanodes. The vapor streams are then mixed and diluted in the carrier gas (dry air), which is targeted at a substrate (FTO, TEC 15, 15 Ω □⁻¹, Hartford Glass Co.) heated at ca. 420°C on a titanium block in a closed chamber. The iron oxide film obtained is formed by the agglomeration of small Fe₂O₃ particles (ca. 5 nm) nucleated in the gas phase, resulting in a cauliflower-like

nanostructure. Silicon doping was measured by XEDS/TEM to be optimal at a level of 1.5 at%.⁴

In one case, an ALD-treated electrode was subjected to a Co²⁺ catalyst deposition. The sample was dipped in a 10mM aqueous solution of cobalt nitrate Co(NO₃)₂ for 30 seconds and rinsed with deionized water according to the method developed previously.⁴

6.2.2. Atomic layer deposition of overlayers

The as-prepared APCVD films (heated at 300 °C in air to remove any surface contamination) were first evaluated for their PEC water oxidation performance (see below) before the conformal deposition of Al₂O₃ or TiO₂ by ALD. Amorphous aluminum oxide (Al₂O₃) was deposited in a layer-by-layer fashion onto the hematite films by ALD (Cambridge Nanotech S100). Deposition using successive pulses of trimethylaluminum (TMA) and deionized water in a nitrogen carrier gas was performed in a vacuum chamber heated at 200°C.¹⁵ The number of cycles (pulse of TMA / vacuum / pulse of water / vacuum) applied to the sample was adjusted to be 1, 3, 6, or 13 which corresponds to a thickness of 0.15, 0.45, 0.9 or 1.95 nm as measured by spectroscopic ellipsometry on Si wafer (Sopra GES 5E, fitted to a Tauc-Lorentz function). For samples covered with TiO₂, 6, 33, 66 and 132 cycles (pulse of titanium isopropoxide/ vacuum/ pulse of water/ vacuum) were necessary to give similar thicknesses due to the lower reactivity of the precursor at 200 °C.

6.2.3. Photoelectrochemical characterizations

Photocurrent measurements were performed to estimate the solar photocurrent of the photoanodes in a three-electrode configuration with 1 M NaOH (pH 13.6) as electrolyte using Ag/AgCl in saturated KCl as a reference electrode and a platinum wire as a counter electrode. The hematite electrode was scanned at 50 mV s⁻¹ between 0.3 and 0.8 V vs. Ag/AgCl. The potential is reported relative to the reversible hydrogen electrode (RHE). The samples were illuminated at the photoanode/electrolyte interface with simulated sunlight from a 450 W xenon lamp (Osram, ozone free) using a KG3 filter (3 mm, Schott) with a measured intensity of 1 sun (100 mW cm⁻²) at the sample's surface. Spectral mismatch factors to estimate the difference of the electrode photoresponse obtained from simulated and real sun light at AM 1.5 G were calculated according to the method described by Seaman *et al.*¹⁶ The hematite electrodes were tested before and after ALD, then annealed in air for 20 min at 300 °C, tested, annealed at 400 °C, and tested once more. A control

electrode was subjected to the same set of conditions but without any overlayer deposition.

The photocurrent transient data were obtained using the set up described above with the addition of a computer-controlled light chopper. The potential was set at -0.1, 0.1 and 0.5 vs. Ag/AgCl for 4 seconds with the chopper programmed to switch the light ON and OFF every 2 seconds.

6.2.4. Additional characterization

Electrochemical impedance spectroscopy (EIS) was performed on an APCVD hematite photoanode before and after being covered with 3 ALD cycles of alumina. The ac-impedance was measured in 1M NaOH as electrolyte using Ag/AgCl in saturated KCl as a reference electrode, using an EG&G 273 potentiometer combined with a frequency response analyzer (FRA) from Solartron. A sinusoidal voltage perturbation of 10 mV amplitude was superimposed on a bias voltage, with a frequency that ranged from 100 kHz to 0.1 Hz. The bias potential was scanned cathodically from 0.8 to -0.3 V vs. Ag/AgCl with a 50 mV interval and is reported again vs. RHE. The raw data were fitted using the Zview software from Scribner Associate Inc.

Photoluminescence spectra (PL) were also obtained for an as-prepared Fe₂O₃ photoanode and one covered with 3 ALD cycle of alumina. Photoluminescence experiment was carried on a Horiba Fluorolog 3-22 spectrofluorometer using a 520 nm excitation wavelength (5 nm bandpass for both entrance and exit) and front-face detection with a standard photomultiplier detector. The emission was scanned from 510 nm to 850 nm with 1 nm increments and a 1 s integration time was used.

6.3. Results and discussion

6.3.1. Photoelectrochemical performances

The nanostructured and silicon-doped hematite thin-films grown by APCVD exhibit a cauliflower-like nanostructure formed by the agglomeration of small Fe₂O₃ particles (*ca.* 5 nm) nucleated in gas phase.³ This nanostructure was conformally coated with Al₂O₃ or TiO₂ by ALD. The number of ALD cycles was varied for each material to obtain a corresponding thickness of about 0.15, 0.45, 0.9 or 1.95 nm (as measured by spectroscopic ellipsometry on Si). Control electrodes were subjected to identical conditions but without precursor pulses. While the TiO₂ overlayer had no positive influence on the Fe₂O₃ (see Appendix B, Figure B1), even the thinnest application of Al₂O₃ (1 cycle corresponding to 0.15 nm on the Si reference) had a

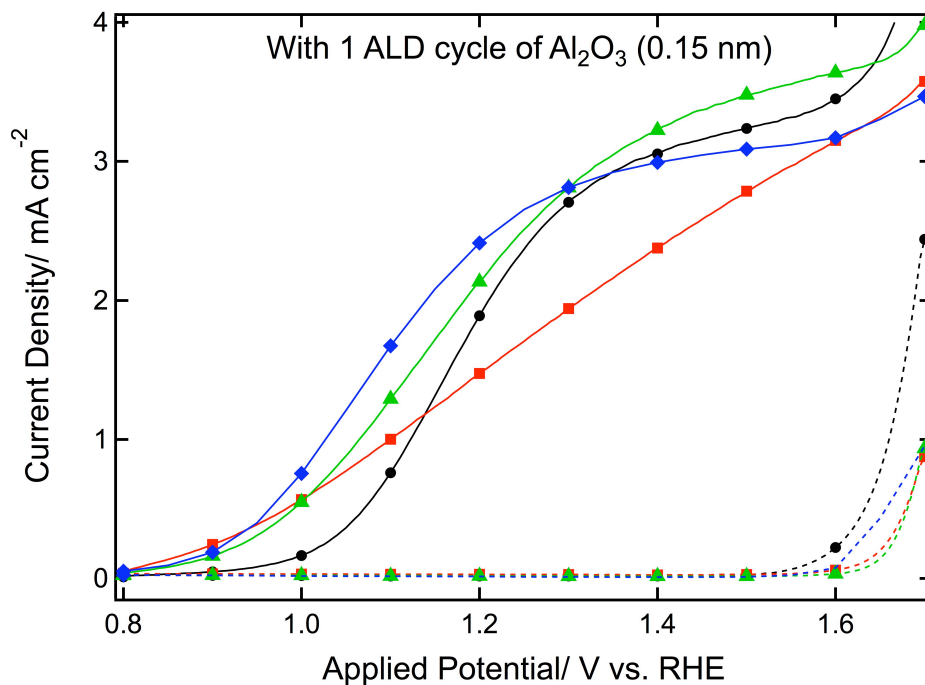


Figure 6.1: Current densities, in mA cm^{-2} of the prepared photoanodes in the dark (broken lines) and under simulated solar illumination (AM 1.5G 100 mW cm^{-2} , solid curves) are shown as a function of the applied potential with respect to the RHE. An APCVD sample covered with 1 ALD cycle of Al_2O_3 has been measured after deposition (red squares), after annealing for 20 minutes at 300°C (green triangles) and after annealing for 20 minutes at 400 °C (blue/diamond) are compared to a control, which is the same sample before ALD (black circles). Reprinted from [1].

significant impact on the photoelectrochemical properties of the iron oxide as shown by the photocurrent density vs. voltage characteristics (at AM 1.5 G 100 mW cm^{-2} simulated illumination) presented in Figure 6.1. Before ALD treatment, the electrode exhibits the typical response of an APCVD grown hematite sample (black trace, circle markers). Water oxidation photocurrent onsets¹⁷ at +1.03 V vs. RHE in 1 M NaOH electrolyte (pH 13.6), the current density then increases rapidly, attaining approximately 2 mA cm^{-2} at 1.23 V vs. RHE bias and reaches a plateau of about 3.1 mA cm^{-2} from 1.4 V to 1.6 V vs. RHE before the dark current rises.

After one ALD cycle, the onset of the photocurrent is dramatically shifted cathodically (red trace with square markers in Figure 6.1) but a resistive behavior characterized by a slow and linear rise of the photocurrent with applied voltage is observed. This behavior is possibly due to a high degree of disorder in the amorphous Al_2O_3 overlayer that inhibits hole injection from Fe_2O_3 into the electrolyte. After annealing in air at 300°C (green trace, triangle markers, Figure 6.1), the electrode's photocurrent curve regains a shape similar to before the ALD. However, the photocurrent onset potential shifts dramatically by *ca.* 80 mV to 0.95 V vs. RHE

while the current density reaches 2.3 mA cm^{-2} at 1.23 V and 3.3 mA cm^{-2} at 1.43 V vs. RHE. These values are superior to that of the control sample over the full bias range. Further annealing at $400 \text{ }^{\circ}\text{C}$ shows an additional cathodic shift in the onset potential to 0.93 V vs. RHE, but a lower plateau (3.0 mA cm^{-2} at 1.43 V) compared to control samples.

This latter decrease in photocurrent plateau is probably due to an increase of the feature size of the hematite nanoparticles when annealing at the higher temperature, which results in a loss of active surface area.¹⁸ Interestingly, this effect is found to subside when using thicker Al_2O_3 overlayers as shown in Figure 6.2.

Figure 6.2 shows the water oxidation photocurrent density attained at 1.03 V (yellow triangles), 1.23 V (orange squares) and 1.43 V (red circles) vs. RHE, with the different thicknesses of Al_2O_3 compared to the control sample. The photocurrent density of the control sample shows its expected evolution with little change until $400 \text{ }^{\circ}\text{C}$ when an increased crystallinity and loss of surface area cause a small increase in the photocurrent at 1.03 V and decrease at 1.43 V , respectively. In contrast, the Al_2O_3 overlayer has a strong effect on the photocurrent-voltage characteristics of the hematite photoanodes regardless of its thickness. Overall, the electrodes with an Al_2O_3 overlayer show: i) a lower photocurrent onset potential resulting in a higher photocurrent at 1.03 V , ii) a decrease in photocurrent at higher potentials after ALD deposition, iii) the recovery (at 1.23 and 1.43 V) and further increase of the photocurrent (1.03 V) after annealing in air at $300 \text{ }^{\circ}\text{C}$, and iv) a slight decrease in photocurrent at 1.43 V vs. RHE after annealing at $400 \text{ }^{\circ}\text{C}$. The latter effect is reduced with increasing Al_2O_3 thickness, indicating that the overlayer may prevent the hematite particle growth through the same mechanism observed when using SiO_2 .¹⁹

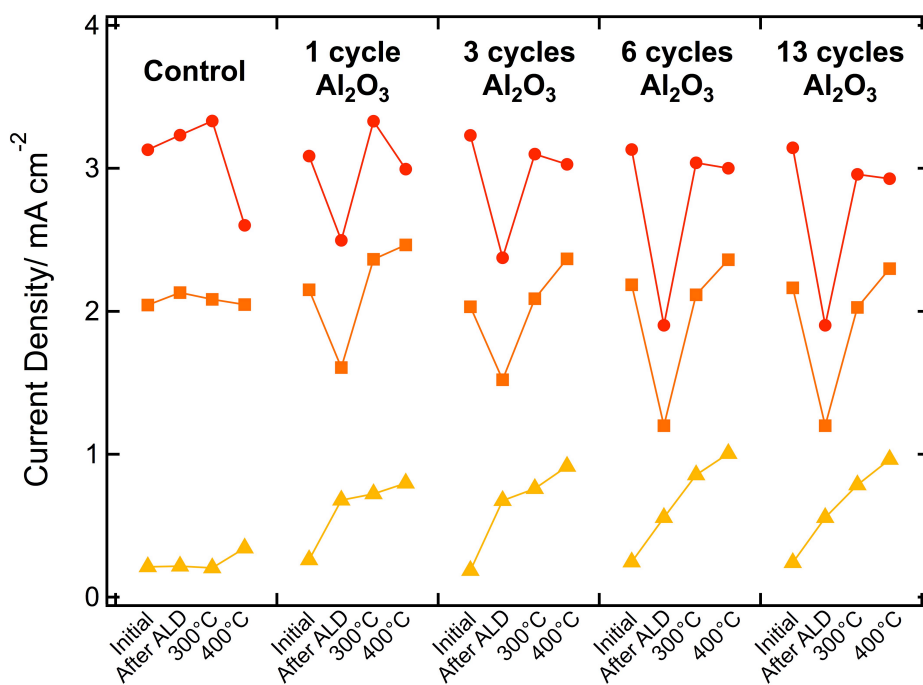


Figure 6.2: Current densities, in mA cm^{-2} of the prepared photoanodes at 1.03V (yellow triangles), at 1.23V (orange squares) and at 1.43V vs. RHE (red circles), are presented for a control sample and samples covered by different thickness of alumina (deposition with 1, 3, 6 and 13 ALD cycles). All samples have been measured before and after ALD as well as after annealing at 300°C and 400°C.

Importantly, the observed thickness-dependent behavior also suggests that the alumina is not dissolving under the basic conditions used for the PEC measurement (pH 13.6) despite the known thermodynamic instability of Al_2O_3 at this pH. Indeed, several scans of the photoanodes exposed to the electrolyte and under illumination as well as the prolonged exposure to the electrolyte in the dark showed no change in the photoanode performance. The hematite thin film covered with Al_2O_3 by ALD was stable for the entire duration of the EIS characterization (*ca.* 30 min) in 1M NaOH electrolyte. This experiment is the longest measurement we performed on a hematite photoanode before and after 3 cycles of Al_2O_3 ALD. We observe in Figure 6.3a that the photoelectrochemical performance (onset potential, photocurrent plateau) of both the ALD-treated electrode and the control stay unchanged before and after the 30 min required for EIS at potentials in the range of 0.7 – 1.8 V vs. RHE and pH 13.6.

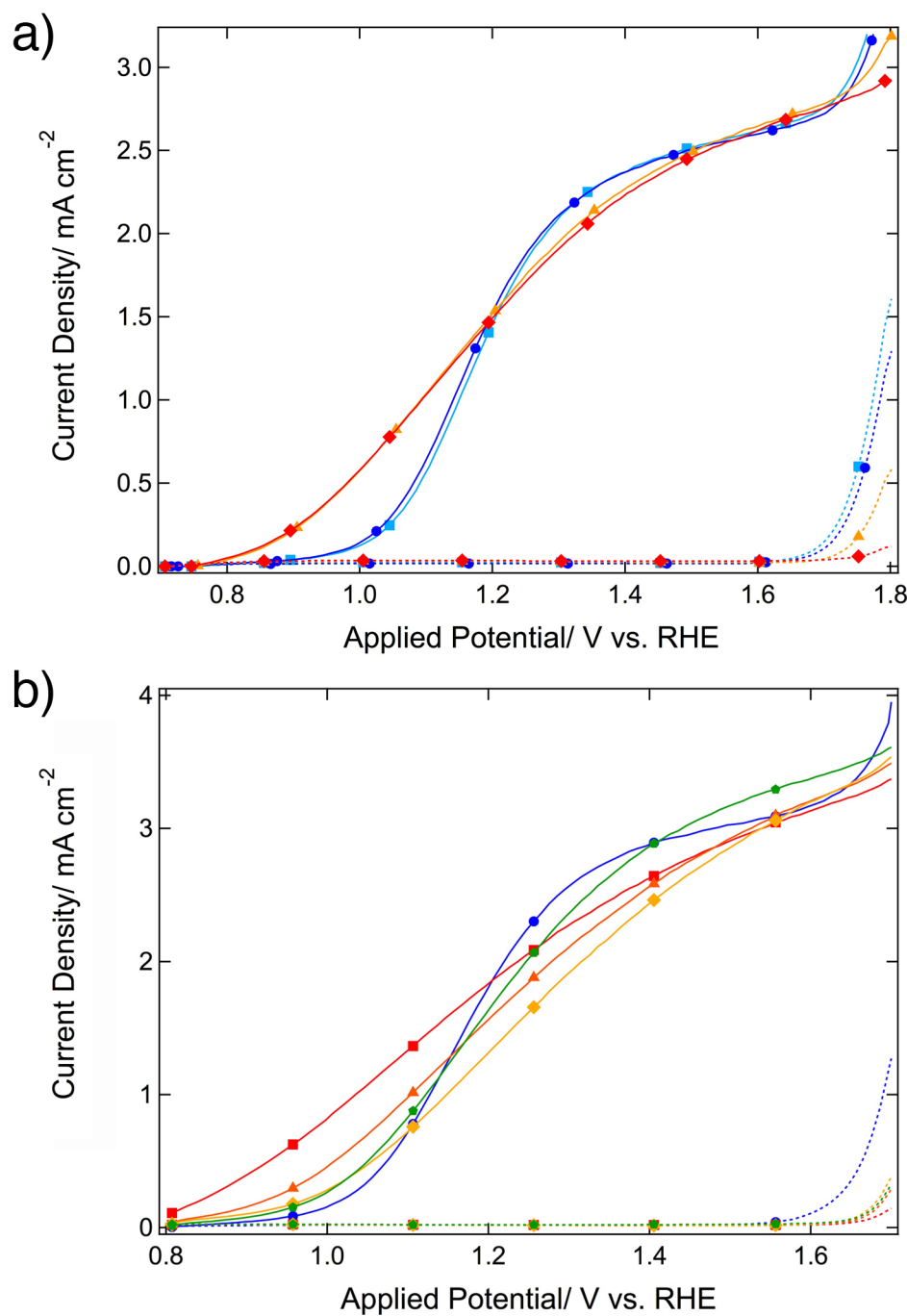


Figure 6.3: Current densities, in mA cm^{-2} of the prepared photoanodes in the dark (dotted lines) and under simulated solar illumination (AM 1.5G 100 mW cm^{-2} , solid curves) are shown as a function of the applied potential vs. RHE. a) A hematite control sample was photoelectrochemically characterized before and after the EIS experiment before (blue circles and blue squares respectively) and after 3 cycles of Al_2O_3 ALD (annealed 20 min at 300°C) (red diamonds and orange triangles respectively). b) A hematite control sample was photoelectrochemically characterized before and after deposition of a 2 nm thick Al_2O_3 layer (blue circles and red squares respectively). The same sample was then held in 1M NaOH electrolyte under AM 1.5 illumination and 1.03 V vs. RHE conditions and characterized after 25 min (orange triangles) and 55 min (yellow diamonds). A subsequent annealing treatment at 300°C for 20 minutes on the same sample (green pentagons) exhibits the recovery of the initial current voltage characteristics.

However, long term exposure (*ca.* 1 h) in 1M NaOH under an applied potential of 1.03 V vs. RHE and 1 sun illumination caused a modified electrode to recover its initial photocurrent properties (Figure 6.3b). The photocurrent onset was found to recover its initial value after 55 min. Since the onset potential did not change upon exposure to electrolyte and bias in the dark (Figure 6.3a), we attribute the recovery of the initial performance in Figure S3 to the photoelectrochemical dissolution of the Al₂O₃ layer (under potential and light). A subsequent annealing treatment at 300°C for 20 min shows the recovery of the initial (pre-ALD deposition) photoelectrochemical characteristics. Despite this long-term instability, the Al₂O₃ was sufficiently stable for further characterization to scrutinize the nature of the photocurrent onset reduction.

6.3.2. Photocurrent transients

Photocurrent transient measurements were performed in order to assess the dynamics of water oxidation and charge recombination at the hematite / electrolyte interface before and after the ALD of the Al₂O₃ overlayer. To summarize, samples are held at key bias potentials and the time-resolved photocurrent is recorded while illumination was turned on and off. The current density is shown with respect to time in Figure 6.4 for a hematite photoanode covered with 3 cycles of alumina ALD (red, thick line) and a control photoanode (blue, thin line). Previous studies of photoanode transients have commented on the typically-observed behavior,^{6,7,9,20} when light reaches the sample, photogenerated holes travel to the SCLJ and accumulate because of the slow OER kinetics,⁹ or because carriers oxidize trap states in the bulk⁸ and on the surface.⁷ This induces a sharp anodic current spike that decays as the accumulation process perturbs the charge distribution of the space charge region until equilibrium is eventually reached between water oxidation and charge recombination. Conversely, the cathodic transient peak observed when the light is turned off has been assigned to electrons diffusing from the external circuit and recombining with the accumulated holes at the SCLJ. The appearance of transients diminishes at higher potential as a larger proportion of holes have sufficient potential to oxidize water. For each potential, an estimate of the number of holes accumulated at the SCLJ can be obtained from the area, *A*, set between the actual photocurrent spectrum and the square wave obtained if the photocurrent had immediately risen to the steady state value.²¹ In Figure 6.4, we qualitatively observe that *A* is smaller for the electrode with an overlayer than for the control at all bias potentials. By integration of the photocurrent at 1.1 V vs. RHE with respect to time, we can confirm

from the estimated values of $A = 71.2 \mu\text{C cm}^{-2}$ and $A = 198 \mu\text{C cm}^{-2}$, for the coated

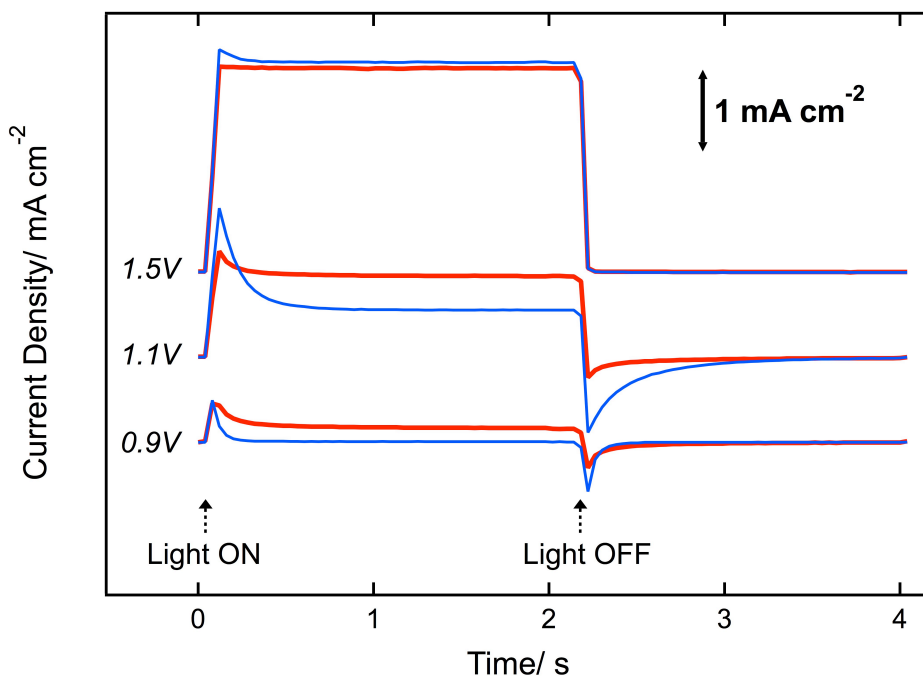


Figure 6.4: Transient photoresponse shown by light chopping current densities (light on/light off) as a function of time. The bias potential, with respect to the RHE, were applied during 4 seconds (2 seconds with light ON and 2 seconds with light OFF) at 0.9, 1.1 and 1.5 V as indicated. Comparison of the transient behavior of iron oxide photoanodes with 3 ALD cycles of Al_2O_3 overlayer (red, thick line) and without (blue, thin line).

hematite and the control, respectively, that the Al_2O_3 overlayer causes fewer holes to accumulate at the SCLJ.

6.3.3. Eliminating the possibility of a catalytic effect

At this stage both the reduction of charge accumulation at the SCLJ implied by the transient results and the cathodic shift of the photocurrent onset potential afforded by the alumina overlayer could be explained as well by a catalytic argument; *i.e.* the Al_2O_3 could simply increase the rate of the OER at the SCLJ. However, three additional details indicate this is not an appropriate explanation. First, upon the surface adsorption of the common Co^{2+} catalyst,⁴ we observe an additional cathodic shift of the overpotential to less than +0.9 V vs. RHE. This is shown in Figure 6.5a and leads to photocurrent density of 0.42 mA cm^{-2} at 0.9 V vs. RHE. To our knowledge, this is the highest water oxidation photocurrent reported for a hematite photoanode at 0.9 V vs. RHE and under standard illumination conditions.

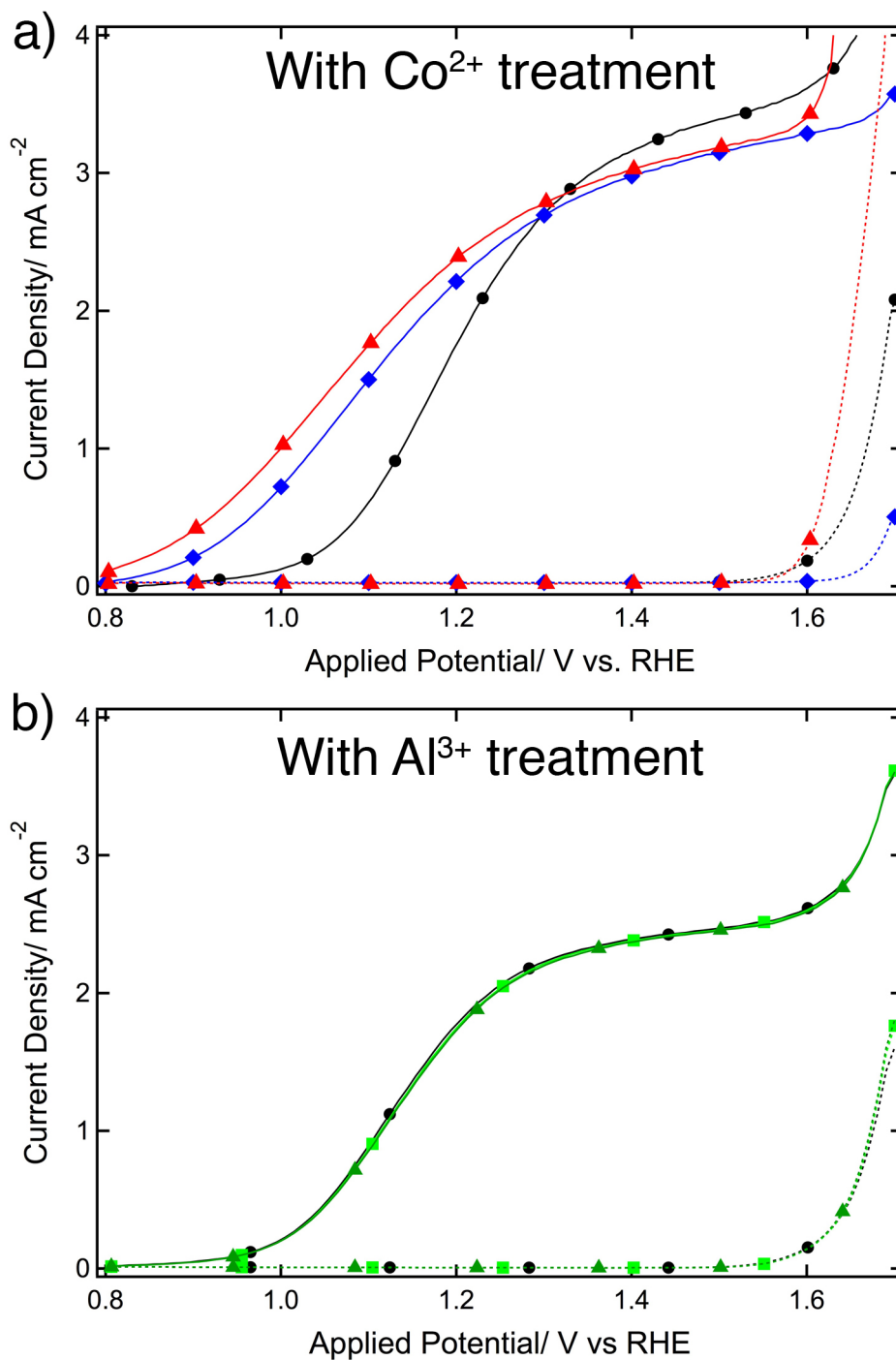


Figure 6.5: Current densities, in mA cm^{-2} of the prepared photoanodes in the dark (broken lines) and under simulated solar illumination (AM 1.5G 100 mW cm^{-2} , solid curves) are shown as a function of the applied potential *vs. RHE*.

a) A hematite photoanode has been characterized before ALD treatment (black circles), after 3 ALD cycles of alumina and annealed to 400°C (blue diamond) and after subsequent cobalt treatment (red triangles).

b) A control (no ALD treatment) hematite photoanode is shown before (black circles) and after one (light green squares) and two (dark green triangles) Al^{3+} (aq) treatments.

The second observation discrediting a catalytic explanation is that the treatment of the hematite photoanode with an aqueous solution containing Al^{3+} species, analogous to the Co^{2+} treatment, does not improve the onset potential. Third

and finally, the deposition of TiO_2 overlayers (0.1 – 2 nm) by ALD on the nanostructured hematite photoanode does not shift cathodically the onset potential despite the superior OER kinetics known with this material.⁷ These latter two arguments are shown in Figure 6.5b and in Appendix B, respectively. Since the beneficial photochemical effects observed after ALD of the alumina overlayer cannot be explained by an improved catalytic process, it is reasonable to assume that the surface of the nanostructured Fe_2O_3 photoanodes present a high density of trap states, which are partially passivated by the deposited Al_2O_3 overlayer.

6.3.4. Other evidence of surface passivation

In order to further support this hypothesis, the effect of the Al_2O_3 overlayer was investigated by electrochemical impedance spectroscopy (EIS) and photoluminescence spectroscopy. EIS was performed in dark conditions on electrodes covered with 3 ALD cycles and a control electrode (without alumina) both annealed at 300°C for 20 minutes. All samples showed, depending on the applied potential, one or two time constant features in the Nyquist plots (Appendix B, Figure B2). Due to the large surface areas and high carrier concentrations in doped nanostructured electrodes like the APCVD samples used here, the capacitance of the space-charge region, C_{SC} , can be the same order of magnitude as the Helmholtz capacitance, C_H . Therefore it cannot be neglected when fitting the EIS data.²² For that reason, we used an equivalent circuit composed of 2 RC elements in series, which account for the semiconductor and surface processes (Figure 6.6a).²²⁻²⁵ Since electronic processes in the bulk are normally faster than charge transfer processes or diffusion of ions in solution, the low frequency response was assigned to the semiconductor-electrolyte charge transfer resistance (R_{CT}) together with C_H while the high frequency response was accordingly designated to events occurring in the semiconductor with a resistance R_{SC} and its accompanying C_{SC} (see Appendix B). This element is the combination of resistances and capacitances related to transport in the oxide (bulk) layer, charge diffusion in the space charge layer and surface trap charging by electrons and holes. Varying with the applied potential, each of these processes nevertheless has similar time constants. This make them difficult to distinguish and it leads to the observation of only one semicircle at high frequency on the Nyquist plot.²⁶ In Figure 6.6b, R_{CT} (red circles) and R_{SC} (blue squares) are plotted vs. the applied potential for one electrode before (plain lines) and after ALD treatment (broken lines).

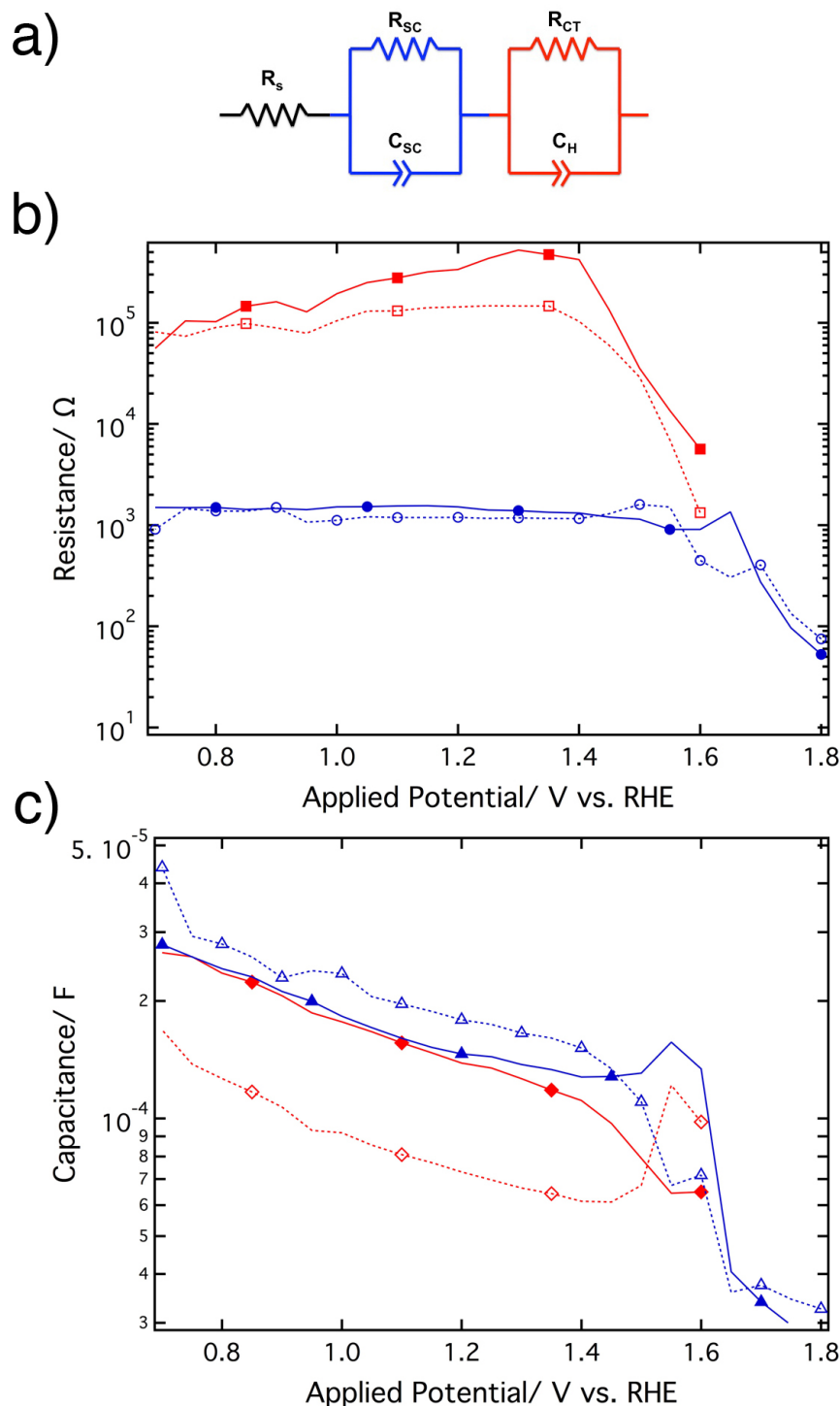


Figure 6.6: a) Electronic equivalent circuit representing the photoanode/electrolyte system used for EIS data modeling. R_s represents a circuit series resistance (constant about 30-40 ohms). The other elements are defined in the main text. b) Representation of the different resistances determined by EIS and plotted vs. the applied potential. The semiconductor resistance (blue circles) and the charge transfer resistance (red squares) are plotted before (full markers, plain line) and after (empty markers, broken line) 3 ALD cycles of Al_2O_3 . c) Representation of the different capacitances determined by EIS and plotted vs. the applied potential. The space charge capacitance (blue triangles) and the Helmholtz capacitance (red, diamonds) are plotted before (full markers, plain line) and after (empty markers, broken line) 3 ALD cycles of Al_2O_3 .

The resistances are stable around 10^5 and $10^3 \Omega$, respectively, before the dark current starts to rise at about 1.6 – 1.65 V vs. RHE causing R_{CT} to drop steeply. We note a decrease in R_{CT} after the ALD treatment, which is consistent with the observed reduction of the overpotential. However, the considerable error associated with fitting such large resistances prohibits any definite conclusions on such a relatively small change in R_{CT} . In contrast, more convincing information on the impact and acting mechanism of the Al_2O_3 overlayer is presented in Figure 6.6c that compares C_{SC} (blue triangles) and C_H (red diamonds) before and after ALD on the same electrode (plain and broken lines, respectively).

The change in C_{SC} with respect to the applied potential before ALD shows the expected relationship: decreasing with increasing applied bias potential because of an increasing space charge (depletion) width. Just as the electrode enters a region of inversion that results in increased capacitance, charge transfer begins due to water oxidation and the capacitance drops suddenly. In accordance with other reports, C_H shows a similar relationship with the applied potential to that of C_{SC} ,²² but the behavior of C_H in highly doped nanostructured devices is not fully understood. Nevertheless, the effect of the Al_2O_3 overlayer becomes clear when comparing C_{SC} and C_H before and after ALD: C_{SC} increases and C_H decreases significantly. This effect was consistently observed on the samples tested. To rationalize this change we first recall that a capacitance is, by definition, the ability of a body to hold charges, and is most simply exemplified by a parallel plate capacitor: $C = Q / V$, with Q for the charge and V for the voltage. Thus the decrease of C_H after the ALD treatment must be caused by a modification of the voltage or charge distribution at the SCLJ. This could be explained by improved charge screening of the anions in the Helmholtz layer due to the relatively high dielectric alumina overlayer or by a reduction of the charge density on the surface due to the passivation of surface states. Both effects would lead to an increase in voltage V , or decrease in charge density Q , and ultimately, would lower the capacitance according to the parallel-plate model. The increase of the space charge capacitance can also be understood by this simplification as well: in the absence of surface states, charges (an increase in Q) are depleted from the space-charge layer (rather than from surface states) to balance the applied voltage. Even though the parallel-plate model represents a significant simplification of the photoelectrochemical processes, it remains clear that the large change in the charge distribution, evidenced by change in capacitances, occurs over the entire voltage range cathodic of the water oxidation onset (i.e. 0.7 – 1.6 V vs.

RHE). This would not be expected if the overlayer was merely acting to enhance the catalytic activity.

Recently, Hu *et al.*²⁷ explained the reduced overpotential they observed when treating hematite photoanodes with CoF₃ by a cathodic shift of the conduction and valence band energies evidenced by a modification of the flat band potential, V_{fb}. To investigate this possibility, we performed Mott-Schottky analysis before and after Al₂O₃ deposition. The Mott-Schottky (MS) equation links the inverse of the square capacitance with the donor density, N_D, and the flat band potential, V_{fb}, starting from Poisson's equation coupled with Boltzmann's distribution to describe the distribution of charges in the space charge region and Gauss' law relating the electric field at the interface.²⁸ The MS equation is given by:

$$\frac{1}{C^2} = \frac{2}{\epsilon \epsilon_0 A^2 e N_D} \left(V - V_{fb} - \frac{k_B T}{e} \right)$$

where C and A are the interfacial capacitance and area, respectively, V the applied voltage, k_B is the Boltzmann constant, ε the dielectric constant of the semiconductor, ε₀ the permittivity of free space, T the absolute temperature and e the electronic charge. The MS analysis of the space charge capacitance (obtained from fitting of the EIS response) was performed in the linear region of the C⁻² plot from 0.7 to 1.3 V vs. RHE. A dielectric constant ε = 80 for α-Fe₂O₃,²⁹ and an active area of 5.94 cm² (*i.e.* a geometric area of 0.283 cm² times a roughness factor of 21)¹⁸ were used to extract the flat band potential and the donor density of a hematite photoanode (full blue markers on Figure 6.7) and a hematite photoanode covered with 3 ALD cycles of alumina (empty blue triangles on Figure 6.7). Linear regression of the MS plots led to coefficients of determination, R², of 0.994 and 0.965 for the hematite electrode before and after ALD of the Al₂O₃ overlayer, respectively.

From the MS analysis, the following figures for the parameters of interest were extracted: V_{fb} = 0.53 V and 0.52 V vs. RHE, and N_D = 7×10²⁰ and 1×10²¹ cm⁻³ for the electrode before and after the Al₂O₃ ALD, respectively. These values are in good agreement with previous results obtained for similar nanostructures¹⁸ and flat band potentials found in the literature^{7,9,29}. In addition, the Mott-Schottky analysis confirms that the alumina overlayer does indeed decrease the overpotential for the photocurrent onset while leaving the flat band potential unchanged as expected for the case of surface-state passivation.

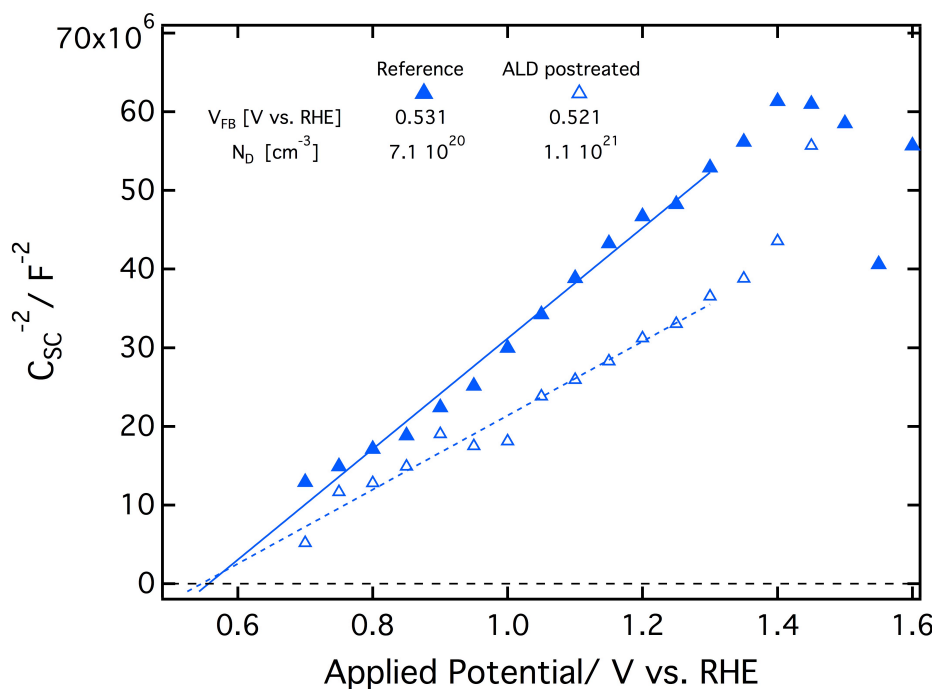


Figure 6.7: Mott-Schottky analysis of a hematite photoanode before (full triangles, plain line) and after (empty triangles, broken line) 3 ALD cycles of alumina. The inverse of the square space charge capacitance is plotted vs. the potential applied during the impedance measurement.

The inferred passivation of surface traps by the Al_2O_3 overlayer is expected to affect the recombination pathways of the photo-excited holes at the SCLJ. This effect is exemplified by an increased photoluminescence quantum yield typically observed in semiconductor quantum dots when coated with a conformal shell to eliminate surface trapping states.³⁰ Various studies on nanocrystalline Fe_2O_3 particles have confirmed that photoluminescence in hematite due to direct hole-electron recombination is highly dependent on surface quality and, especially, on surface trap density.^{31,32} The absorption of a photon with energy greater than the band gap in hematite can be considered to create highly-localized excitonic states.³¹ In the bulk these excitons do not exhibit photoluminescence due to resonant energy transfer between cations and efficient lattice and magnetic relaxation pathways. Accordingly, photoluminescence is generally not observed in hematite except in nanocrystalline systems with specific surface capping agents.³² Since surface traps play a role in the nonradiative recombination of excitons present at the surface in hematite, photoluminescence should be enhanced if surface states are even partially eliminated by the alumina overlayer. Figure 6.8 shows the results of a photoluminescence study of our hematite films with and without the ALD overlayer measured in air and without applied bias.

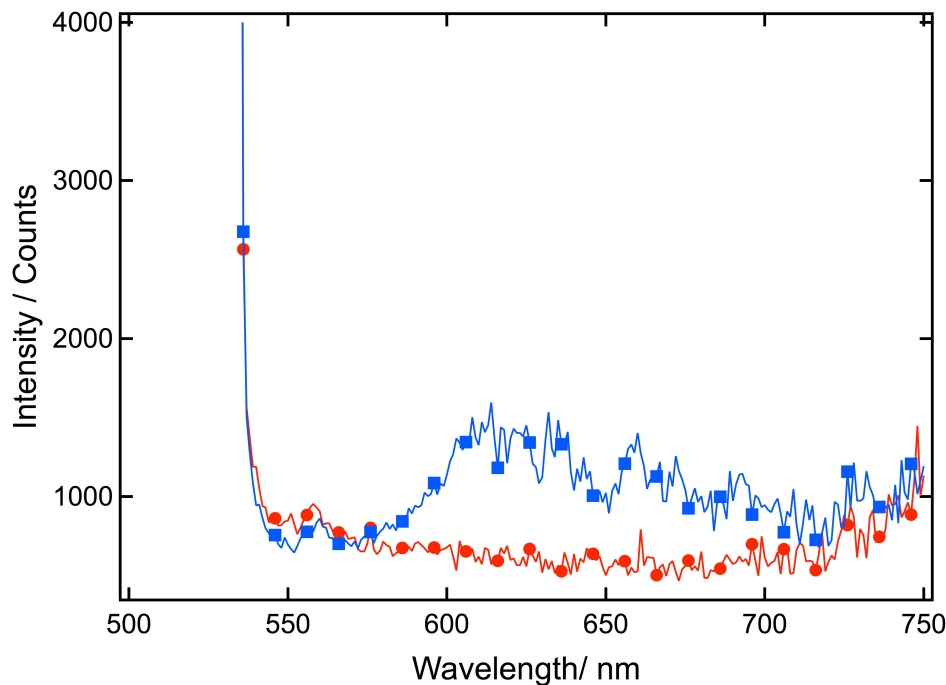


Figure 6.8: Photoluminescence emission spectra (excitation wavelength = 520 nm) of a hematite cauliflower-type nanostructure photoanode before (red circles) and after 3 ALD cycles of Al_2O_3 , on its surface (blue squares).

While the control photoanode shows no presence of photoluminescence when excited at 520 nm, the electrode with 3 ALD cycles shows a weak and broad emission beginning at 580 nm (2.1 eV), peaking at 620 nm and tailing off at 720 nm to match the increasing background of the control sample. The onset of the emission at 2.1 eV is similar to other reports of photoluminescence in hematite,³² and corresponds well with the reported optical band gap. Moreover, this emission shows that a portion of photogenerated excitons is recombining radiatively. The induced photoluminescence after ALD is strong evidence that a fraction of the inter-bandgap surface states are passivated by the Al_2O_3 overlayer. Finally, no photoluminescence was observed when a control $\alpha\text{-Fe}_2\text{O}_3$ electrode was treated only with the Co^{2+} catalyst indicating that surface states are not passivated by this treatment and further discounting a possible catalytic role of the alumina overlayer.

The results obtained from the various analytical techniques confirm the presence of surface trapping states on the nanostructured hematite photoanodes prepared by APCVD. Physically, the energetic traps could be a result of a disordered crystalline surface¹⁸ creating dangling bonds or oxygen vacancies. The filling of oxygen vacancies by the alumina overlayer is likely given that Al_2O_3 is generally thought to have negligible nonstoichiometry³³ while oxygen vacancies are often observed in Fe_2O_3 as the presence of Fe^{2+} .^{7,34,35} Although the alumina overlayers

showed a cathodic shift in the onset of the photocurrent, there remains a significant overpotential even after the addition of the Co^{2+} catalyst (attempts to attach recently reported IrO_2 nanoparticles³ to the Al_2O_3 modified surface were unsuccessful) suggesting that all of the traps are not passivated by the ALD treatment, bulk trapping states are a limiting factor, or a limitation due to tunneling and OER surface intermediates is present.³⁶ This, and the long-term instability of Al_2O_3 under the basic testing conditions will motivate the future investigation of new materials for the overlayer-based passivation, the mechanism of charge transfer and the OER with these materials, and the continued study of the factors limiting hematite photoanodes for solar water splitting.

6.4. Conclusion

In conclusion, the coating of nanostructured hematite photoanodes with a very thin layer (0.1 to 2 nm) of alumina by ALD resulted in a significant decrease in the overpotential required to photo-oxidize water. The photocurrent onset was shifted cathodically by as much as 100 mV and a record water oxidation photocurrent density of 0.42 mA cm^{-2} was obtained at 0.9 V vs. RHE under standard testing conditions after applying a Co^{2+} catalyst. Further investigation by analyzing transient photocurrents, electrochemical impedance, and photoluminescence spectra provided convincing evidence that the cathodic shift afforded by the Al_2O_3 overlayer is due to the passivation of surface trapping states.

Importantly, this study identifies two distinct causes—surface traps and slow oxidation kinetics—for the high overpotential observed in state-of-the-art nanostructured hematite photoanodes. Future studies should focus on such surface treatments of hematite in order to further reduce the overpotential as well as the application of these overlayers to other metal oxide surfaces in order to facilitate interfacial electron transfer in different systems. In general, such post-treatments of metal oxide surfaces, like the one reported here, are of great interest to many research fields such as fuel cells, photovoltaics, sensors, and light-emitting electrochemical cells. The realization of high efficiency electron transfer at nanostructured interfaces in these systems will ultimately allow the use of inexpensive materials and processing techniques for high performance devices.

6.5. References

- (1) Le Formal, F.; Tétreault, N.; Cornuz, M.; Moehl, T.; Grätzel, M.; Sivula, K. *Chem. Sci.* **2011**, 2, 737.

- (2) Brillet, J.; Cornuz, M.; Le Formal, F.; Yum, J.-H.; Graetzel, M.; Sivula, K. *J. Mater. Res.* **2010**, *25*, 17.
- (3) Tilley, S. D.; Cornuz, M.; Sivula, K.; Graetzel, M. *Angew. Chem. Int. Edit.* **2010**, *49*, 6405.
- (4) Kay, A.; Cesar, I.; Graetzel, M. *J. Am. Chem. Soc.* **2006**, *128*, 15714.
- (5) Zhong, D. K.; Sun, J.; Inumaru, H.; Gamelin, D. R. *J. Am. Chem. Soc.* **2009**, *131*, 6086.
- (6) Iwanski, P.; Curran, J.; Gissler, W.; Memming, R. *J. Electrochem. Soc.* **1981**, *128*, 2128.
- (7) Dare-Edwards, M.; Goodenough, J.; Hamnett, A.; Trevellick, P. *J. Chem. Soc. Farad. T. 1* **1983**, *79*, 2027.
- (8) Horowitz, G. In *J. Electroanal. Chem.* **1983**, *159*, 421.
- (9) Sanchez, C.; Sieber, K.; Somorjai, G. *J. Electroanal. Chem.* **1988**, *252*, 269.
- (10) Ahmed, S.; Leduc, J.; Haller, S. *J. Phys. Chem.-Us* **1988**, *92*, 6655.
- (11) Leduc, J.; Ahmed, S. *J. Phys. Chem.-Us* **1988**, *92*, 6661.
- (12) Kim, H.; Lee, H.-B.-R.; Maeng, W.-J. *Thin Solid Films* **2009**, *517*, 2563.
- (13) Li, T. C.; Goes, M. S.; Fabregat-Santiago, F.; Bisquert, J.; Bueno, P. R.; Prasittichai, C.; Hupp, J. T.; Marks, T. J. *J. Phys. Chem. C* **2009**, *113*, 18385.
- (14) Cornuz, M.; Grätzel, M.; Sivula, K. In *Chem. Vap. Deposition* 2010; Vol. 16, p 291.
- (15) Puurunen, R. *J. Appl. Phys.* **2005**, *97*, 121301.
- (16) Seaman, C. *Sol. Energy* **1982**, *29*, 291.
- (17) The photocurrent onset potential is defined for this work as the potential where the line tangent to the inflection point of the photocurrent rise intersects the dark current. This method overestimates the onset potential as compared to visual inspection, but provides a quantitative measure.
- (18) Cesar, I.; Sivula, K.; Kay, A.; Zboril, R.; Grätzel M. *J. Phys. Chem. C* **2009**; *113*, 772.
- (19) Brillet, J.; Grätzel, M.; Sivula, K. *Nano Lett.* **2010**, *10*, 4155.
- (20) Le Formal, F.; Graetzel, M.; Sivula, K. *Adv. Funct. Mater.* **2010**, *20*, 1099.
- (21) By integrating the measured photocurrent density minus the steady-state value of the photocurrent ($C\text{ cm}^{-2}\text{ s}^{-1}$) with respect to time, we obtain a value proportional to the number of positive charges accumulated at the surface (i.e. $C\text{ cm}^{-2}\text{ s}^{-1}\times s = C\text{ cm}^{-2}$) in analogy to calculating the charge accumulated at a capacitor by integrating $i(t)dt$.

- (22) Wielant, J.; Goossens, V.; Hausbrand, R.; Terryn, H. *Electrochim. Acta* **2007**, *52*, 7617.
- (23) McAlpine, N.; Fredlein, R. *J. Electroanal. Chem.* **1988**, *252*, 61.
- (24) Aroutiounian, V.; Arakelyan, V.; Shahnazaryan, G.; Stepanyan, G.; Turner, J.; Kocha, S. *Electrochim. Acta* **2000**, *45*, 1999.
- (25) Aroutiounian, V.; Arakelyan, V.; Shahnazaryan, G.; Stepanyan, G.; Khachaturyan, E.; Turner, J. *CR. Chim.* **2006**, *9*, 325.
- (26) Leng, W.; Zhang, Z.; Zhang, J.; Cao, C. *J. Phys. Chem. B* **2005**, *109*, 15008.
- (27) Hu, Y.-S.; Kleiman-Shwarscstein, A.; Stucky, G. D.; McFarland, E. W. *Chem. Commun.* **2009**, 2652.
- (28) Gelderman, K.; Lee, L.; Donne, S. W. *J. Chem. Educ.* **2007**, *84*, 685.
- (29) Kennedy, J.; Frese, K. *J. Electrochem. Soc.* **1978**, *125*, 723.
- (30) Reiss, P.; Protiere, M.; Li, L. *Small* **2009**, *5*, 154.
- (31) Sherman, D. M.; Waite, T. D. *Am. Mineral.* **1985**, *70*, 1262.
- (32) Zou, B. S.; Volkov, V. *J. Phys. Chem. Solids* **2000**, *61*, 757.
- (33) Atkinson, K.; Grimes, R.; Levy, M.; Coull, Z.; English, T. *J. Eur. Ceram. Soc.* **2003**, *23*, 3059.
- (34) Gardner, R.; Tanner, D.; Sweett, F. *J Phys Chem Solids* **1963**, *24*, 1183.
- (35) Rosso, K.; Smith, D.; Dupuis, M. *J Chem Phys* **2003**, *118*, 6455.
- (36) The conformal nature of ALD and the large number of cycles used for the thickest case suggest that a tunneling mechanism is necessary for electron transfer. A recent report with TiO₂ electrodes and a tunnel-barrier overlayer of MgO (L. Guo, D. Hung, W. Wang, W. Shen, L. Zhu, C.-L. Chien, P. C. Searson, *Appl. Phys. Lett.* **2010**, *97*, 063111-063113) showed that high water oxidation photocurrents can be obtained through a tunnel barrier without a transition metal oxide surface. The OER reaction presumably occurs through the homolytic decomposition of OH⁻ groups as was shown by F. Freund, N. Scheikh-ol-Eslami, H. Gentsch, *Angew. Chem. Int. Edit.* **1975**, *8*, 568.

CHAPTER 7.

PHOTOVOLTAGE AND PHOTOCURRENT

TRANSIENTS OF HEMATITE

PHOTOANODES

This chapter presents a study of the photocurrent and photovoltage behavior of water splitting $\alpha\text{-Fe}_2\text{O}_3$ photoanodes. Hematite thin film electrodes were prepared by atmospheric pressure chemical vapor deposition, exhibiting cauliflower-type nanostructures. Photocurrent transients were measured under white light bias and potentiostatic conditions in two different electrolytes: 1M NaOH and 1 M NaOH + 0.5 M H_2O_2 . Photovoltage transients were also measured under white light bias and galvanostatic conditions in the same electrolytes.

A quantitative method is developed to characterize the charges accumulating in the material during water oxidation (but not during hydrogen peroxide oxidation). This accumulation is also assumed to occur in surface states due the different accumulation observed at different white light bias. The amplitudes of the photocurrent transients in H_2O_2 are fit with two different models: a classical paradigm including a space charge layer and a more modern description which considers no space charge layer and electron conduction based on multiple trapping. The classical model shows a better fit and reasonable values of the space charge width (5 – 10 nm) and the hole diffusion length (0.5 – 1.5 nm) are extracted. Characterization of the photovoltage transients suggests the presence of Fermi level pinning at small applied

potential due to the presence of surface states. Finally, two time constants are determined from photovoltage and photocurrent dynamics. These time constants are compared to those found with other dynamic techniques and assigned to bulk transport and to surface events for holes.

Overall this work represents a new method to characterize the surface of water splitting photoelectrodes and especially the charge accumulation occurring during water splitting. It also confirms that nanostructuring with a maximum feature size of 5 – 10 nm (corresponding to the space charge layer width added to the hole diffusion length) is required for hematite, and suggests that surface control with trap passivation is necessary to decrease the high overpotential observed for water oxidation.

7.1. Introduction

While the nanostructuring efforts with hematite discussed in this thesis (see Chapter 2) and by others have been successful at increasing the photocurrent delivered by hematite photoelectrodes for solar water splitting, the commercial application of a hematite-based tandem cell remains limited by the large overpotential. The high overpotential and late onset of the photocurrent has been observed by several groups using different material preparation techniques. It corresponds to 0.4 – 0.6 V anodic of flat band potential, if we consider it a value of + 0.55 V vs. RHE for V_{fb} (as measured by impedance spectroscopy for these nanostructures).¹ This late onset has been assigned to poor oxygen evolution (OER) kinetics on $\alpha\text{-Fe}_2\text{O}_3$ surfaces and the successful reduction of the overpotential has been attained with deposition of an OER catalyst such as Co^{2+} ,² CoPi ,³ or IrO_2 nanoparticles.⁴ The study presented in chapter 6, showed that the large overpotential was not only a kinetic issue as an Al_2O_3 passivating layer also decreases the onset potential. That study suggested that surface states play a key role in the observed large overpotential for water splitting.

Despite these recent efforts, much more understanding is needed to fully characterize operation and limitations of the state-of-the-art nanostructured hematite electrodes. To this end, this chapter presents a new method using photocurrent and photovoltage transients to examine the events occurring on the surface at biases between the flat band potential and the onset of the photocurrent. Previous studies of iron oxide photocurrent transients have qualitatively explained the observed behavior when illumination is chopped (i.e. alternated between dark and illuminated) under

potentiostatic control according to the Gerischer model. When light reaches the sample, photoinduced charges migrate (driven by the space charge electric field) and accumulate at interfaces, especially holes at the semiconductor-liquid-junction (SCLJ). During the accumulation process, an anodic current spike is measured which decreases rapidly as the accumulated holes perturb the charge distribution in the space-charge layer. Eventually, a steady state between water oxidation and carrier recombination is attained which depends on the light intensity and the applied potential.⁵ When the light is turned off, electrons from the circuit rush in to recombine with the accumulated holes and a cathodic transient spike is then observed. However the high donor density brought by significant doping lead to formation a space charge in the same length scale than the feature size. The accumulation of charges at the surface will also perturb the depletion layer. Therefore this chapter will also discuss the existence of a space charge layer in water at low biases.

When performed at fixed applied external potential, the photocurrent transient response can be analyzed to characterize electrode limitations and reaction pathways. The hole accumulation observed as an anodic current transient upon illumination has been attributed to slow OER kinetics but also to presence of hole trapping states at the hematite.⁶ These trap states, sometimes only observable with transient studies,⁷ are also considered for a cause of the large required overpotential because they offer possibilities of recombination for holes at the surface and back-reaction with redox species⁸ but were assumed by Wilhelm et al. to be causing the primary mechanism of charge transfer at the surface through resonance tunneling.⁹ Surface states were also presumed to cause Fermi level pinning in some cases.^{5,10,11}

The previous studies have offered a qualitative assessment of these transients, however systematic studies enumerating the accumulated charges and discussing numerically the effect of these stored holes on the current and voltage transients are missing. It is therefore needed to develop a method to give numbers to this accumulation process. Achieving this is expected to facilitate the establishment of a comprehensive electric model for the photanodes. When established, this model could be compared with those developed through other analytical techniques (EIS, PEIS). This study presents a quantitative analysis of these photocurrent transients as well as photovoltage transients obtained in the same conditions (bias light and a bias current corresponding to the bias voltage used in the photocurrent study). First the methodology used to quantify the dynamic measurements is detailed. Then the transient photocurrent amplitudes are investigated and two models are introduced

leading to the quantification of some material properties. In the third part, the accumulated charge density is measured, which brings insights into the electronic nature of surface states. The photovoltage transients are studied in the fourth part, and the surface states are further characterized. Finally, the time constants determined with the exponential fitting of the transients are discussed.

7.2. Experimental

7.2.1. Hematite photoanode preparation

Nanostructured iron oxide films were prepared in a home-made APCVD chamber according to the method presented at first by Kay et al.² and optimized in 2010.¹² The deposition can be briefly summarized as follows. Argon (99.9999%) was bubbled through a small amount (0.5 mL) of iron ($\text{Fe}(\text{CO})_5$, Aldrich 99.999%) and silicon (TEOS, Aldrich 99.999%) precursor vials (2 mL) before being mixed with dry air (molecular sieve 5 \AA and a 0.22 μm Millipore filter) and carried through a 12 mm deposition tube arriving perpendicular to the substrate from a distance of 25 mm. The tube carrying the precursors was embedded in a larger cold-wall reactor cylinder (borosilicate glass, ID = 93 mm, OD = 100 mm, height 250mm) and surrounded by a dry air sheath-flux (ca. 20 L min⁻¹). Substrates consisted of 12mm x 30 mm F: SnO_2 on float glass, TEC 15, lying on a 50mm x 25mm x 12mm titanium block heated by two 250W Probag cartridge heaters. Temperature was controlled by a proportional controller using a type-k thermocouple.

The deposition time and doping level were optimized to obtain the best photocurrent voltage characteristics.¹² An interfacial layer of SiO_x was first deposited on the FTO substrate by starting the TEOS flux 3 minutes before adding the $\text{Fe}(\text{CO})_5$ flux to the carrier gas. A circular spot of Fe_2O_3 (with a diameter of ca. 1.5 cm) was then obtained on the SnO_2 substrate showing a radial thickness profile. The hematite sample used in this study was deposited with a carrier gas flow of 6 L min⁻¹ (3 min deposition resulting in a thickness of 600-800 nm) and the silicon doping was assumed to be about 1.5 at. % (according to the last optimization).²

7.2.2. Photoelectrochemical characterization

The APCVD sample was characterized photoelectrochemically in a closed cell (“cappuccino cell”) allowing contact with a sufficient volume of electrolyte (about 20 mL) and a 0.502655 cm² aperture for illumination. The total surface immersed into the electrolyte was about 2.5 cm². The sample was always characterized from front

side illumination, *i.e.* the light path is first arriving on the hematite layer before reaching the substrate.

Two different electrolytes were used in this study: first a 1 M NaOH (Reactolab SA) solution is prepared in distilled water (proanalysi Milli-Q water, 25°C), pH = 13.6¹³ and a second one is prepared by adding 0.5 M H₂O₂ (Reactolab SA) to the first one. The sample was measured within the two hours following the preparation of the second electrolyte to avoid any bubble formation.

Electric currents and voltages were applied or measured, depending on the characterization, with a Keithley 2602 Meter. The source meter is controlled by a computer with a custom program (IGOR PRO software) through a PCI-GPIB card. The source meter was used in a 4-wires configuration, with the sense wires connecting the working electrode and the reference electrode (to control/measure the voltage), the other wires connecting the working electrodes and the counter electrode (to control/measure the current). Potentials are applied to the Ag/AgCl reference electrode but are reported here against the reversible hydrogen electrode (RHE) according to the Nernst equation.²

The white light bias is brought by an array of white photodiodes (Philips Lumileds, Model white star LXHL-NWE8). The same application that is used to apply or measure photocurrent or photovoltage, also controlled the intensity of the white photodiodes through a DAQ card (National Instrument). The power of illumination has been set to 100 mW cm⁻², 50 mW cm⁻², and 10 mW cm⁻² as measured with a Si diode. These white light bias powers are labeled as 1 sun, 0.5 sun and 0.1 sun in the following text, since it corresponds to AM 1.5 G standards in terms of power (but not in terms of spectrum). The white LEDs have an emission spectrum with fewer UV photons but a larger blue component as compared to the xenon arc lamp typically used. Therefore photocurrent densities measured here are slightly higher than the ones measured with a xenon lamp because hematite is known to be more efficient for short wavelengths (blue light) than for the long wavelengths (red light). This setup has only small modifications from the one used in a study of dye sensitized solar cells by our group.^{14,15}

The light perturbation used to measure the transients is also induced by an array of blue photodiodes (Philips Lumileds, Model LXHL-NB98). The blue photodiodes presents a narrow emission around 470 nm and were used due to the high absorption coefficient of hematite at short wavelengths. The intensity of the diodes was manually controlled and set in a way to observe photocurrent and

photovoltage transient signal for each applied potential or current and for each white light bias. This power has been converted in a maximum photocurrent of 4.34 mA cm⁻² with the measurement of a Si diode photocurrent. Unless otherwise stated, the power of the blue pulse perturbation has been maintained constant at this power for all experiments. A pulse width of 0.5 s was produced after a stabilization of 4 s under the base experimental conditions (i.e. under white light bias and applied potential or current bias). Photocurrent or photovoltage data were recorded every 0.001 s approximately for 2.2 s after the beginning of the measurement.

For the photocurrent measurements, the sample was held in the electrolyte under a fixed potential and a fixed white light bias (1 sun, 0.5 sun or 0.1 sun) for 4 seconds before the blue light pulse was emitted for 0.5 s. The intensity of the blue diode pulse was minimized as much as possible, in a way that a current transient is still observable in 1 M NaOH at 0.7 V vs. RHE. Photocurrent transients are recorded every 50 mV from 0.7 V to 1.2 V vs. RHE and every 100 mV from 1.2 V to 1.4 V vs. RHE.

The photovoltage transients were recorded while the photoelectrode was held in the electrolyte at a fixed current flowing between the working electrode and the counter electrode, and again white light bias (1 sun, 0.5 sun and 0.1 sun). The blue diode pulse is switched on after 4s and for 0.5 s. In order to allow comparison between photocurrent transient and photovoltage transient measurements, the applied current was fixed for all measurements (at 0.1, 0.5 and 1 sun in 1 M NaOH and in 1 M NaOH + 0.5 M H₂O₂ electrolytes) with the current obtained in the JV characterization (see Figure 7.1) at the same potentials where photocurrent transients are measured. The dark current obtained for both hydrogen peroxide and water oxidation is close to zero at applied potentials lower than 1.5 V vs. RHE. Therefore, it is impossible to fix a current corresponding to the fixed potential, where the photocurrent transient is measured. To allow comparisons of photocurrent and photovoltage transient in similar conditions, this study has consequently not been performed in dark conditions.

7.3. Methodology

7.3.1. Photocurrent characterization

Figure 7.1 shows the performance of the APCVD hematite photoanode measured in 1 M NaOH electrolyte (plain lines) and in 1 M + 0.5 M H₂O₂ (broken lines), under three different light fluxes brought by a white diode array and

corresponding to 1 sun (red circles), 0.5 sun (orange squares) and 0.1 sun (blue triangles). Dark currents are not shown on Figure 7.1 but can be found in another study of the same nanostructured hematite photoanodes in the two electrolytes investigated here.¹

The measured photoelectrode exhibits a typical response of an APCVD grown hematite sample under 1 sun. Water oxidation photocurrent onsets at *ca.* 0.9 – 1.0 V vs. RHE in 1 M NaOH electrolyte (pH 13.6), the current density then increases rapidly, attaining approximately 2.2 mA cm^{-2} at 1.23 V vs. RHE bias and reaches a plateau of about 3.5 mA cm^{-2} from 1.4 V to 1.6 V vs. RHE. One can notice the slightly better photocurrent obtained after the onset as compared to the previous reports with the same nanostructured photoanodes ($3.1 - 3.3 \text{ mA cm}^{-2}$).^{4,6,12} This is explained by the solar illumination source used in this study, which has a spectrum with a greater blue light component than conventional illumination source, as detailed in the experimental section. Under 0.5 sun (50 mW cm^{-2} , orange squares) and 0.1 sun (10 mW cm^{-2} , blue triangles) solar illumination, the photocurrent plateau is decreased compared to 1 sun condition as expected. Indeed, the photocurrent plateau is found to be almost linear *vs.* the solar illumination power with the following current density measured at 1.43 V vs. RHE: 0.38, 1.89 and 3.51 mA cm^{-2} for 0.1 sun, 0.5 sun and 1 sun respectively.

The onset potential of the water splitting photocurrent can be most clearly defined by the potential where the tangent of the photocurrent at the onset inflection point crosses the linear extrapolation of the exchange current observed before the photocurrent onset. This onset is measured to be similarly around 1.05 V vs. RHE for all bias light (1.055, 1.053 and 1.049 V for 1 sun, 0.5 sun and 0.1 sun respectively).

The same electrode was also photoelectrochemically tested in an aqueous electrolyte containing 1 M NaOH and 0.5 M H₂O₂ (empty markers and dotted line on Figure 7.1). Under 1 sun illumination (empty red circles), the photocurrent density onsets (defined here as the potential where the photocurrent become positive) at *ca.* 0.72 V vs. RHE and reaches a plateau (with still a slight increasing slope), similar to the one obtained in the aqueous electrolyte not containing hydrogen peroxide. This plateau is attained at 1.0 V vs. RHE, followed by a slow and linear increase (see section 7.4.2) up to the onset of the dark current observed at 1.5 V vs. RHE. Under lower bias light, the behavior of the photoanode is similar to what is obtained at an illumination power of 100 mW cm^{-2} . The onset potentials of the photocurrent appear at 0.74 V and 0.79 V *vs.* RHE for 0.5 sun (orange empty squares) and 0.1 sun

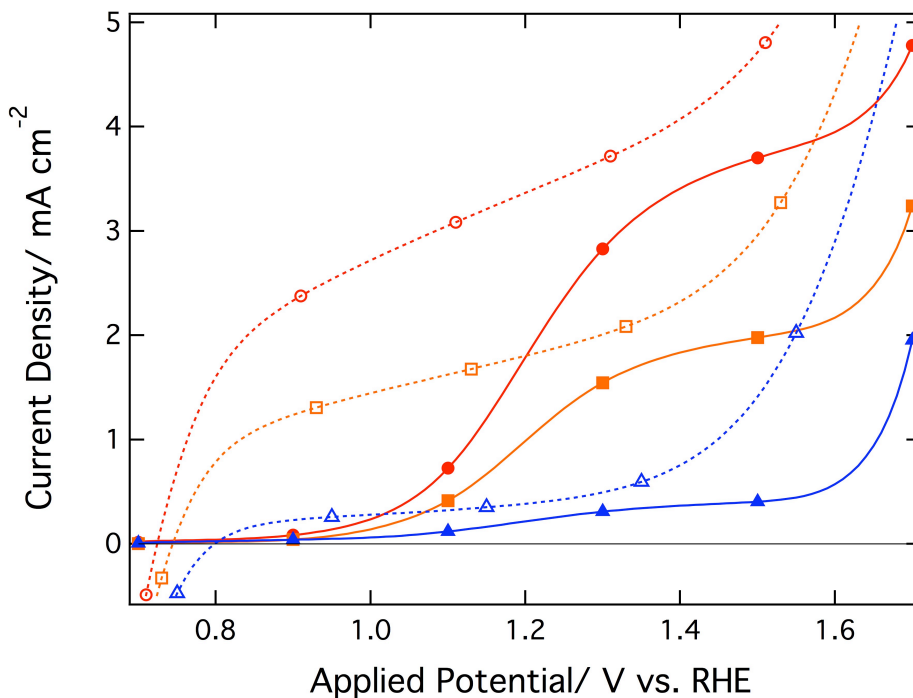


Figure 7.1: Current densities, in mA cm^{-2} of the prepared photoanodes in 1 M NaOH electrolyte (plain lines) and in 1 M NaOH + 0.5 M H_2O_2 electrolyte (broken lines) are shown as a function of the applied potential, with respect to the reversible hydrogen electrode (RHE). Current densities were measured under three different illumination conditions: 1 sun (100 mW cm^{-2} , red squares), 0.5 sun (50 mW cm^{-2} , orange circles) and 0.1 sun (10 mW cm^{-2} , blue triangles).

(empty blue triangles) illumination respectively. A photocurrent plateau, close to the one obtained in 1 M NaOH, is then attained and a slight increase is observed before the dark current onset. The maximum value of the plateau current being similar for both electrolytes is expected as this value has been shown to be related to the nanostructure and especially the amount of material in a certain proximity to the SCLJ.¹

The flat band potential of hematite in the two electrolytes tested in this chapter is about 0.55 V vs. RHE as shown by Dotan *et al.*¹; In 1 M NaOH, this important parameter, *i.e.* the potential where the electronic bands are flat and from which, at more anodic potentials, it should be possible to observe water oxidation photocurrents (in the classical model), has also been determined between 0.4 and 0.6 V vs. RHE and especially around 0.5 to 0.55 V for this type of nanostructures.^{6,16} In the electrolyte containing hydrogen peroxide, the photocurrent onset is close to this flat band potential with an observed overpotential of 0.1 – 0.2 V. In contrary, a large overpotential is observed in the 1 M NaOH electrolyte, in order of 0.5 – 0.6 V.

Classically, the onset potential should be linearly dependent on the logarithm of the light intensity. This onset potential has been shown to be related linearly with

the open-circuit potential, which depends logarithmically on the intensity of the incident light.⁵ It is interesting to observe that the onset is not varying with the bias light intensity in 1 M NaOH but varies in the electrolyte containing hydrogen peroxide. This suggests that additional factors may limit the appearance of photocurrent in NaOH but not in H₂O₂ electrolyte. It could be straightforwardly explained by a difference in oxidation kinetics of hydrogen peroxide and water but other factors such as the accumulation of positive charge in (surface) traps being localized energetically at a level where they can oxidize H₂O₂ but not H₂O are conceivable. Current doubling is not considered in this study for the H₂O₂ electrolyte as it has been shown previously not to occur on the same type of hematite photoanode under anodic polarization in this same electrolyte.¹

7.3.2. Photocurrent and photovoltage transients

Examples of photocurrent and photovoltage transients, obtained in 1 M NaOH at representative conditions (key potentials and their related current) are shown in Figure 7.2. At very low potential, before the onset of photocurrent (Figure 7.2a), a sharp anodic peak appears when the blue light pulse starts. Just after, the current exponentially decreases to reach the steady state photocurrent established with the bias light and the applied potential in the first 0.5 s. Photovoltage transients measured at currents corresponding to the same low applied potential under bias light are shown on Figure 7.2d. First, before the light pulse is switched on, a drift in the steady state potential is observed towards higher potential. Once can also notice that the observed steady state photovoltage does not correspond to the “expected” values as set in the experiments (0.85 V vs. RHE). The drift and the difference between the observed steady state and the expected value is greater at low light intensity (C, blue for 0.1 sun) than at high bias light intensity (B, orange for 0.5 sun and C, red for 1 sun). After the blue pulse is switched on, the photovoltage decreases significantly and quickly reaches a new steady state value. This is explained by the increase in the quasi Fermi level (QFL) of electrons when more light is incident on the sample, decreasing the measured potential. When the light perturbation stops, the photovoltage recovers its original value (after correction of the drift) in a faster manner for high light bias than for the low light bias.

The behavior of the hematite photoanode, in 1 M NaOH, at intermediate conditions is described in Figure 7.2 b and e. The intermediate conditions correspond to potentials ranging from the photocurrent onset and the photocurrent plateau on the JV characterization. The photocurrent transients also exhibit anodic and cathodic

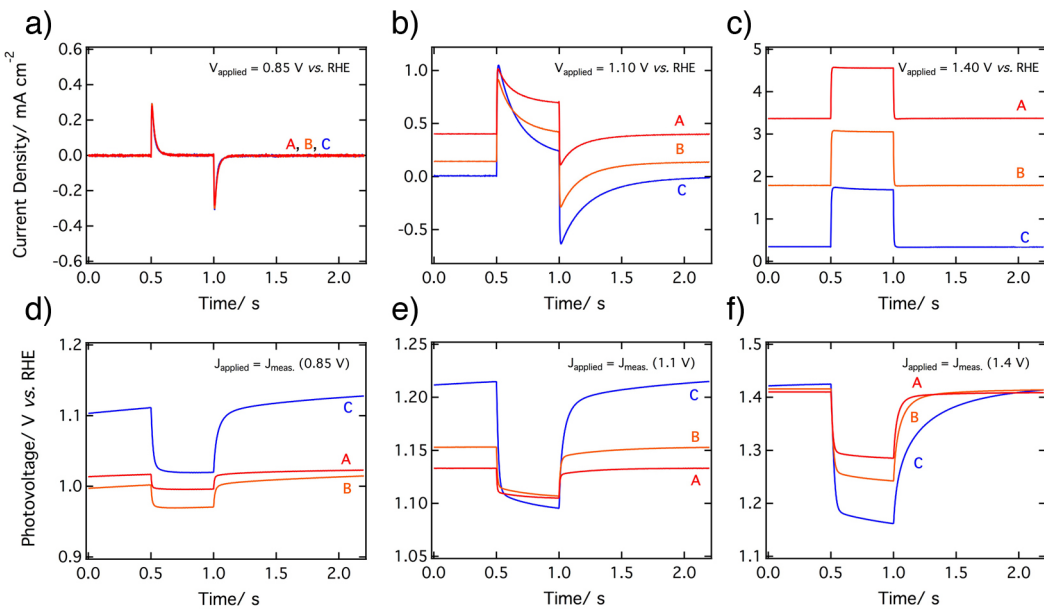


Figure 7.2: Examples of photocurrent transient (a, b and c) and photovoltage transient (d, e and f) recorded in 1 M NaOH electrolyte. Photocurrent transients were recorded while the hematite sample was held at an applied fixed potential of 0.85 V (a), 1.10 V (b) and 1.40 V (c) vs. RHE. A white light bias at an intensity of 1 sun (A, red), 0.5 sun (B, orange) and 0.1 sun (C, blue) was superimposed on the voltage signal. Photovoltage transients were recorded while the hematite sample was held under an applied fixed current that corresponds to photocurrent measured at 0.85 V (d), 1.10 V (e) and 1.40 V (f) vs. RHE and under white light bias at an intensity of 1 sun (A, red), 0.5 sun (B, orange) and 0.1 sun (C, blue). The blue light pulse was in every case started at 0.5 s and length for 0.5 s.

peaks but during the light perturbation pulse, the photocurrent stabilizes to a new steady state value because at these conditions the photocurrent can flow and is proportional to the light intensity. Nevertheless charge accumulation and discharge are still observed. The photovoltage characterization is similar in shape to the one observed in the previous conditions with two exceptions. First the photopotential drift is only observed for the lowest bias light intensity (C, blue for 0.1 sun) and second the measured value of the photopotential is closer to the expected value for the highest bias light intensity: 1.13 and 1.15 V vs. RHE for the measured photopotential at 1 sun and 0.5 sun respectively to be compared to 1.1 V vs. RHE for the expected value.

Finally Figure 7.2 c and f shows the behavior of the photoanode at conditions corresponding to large applied potentials. The photocurrent transient does not exhibit any anodic or cathodic peak for all the bias light used. The photocurrent quickly rises to a new steady state value after the blue light pulse without showing charge accumulation and discharge when the light perturbation is switched off. The photopotentials also show no drift, contrary to lower bias, and are close to the expected value of 1.4 V vs. RHE before the light pulse is switched on. The amplitude

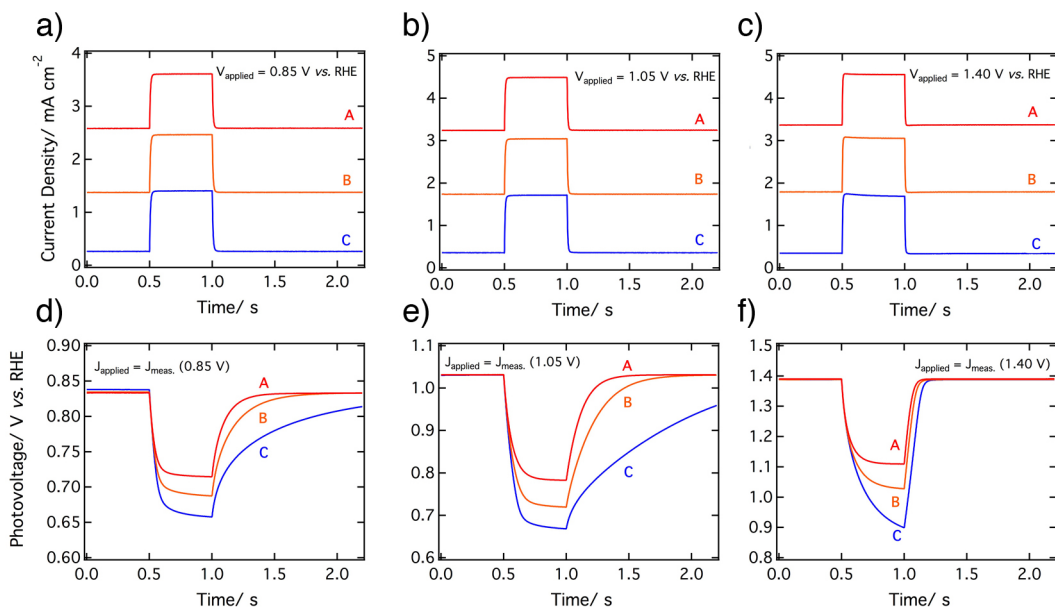


Figure 7.3: Examples of photocurrent transients (a, b and c) and photovoltage transients (d, e and f) recorded in 1 M NaOH + 0.5 M H₂O₂ electrolyte. Photocurrent transients were recorded while the hematite sample was held at an applied fixed potential of 0.85 V (a), 1.10 V (b) and 1.40 V (c) vs. RHE. A white light bias at an intensity of 1 sun (A, red), 0.5 sun (B, orange) and 0.1 sun (C, blue) was superimposed on the voltage signal. Photovoltage transients were recorded while the hematite sample was held under an applied fixed current that corresponds to photocurrent measured at 0.85 V (d), 1.10 V (e) and 1.40 V (f) vs. RHE and under white light bias at an intensity of 1 sun (A, red), 0.5 sun (B, orange) and 0.1 sun (C, blue). The blue light pulse was in every case started at 0.5 s and length for 0.5 s.

of the photovoltage perturbation is larger for the lowest bias light and it seems that a longer time is required for the stabilization of the photocurrent during and after the blue light pulse. This latter observation can be actually considered for all the different photovoltage transients obtained in 1 M NaOH (Figure 7.2 d, and f).

For comparison, a similar example of photocurrent and photovoltage transients obtained in the electrolyte containing H₂O₂ is shown on Figure 7.3. Contrary to the measurement performed in sodium hydroxide, photocurrent transients (Figure 7.3 a, b and c) are similar at the three key potentials shown here. As was similarly observed by Dotan et al.¹, there are neither anodic and cathodic peaks, nor is there charge accumulation. The photocurrent rises promptly to a new steady state value after the blue light pulse and decreases as fast to the ancient steady state value when this one stops. Moreover the additional photocurrent density caused by the blue light pulse absorption (measured with the difference between the steady state photocurrents under the bias light and under both the bias light and the blue light pulse) does not show any dependence of the light bias intensity. In terms of photovoltage, the same behavior is once again observed at every applied current condition. No drift is observed at the lowest bias light and bias applied current. The

measured photopotential is also always close to the expected value. However, in similarity to the measurements performed in NaOH, the amplitude and the time length required for stabilization, seems to increase when the light bias intensity decreases (C – blue for 0.1 sun, B – orange for 0.5 sun and A – red for 1 sun measurements).

In order to perform quantitative comparisons and to extract relevant figures, the raw photocurrent transients and photovoltage transients presented in section 7.3.2 were treated and analyzed. The data treatment and the definition of the quantity discussed in section 7.4 are presented in the next section.

7.3.3. Data treatments

Figure 7.4a shows a typical photocurrent curve obtained in NaOH. The anodic and cathodic peaks are related respectively to positive charge accumulation, and to charges diffusing from the external circuit to recombine with the accumulated hole. These phenomena are both more significant at low bias light and low bias voltage. For applied bias larger than the photocurrent onset potential, a new steady state photocurrent is established under white light bias and the blue pulse. This type of curve is separated in 4 different time domains: t_1 is set between the beginning of the light pulse and the transient maximum, the second one t_2 between the transient maximum and end of the light pulse, the third region t_3 was defined between end of the light pulse and the transient minimum and finally t_4 is set between the transient minimum and the last point of the measurement. The current densities recorded during these different regions are fitted with monoexponential functions (Eq. 7.1) with t_0 being a fixed value equal to the time of the first point of the relative region.

$$J = J_0 + A e^{-\frac{(t-t_0)}{\tau}} \quad (\text{Eq. 7.1})$$

This fitting equation describing the current density can also be found under another form (Eq. 7.2)

$$\frac{J(t)-J_{ss}}{J(t=0)-J_{ss}} = e^{-\frac{t}{\tau}} \quad (\text{Eq. 7.2})$$

Four different time constants are thus obtained for the defined time domains: τ_{J1} , τ_{J2} , τ_{J3} and τ_{J4} . The value J_0 (in Eq. 7.1) related to the second region is defined as the new steady state photocurrent (white light bias + blue pulse). The area set between the measured current density and a square wave defined by the measured steady state photocurrent (only under white light bias) when the blue light pulse is off and equal to J_0 when blue light pulse is on, define the quantity of accumulated charges in the region when light blue pulse is on (red diagonal stripes, approximately

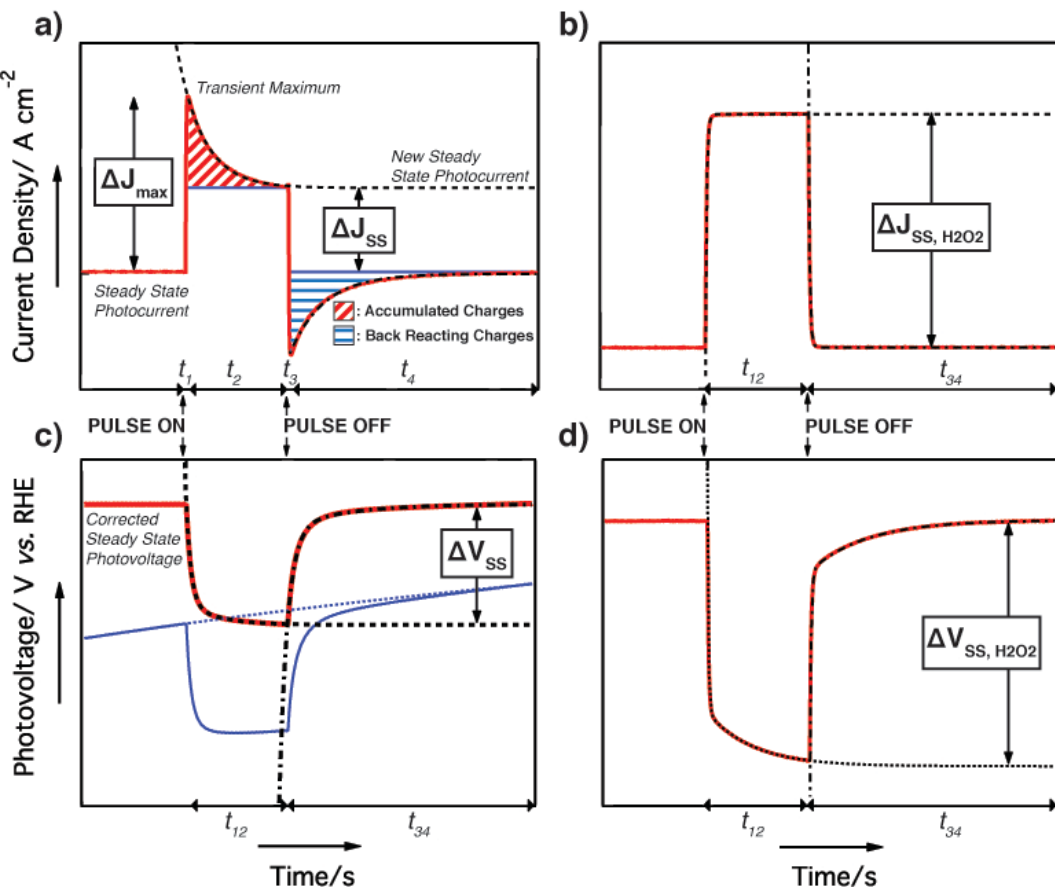


Figure 7.4: Schemes explaining the data treatment of the photocurrent and photovoltage transients studied in this chapter for the following cases. a) Photocurrents transients measured in 1 M NaOH. b) Photocurrents transients measured in 1 M NaOH + 1M NaOH+ 0.5 M H₂O₂. c) Photovoltage transients measured in 1 M NaOH at low bias light intensity and low applied current. d) Photovoltage transients measured in 1 M NaOH at high bias light intensity and large applied current or in 1 M NaOH + 1M NaOH+ 0.5 M H₂O₂. The photocurrent transient peak height is labeled as ΔJ_{max} whereas the amplitude of the photocurrent transient is indicated by ΔJ_{ss} and $\Delta J_{\text{ss}, \text{H}_2\text{O}_2}$ in NaOH and NaOH + H₂O₂ electrolytes respectively. The amplitude of the photovoltage transient is referred with ΔV_{ss} and $\Delta V_{\text{ss}, \text{H}_2\text{O}_2}$ in NaOH and NaOH + H₂O₂ electrolytes respectively.

from 0.5s to 1s) and to the quantity of back reacting charges after the blue light pulse (blue horizontal stripes, approximately from 1s to last point). By integrating the measured photocurrent density minus the steady state value of the photocurrent ($C \text{ cm}^{-2} \text{ s}^{-1}$) with respect to time, we obtain a value proportional to the number of positive charges accumulated at the surface (*i.e.* $C \text{ cm}^{-2} \text{ s}^{-1} \times s = C \text{ cm}^{-2}$) in analogy to calculating the charge accumulated at a capacitor.

When the photocurrent was recorded in the electrolyte containing hydrogen peroxide (Figure 7.3 a, b,c and Figure 7.4b), no charge accumulation was observed during the light pulse. This type of curve is fitted to a monoexponential function in two regions: the first one is between the beginning and the end of the light pulse, and defines a new steady state value (J_0) and one time constant ($\tau_{J_{12}-\text{H}_2\text{O}_2}$). The second

time region, between the end of the light pulse and the last measured point, is fitted in order to define a second time constant ($\tau_{J34-H2O2}$).

Figure 7.4c shows the typical photovoltage transient obtained under low bias potential in 1 M NaOH (blue curve). This curve exhibits a drift before the blue light pulse is switched on. To correct this, the measured photovoltage curve has been fitted between $t = 0$ and the beginning of the blue light pulse to an exponential function (Eq. 7.1, dotted blue line) and the corrected photovoltage (red curve) was obtained with subtracting the exponential part of the fitting function ($A e^{\frac{-(t-t_0)}{\tau}}$). The corrected curve was then fitted to a two exponential function (Eq. 7.3, dotted line broken lines on Figure 7.4 c and d) in two distinct regions: one during the blue light pulse and the second after the pulse.

$$V = V_0 + A_1 e^{\frac{-(t-t_0)}{\tau_a}} + A_2 e^{\frac{-(t-t_0)}{\tau_b}} \quad (\text{Eq. 7.3})$$

Again, four time constants were obtained for each characterization, two for the photovoltage rise (τ_{V12a} and τ_{V12b}) and two for the photovoltage decay (τ_{V34a} and τ_{V34b}). The value of V_0 obtained during the light pulse was used to quantify the photovoltage amplitude (ΔV_{ss}). When measured at high potential in sodium hydroxide and for all bias potential in hydrogen peroxide, the drift before the light pulse is not observed (Figure 7.4d). These photovoltage characterizations are treated in a similar way to the one presented in Figure 7.4c without the drift correction.

The quantities obtained after the data treatment are discussed in the following section in terms of photocurrent transient amplitude, density of accumulated charges, photovoltage transients and time constants.

7.4. Results and discussion

7.4.1. Photocurrent transient amplitudes

The amplitudes of the photocurrent transients, ΔJ_{ss} , are plotted vs. the applied potential referenced to the RHE on Figure 7.5 (plain lines). In 1 M NaOH, these amplitudes are similar to the current voltage characterization presented in Figure 7.1 for the three different white light bias intensities: 1 sun (full red circles), 0.5 sun (full orange squares) and 0.1 sun (full blue triangles). ΔJ_{ss} increased steeply from an applied voltage of ca. 1.0 V vs. RHE (close to the onset potential of the photocurrent), and seems to saturate at about 1.4 V (in the potential range where the photocurrent plateaus) as an inflection point is observed around 1.15 – 1.25 V vs. RHE. The rise of transient amplitudes after the onset, and the height of the saturation

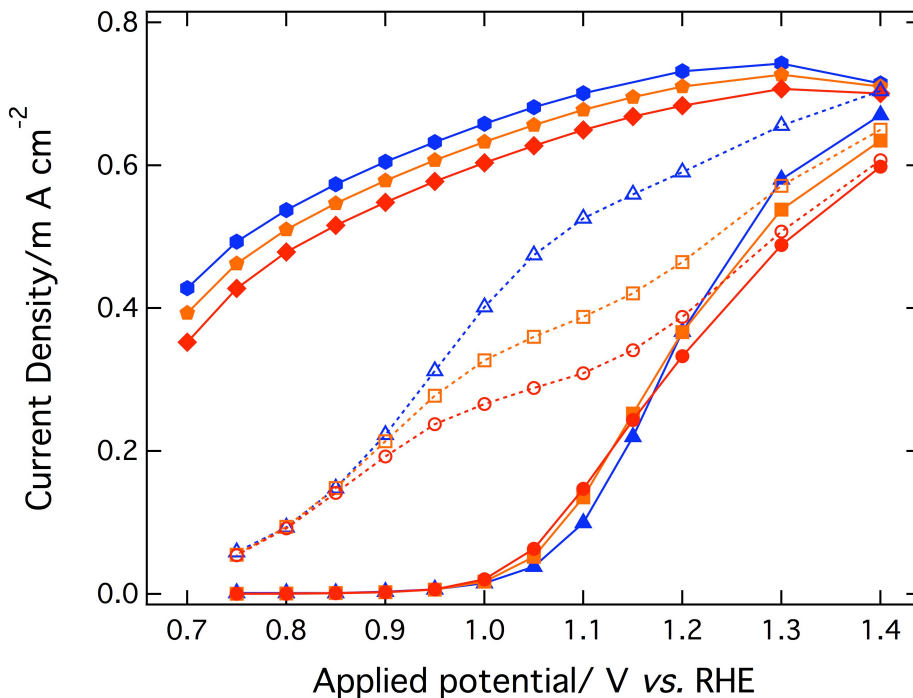


Figure 7.5: The amplitudes of the photocurrent transient (ΔJ_{ss} and $\Delta J_{ss, H_2O_2}$, plain lines and full markers), in mA cm^{-2} , are shown as a function of the applied potential, with respect to the reversible hydrogen electrode (RHE). These photocurrent transients were obtained with a blue light pulse of 0.5 s (corresponding to a maximum current flux of 4.34 mA cm^{-2}) at different bias potential and with a superimposed white light bias of 1 sun (red circles in 1 M NaOH electrolyte, red diamonds in 1 M NaOH + 0.5 M H_2O_2 electrolyte), 0.5 sun (orange squares and orange pentagons for the two different electrolytes), and 0.1 sun (blue triangles and blue hexagons for the two electrolytes). Transient peak heights (ΔJ_{max}) are also shown, for measurement performed in 1 M NaOH, with respect to the reversible hydrogen electrode (RHE) in broken lines. Once more, measurement performed under 1 sun white light bias (empty red circles) are compared to experiments performed under 0.5 sun (empty orange squares) and 0.1 sun white light bias (empty blue triangles).

level are influenced by bias light intensity. The different ΔJ_{ss} are crossing around the inflection point as ΔJ_{ss} has a more anodic onset but a larger value at 1.4 V vs. RHE with decreased bias light intensity.

In the electrolyte containing hydrogen peroxide, the $\alpha\text{-Fe}_2\text{O}_3$ film also exhibits a behavior similar to what is observed in Figure 7.1. $\Delta J_{ss, H_2O_2}$ reaches a photocurrent plateau at about 0.8 – 0.9 V vs. RHE and shows a slight increase with the applied potential. The relation between this amplitude increase and the bias potential will be discussed shortly after. In analogy to measurements performed in sodium hydroxide, the photoelectrochemical performance of the electrode is enhanced at lower white light bias (blue hexagons for 0.1 sun, orange pentagons for 0.5 sun and red diamonds for 1.0 sun). As the photocurrent is predicted to be linear with respect to the photon flux, the slightly more efficient harvesting of the pulsed light observed at

lower bias light is unexpected, and likely indicates a small deviation from linearity in our system.

The heights of the anodic transient peak when the sample is immersed in 1 M NaOH, ΔJ_{max} , are also shown on Figure 7.5 for the three different bias light intensities used: 1 sun (empty red circles), 0.5 sun (empty orange squares) and 0.1 sun (empty blue triangles). For all bias light, ΔJ_{max} is the same at low bias potential and increases modestly up to 0.85 V vs. RHE. At higher bias potential, the transient peak height increases more importantly for lower bias light (blue > orange > red) before attaining saturation at 1.0 V for 1 sun, 1.05 V for 0.5 sun and 1.15 V vs. RHE for 0.1 sun bias light measurement. Then ΔJ_{max} increases to reach ΔJ_{ss} . This corresponds to the disappearance of the anodic and cathodic peaks and is attained at 1.4 V vs. RHE for 1 sun bias light illumination. According to the tendency observed on Figure 7.5, the disappearance of the transient peaks will be attained at a potential slightly higher than 1.4 V vs. RHE for 0.5 sun bias light measurement and at even higher potential for 0.1 sun measurements. The difference between the height of the transient peak and the rise in steady states ($\Delta J_{max} - \Delta J_{ss}$) gives a qualitative characterization of the accumulated charges but depends on the time delay between points recording. In order to compare quantitative characterization of charge accumulation, another method is described in section 7.4.2.

As previously stated, the relationship between $\Delta J_{ss, H_2O_2}$ with the applied potentials can be discussed according to analytical models. The classical model, derived by Gerischer¹⁷ and detailed in Chapter 1, considers the conduction and the valence bands as energetically flat in the bulk of the material, and the formation of an electric double layer at the SCLJ which results in band bending at the interface with the electrolyte. However, it has been suggested recently that this band bending model does not apply to the nanoporous structures investigated here due to the small feature size.¹⁶ The increase in $\Delta J_{ss, H_2O_2}$ with the applied potential is then interpreted with an alternative model by the decrease of the background electron density throughout the film.¹⁸ It is interesting to discuss here which model is the most consistent the additional photocurrent brought by the blue light pulse in hydrogen peroxide electrolyte.

According to Gerischer's theory, the space charge layer is responsible for charge separation when the semiconductor absorbs light. The space charge layer width depends on several factors such as the donor density N_D and the material dielectric constant according to Eq. 7.4.¹⁷

$$W_{SC} = W_0 \sqrt{V_{appl.} - V_{fb}} = \sqrt{\frac{2 \varepsilon \varepsilon_0}{e N_D}} \sqrt{V_{appl.} - V_{fb}} \quad (\text{Eq. 7.4})$$

where ε the relative dielectric constant (taken as 80 for iron oxide)¹³, ε_0 the permittivity of vacuum ($= 8.85 \times 10^{-12} \text{ F m}^{-1}$), e the electronic charge ($= 1.6 \times 10^{-19} \text{ C}$), N_D the donor density, $V_{appl.}$ the applied potential and V_{fb} the flat band potential. As $V_{appl.}$ becomes larger compared to V_{fb} (i.e. as the applied potential becomes more anodic), W_{SC} is predicted by this model to grow with $(V_{appl.})^{0.5}$.

This model neglects charge recombination in the space charge layer and on the surface (electrons should be repelled from the surface by the space charge layer field). Thus we can consider that all positive charges reacting at the surface of the hematite photanode with H_2O_2 are photogenerated from a distance D inside the semiconductor, described by Eq. 7.5.

$$D = W_{SC} + L_{D,Eff.} \quad (\text{Eq. 7.5})$$

where W_{SC} is the space charge layer width, $L_{D,Eff.}$ is the effective hole diffusion length. The actual diffusion length, L_D of the holes is larger than the effective one as only a portion of the charges harvested in a region set between a distance W_{SC} and $W_{SC} + L_D$ will diffuse towards the space charge layer. Invoking another assumption, which is to consider the hole diffusion length as independent of the applied potentials, the active distance in the classical model can be described as a function of the applied potential according to Eq. 7.6.

$$D(V_{appl.}) = \sqrt{\frac{2 \varepsilon \varepsilon_0}{e N_D}} \sqrt{V_{appl.} - V_{fb}} + L_{D,Eff.} \quad (\text{Eq. 7.6})$$

It is not clear if the electrode behavior fits well the classical model due to the small space-charge layer that is in the same length scale as the feature size. For that reason an alternative model is investigated. This alternative model has been developed for materials where electron conduction occurs still in the conduction band but with multiple trapping.^{19,20} In addition, the valence band and the conduction band are flat, from the bulk to the interface with electrolyte, at all applied potentials, predominantly due to charge screening in the semiconductor by ions on the surface. The electron conduction occurs in the conduction band with considering multiple trapping/detrapping of electrons. This conduction is Fermi level dependent, more precisely to take in account the density of filled and unfilled trap states. The jumping rate between states has been found to be optimized at certain Fermi level, called the transport energy. It is common to consider an exponential distribution of energetic states below the band gap. In this case, the chemical diffusion coefficient of majority

charge carriers has can be expressed as an exponential function of the difference of the Fermi level energy and the transport energy. If we apply this multiple trapping conduction based model to our system, the holes reaching the interface with the electrolyte do so only by diffusion. The diffusion length of these holes can be considered dependent on the concentration of electrons in traps. As explained above, the concentration of filled traps decreases exponentially with the Fermi level, which leads to an exponential increase of the hole diffusion length and consequently on the photocurrent with increasing applied potential (accounting for no losses on the surface).

As no charge accumulation (anodic transient peak) is observed in 1 M NaOH + 0.5 M H₂O₂, the current measured is assumed to correspond to positive charges reacting on the surface. The distance inside the iron oxide film responsible for $\Delta J_{ss, H_2O_2}$ has been calculated as followed. First, the maximum amount of additional photocurrent brought by the blue diode pulse was normalized to the pulse intensity (corresponding to 4.34 mA cm⁻², and neglecting reflective losses). A ratio of reacted photogenerated holes to the number of incident photons as a function of the applied potential is thus obtained (between 20 and 30 %, not shown here). As no recombination on the surface is considered, this ratio corresponds to the light absorption of hematite layer within a distance D in the semiconductor, described in Eq. 7.6 for the classical model, and corresponding to the hole diffusion length for the alternative model. Giving a Lambertian absorption, described by Eq. 7.7, and considering negligible reflection losses (with *Transmittance* = 1 – *Absorptance*), one can obtain the distance D (Eq. 7.8).

$$\log(T) = \log(1 - A) = -\alpha D \quad (\text{Eq. 7.7})$$

where *T* the sample transmittance, *A* is the sample absorptance and α the absorption coefficient of hematite at 470 nm (corresponding to the blue diode emission) and taken as 46 nm⁻¹ at this wavelength.¹⁶

$$D = -\alpha^{-1} \log(1 - A) = -\alpha^{-1} \log\left(1 - \frac{\Delta J_{ss-H_2O_2}}{J_{pulse\ intensity}}\right) \quad (\text{Eq. 7.8})$$

where $J_{pulse\ intensity}$ is the photon flux converted in terms of current density with a Si photodiode.

According to the classical model, the distance *D* should increase linearly with the square root of ($V_{appl.} - V_{fb}$) whereas in the multiple trapping model, given the Lambertian function used to obtain *D*, this distance can be approximated to be linear

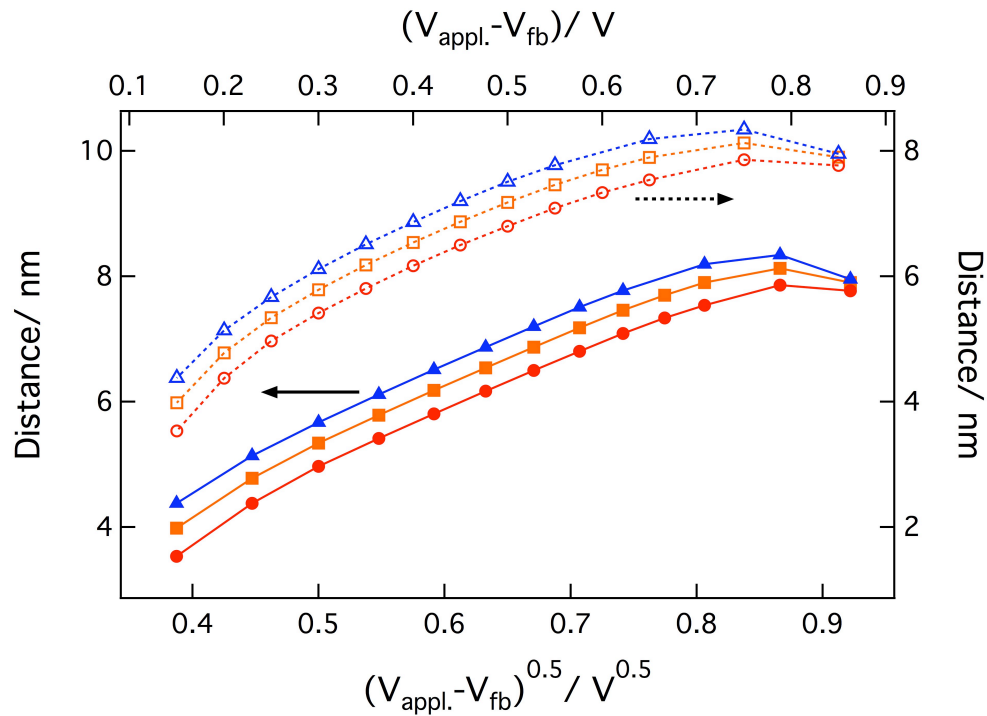


Figure 7.6: Distance D , in nm, representing the thickness inside the hematite film thickness where reacted photogenerated holes are originated from (see text for details), is shown as a function of the square root of the difference between the applied potential $V_{\text{appl.}}$ and the flat band potential V_{fb} (full markers, plain lines, left and bottom axis). This distance D is also shown as a function of the difference between the applied potential $V_{\text{appl.}}$ and the flat band potential V_{fb} (empty markers, broken lines, right and top axis). Data obtained with 1 sun bias light (red squares) is compared to the ones obtained at 0.5 sun (orange circles) and at 0.1 sun bias light (blue triangles).

with $V_{\text{appl.}}$. Figure 7.6 shows the representation of the calculated distance D as a function of the applied bias potential (Fermi level) according to the two models described above. First, the distance D (full markers plain lines) is shown vs. the square root of the difference of the applied potential and the flat band potential (taken as $V_{\text{fb}} = 0.55$ V).¹ This same distance has also been represented vs. the difference of the applied potential and the flat band potential (right and top axis). The use of the flat band potential in the second representation is arbitrary because the flat band potential does not exist in the multiple trapping model.

Visually the distance D appears to better follow linear behavior when plotted vs. the square root of the potentials than vs. the applied potential. For all white light bias intensities, the distance D is found to be linear with $(V_{\text{appl.}} - V_{\text{fb}})^{0.5}$ in the applied potential range 0.8 – 1.1 V vs. RHE with coefficient of determination, R^2 , of the linear regression analysis is over 0.999. In the case of the multiple trapping model, coefficients of determination of ca. 0.99 are found for all white light bias. This latter

model to characterize the behavior of hematite photoanodes cannot be disregarded from this experiment, but the classical model offers a better fit of our results. Additionally, when the semiconductor is highly doped and/or the particle size increases, the screening length shrinks well below the feature dimension and an internal field distribution, associated with band bending, is obtained.¹⁹ The high doping level in hematite may limit the use of this model for hematite photoanodes.

Using Eq. 7.6, the donor density and the effective hole diffusion length can be estimated using the fitting of D vs. $(V_{appl} - V_{fb})^{0.5}$. These numbers are presented in Table 7.1 with figures estimated from a measurement performed at a lower blue light pulse intensity (corresponding to 1.96 mA cm^{-2}). Considering a flat band potential of 0.55 V , the effective hole diffusion length obtained with this model is between 0.6 and 1.4 nm . These values are lower the numbers presented by Kennedy and Frese ($2 - 4 \text{ nm}$)²¹ but in the same order of magnitude. The factor 3 differentiating the numbers shown here and those presented in the 80's may arise from the assumption of a lambertian light absorption similarly than on a flat interface, whereas the samples studied here are nanostructured.

Blue Light Diode Power ^[a] / mA cm^{-2}	White Light Bias Intensity	$L_{D, \text{Eff.}}$ / nm	W_0 / $\text{nm V}^{-0.5}$	N_D / cm^{-3}
4.34 mA cm^{-2}	0.1 sun	1.12	9.08	1.16×10^{20}
	0.5 sun	0.98	8.77	1.15×10^{20}
	1 sun	0.61	8.76	1.15×10^{20}
1.96 mA cm^{-2}	0.1 sun	1.40	8.49	1.23×10^{20}
	0.5 sun	1.24	8.22	1.31×10^{20}
	1 sun	0.69	8.51	1.22×10^{20}

[a]: The power has been converted in term of maximum photocurrent reachable considering an quantum efficiency of unity and measured with a Si diode.

Table 7.1: Effective Hole diffusion length $L_{D, \text{Eff.}}$ in nm, depletion width at an applied potential of one volt over the flat band potential, W_0 in $\text{nm V}^{-0.5}$ and the donor density N_D in cm^{-3} obtained from fitting the data presented in Figure 7.6 with the classical model. These data where obtained at two different blue light diode power (characterized with the maximum photocurrent obtained with a Si diode).

Nevertheless, the figures obtained from this study confirm the very small diffusion length of holes in hematite, which is mentioned in most of hematite

photoanode investigations. The effective hole diffusion length is also found to be shorter at higher bias light intensity than at lower bias light intensity. This can be explained by the increased number of photogenerated electrons located in the diffusion length area at high bias light intensity. A greater density of excited electrons in this area would increase recombination with holes because these photogenerated electrons are not repelled by the space charge field.

The depletion layer width calculated with this method is also in good agreement with the literature reports, which give a value on the order of 8 to 9.5 nm at an applied potential of 1 V *vs.* the flat band potential (W_0). Consequently we found very small depletion layers at lower applied potential, below 6 nm when the applied potential is lower than 0.9 V *vs.* RHE as shown on Figure 7.6. The donor density extracted from W_0 is relevant with the figures calculated earlier with these nanostructures.^{6,16}

This study confirms that the hole diffusion length is smaller than 5 nm in hematite and that the depletion layer is in the 5 – 10 nm range for a donor density of 10^{20} cm⁻³. This high donor density is obtained by heavy doping with silicon at a level of 1.5 at% in this case² and is required to afford efficient electron transport through the $\alpha\text{-Fe}_2\text{O}_3$ film. The depletion layer width and the hole diffusion length have been calculated in 1 M NaOH + 0.5 M H₂O₂ electrolyte, and these parameters would vary in a 1 M NaOH electrolyte as positive charge accumulation at the surface will decrease the band bending and therefore reduce the depletion layer width. However, these numbers could only be considered for Fe₂O₃ photanode only if we can prevent the charge accumulation during water splitting. Thus, this study also justifies the requirement of nanostructures with feature size of about 5 – 10 nm in order to produce efficient water splitting photoanodes based on hematite.

7.4.2. Charge accumulation

In the previous section, the accumulation of holes in traps of an $\alpha\text{-Fe}_2\text{O}_3$ photoanode immersed in NaOH, is assumed to occur on the surface and cause the reduction of the space charge layer width. This phenomenon presumably explains the high onset of the photocurrent and recently, its effect has been reduced by applying an OER catalyst or a passivation layer (see Chapter 7) on the $\alpha\text{-Fe}_2\text{O}_3$ photoanode surface. It is therefore interesting to characterize the number of charges accumulating at the surface at different applied potentials in order to gain understanding of this phenomenon and find methods to eliminate these losses.

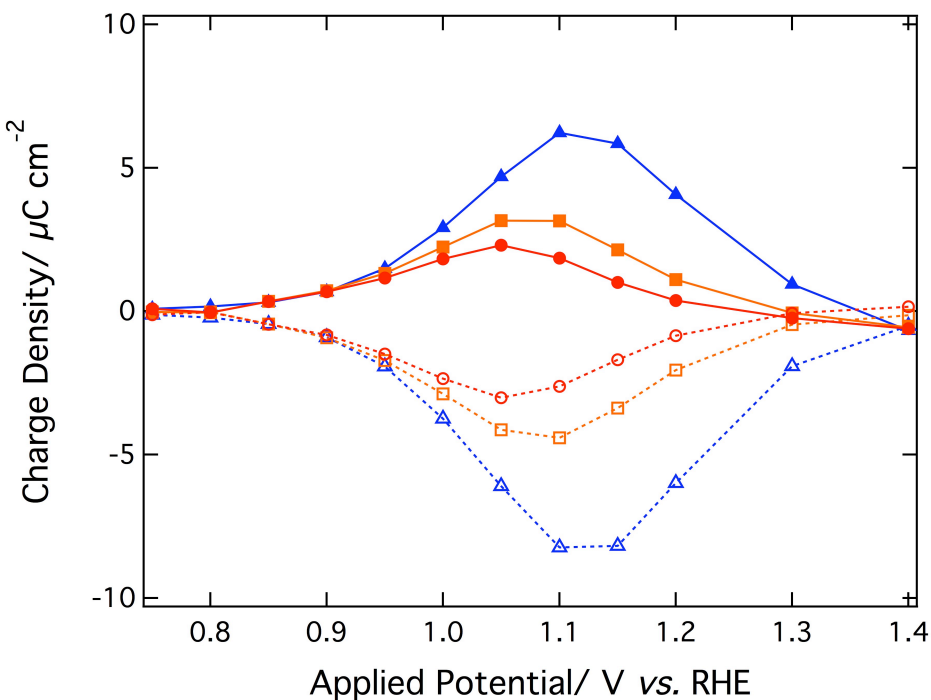


Figure 7.7: Accumulated charge density (full markers, plain lines) and Back reacting charges (empty markers, broken lines) are shown as a function of applied potential with respect to the reversible hydrogen electrode (RHE). The quantities represented in this figure are defined in section 7.3.3. Accumulated and back reacting charges are compared for measurements performed under 1 sun white light bias (100 mW cm^{-2} , red circles), 0.5 sun white light bias (50 mW cm^{-2} , orange squares) and 0.1 sun white light bias (10 mW cm^{-2} , blue triangles).

In order to characterize quantitatively the accumulated charge density, one can consider the area set between the measured photocurrent transient and the square wave defined by the steady state photocurrent before and after the blue light pulse and by the new steady state photocurrent attained during the pulse. The accumulated charges and the back reacting charges (defined in section 7.3.3) are shown *vs.* the applied potential in Figure 7.7. Unlike photocurrent densities, which are normalized to the geometric area (0.502655 cm^2 , corresponding to the illuminated area), the measured charge densities have been normalized to the real Fe_2O_3 surface area, which is equal to the geometric area times the roughness factor, taken as 21 for these nanostructures.¹⁶

First, one can observe that the back reacting charge density corresponds to the inverse of the accumulated charge density. It therefore confirms that during the light pulse a part of the charges are accumulated in the material during the light pulse and that the cathodic current observed after the light pulse arises to bring electrons recombining with the stored holes. The charge accumulation starts at an applied potential of 0.8 V *vs.* RHE for all the different light bias applied. At higher potential, it

rises to reach a maximum, which appears to be increasing with decreasing white light bias. The maximum stored charge density on the surface is 6.3 C cm^{-2} , 3.2 C cm^{-2} and 2.3 C cm^{-2} for 0.1 sun, 0.5 sun and 1 sun bias light respectively. The applied potential required to attain this maximum is cathodically shifted when the bias light is increased, and measured to be 1.05 V, 1.10 V and 1.15 V vs. RHE for increased bias light intensities.

The previous section showed that the effective diffusion length of holes was decreasing with the light intensity. The higher density of accumulated charges can be therefore explained by a greater hole diffusion length at low light intensity allowing more photogenerated holes to reach the surface. However, the hole diffusion length has been measured to be 10 times smaller than the depletion layer width, the former being consequently the main region where photogenerated holes are originated from. This depletion layer width does not depend on the light intensity and makes this assumption unrealistic. Another explanation of the light intensity dependency arises by considering accumulated charges located in energetic traps on the surface, energetically positioned between the valence and the conduction band. The quasi Fermi level (QFL) describes the population of each type of charge carrier (electrons and holes) in a semiconductor separately when their populations are displaced from equilibrium, by light absorption for example. Its position is known to vary logarithmically with light intensity,²² and will influence the occupancy or the vacancy of the surface states if we consider them uniformly distributed in the band gap. Accordingly the relative increase in the QFL will be greater for the measurement performed in 0.1 sun compared to those performed at higher bias light. This would lead to a relatively greater change in the number of trap states emptied as the QFL moves as a result of the pulse light and therefore a higher charge density on the surface can be accumulated on the surface. These traps may be the origin of the difference in overpotential observed in NaOH and H₂O₂ electrolytes even if the different kinetics of the involved reaction cannot be neglected.

These accumulated holes, if located on the surface, will perturb the space charge layer, as they will create a repulsive field for holes locally. Consequently the space charge layer width will decrease while increasing the charge density accumulated at the SCLJ. This phenomenon may explain that charge accumulation is only observable at more anodic potential than 0.8 V vs. RHE, whereas photocurrent is appearing from 0.7 V vs. RHE with hydrogen peroxide electrolyte. The very small depletion layer width at low applied potential (3 – 4 nm) will be very much perturbed

by a small quantity of accumulated holes, repulsing the other photogenerated holes from the surface. If the number of positive charges on the surface, required to cancel the depletion layer field by the accumulated holes repulsion, is small, then no accumulated charges can be measured (no anodic peak in photocurrent transients). The energetic states hosting the accumulated holes in the potential range from the flat band to 0.5 V anodic to V_{fb} may also be responsible for the Fermi level pinning reported with hematite photoanodes.^{5,10,11} The decrease in accumulated charges at applied potential over 1.2 V can be assumed to be due to a greater portion of these traps being inactive for recombination or that the ones filled with holes are at potential low enough compared to O₂/H₂O redox potential to perform the water oxidation reaction. The quasi Fermi level playing an important role on the occupancy of the states or on the potential up to which traps are filled would explain the later decrease of the accumulated charges density at lower light intensity (blue markers for 0.1 sun bias light + blue pulse as compared to the red markers for 1 sun bias light + blue pulse).

7.4.3. Photovoltage amplitudes

The effect of the blue light pulse on the photovoltage has been qualitatively described in section 7.3.4. In particular cases (low bias light and low applied voltage in 1 M NaOH electrolyte), the photovoltage shows a drift before the blue pulse excitation. This drift has been corrected with an exponential function, which has been subtracted, to obtain a flat steady state (before the pulse). This steady state photopotential attained when applying a fixed current under 0.1, 0.5 or 1.0 sun white light bias conditions, is shown *vs.* the expected photopotential (based on the *J-V* characterization, Figure 7.1) on Figure 7.8 for measurement performed in 1 M NaOH and in 1 M NaOH + 0.5 M H₂O₂.

The photopotentials recorded in the electrolyte containing hydrogen peroxide show a very good linearity with the expected potential for all bias light used. When measured in a 1 M NaOH electrolyte, the situation is quite different. At high applied current (corresponding to high expected potentials, 1.3 and 1.4 V *vs.* RHE), the measured photopotential is close to what is expected but under these applied currents, the measured photopotential deviates from the ideal case (when the measured photocurrent = the expected photocurrent). This deviation is more significant for lower white light bias and the photopotential could not reach a value under 1.15 V *vs.* RHE at 0.1 sun light bias (full blue triangles) whereas a

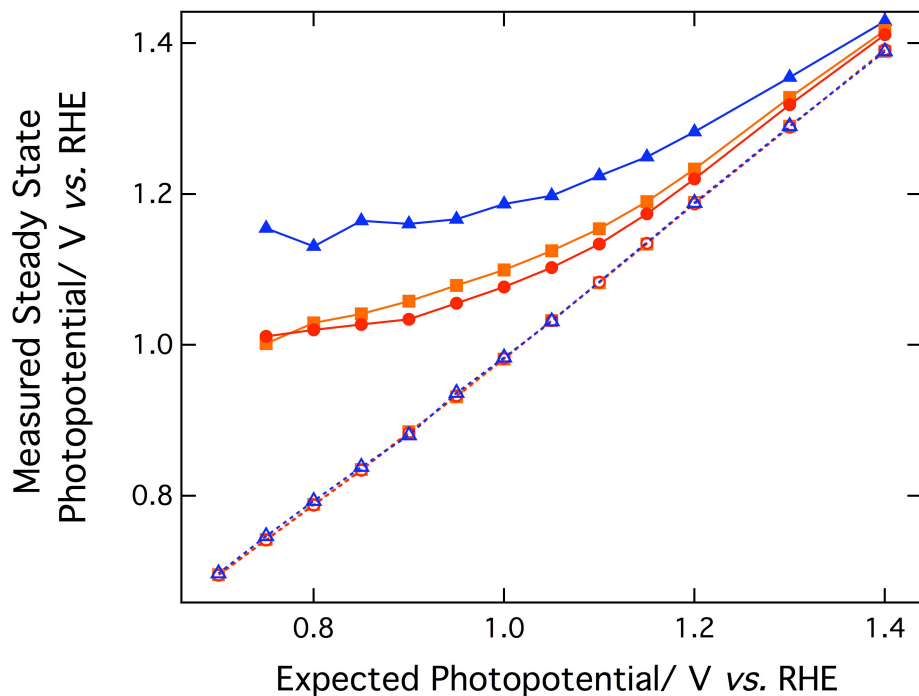


Figure 7.8: Measured steady state photopotential in V vs. RHE is shown as a function of the expected potential in V vs. RHE for measurements performed in 1 M NaOH electrolyte (full markers, plain lines) and in 1 M NaOH + 0.5 M H₂O₂ electrolyte (empty markers, broken lines). The measured photopotential is recorded while applying a fixed current between the photoanode and the counter electrode and three different white light bias: 0.1 sun (10 mW cm⁻², blue triangles), 0.5 sun (50 mW cm⁻², orange squares) and 1.0 sun (100 mW cm⁻², red squares). The expected photopotential was calculated according to potential corresponding to the applied current in Figure 7.1. Measurements exhibiting a drift in steady state conditions (at low applied current and low light intensity) have been corrected by an exponential function. In these cases, the new steady state photopotential obtained after correction replaced the measured photopotential steady state.

photopotential of 1.0 V vs. RHE is attained at low applied current with a light bias of 0.5 sun (full orange squares) or 1 sun (full red circles).

The inability of the photoanode to reach a photopotential close to the expected value occurs in the same potential range of positive charge accumulation at the surface, i.e. 0.8 – 1.2 V vs. RHE. Additionally the bias light dependence seems to indicate that the deviation from linearity is linked with the positive charge carriers being placed in surface states located energetically in the band gap (trap states). The deviation could possibly be a manifestation of Fermi level pinning induced by the presence of these surface states.

Figure 7.9 shows the photovoltage transient amplitude induced by the blue light pulse as a function of the measured steady state photopotential before the light pulse. In 1 M NaOH + 0.5 M H₂O₂ electrolyte (broken lines, empty markers), the amplitude varies linearly with the measured steady state potential up to 1.2 – 1.3 V

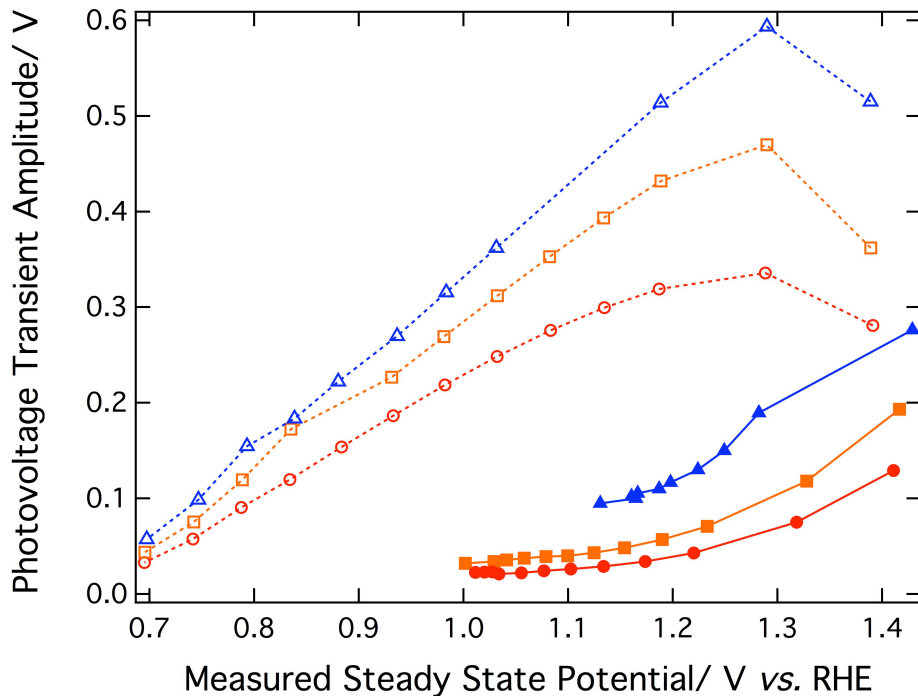


Figure 7.9: Photovoltage transient amplitude in V is shown as a function of the measure steady state photopotential in V vs. RHE for measurements performed in 1 M NaOH electrolyte (ΔV_{ss} , full markers, plain lines) and in 1 M NaOH + 0.5 M H_2O_2 electrolyte ($\Delta V_{ss, H_2O_2}$ empty markers, broken lines). The photovoltage transients are recorded while applying a fixed current between the photoanode and the counter electrode and three different white light bias: 0.1 sun (10 mW cm⁻², blue triangles), 0.5 sun (50 mW cm⁻², orange squares) and 1.0 sun (100 mW cm⁻², red circles). The applied currents are calculated according to correspond to the applied potential in the JV characteristics shown in Figure 7.1.

vs. RHE before curving down and even decreasing. The increase in $\Delta V_{ss, H_2O_2}$ is consistent with the increase in the QFL of electrons due to the increase in light intensity during the pulse (bias light + blue light pulse). As explained before, the QFL increases logarithmically with the light intensity,²⁰ leading to a greater relative increase between the measurement performed with 0.1 sun compared to 1 sun light bias. Accordingly, Figure 7.9 shows higher photocurrent transient amplitude with decreasing white light bias for both electrolytes.

The amplitudes measured in 1M NaOH (ΔV_{ss}) are much less significant compared to those observed in the H_2O_2 containing electrolyte (10 times less approximately). In the potential range where charge accumulation occurs, the photovoltage transient amplitudes showed a very small increase whereas after 1.2 V vs. RHE the increase is much more significant. It suggests again that surface states play a role in this potential range for the photovoltage transient amplitudes. Surface states seem to only play a role in the 1 M NaOH electrolyte, possibly explained by their different reactivity. A hole located in a surface state might be able to oxidize

H_2O_2 but cannot oxidize water which would ultimately lead to a different participation in the increase of the photovoltage. As H_2O_2 oxidation is a more simple reaction than water oxidation (one electron transfer), it is also possible that direct hole transfer occurs from the valence band to the redox potential species and in this case surface states would not participate in the photocurrent or photovoltage transient.²³

7.4.4. Time Constants

The photocurrent transients are fitted with monoexponential functions in four different regions when measured in NaOH electrolyte: between the beginning of the blue pulse and the photocurrent transient maximum (τ_{J1}), between the maximum and the end of blue pulse (τ_{J2}), between the end of the blue pulse and the transient minimum (τ_{J3}), and between the transient minimum and the last point of measurement (τ_{J4}). When the photocurrent transient is measured in the electrolyte containing H_2O_2 , only two time constants are determined: $\tau_{J12-\text{H}_2\text{O}_2}$, obtained with a monexponential fitting of the photocurrent transient between the beginning and the end of the blue light pulse, and $\tau_{J34-\text{H}_2\text{O}_2}$ obtained in the time region after the end to the blue pulse. These times constants are compared in Figure 7.10 a and b.

The six time constants can be separated in two different ranges: first the rise and the decay of the photocurrent transient (red squares and orange circles for both experiments) are at low applied potentials around 0.01 s and decrease to a value of 0.005 – 0.006 s with increasing applied potential. These time constants are the same for measurements performed in only sodium hydroxide and in sodium hydroxide and hydrogen peroxide electrolytes and are therefore likely to be related to the same phenomena.

Two time constants (τ_{J2} and τ_{J4} , in NaOH) behave differently with the applied potential and correspond to the decay of the photocurrent in the time period when charge accumulation occurs and to the rise of the photocurrent in the time period when electrons rush from the external circuit to recombine with the accumulated charges. τ_{J2} and τ_{J4} are slower processes (0.02 s at low bias potential), increases after 0.8 V vs. RHE and reach a plateau (0.2 s) at about 1.1 – 1.2 V vs. RHE. This increase is in the potential range where charge accumulation occurs at the surface of the photoanode and suggests a relation between these time constants with the processes related to the accumulation/recombination of the stored charges on the surface.

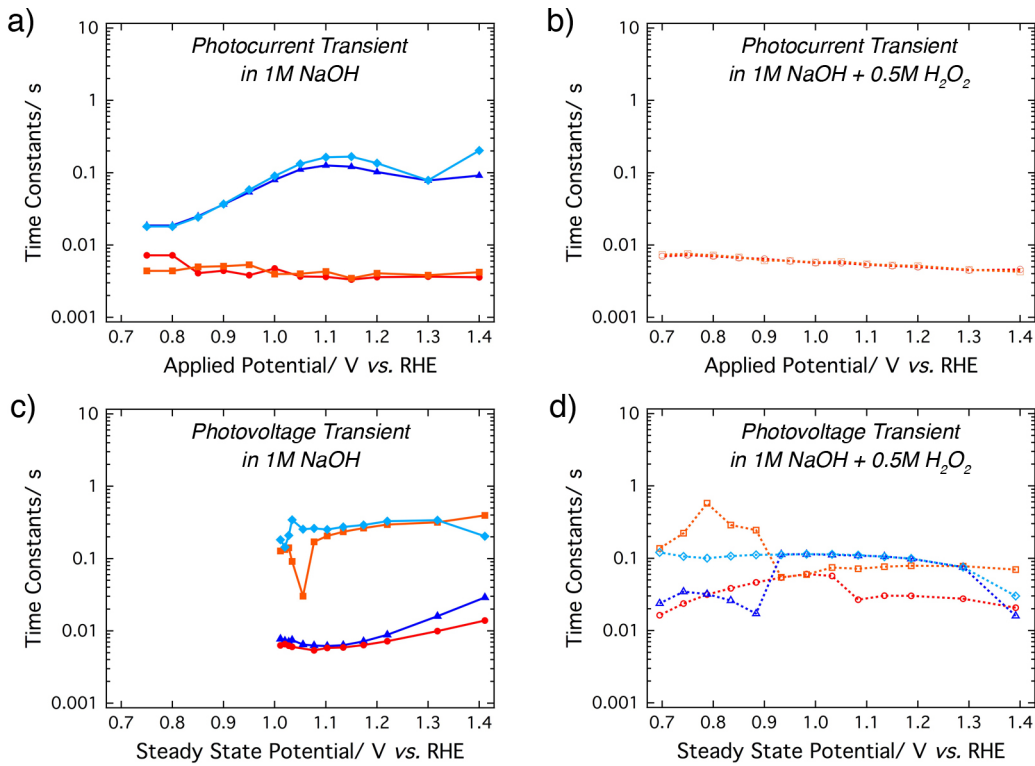


Figure 7.10: Time constants obtained from the fitting of photocurrent and photovoltage transients measured with 1 sun white light bias (100 mW cm^{-2}) and respectively applied potential (vs. RHE) and applied current (between the photoanode and the counter electrode). (a) τ_{J1} (full red circles, plain lines), τ_{J2} (full blue triangles, plain lines), τ_{J3} (full orange squares, plain lines) and τ_{J4} (full light blue diamonds, plain lines), obtained from measurement in 1 M NaOH, are shown as a function of the applied potential with respect to RHE. (b) $\tau_{J12-H_2O_2}$ (empty red circles, broken lines) and $\tau_{J34-H_2O_2}$ (empty orange squares, broken lines) obtained from measurement in 1 M NaOH + 0.5M H₂O₂, are shown as a function of the applied potential with respect to RHE. (c) τ_{V12a} (full red circles, plain lines), τ_{V12b} (full orange squares, plain lines) characteristics of the photovoltage rise in 1 M NaOH, and τ_{V34a} (full blue triangles, plain lines), τ_{V34b} (full light blue diamonds, plain lines) characteristics of the photovoltage decay are shown in function of the steady state potential measured before the beginning of the pulse. (d) $\tau_{V12a-H_2O_2}$ (empty red circles, broken lines), $\tau_{V12b-H_2O_2}$ (empty orange squares, broken lines) characteristics of the photovoltage rise in 1 M NaOH + 0.5 M H₂O₂, and $\tau_{V34a-H_2O_2}$ (empty blue triangles, broken lines), $\tau_{V34b-H_2O_2}$ (empty light blue diamonds, broken lines) characteristics of the photovoltage decay are shown in function of the steady state potential measured before the beginning of the pulse. All time constants are defined in the text.

Figure 7.10 also shows the time constants obtained from the fitting of the photovoltage transients, when measured in 1 M NaOH (c) and in 1 M NaOH + 0.5 M H₂O₂ (d). In both cases, the rise and the decay of the photovoltage are fitted with a biexponential giving for each two time constants: τ_{V12a} (red circles), τ_{V12b} (orange squares) and τ_{V34a} (blue triangles), τ_{V34b} (light blue diamonds) respectively. In Figure 7.10c, two different processes (according to their time constants) can be clearly separated and appear in the rise and the decay of the photovoltage. The fastest process (τ_{V12a} and τ_{V34a}) has been determined to happen within a time of 0.01 s whereas the slowest process (τ_{V12b} and τ_{V34b}) within a time of 0.1–1 s. The four time

constants determined in Figure 7.10d are also in this range (0.01 – 1 s) but do not show any trends. It is possible that the time constants for the different processes are so close in this electrolyte that it is difficult to separate them and therefore mixing or exchange of the time constants occur during the fitting.

From this experiment, it seems that two phenomena can be separated in the photocurrent transient and photovoltage transient experiments. One is faster and occurs with a time length of 0.01 s while the slower phenomenon occurs on a time scale from 0.1 to 1 s. It is possible that the value of fast process (0.01 s) is a limitation of our system as the points were taken every 0.001 s. Nevertheless, it would correspond to an overestimation of this time constant and would mean that the process is slightly faster (maybe in the range of 0.001 – 0.01 s) as it was still detectable.

As the slower process cannot be determined from photocurrent transients in H_2O_2 , this phenomenon can be related to the filling of surface states or recombination of charges on the surface (hole and electron capture by surface traps, hole transfer from these traps to electrolyte species). The faster process can be related to the conduction of electrons (electron diffusion, bulk recombination) through the nanostructure to the external circuit. However, a model is required to properly assign the determined time constants to specific processes or phenomena in the photoanodes. Nevertheless it is interesting to compare the time constants measured here with ones found literature.

Glasscock *et al.* determined two time constants from the fit of photocurrent transients with mean values of 0.03 s and 3 s for doped films (Ti and Si doping).²⁴ The fast process has been determined to be in the same range as the one found in this study. The slow process has been measured to be one order of magnitude higher than measured here, possibly due to the different surface properties of their reactive magnetron sputtered films. Recently, the dynamics of photogenerated holes has been measured by transient absorption spectroscopy in the μs to ms time scale.¹⁸ The decay of the transient absorption data has been fitted with a stretched exponential function with a lifetime of 3 s (± 1 s) and the signal has been assigned to long lived holes that avoid rapid recombination and become active for water splitting. For the oxidation of methanol, the lifetime has been measured at 0.4 s. Even if these values have been found to be 10 times longer than the slower process here, they are also related to events involving holes on the surface. Wijayantha *et al.* have developed a model including two processes with separated time scale to discuss

photoelectrochemical impedance spectra of iron oxide photoanodes (deposited by aerosol assisted chemical vapor deposition).²³ The slower process is measured to last between 0.1 and 10 s, and is assigned to the hole transfer from surface states to the redox couples while the faster process is in the time scale range 0.01 – 1s and has been assigned to the electron capture by surface traps. Finally, in conventional electrochemical impedance spectroscopy (in dark conditions), two features occurring at different frequencies are also observed.²⁵ The fast process is characterized at high frequencies (in the kHz – 100 Hz frequency range, corresponding to 0.001 – 0.01 s) and is assigned to bulk and space charge events. The slow process (from 10 Hz to 0.1 Hz, corresponding to 0.1 to 10 s) has been assigned to surface events⁶ or to the influence of intra band gap states in the bulk or on the surface.^{13,26,27}

In conclusion, these studies using different electrochemical techniques confirm that two different processes are happening in the ms to s time scale. The faster process, measured from 0.001 s to 0.1 s and at 0.01s in our study is likely to be related to electron conduction (by diffusion outside the depletion layer) or to the electron capture by energetic traps. The slower one determined between 0.01 s to the 3 s, and measured between 0.1 and 1s in our study is likely to be related to the lifetime of holes on the surface or on the filling of surface traps. However the latter process is usually considered to occur at a faster time scale.

7.5. Conclusion

This work establishes a new technique to quantitatively analyze photocurrent and photovoltage transient spectra and gain knowledge on both bulk and surface events occurring on the surface of hematite during water oxidation. Photocurrent and photovoltage transients were obtained with a short blue light pulse on an APCVD hematite held at a bias potential (or current) under white bias light.

Photocurrent transient exhibits charge accumulation during the light pulse and a cathodic peak after due to the recombination of theses accumulated holes with electrons diffusing from the external circuit. The establishment of a new steady state photocurrent (due to the light pulse) shows the same behavior with applied potential than the *J-V* characterization with a large onset for water oxidation. When hydrogen peroxide was added to the electrolyte, the classical model (with formation of a depletion layer) and diffusion based model (with flat bands and conduction based on multiple trapping) were applied to fit the relation between transient amplitude and applied potential. Without disregarding the possible application of the second model,

the classical model showed a better fit to our result. A space charge layer of 8 – 9 nm (at an applied potential of 1 V vs. V_{fb}) and a very small hole diffusion length (0.5 – 2 nm depending on the bias light intensity) were calculated according to the classical model. This technique gives a reasonable value as compared to the value calculated by Kennedy and Frese, that is often taken as a reference in the literature.

The density of accumulated charges was found to be dependent on the applied potential and measured between 2 and 6 $\mu\text{C cm}^{-2}$. Because of the white light bias dependence, the accumulation was assumed to occur in surface states that can be deactivated with increasing bias light intensity. The appearance of charge accumulation (and of the later onset of the photocurrent in 1 M NaOH electrolyte) at higher applied potential than the onset of the photocurrent in H_2O_2 electrolyte was explained by the disappearance of the space charge field due to accumulated charges at the interface. The photovoltage transients showed different behaviors in the two different electrolytes tested here. It was again assumed to be due to the charging/discharging of surface states causing Fermi level pinning.

Different time constants were also obtained from the fitting of the photocurrent and photovoltage transients. Two different processes were determined and their related time constants were compared to others found in the literature. The fast process (on the order of 0.01 s) has been assigned to electron transport in the bulk and the slow process (in the range of 0.1 to 1 s) has been assigned to the hole trapping in surface states and/or to the transfer of holes from surface states to the electrolyte.

This study provides a new tool to compare iron oxide photoanodes and especially the quality of their surface with the charge accumulation quantification. The use of different electrolytes with different catalyst or surface passivation layer would help in assigning the processes observed during this transient. The better understanding of surface events brought by this novel technique should ultimately lead to the decrease of the overpotential for water splitting, i.e. the additional energy given by the second solar system in a tandem cell, enhancing the performance of hematite for the efficient and sustainable storage of solar energy through water splitting.

7.6. References

- (1) Dotan, H.; Sivula, K.; Graetzel, M.; Rothschild, A.; Warren, S. C. *Energy Environ. Sci.* **2011**, 4, 958.
- (2) Kay, A.; Cesar, I.; Graetzel, M. *J Am Chem Soc* **2006**, 128, 15714.

- (3) Zhong, D. K.; Cornuz, M.; Sivula, K.; Graetzel, M.; Gamelin, D. R. *Energy Environ. Sci.* **2011**, *4*, 1759.
- (4) Tilley, S. D.; Cornuz, M.; Sivula, K.; Graetzel, M. *Angew Chem Int Edit* **2010**, *49*, 6405.
- (5) SANCHEZ, C.; SIEBER, K.; SOMORJAI, G. *J Electroanal Chem* **1988**, *252*, 269.
- (6) Le Formal, F.; Tétreault, N.; Cornuz, M.; Moehl, T.; Grätzel, M.; Sivula, K. *Chem. Sci.* **2011**, *2*, 737.
- (7) Dare-Edwards, M.; Goodenough, J.; Hamnett, A.; Trevellick, P. *J Chem Soc Farad T 1* **1983**, *79*, 2027.
- (8) Iwanski, P.; Curran, J.; Gissler, W.; Memming, R. *J Electrochem Soc* **1981**, *128*, 2128.
- (9) Wilhelm, S.; Yun, K.; Ballenger, L.; Hackerman, N. *J Electrochem Soc* **1979**, *126*, 419.
- (10) Duret, A.; Gratzel, M. *J Phys Chem B* **2005**, *109*, 17184.
- (11) Shinar, R.; Kennedy, J. *J Electrochem Soc* **1983**, *130*, 392.
- (12) Cornuz, M.; Grätzel, M.; Sivula, K. In *Chem. Vap. Deposition* 2010; Vol. 16, p 291.
- (13) Kennedy, J.; Frese, K. *J Electrochem Soc* **1978**, *125*, 723.
- (14) Zhang, P.; Chi, M.; Sharma, S.; McFarland, E. *J. Mater. Chem.* **2010**, *20*, 2013.
- (15) Zhang, Z.; Zakeeruddin, S.; O'Regan, B.; Humphry-Baker, R.; Grätzel, M. *J Phys Chem B* **2005**, *109*, 21818.
- (16) Cesar, I.; Sivula, K.; Kay, A.; Zboril, R.; Grätzel, M. *J. Phys. Chem. C* **2009**, *113*, 772.
- (17) Gerischer, H. *J Electroanal Chem* **1975**, *58*, 263.
- (18) Pendlebury, S. R.; Barroso, M.; Cowan, A. J.; Sivula, K.; Tang, J.; Graetzel, M.; Klug, D.; Durrant, J. R. *Chem Commun* **2011**, *47*, 716.
- (19) Bisquert, J. In *Phys. Chem. Chem. Phys.* 2008; Vol. 10, p 49.
- (20) Bisquert, J. *J Phys Chem C* **2007**, *111*, 17163.
- (21) Kennedy, J.; Frese, K. *J Electrochem Soc* **1978**, *125*, 709.
- (22) Memming, R. *Semiconductor electrochemistry*, **1998**, Wiley-VCH, Weinheim
- (23) Upul Wijayantha, K. G.; Saremi-Yarahmadi, S.; Peter, L. M. *Phys. Chem. Chem. Phys.* **2011**, *1*.
- (24) Glasscock, J. A.; Barnes, P. R. F.; Plumb, I. C.; Savvides, N. *J Phys Chem C* **2007**, *111*, 16477.

- (25) Sivula, K.; Le Formal, F.; Grätzel, M. In *Chemsuschem* 2011; Vol. 4, p 432.
- (26) Horowitz, G. *J Electroanal Chem* **1983**, *159*, 421.
- (27) Leduc, J.; Ahmed, S. *J Phys Chem-Us* **1988**, *92*, 6661.

CHAPTER 8.

FINAL CONCLUSIONS AND

OUTLOOK

The work conducted during this thesis aimed at improving nanostructured film efficiency and enhancing the understanding of hematite photoanodes for water splitting. In chapter 2, we have discussed the recent efforts to increase the solar-to-hydrogen efficiency of hematite and the major limitations of this material were also outlined.

As shown in the introduction, the first constraint, namely the conduction band below the hydrogen evolution potential, can be straightforwardly overcome with connecting in series a second solar system (a photocathode or a photovoltaic cell) to supply the additional energy for the electrons to reduce water into hydrogen. Therefore this thesis presented new strategies and techniques developed to address and characterize the two other main limitations. As discussed in details in the respective chapters, the host-guest approach (Chapter 3), investigations on the thin film photoactivity (Chapters 4 and 5) and the study of trap passivation on surface and the interface characterization (Chapters 6 and 7) contributed to increase in performance and in understanding. The conclusions for each section are summarized below.

8.1. The Host-Guest Approach

To address the second limitation of hematite, namely the short carrier diffusion lengths compared to the long light penetration depth, we demonstrated a new concept for water splitting in Chapter 3: the host-guest approach. Within this approach, the light absorption and water oxidation roles are decoupled from the electron conduction by depositing an extremely thin layer of hematite onto a mesoporous host. The effectiveness of the host guest concept was evidenced by a photoanode composed of a thin layer of hematite coating a WO_3 scaffold that exhibited a *ca.* 20 % increase in photocurrent as compared to control devices. Accordingly, increased quantum efficiency, especially from wavelengths near the hematite absorption edge (where photons have the longest penetration depths) was also observed, as a greater fraction of photons could be absorbed closer the hematite/electrolyte interface.

Interestingly, this new approach allows using undoped hematite layers, and therefore deposition of thicker hematite films (due to the larger space charge layer width). In this investigation, the enhancement in performance was nevertheless limited by the host material (WO_3 absorbs a significant part of the solar spectrum with a band gap of 2.6 eV) and the minimum thickness of hematite required to observe photoactivity. Indeed in this study, a 60 nm thick layer of hematite had to be used to show photoelectrochemical enhancement. This minimum thickness corresponds to 5 – 10 times the space charge layer width and ideally, it should be decreased in order to fully achieve the potential of the host guest approach. The inactivity of extremely thin films, also observed with other techniques, was therefore investigated in the second part of the thesis.

8.2. Hematite extremely thin film photoactivity

The photoactivity of hematite extremely thin films was investigated by two means: first by controlling the nucleation of films deposited by spray pyrolysis and second by comparing the effect of embedded plasmonic particles in the thin films to plasmonic particles deposited on the surface of iron oxide nanoplatelets.

In Chapter 4, we showed the critical influence of a substrate pretreatment on the photoelectrochemical performance of iron oxide thin film. The pretreatment, which consists in spraying TEOS on the FTO substrate at high temperature, was evidenced to form a SiO_x sub-monolayer and to modify the properties of hematite thin films prepared atop by the spray pyrolysis of $\text{Fe}(\text{acac})_3$. These films were photoactive from

a 12.5 nm optical thickness exhibiting a surprisingly high photocurrent density of 0.55 mA cm⁻² at 1.43 V vs. RHE (only absorbing 25 % of the incident light), whereas the films formed on untreated substrate required a 25 nm thickness to be photoactive. Further investigations attributed the improved photoelectrochemical performance on the modified substrate to a different nucleation process (Franck-van der Merwe growth), leading to enhanced crystallinity and surface organization. This study emphasized the critical roles of film formation and crystallinity on the performance of hematite thin films. The effect of a buffer layer on the nucleation of ultrathin hematite films was recently confirmed by another study employing a Ga₂O₃ underlayer.¹

Chapter 5 focused on the impact of gold plasmonic nanoparticles, approximately 50 nm in diameter, on α-Fe₂O₃ photoelectrochemical performance. No enhancement was observed when the nanoparticles were embedded in a flat film, possibly due to poor spectral overlap between the plasmonic resonance and semiconductor absorbance. A relative enhancement in the spectral response of the electrode with the surface configuration was observed, which was assigned to the energy transfer from plasmons to the semiconductor. However, the water splitting performance were lowered due to recombination at the semiconductor / metal interface. This investigation established that plasmons can be employed in hematite to localize the electron – hole pair photogeneration at a short distance from the interface with the electrolyte but it is necessary to have a large overlap between the spectral responses and to electrically isolate the nanoparticles to avoid charge recombination at their surface. For the latter issue, one can coat the nanoparticles with a high dielectric layer. Whilst their isolation should be carefully controlled due to silver instability it would also be interesting to explore Ag nanoparticles because of silver plasmonic resonance that is blue-shifted as compared to gold.

8.3. Surface passivation and characterization

The two last chapters of the thesis tackled the third limitation of hematite, *i.e.* the large overpotential required for the water splitting photocurrent to onset.

The study, presented in Chapter 6, identified two distinct causes—surface traps and slow oxidation kinetics—for the high overpotential observed in state-of-the-art nanostructured hematite photoanodes. The coating of nanostructured hematite photoanodes with a very thin layer (0.1 to 2 nm) of alumina by ALD, cathodically shifted the onset of the photocurrent by as much as 100 mV. A record water oxidation photocurrent density of 0.42 mA cm⁻² was then obtained at 0.9 V vs. RHE

under standard testing conditions after applying a Co^{2+} catalyst. Further investigation by analyzing transient photocurrents, electrochemical impedance, and photoluminescence spectra provided convincing evidences that the cathodic shift afforded by the Al_2O_3 overlayer is due to the passivation of surface trapping states. A later study confirmed that the onset potential can be cathodically shifted by coating the hematite photoanodes with 13-group oxides (Al_2O_3 , Ga_2O_3 and In_2O_3) thin overlayer.² The overlayers were deposited by chemical bath deposition and a decrease by *ca.* 200 mV of the onset potential was observed.

These surface traps, assumed to cause Fermi level pinning and charge accumulation at low bias potential, were also evidenced in the photocurrent and photovoltage transient study shown in Chapter 7. The measurements of additional photocurrent obtained with a blue light perturbation in H_2O_2 electrolyte enabled the determination of the space charge layer width (8 – 9 nm at 1 V vs. V_{fb}) and a significantly small hole diffusion length (0.5 – 2 nm). However the charge accumulation in NaOH electrolyte are assumed to reduce the space charge layer width at low bias potential, severely restricting the application of the Gerischer model on hematite photoanodes performing water splitting. The density of accumulated charges was quantified to be between 2 and 6 $\mu\text{C cm}^{-2}$ and because of the white light bias dependence, the accumulation was assumed to occur in surface states. The different photovoltage transient behaviors observed in the two electrolytes were also assumed to be due to the charging/discharging of surface states causing Fermi level pinning. The two different time constants determined in this study were compared to the literature and assigned to electron conduction and surface processes respectively. This investigation provides a new tool to characterize photoelectrochemical events occurring in hematite during water splitting (under bias potential and illumination), and future studies using this technique should further the understanding of the limiting factors.

8.4. Outlook

Iron oxide remains very promising to convert the sun energy into hydrogen through the water photolysis reaction. Nevertheless, the present study, as others in the recent literature, has shown that nanostructuring is required for this material, and the feature size should not be larger than 5 – 10 nm in order to obtain efficient sunlight conversion. This is particularly true when iron oxide is highly doped to provide good electron conductivity, causing the space charge layer to be very small.

One method to enlarge the depletion layer width is to use undoped hematite to absorb the light and drive the hole towards the surface whereas a transparent mesoporous host achieves the electron conduction to the substrate. This concept demonstrated in this thesis, has exhibited in another study the highest reported external quantum efficiency by an undoped hematite based photoanode (46% at $\lambda = 400$ nm) using a TiSi_2 nanonet as host and a 25 nm hematite layer deposited by ALD.³ Investigations on this strategy should be pursued and development of deposition techniques producing efficient thin films (such as ALD) should be carefully scrutinized. In particular control of the interface between the host (or substrate) and the hematite layer has been shown to be a key parameter for the thin film photoactivity.

Another method to enhance the conversion efficiency of hematite photoanode would be to increase the distance where photogenerated holes are attracted towards the surface, using gradient doping for instance.

Finally, we can also mention that the different techniques (underlayers / overlayers) developed in this study can be employed for other applications using charge transfer at metal oxide semiconductor interfaces such as fuel cells, photovoltaics, sensors, and light-emitting electrochemical cells.

While there is still a long road before reaching solar-to-hydrogen efficiencies suitable for commercial application, the work presented in this thesis allowed us to reach the best photocurrent density attained at low bias potential (0.9 V vs. RHE) with hematite. This significant improvement could only be achieved by both improving our understanding of processes occurring in the semiconductor during water photolysis and controlling device fabrication techniques. The use of inexpensive materials to convert our most renewable source of energy will ultimately lead to secure our energetic and economic future. To update Thomas Edison's quote, we should continue to put money on the sun and solar energy. What a source of power!

8.5. References

- (1) Hisatomi, T.; Brillet, J.; Cornuz, M.; Le Formal, F.; Tetreault, N.; Sivula, K.; Graetzel, M. *Accepted in Faraday Discussion*, **2011**
- (2) Hisatomi, T.; Le Formal, F.; Cornuz, M.; Brillet, J.; Tetreault, N.; Sivula, K.; Graetzel, M. *Energy Environ. Sci.* **2011**, *4*, 2512.
- (3) Lin, Y.; Zhou, S.; Sheehan, S. W.; Wang, D. *J. Am. Chem. Soc.* **2011**, *133*, 2398.

APPENDIX A.

SUPPORTING INFORMATION TO CHAPTER 5

Interband absorption.

The goal here is to determine the functional form of the component in the absorbance spectrum arising from interband absorption, to subtract it from the measured UV-Visible absorbance spectra and arrive at the absorbance from the surface plasmon resonance. The optical properties of a material can be described by its frequency dependent, complex dielectric function:

$$\epsilon(\omega) = \epsilon_1(\omega) + i\epsilon_2(\omega) \quad (\text{Eq. A1})$$

Where ϵ_1 is the real component and ϵ_2 is the imaginary component. In free-electron metals, the dielectric function contains a component that arises from absorption by conduction electrons, resulting in an oscillation of the electron density at a resonance frequency, which is an intraband transition. In noble metals, the dielectric function also contains a component arising from the excitation of single electrons to an excited state above the Fermi level, which is an interband transition. It is assumed here that the interband component is not size dependent, if the particle diameter is greater than 10 nm.¹ In Au, the frequencies of the intraband and interband transitions can partially overlap.¹ The total (experimental) complex dielectric function can be expressed in terms of its components from the two transitions:²

$$\epsilon(\omega) = \epsilon^f(\omega) + \delta\epsilon^b(\omega) \quad (\text{Eq. A2})$$

$$\epsilon^f(\omega) = \epsilon_1^f(\omega) + i\epsilon_2^f(\omega) \quad (\text{Eq. A3})$$

$$\delta\epsilon^b(\omega) = \delta\epsilon_1^b(\omega) + i\delta\epsilon_2^b(\omega) \quad (\text{Eq. A4})$$

Where ϵ^f is the intraband component and $\delta\epsilon^b$ is the interband component. From equation (Eq. A2), it can be seen that once either component has been

Appendix A

calculated, the other can be readily determined by simply subtracting from the experimental dielectric function. The intraband component can be calculated using the Drude-Lorentz-Sommerfeld model:¹

$$\epsilon^f(\omega) = 1 - \frac{\omega_p^2}{\omega^2 + i\Gamma\omega} = 1 - \frac{\omega_p^2}{\omega^2 + \Gamma^2} + i \frac{\omega_p^2 \Gamma}{\omega(\omega^2 + \Gamma^2)} \quad (\text{Eq. A5})$$

Where $\omega_p = \sqrt{ne^2/\epsilon_0 m_e}$ is the Drude plasma frequency (with $\hbar\omega_p = 8.8 \text{ eV}$ for Au)² $\Gamma = v_f/l$ is the relaxation frequency, $v_f = 1.39 \times 10^6 \text{ m/s}$ is the Fermi velocity,³ and $l = 42 \times 10^{-9} \text{ m}$ is the electron mean free path length.¹ After calculation of the intraband component from equation (Eq. A5), the interband component is obtained from (Eq. A2) using experimental data from the literature.⁴

The interband absorption is a function of the joint density of states of the Au band structure and the transition matrix.⁵ If it is assumed that the transition matrix is constant, i.e. the transition probability is constant, then:⁵

$$\delta\epsilon^b(\omega) \propto J(\hbar\omega) \propto c_A(\hbar\omega) \quad (\text{Eq. A6})$$

Where $J(\hbar\omega)$ is the joint density of states and $c_A(\hbar\omega)$ is the absorption cross section, which is proportional to the absorbance by the concentration and path length. The term $\delta\epsilon^b(\omega)\omega^2$ is plotted as a function of photon wavelength along with the absorbance spectrum of the 48 nm Au nanoparticles on hematite on Figure A1. The $\delta\epsilon^b(\omega)\omega^2$ term was adjusted using a linear scaling factor to set the two spectra equal at $\lambda = 350 \text{ nm}$, where the interband absorbance is expected to dominate the spectra.

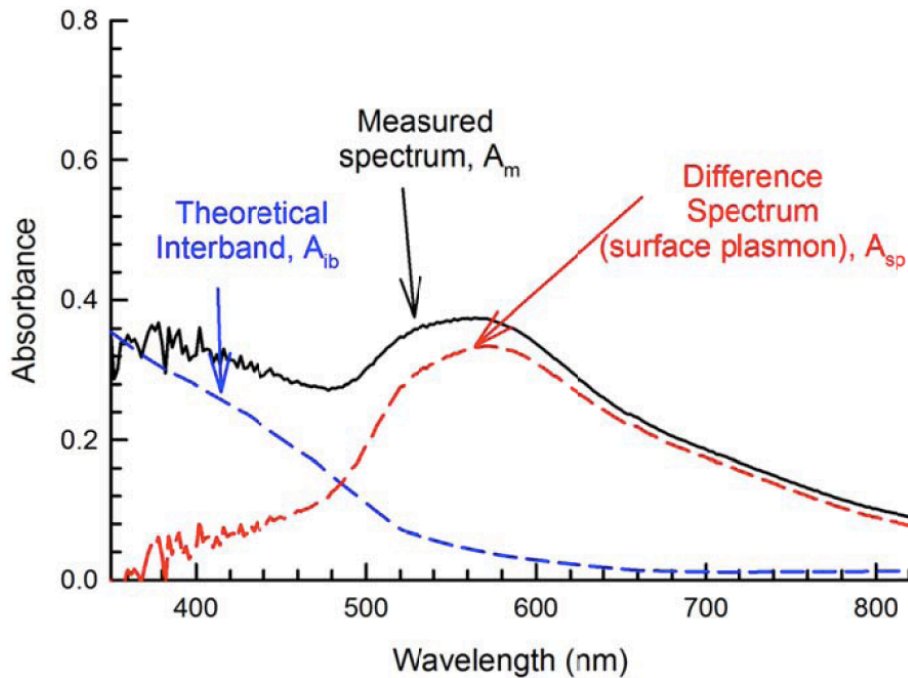


Figure A.1: Measured Absorbance spectrum of the 48 nm Au nanoparticles on silicon-doped Fe₂O₃ platelets taken from Figure 5.3 (black-solid); calculated interband absorbance spectrum using equation (A6) with rad.s⁻¹ as the frequency unit and a linear scaling factor of 2.2 10⁻³³ (blue-dashed); difference spectrum (dashed-red) between the measured spectrum and theoretical interband, which approximates the surface plasmon absorbance of the sample.

Calculation of the absorption and scattering cross sections of the Au nanoparticles.

The ratio of the absorption to the scattering cross section can be used to estimate the probability of one process occurring over the other, with the larger cross section having a higher probability of occurrence.

The absorption and scattering cross sections of spherical particles that are small with respect to the wavelength of light can be estimated by the following equations:⁶

$$C_{sca} = \frac{k^4}{6\pi} |\alpha|^2 \quad (\text{Eq. A7})$$

$$C_{abs} = k \operatorname{Im}(\alpha) \quad (\text{Eq. A8})$$

Where k is the wave number, α is the complex particle polarizability, and $\operatorname{Im}(\alpha)$ is the imaginary component of the complex polarizability.

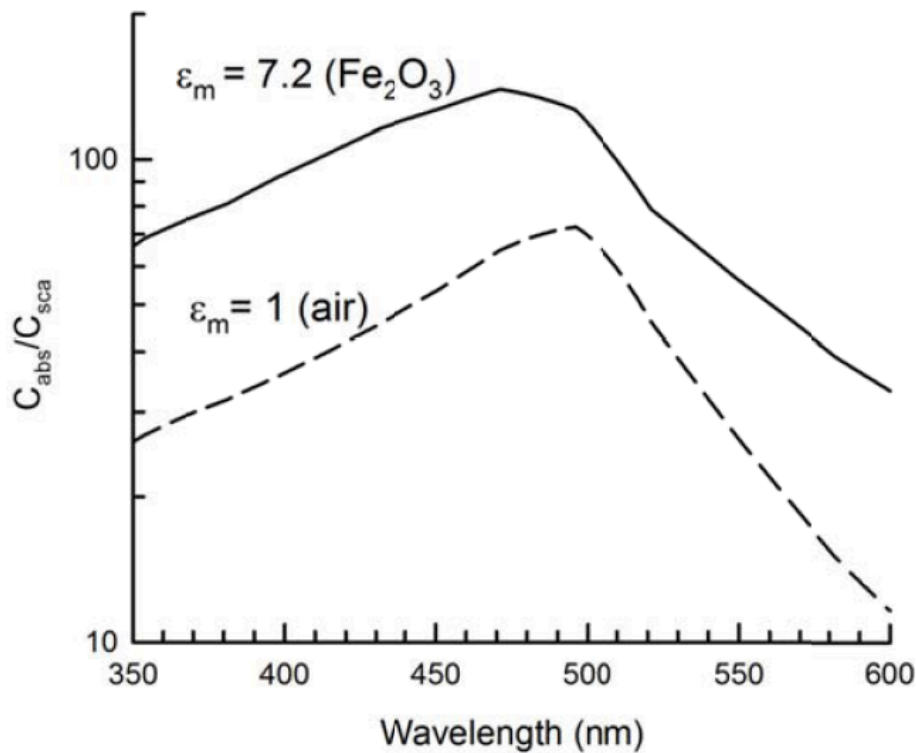


Figure A.2: Ration of the absorbance to the scattering cross sections for 48 nm diameter Au nanoparticles embedded in air and Fe_2O_3

The complex polarizability can be calculated using the following equation:⁶

$$\alpha = 4\pi a^3 \frac{\epsilon - \epsilon_m}{\epsilon + 2\epsilon_m} \quad (\text{Eq. A.9})$$

Where a is the particle radius, ϵ is the complex dielectric function for Au, and ϵ_m is the dielectric constant of the embedding medium (80 for iron oxide)⁷. The ratio of the absorption cross section to the scattering cross section is plotted in Figure A2 for embedding in air and Fe_2O_3 . In both cases it can be clearly seen that the absorption cross section is more than 10 times larger than the scattering cross section.

Comparison of nanoparticles in solution with those adsorbed onto an electrode.

Gold nanoparticles with a diameter of 50 nm were synthesized following literature protocols using a sodium citrate-driven reduction to form seed with a 15 nm size, followed by a hydroxylamine hydrochloride-driven growth to a 50 nm diameter.⁸ UV-Vis spectra were recorded between 380 nm and 800 nm before and after adsorption of the gold particles onto platelet-type USP hematite electrode.

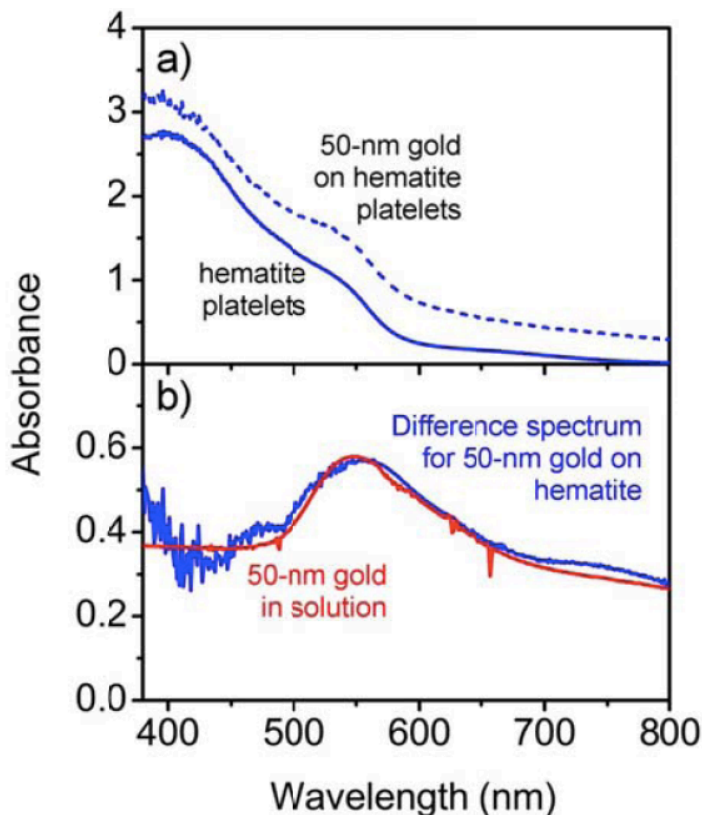


Figure A.3: (a) UV-Visible absorbance of the as-made hematite platelets modified with 50 nm Au nanoparticles. (b) UV-visible absorbance: the blue line is the difference spectrum of the spectra in part (a) of the figure; the red line is for 50 nm gold nanoparticles in aqueous solution.

Adsorption of the particles onto the hematite electrode was achieved using electrophoretic deposition, as described below.

Au nanoparticles deposited by electrophoresis.

Citrate-stabilized Au nanoparticles were synthesized following a procedure from the literature,⁹ and had a mean size of 15.0 nm and standard deviation of 1.5 nm, as measured by transmission electron microscopy (TEM). The citrate-stabilized gold nanoparticles were deposited by electrophoretic deposition. A field of 30 V cm^{-1} was applied for 30 minutes to deposit the nanoparticles using a Pt counter electrode held at negative potentials relative to the working electrode ($\alpha\text{-Fe}_2\text{O}_3$ nanoplatelet thin film). After deposition, the particles size distribution had broadened, with a mean particle size of 11.6 nm and a standard deviation of 3.8 nm as measured by scanning electron microscopy (SEM). The photoelectrochemical performance of hematite electrodes modified with 15 nm particles is compared to control samples (only hematite) on Figure A.5 and A.6.

Appendix A

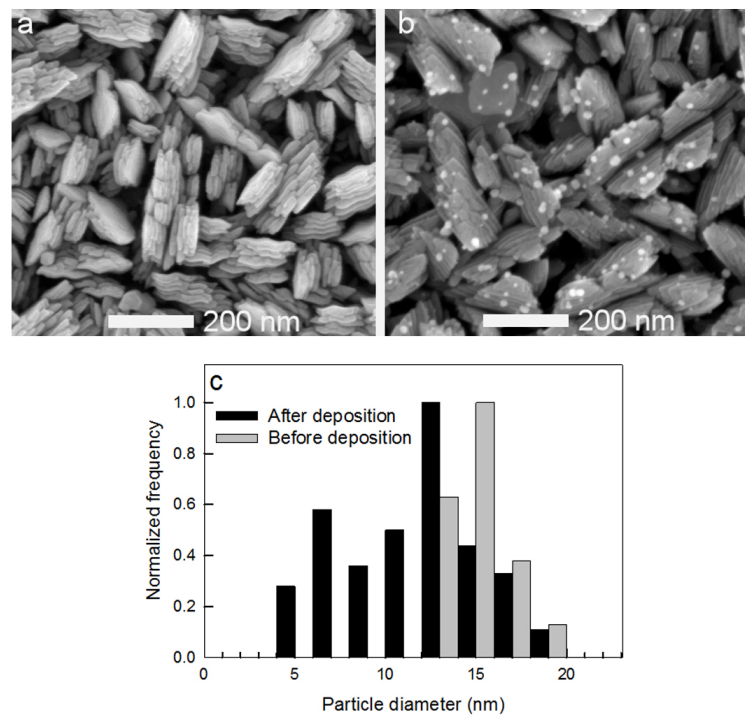


Figure A.4: SEM images of the hematite platelets (a) before and (b) after electrophoretic deposition of 15 nm Au nanoparticles; (c) size distribution of Au nanoparticles measured from TEM images before deposition and SEM images after deposition onto hematite platelets

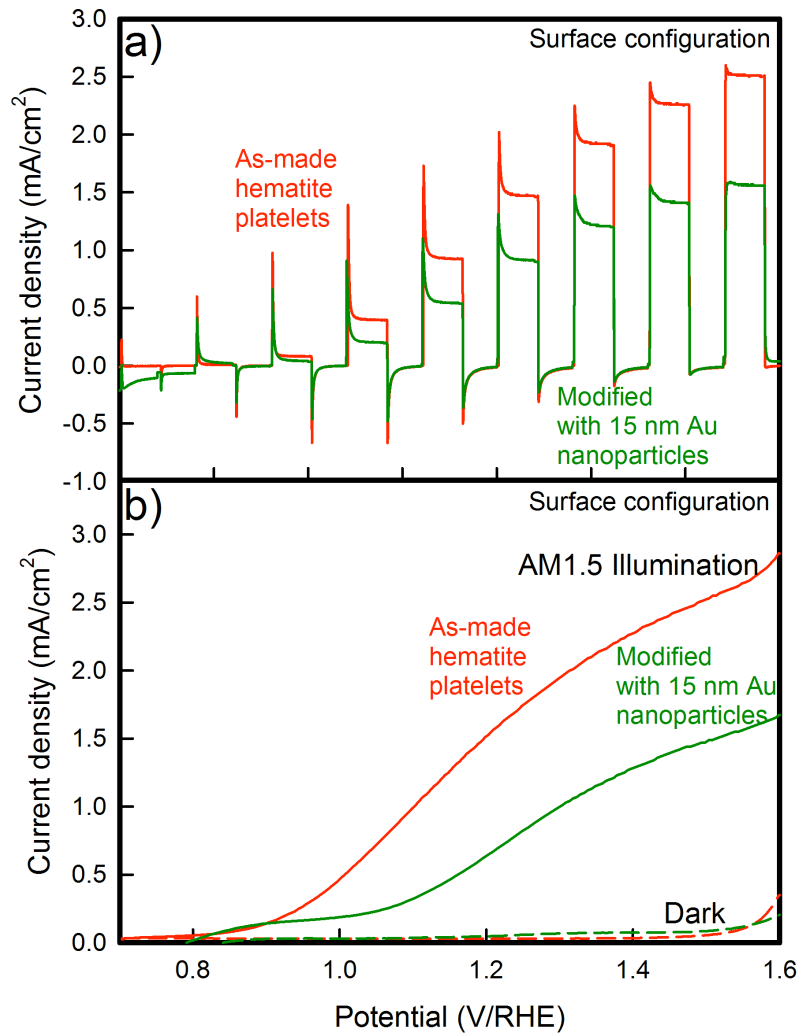


Figure A.5: Current density as a function of electrode potential under (a) chopped simulated AM1.5 illumination at a frequency of 0.5 Hz (b) under continuous simulated AM 1.5 illumination.

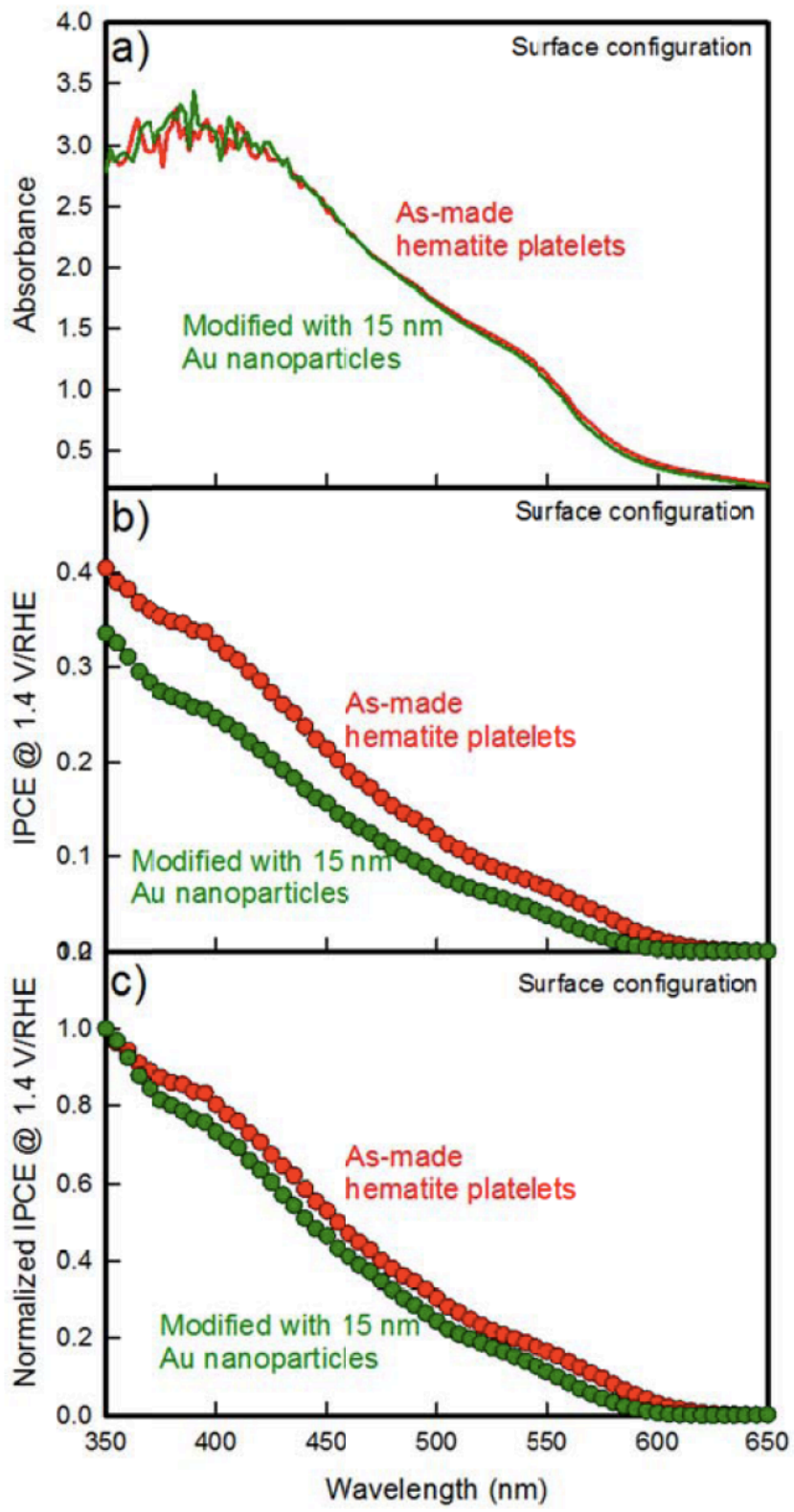


Figure A.6: Spectral characteristics of the as-made hematite platelets and hematite platelets modified with 15 nm Au nanoparticles: (a) UV-visible absorbance, (b) IPCE measured at 1.4 V vs. RHE and (c) normalized IPCE (at 350 nm) measured at 1.4 V vs. RHE.

References

- (1) Kreibig, U.; Vollmer, M. *Optical properties of metal clusters*; Springer: Berlin; New York **1995**
- (2) Cooper, B.; Ehrenrei, H.; Philipp, H. *Phys Rev* **1965**, *138*, A494.
- (3) Kittel, C. *Introduction to solid state physics*; 8th ed.; Wiley: Hoboken, NJ, **2005**.
- (4) Johnson, P.B.; Christy, R.W. *Phys. Rev. B* **1972**, *6*, 4370
- (5) Christensen, N.; Seraphin, B. *Phys Rev B-Solid St* **1971**, *4*, 3321.
- (6) Bohren, C.F.; Huffman, D.R. *Absorption and scattering of light by small particles*; Wiley: New York **2004**
- (7) Kennedy, J.; Frese, K. *J Electrochem Soc* **1978**, *125*, 723.
- (8) Turkevich, J.; Stevenson, P.C.; Hillier, J. *Discuss. Faraday Soc.* **1951**, *11*, 55.
- (9) LizMarzan, L. M.; Giersig, M.; Mulvaney, P. *Langmuir* **1996**, *12*, 4329

APPENDIX B

SUPPORTING INFORMATION TO CHAPTER 6

TiO₂ overlayer test.

In addition to the alumina treatment by ALD (see chapter 6), APCVD hematite photoanodes were covered with an amorphous layer of TiO₂ by ALD to investigate its role as an overlayer. Figure B1 is analogous to Figure 6.2 and shows the water oxidation photocurrent density at 1.03 V (yellow triangles), 1.23 V (orange squares) and 1.43 V (red circles) vs. RHE, for a control photoanode and samples covered with different thicknesses of TiO₂ (adjusted to correspond to the Al₂O₃ thicknesses applied).

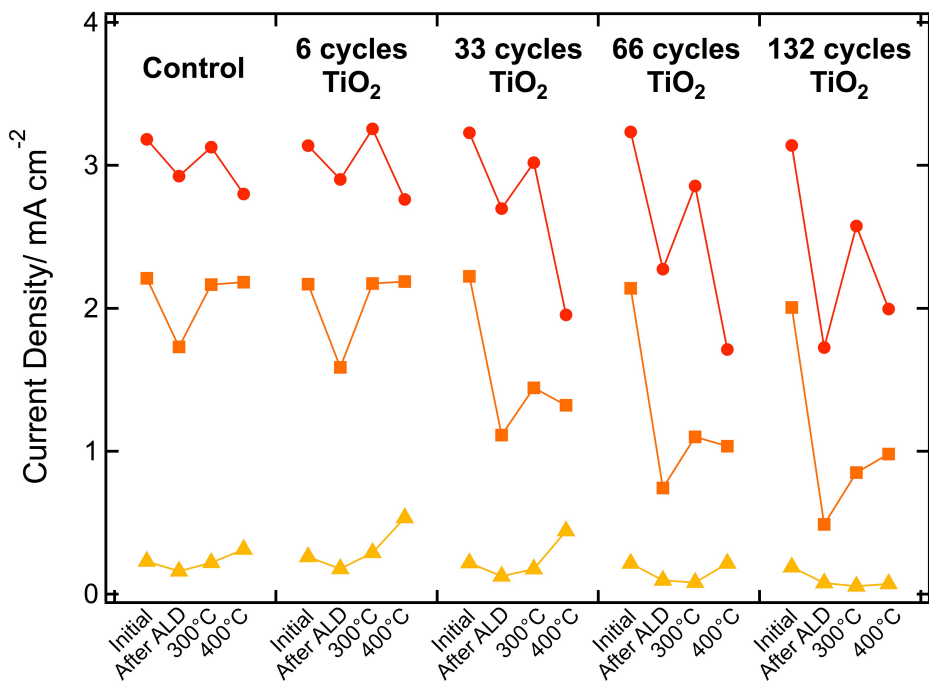


Figure B.1: Current densities, in mA cm^{-2} of the prepared photoanodes at 1.03 V (yellow triangles), at 1.23 V (orange squares) and at 1.43 V (red circles) vs. RHE, are presented for a control and samples covered by different number of cycles of TiO₂ ALD (6, 33, 66 and 132 ALD cycles at 200 °C) to obtain thicknesses comparable to that of the Al₂O₃ overlayers (0.1, 0.5, 1.0 or 2.0 nm as measured by ellipsometry on a Si reference). All samples were measured before and after ALD as well as after annealing at 300°C and 400°C.

EIS characterization of an hematite photoanode.

Figure B2 shows the Nyquist plots of an APCVD photoanode (without alumina overlayer) corresponding to the electrochemical impedance measurements (EIS) performed in dark and under illumination conditions at key applied potentials. Before the onset of the photocurrent by the illuminated sample, the two measurements exhibit the same features: two superimposed semicircles (as shown by the inflection point observed in the figures below) but with a smaller high frequency arc for the electrode under illumination, resulting in a smaller R_{SC} according to our model and as expected according to the increased conductivity in the semiconductor afforded by illumination. At a potential when photocurrent onsets in the illuminated electrode, two features are still apparent in the Nyquist plots for both conditions but the two arcs are more distinguishable on the light measurement due to the lower value of R_{CT} (current is now flowing through the SCLJ during illumination). Finally, when EIS was performed at high bias potential (when water oxidation current starts to flow also in the dark sample), the same behavior for both conditions was observed (i.e. only the low frequency arc is now noticeable and decreasing as the dark current starts to flow). From these observations we are confident to assign the high frequency arc to processes occurring in the semiconductor and the low frequency arc to charge transfer processes. Overall, there is no evidence that a distinct process is occurring (e.g. surface intermediates specific to photo-oxidation) in the illuminated sample, which would be evidenced by a third arc.

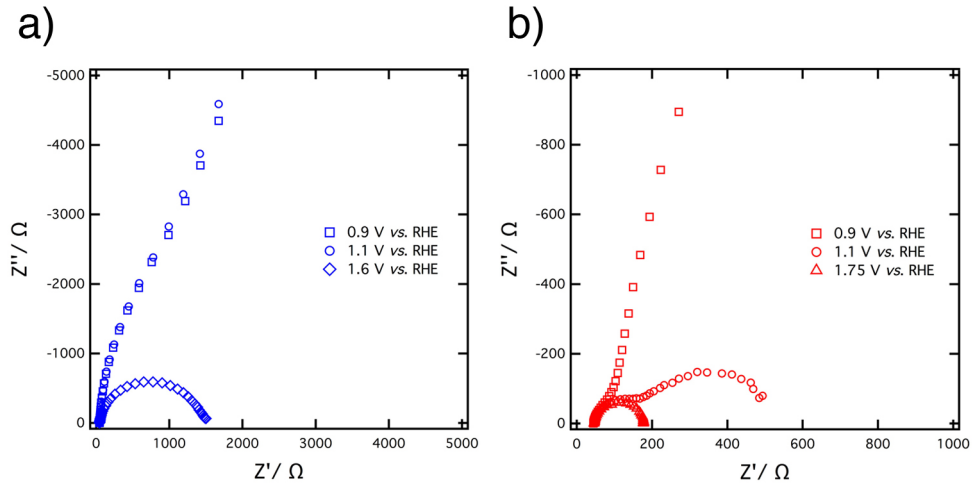


Figure B.2: Nyquist plots representing the EIS measurements performed on a hematite APCVD sample (not covered with alumina) in the dark (a - blue markers) and under AM 1.5 illumination (b – red markers) at three key applied potentials: before onset of the photocurrent (squares - 0.9V vs. RHE), when photocurrent is flowing in the illuminated sample (circles - 1.1V vs. RHE) and at the onset of dark current (triangles - 1.6 V and 1.75 V vs. RHE for measurement under dark and illumination respectively). Two different applied potentials are shown for the last condition to enable observation on the disparate scales.

ACKNOWLEDGEMENTS

First of all, I thank Prof. Grätzel for giving me the opportunity to conduct a thesis in his prestigious and stimulating research group. I am particularly thankful for allowing me to work in the fascinating field of photoelectrochemical water splitting. I appreciated the freedom I was granted to follow my research interests and the good advice received during meetings.

I would like to warmly thank Dr. Kevin Sivula for supervising my work, especially in the lab and for written reports. He acted as a research mentor for me and a significant part of my research skills have been obtained from him.

Since research is much more interesting and exciting when it is done in a team, I also want to thank people I had the chance to work with in the *hydrogen production* sub-group: Dr. Elijah Thimsen, Dr. Scott Warren, Dr. S. David Tilley, Dr. Céline Leroy, Dr. Takashi Hisatomi, Adriana Paracchino, Jérémie Brillet and Maurin Cornuz. Thank you for your precious advice, tips and fruitful discussions during meetings.

I highly appreciated working in the great and stimulating atmosphere offered by the LPI. I would like to express my gratitude to LPI as a whole and to the several visitors that came to Lausanne for teaching and guiding me to where I am now. I especially thank Dr. Robin Humphry-Baker (for IGOR programming, photoelectrochemical setup and ski skills), Dr. Etienne Baranoff (for being a pleasant office mate and for passionate debates on Science and Chemistry) and Dr. Pierre Infelta (for computer support and thermodynamics teaching classes). I also thank Dr. Nazeeruddin and Dr. Shaik Zakeeruddin for the Hydrogen network fund and for taking care of me during my master respectively. This thesis at EPFL was accompanied by the reliable administrative support of Mme Gonthier, Mme Gourdou, and Anne-Lene Odegaard from the Doctoral School – thank you.

I would like to acknowledge the FP6 Marie Curie Program (*hydrogen network*), managed by G.E. Kroes, which provided financial support during the three first years of my PhD. I also appreciated the several conferences / workshops I attended through this program and during which I exchanged with great researchers and met a lot of interesting people. A special thank here for Jérémie who was a great companion for all these trips. I am also thankful to Dr. Thomas Dittrich from the Helmholtz Center (Berlin, Germany) who accommodated me during a two weeks visit

in Berlin, and people from CIME (M. Cantoni and F. Bobard) for their help in electron microscopy.

A special word of thanks goes to the people who proof-read this thesis and made it readable: Dr. Robin Humphry-Baker, Dr. Kevin Sivula, Dr. Nicolas Tétreault, Dr Etienne Baranoff and Dr. Thomas Moehl.

This experience in EPFL was very pleasant and enjoyable, and this was largely due to the many friends I made here. So many thanks to Takeru, Nicolas, Leo-Philipp, Sophie, Adriana, David, Etienne, Soo-Jin, Jun-ho, Julien, Maurin, Hugues, Francine, Pierre, Kevin, Joel, Thomas, Jan, Angela, Jelissa... and all the others for the countless discussions and the good moments spent around coffee, lunch or beer. Special thanks to Arianna who brought me a lot of support and great times this past year.

Finalement, je tiens à remercier chaleureusement mes parents pour leur soutien sans faille durant toutes les années qui m'ont amené jusqu'ici. Je remercie également ma soeur (et sa famille) pour m'avoir entraîné vers des études de chimie (sûrement sans le vouloir) et pour m'avoir reçu si gentiment durant mes pérégrinations anglaises. Je remercie également mes amis d'Athis Mons pour avoir maintenu leur constante amitié depuis des années malgré la distance qui nous sépare.

CURRICULUM VITAE

Florian Le Formal
Born January 6th, 1984 in Juvisy sur Orge (91), France
florian.leformal@gmail.com

Education

- 2007-2011: PhD in the Chemistry and Chemical Engineering Department of EPFL (Lausanne, Switzerland). Thesis Advisor: Pr. Michael Grätzel
Thesis work: *On the Morphology and Interfaces of Hematite Photoanodes for Solar Photoanode for Solar-Driven Water.*
- 2007: European M.Sc. in the Materials Science department at the European School of Chemistry, Polymers and Materials Science (ECPM, Strasbourg, France)
Master thesis: *Stability of Dye-Sensitized Solar Cells,*

Professional Activities and Research Experience

- 2007-2010: Co-management of European Marie Curie Project “hydrogen”
FP6 European network including 7 academic and 1 industrial partners, grouping theoretical and experimental chemists to work on sustainable use of hydrogen as an energy vector.
Activities: writing scientific and financial reports, participation in meetings with partners, organization and discussion of the project audit.
- 2006-2007 Assistant Researcher, SINTEF, Trondheim, Norway
In collaboration with NTNU (Technical university of Trondheim).
Research Topics: electrochemical characterization of Transparent Conductive Oxide (TCO) layers, synthesis of Alkaline Fuel Cell cathodes, purification of Silicon by electrolysis at high temperature.
- 2005: Internship at the *Institut de Science et d’Ingenierie Supramoléculaires* (Strasbourg, France)
Transfer of scientific contents on new medias for Pr. J.M. Lehn (Nobel Prize 1987).

Teaching experience

- Atoms, Ions and Molecules (Basic Chemistry) for first year bachelors in chemistry, biology and pharmacy.
- Chemical Thermodynamics (4 semesters) for second year bachelor in chemistry.

Research Interests

- Solar Energy Conversion
- Nanoscale properties
- Metal oxide semiconductors
- Semiconductor electrochemistry
- Charge Transfer at Interfaces
- Bottom-Up approach

Languages

French, English, German

Honor and Awards

- Gold AA (Advances in Advance) medal for the publication “Controlling Photoactivity in Ultrathin Films of Hematite For Solar Water Splitting” (Adv. Funct. Mater.)
- Best Speaker of the day at the 3rd European Research Training Network «hydrogen» meeting, “Hydrogen For the Future”, Warsaw (Poland)

List of scientific publications

1. Solar hydrogen production with semiconductor metal oxides: New directions in experiment and theory.
A. Valdés, J. Brillet, M. Grätzel, H. A. Hansen, H. Jónsson, P. Klüpfel, S. Klüpfel, G.-J. Kroes, F. Le Formal, I. C. Man, R. S. Martins, Jens K. Nørskov, J. Rossmeisl, K. Sivula, and M. Zäch, *Submitted to PCCP 2011*
2. A Ga₂O₃ underlayer as an isomorphic template for ultrathin hematite films toward efficient photoelectrochemical water splitting
T. Hisatomi, J. Brillet, M. Cornuz, F. Le Formal, N. Tetreault, K. Sivula, M. Grätzel *Accepted in Faraday Discussion, 2011*
3. Cathodic shift in onset potential of solar oxygen evolution on hematite by 13-group oxide overayers
T. Hisatomi, F. Le Formal, M. Cornuz, J. Brillet, N. Tetreault, K. Sivula, M. Grätzel *Energy Environ. Sci. (2011)*, 4 (7) pp. 2512-2515
4. Solar water splitting: progress using hematite (α -Fe₂O₃) photoelectrodes
K. Sivula, F. Le Formal, M. Grätzel. *Chem. Sus. Chem. (2011)* 4 (4) pp. 432-449
5. Passivating surface states on water splitting hematite photoanodes with alumina overayers
F. Le Formal, N. Tétérault, M. Cornuz, T. Moehl, M. Grätzel, K. Sivula. *Chem. Sci. (2011)* 2 (4) pp. 737
6. Adsorbate-localized states at water-covered (100) SrTiO₃ surfaces
S. Raghavan, A. Carvalho, F. Le Formal, N. Setter, S. Öberg, P.R. Briddon, *Appl. Phys. Lett. (2011)* 98 (1) pp. 012106

7. Influence of plasmonic Au nanoparticles on the photoactivity of Fe_2O_3 electrodes for water splitting
E. Thimsen, F. Le Formal, M. Grätzel, S. C. Warren. *Nano. Lett.* (2011) 11 (1) pp. 35-43
8. Enhanced-light-harvesting amphiphilic ruthenium dye for efficient solid-state dye-sensitized solar cells
M. Wang, .S.J Moon, D. Zhou, F. Le Formal, N.L. Cevey-Ha, R. Humphry-Baker, C. Grätzel, P. Wang, S.M. Zakeeruddin, M. Grätzel *Adv. Funct. Mater.* (2010) 20 (11) pp. 1821-1826
9. Photoelectrochemical water splitting with mesoporous hematite prepared by a solution-based colloidal approach
K. Sivula, R. Zboril, F. Le Formal, R. Robert, A. Weidenkaff, J. Tucek, J. Frydrych, M. Grätzel *J Am Chem Soc* (2010) 132 (21) pp. 7436-7444
10. Controlling photoactivity in ultrathin hematite films for solar water-splitting
F. Le Formal, M. Grätzel, K. Sivula *Adv. Funct. Mater.* (2010) 20 (7) pp. 1099-1107
11. Multi-walled carbon nanotubes functionalized by carboxylic groups: Activation of TiO_2 (anatase) and phosphate olivines (LiMnPO_4 ; LiFePO_4) for electrochemical Li-storage
L. Kavan, R. Bacsa, M.Tunckol, P. Serp, S.M.. Zakeeruddin, F. Le Formal, M. Zukalova, M. Grätzel *J. Power Sources* (2010) 195 (16) pp. 5360-5369
12. Examining architectures of photoanode-photovoltaic tandem cells for solar water splitting
J. Brillet, M. Cornuz, F. Le Formal, J.-H. Yum, M. Grätzel, K. Sivula *J. Mater. Res.* (2010), 25 (1) pp. 17-24
13. $\text{WO}_3\text{-Fe}_2\text{O}_3$ photoanodes for water splitting: A host scaffold, guest absorber approach
K. Sivula, F. Le Formal, M. Grätzel *Chem. Mater.* (2009) 21 (13) pp. 2862-2867

International conferences, workshop, collaboration abroad

Oral presentation

1. *Hydrogen* MCRTN network final meeting, Noordwijkerhout, The Netherlands, Nov. 2010
Oral presentation: “Hematite Thin Films for Solar Driven Water Splitting”
2. Invited speaker at the Helmholtz Center, Berlin, Germany, July 2010. This talk was given at the occasion of a two weeks visit to Dr. Thomas Dittrich (collaboration) for testing material developed during the PhD with surface photovoltage (SPV) characterization.
Oral presentation: “Solar Driven Water Splitting Using Hematite Thin films”
3. Hydrogen for the future, MCRTN *hydrogen* network conference, Warsaw, Poland, October 2009. This talk was awarded as the best talk of the day.
Oral presentation: “Solar Driven Water Splitting : Principle and An Example with Hematite”

4. European Materials Research Society (EMRS) – Spring Meeting, Strasbourg, France, June 2009
Oral presentation: “Solar Water-Splitting With Hematite Thin Film”
5. *Hydrogen MCRTN* network mid-term meeting, Reykjavik, Iceland, Sept. 2010
Oral presentation: “Recent Progress in α - Fe_2O_3 photoanodes for water photoelectrolysis”

Poster presentation

1. CUSO Summer school *From Structure to Function in Nanomaterials*, Villars, Switzerland, August 2010
Poster presentation: “Extremely Thin films of Hematite for Solar Water Splitting”
2. Material research Society (MRS) – Spring Meeting, San Francisco, USA, April 2010
Poster presentation: “Extremely Thin films of Hematite as a Sensitizer for Water Photolysis”
3. Swiss Chemical Society (SCS) – Fall Meeting, Lausanne, Switzerland, September 2009
Poster presentation: “Nanostructured Hematite Photoanodes For Solar Hydrogen Production”
4. DTU Summer School, Sandbjerg Estate, Denmark, August 2009
Poster presentation: “Extremely Thin films of Hematite as a Sensitizer for Water Photolysis”
5. 3rd International Conference on the Industrialisation of DSC, Nara, Japan, April 2009
Poster presentation: “Solar Water Splitting Using a α - Fe_2O_3 /DSSC Tandem Cell Architecture”
6. Energissima, Swiss Forum on Energy, Freiburg, Switzerland, April 2008
Poster presentation: “Direct Production of Hydrogen from Water and Sunlight”

Scientific society membership

- Material research society (MRS)
- European Material Research Society (EMRS)